

ESD-TDR-64-148

Vol. II

PROCEEDINGS OF THE THIRD TROPOSPHERIC REFRACTION

EFFECTS MEETING

(In Two Volumes)

VOLUME II

**ESD RECORD COPY**

RETURN TO  
SCIENTIFIC & TECHNICAL INFORMATION DIVISION  
(ESTI), BUILDING 1211

Analytical and Experimental Refraction Research Results

JANUARY 1966

Prepared for

DIRECTORATE OF AEROSPACE INSTRUMENTATION

ELECTRONIC SYSTEMS DIVISION

AIR FORCE SYSTEMS COMMAND

UNITED STATES AIR FORCE

L. G. Hanscom Field, Bedford, Massachusetts



**ESD ACCESSION LIST**

ESTI Call No. AL 49367

Copy No. 1 of 1 cys.

Distribution of this document is unlimited.

Project 705.1

Prepared by

THE MITRE CORPORATION  
Bedford, Massachusetts

Contract AF19(628)-2390

ESRI

AD0628772



When US Government drawings, specifications, or other data are used for any purpose other than a definitely related government procurement operation, the government thereby incurs no responsibility nor any obligation whatsoever, and the fact that the government may have formulated, furnished, or in any way supplied the said drawings, specifications, or other data is not to be regarded by implication or otherwise, as in any manner licensing the holder or any other person or corporation, or conveying any rights or permission to manufacture, use, or sell any patented invention that may in any way be related thereto.

Do not return this copy. Retain or destroy.

ESD-TDR-64-148

Vol. II

PROCEEDINGS OF THE THIRD TROPOSPHERIC REFRACTION

EFFECTS MEETING

**ESD RECORD COPY**

(In Two Volumes)

RETURN TO  
SCIENTIFIC & TECHNICAL INFORMATION DIVISION  
(ESTI), BUILDING 1211

VOLUME II

Analytical and Experimental Refraction Research Results

JANUARY 1966

Prepared for

DIRECTORATE OF AEROSPACE INSTRUMENTATION

ELECTRONIC SYSTEMS DIVISION  
AIR FORCE SYSTEMS COMMAND  
UNITED STATES AIR FORCE  
L. G. Hanscom Field, Bedford, Massachusetts



**ESD ACCESSION LIST**

ESTI Call No. AL 49367

Copy No. 1 of 1 cys.

Distribution of this document is unlimited.

Project 705.1

Prepared by

THE MITRE CORPORATION  
Bedford, Massachusetts

Contract AF19(628)-2390

ESRI

AD0628772



ESD-TDR-64-148

Vol. II

PROCEEDINGS OF THE THIRD TROPOSPHERIC REFRACTION

EFFECTS MEETING

**ESD RECORD COPY**

(In Two Volumes)

RETURN TO  
SCIENTIFIC & TECHNICAL INFORMATION DIVISION  
(ESTI), BUILDING 1211

VOLUME II

Analytical and Experimental Refraction Research Results

JANUARY 1966

Prepared for

DIRECTORATE OF AEROSPACE INSTRUMENTATION

ELECTRONIC SYSTEMS DIVISION

AIR FORCE SYSTEMS COMMAND

UNITED STATES AIR FORCE

L. G. Hanscom Field, Bedford, Massachusetts



**ESD ACCESSION LIST**

ESTI Call No. AL 49367

Copy No. 1 of 1 cys.

Distribution of this document is unlimited.

Project 705.1

Prepared by

THE MITRE CORPORATION  
Bedford, Massachusetts

Contract AF19(628)-2390

ESRI

AD0628772



When US Government drawings, specifications, or other data are used for any purpose other than a definitely related government procurement operation, the government thereby incurs no responsibility nor any obligation whatsoever, and the fact that the government may have formulated, furnished, or in any way supplied the said drawings, specifications, or other data is not to be regarded by implication or otherwise, as in any manner licensing the holder or any other person or corporation, or conveying any rights or permission to manufacture, use, or sell any patented invention that may in any way be related thereto.

Do not return this copy. Retain or destroy.

**PROCEEDINGS OF THE THIRD TROPOSPHERIC  
REFRACTION EFFECTS MEETING**

**(In Two Volumes)**

**Volume II**

**Analytical and Experimental Refraction Research Results**

**Presented at**

**The MITRE Corporation  
Bedford, Massachusetts**

**on**

**July 28, 29 and 30, 1964  
(AF Task 5930.07 — 650A)**

**L. J. Galbiati  
Technical Staff  
The MITRE Corporation**

**Capt. E. G. Eames  
Task Manager for the Air Force  
Electronic Systems Division**



## FOREWORD

The collection of papers in this publication covers the presentations made at the Third Tropospheric Refraction Effects Meeting, sponsored by the Electronic Systems Air Force Systems Command of the Air Force. It should be noted that since the speakers were limited in time, they would not cover all of the details on their work at that time. The papers contained in this document, in some cases, extend the details of the oral presentations in that they much more comprehensively treat the topics. Furthermore, the results of the most recent measurements data have been included where feasible.

The publication of these proceedings does not constitute official Air Force or MITRE endorsement, acceptance, or approval of the techniques proposed and used in the work, or of the results reported. Rather, it is a record of what work was covered, and provides a useful collection of basic data and measurement results to stimulate an exchange of ideas which will advance the state-of-the art. In addition, it serves as a ready reference of the most up-to-date thinking.

I wish to express my appreciation to the representatives of the various agencies for their excellent cooperation, to all the participants of the meeting, and to the Range Measurements Division of the Directorate of Aerospace Instrumentation for suggestions and assistance. I thank the members of the Technical Services and the Radar Systems and Techniques Departments of The MITRE Corporation for the excellent support they have given me during the meeting and in the preparation of this publication. The success of the meeting was greatly enhanced by their assistance. No acknowledgement would be complete without the mention of Mrs. Dorothy Pierce, who typed this document, of Miss Margy Lawlor, who spent many hours in the preparation of the artwork, and to Mrs. Patricia Chatta, who coordinated, planned, edited and guided this document through all stages of its preparation.

L. J. Galbiati,  
Chairman

PROCEEDINGS OF THE THIRD TROPOSPHERIC  
REFRACTION EFFECTS MEETING

(in Two Volumes)

VOLUME II

Analytical and Experimental Refraction Research Results

ABSTRACT

This publication covers the presentations made at the Third Tropospheric Refraction Effects Meeting, sponsored by the Electronic Systems Division of The Air Force Systems Command. The Meeting was held at The MITRE Corporation on July 28, 29 and 30, 1964. The Proceedings are being published in two volumes for ease in handling. This volume contains presentations on certain refraction activities at the Eastern Test Range, the Electronic Systems Division, the Pacific Missile Range, the National Bureau of Standards, Ft. Huachuca, Ballistic Research Laboratory, M. I. T. Round Hill, Cold Lake Canada, on new measurement techniques, and on Tropospheric and Ionospheric Effects on Interferometer System.

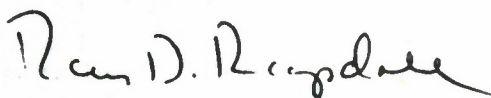
The papers covering the other work on tropospheric refraction, sponsored by the Electronic Systems Division in support of metric instrumentation on the national missile ranges, are contained in Volume I. It also contains the "Findings and Recommendations of the National Academy of Science 'Panel on Tracking Data Analysis' in the Area of Tropospheric Propagation and Refraction," and papers on the refractometer and humidimeter development at the Naval Research Laboratory, the spaced refractometer program of the Eastern Test Range, and on the Canadian tropospheric measurement activities.

While these papers are complete in themselves, many of the specific details on the work covered in the Proceedings of the second refraction meeting (ESD-TDR-64-103) have not been repeated.



## REVIEW AND APPROVAL

Publication of this technical documentary report does not constitute Air Force approval of the report's findings or conclusions. It is published only for the exchange and stimulation of ideas.

A handwritten signature in dark ink, appearing to read "Roy D. Ragdale". The signature is fluid and cursive, with a long horizontal stroke at the end.

ROY D. RAGSDALE

Col, USAF

Director, Aerospace Instrumentation

.

# CONTENTS

## VOLUME II

	<u>Page</u>
Contents, Volume I	vii
Agenda	ix
S. M. Newman	
Tropospheric and Ionospheric Effects on Interferometer Systems	235
A. V. Carlson	
Atmospheric Refraction Studies at Fort Huachuca	265
K. A. Norton	
Refraction Corrections to Electrical Range Measurements	275
R. E. McGavin, R. O. Gilmer and B. R. Bean	
The Response of Microwave Refractometer Cavities to Atmospheric Variations	301
K. A. Norton and E. C. Barrows	
Observed Vertical Wave Number Spectra of Refractivity Near the Ground	313
C. Gardner	
Comparison of Refraction Effect Correction Techniques	347
E. W. Heinzerling	
Multipath Propagation Experiments	367
G. J. Stiles	
The Ballistic Research Laboratories' Propagation Range	393
H. I. Ewen and P. M. Kalaghan	
Refraction Measurements by Lunar Tracking	405



## CONTENTS (Concl'd.)

		<u>Page</u>
W. G. Tank	A Long-Path Absorption Refractometer	431
L. G. Rowlandson	Experiments at Cold Lake, Canada	447
J. E. Tillman	Water Vapor Density Measurements Utilizing the Absorption of Vacuum Ultraviolet Radiation	453
L. J. Galbiati	Summary of Refraction Research Activities	485
	Bibliography	487

# CONTENTS

## Volume I

	<u>Page</u>
Agenda	vii
Col. R. D. Ragsdale	
Opening Remarks: Tropospheric Refraction Meeting	xi
Capt. E. G. Eames	
Introduction	xiii
L. J. Galbiati	
Review of ESD Refraction Task	1
T. S. Weaver and D. L. Ringwalt	
Simultaneous Refractive Index Measure- ments by Three Aircraft	9
R. M. Cunningham	
Scale and Type of Atmospheric Refractive Index Anomalies	33
J. H. Meyer	
Digital Atmospheric Profile Generation	43
R. K. Crane	
Ray-Tracings in Cloud Cross Sections for a Long Baseline Interferometer	57
M. C. Thompson	
ESD Maui, Hawaii, Measurements	89
H. M. Richardson	
Field Test Results of the Line Integral Refractometer	95
J. R. Meyer-Arendt	
Optical Depolarization and Scintillation Measurements over a Terrestrial Path	115



## CONTENTS (CONTINUED)

	<u>Page</u>
H. T. Dougherty	
Fading on Microwave Line-of-Sight Paths	125
B. M. Hadfield	
Some Comments on Microwave Characteristics and Problems	137
A. T. Waterman, Jr.	
Findings and Recommendations of the National Academy of Science "Panel on Tracking Data Analysis" in the Area of Tropospheric Propagation and Refraction	157
C. F. Martin	
Spaced Refractometer Experiment	163
F. C. MacDonald, D. L. Randall, and D. Stillwell	
The Fabry-Perot Refractometer and the Precision NRL Lyman-Alpha Humidiometer	173
D. R. Hay	
Instrumentation for Lower Tropospheric Soundings of Refractivity	195
L. J. Galbiati	
Bibliography	207
List of Attendees	
Third Tropospheric Refraction Effects Meeting, 28-30 July 1964	229

## AGENDA

### THIRD TROPOSPHERIC REFRACTION EFFECTS MEETING

July 28, 29 and 30, 1964

Gaither Building, Room 1A-401  
THE MITRE CORPORATION  
Bedford, Massachusetts

#### DATE AND TIME

#### SUBJECT AND SPEAKER

July 28, 1964  
Morning Session

Dr. L. J. Galbiati, Moderator

8:50	Opening Remarks Col. R. D. Ragsdale
8:55	Introduction Capt. E. G. Eames
9:00	Review of ESD Refraction Task Dr. L. J. Galbiati
9:15	Tropospheric Measurements of MISTRAM Site T. S. Weaver and D. L. Ringwalt
10:05	Digital Atmospheric Profile Generation Dr. R. M. Cunningham
10:25	Scale and Type of Atmospheric Refractive Index Anomalies J. H. Meyer
10:45	ESD Maui, Hawaii, Measurements Dr. M. C. Thompson
11:25	Field Test Results of Line Integral Refractometer H. M. Richardson



DATE AND TIME

SUBJECT AND SPEAKER

Afternoon Session

Dr. A. W. Straiton, Moderator

- |      |   |
|------|---|
| 1:05 | Findings and Recommendations of the National Academy of Science "Panel on Tracking Data Analysis" in the Area of Tropospheric Propagation and Refraction<br>Dr. A. T. Waterman, Jr. |
| 1:25 | Comparison of Refraction Effects Correction Techniques<br>C. Gardner  |
| 1:55 | Spaced Refractometer Program at Eastern Test Range<br>Dr. C. F. Martin  |
| 2:40 | Fabry-Perot Refractometer and Precision Humidiometer Development at the Naval Research Laboratory<br>D. L. Randall  |
| 3:15 | Canadian Tropospheric Measurement Activities<br>Dr. D. L. Hay   |
| 3:45 | Response of Microwave Refractometer Cavities to Atmospheric Variations<br>R. E. McGavin   |
| 4:00 | Tropospheric and Ionospheric Effects on Interferometer Systems<br>S. Newman   |

DATE AND TIMESUBJECT AND SPEAKER

July 29, 1964

Morning Session

Dr. W. A. Dryden, Moderator

8:45	Multipath Effects Measurements Results E. W. Heinzerling
9:30	Results of Study of MISTRAM Data-Link Fading H. T. Dougherty
10:15	Some Comments on Microwave Link Characteristics and Problems B. Hadfield
10:30	Ft. Huachuca Atmospheric Refraction Effect Studies A. V. Carlson
11:00	Ballistic Research Laboratory Measurement Range G. Stiles
11:25	Ray-Tracings in Cloud Cross Sections for a Long Baseline Interferometer R. K. Crane
12:10	Refraction Correction on C. W. Tracking Systems K. A. Norton

DATE AND TIME

SUBJECT AND SPEAKER

Afternoon Session

Dr. G. D. Sheckels, Moderator

- |      |  |
|------|--|
| 1:20 | Experiments at Cold Lake, Canada<br>L. G. Rowlandson   |
| 1:50 | M. I. T. Round Hill Measurement Results<br>Dr. H. Cramer and J. Tillman                                    |
| 2:35 | Refraction Measurements by Lunar Tracking<br>P. Kalaghan   |
| 3:05 | Progress on Long Path Absorption Refractometer<br>W. G. Tank   |
| 3:35 | Optical Depolarization and Scintillation Measurements<br>over a Terrestrial Path<br>Dr. J. R. Meyer-Arendt |
| 4:00 | Summary of Meeting<br>Dr. L. J. Galbiati   |

July 30, 1964

Tours and Special Discussions: Arranged by J. T. Willis and T. E. Johnson



# TROPOSPHERIC AND IONOSPHERIC EFFECTS ON INTERFEROMETER SYSTEMS

S. M. Newman<sup>\*</sup>

## INTRODUCTION

In an interferometer, the angle and angular rate are computed from the measurement of two path lengths and their rate of change. The propagation medium introduces errors in the determination of range and range rate. This paper describes a computer program used to determine the effects of the propagation medium on a particular interferometer system having a baseline of 10 nautical miles (n. m.) and operating at a frequency of 1280 mc.<sup>[1]\*\*</sup>

## INTERFEROMETRY: GENERAL

In radio interferometry, the target can be considered to be at an infinite range as shown by the geometry in the upper portion of Figure 1.

The interferometer angle ( $\alpha$ ) is given by

$$\alpha = \cos^{-1} \frac{\Delta R}{B}, \quad (1)$$

while the angular rate  $\dot{\alpha}$  is given by

$$\dot{\alpha} = \frac{\Delta \dot{R}}{-B \sin \alpha}. \quad (2)$$

If the effect of the propagation medium causes an error in the determination of range, then, from Equations (1) and (2), it is clear that only the

---

<sup>\*</sup> The MITRE Corporation, Bedford, Massachusetts.

<sup>\*\*</sup> Numbers in brackets designate References at the end of this paper.

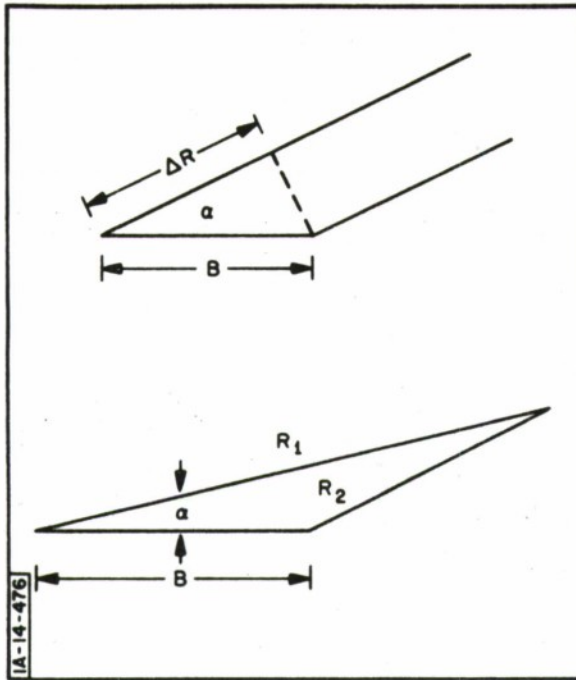


Figure 1. Interferometer Geometry

uncorrelated portion of the range errors along the two paths will contribute to errors in angle and angular rate. This is only true, however, when the target is at an infinite range.

In the radar interferometry case, where the target is at a finite range, the geometry is shown in the lower portion of Figure 1. From the law of cosines

$$R_2^2 = R_1^2 + B^2 - 2R_1B \cos \alpha \quad (3)$$

Thus

$$\cos \alpha = \frac{1}{B} \left( \frac{R_1^2}{2} - \frac{R_2^2}{2R_1} + \frac{B^2}{2R_1} \right) \quad (4)$$

and the angular rate is

$$\dot{\alpha} = - \frac{1}{B \sin \alpha} \left[ \left( \frac{1}{2} + \frac{R_2^2 - B^2}{2R_1^2} \right) \dot{R}_1 - \frac{R_2}{R_1} \dot{R}_2 \right] \quad (5)$$

Both  $\alpha$  and  $\dot{\alpha}$  are more usually expressed as functions of  $R_1$  and  $\Delta R$ ; that is,  $\Delta R = R_1 - R_2$ , and

$$\cos \alpha = \frac{1}{B} \left( \Delta R + \frac{B^2 - \Delta R^2}{2R_1} \right), \quad (6)$$

$$\dot{\alpha} = \frac{1}{-B \sin \alpha} \left[ \left( 1 - \frac{\Delta R}{R_1} \right) \dot{\Delta R} + \frac{1}{2R_1^2} \left( \Delta R^2 - B^2 \right) \dot{R}_1 \right]. \quad (7)$$

## INTERFEROMETRY: PROPAGATION EFFECTS

The presence of a propagation medium with a nonunity index of refraction complicates the picture. Qualitatively, the propagation medium introduces errors in the path length. The slowly varying components of the errors result in range and range rate (and thus angle and angular rate) bias errors. The faster components introduce noiselike errors in range and range rate.

The propagation media can be divided into two shells for discussion: the troposphere, characterized by an index of refraction greater than 1, and the ionosphere, characterized by an index of refraction less than 1. The range error introduced by the troposphere is closely approximated by

$$\Delta R_T \approx \csc \theta_0 \int_0^{h_T} N(h) \times 10^{-6} dh + \int_0^{h_T} \cos [\theta(h)] dh - R_0, \quad (8)$$

where

$\Delta R_T$  = error in measured range caused by tropospheric refraction,

$\theta_0$  = apparent elevation angle at the radar,

$\theta(h)$  = local elevation angle as a function of height,

$N(h)$  = refractivity as a function of height,

$h_T$  = target height, and

$R_0$  = geometric range to target.



The first term of Equation (8) is the effect of the change in propagation velocity, and the second term the length of the curved-ray path. The difference between the curved-ray path length and the true range is small compared to the first term. Therefore, the tropospheric range error is closely approximated by

$$\Delta R_T \approx \csc \theta_o \int_0^{h_T} N(h) \times 10^{-6} dh . \quad (9)$$

The ionosphere range error can be expressed in a similar fashion:

$$\Delta R_I = \frac{4 \times 10^7}{f^2} \int N_e dS , \quad (10)$$

where

$f$  = frequency (cps),

$N_e$  = electron density ( $e/cm^3$ ) ,

and the integration is performed along the ray path. Thus, for targets above the troposphere, the range error produced by the propagation medium is approximated by

$$\Delta R_P \approx \csc \theta_o \int_0^{70 \text{ km}} N(h) \times 10^{-6} dh \pm \csc \theta_I \frac{4 \times 10^7}{f^2} \int_{70 \text{ km}}^{h_T} N_e dh . \quad (11)$$

The plus (+) sign is used to denote envelope delay, while the minus (-) sign is used when phase is measured. The elevation angle,  $\theta_I$ , applies at the point where the ray penetrates the ionosphere.

In order to estimate the effect of the bias errors, mean values of the integral will be used:

$$\int_0^{70 \text{ km}} N(h) \times 10^{-6} dh \approx +2.4 \text{ meters, and}$$

$$\frac{4 \times 10^7}{f^2} \int_{70 \text{ km}}^{1000 \text{ km}} N_e dh \approx -12.2 \text{ meters,}$$

where

$h_T \geq 1000 \text{ km}$ , phase measured (daytime electron density profile).

A mathematical model based on these expressions can be used to determine the angle and angular rate errors introduced by the propagation medium. This model, used only to generate target parameters, is described in the next section.

The target is assumed to be moving from site 1 at a constant range and angular rate in the plane determined by the two sites and the center of the earth. The baseline is horizontal at site 1. The geometric range and angular rate are input parameters. The geometric ranges and range rates encountered in a satellite pass could be substituted for those generated by the model.

#### ERROR MODEL

The interferometer angle at site 1 is  $\alpha$ , an input parameter. The geometric range from site 2 is

$$\begin{aligned} R_2 &= \left[ \left( R_1 \cos \alpha - B \right)^2 + \left( R_1 \sin \alpha \right)^2 \right]^{\frac{1}{2}} \\ &= \left( R_1^2 - 2R_1 B \cos \alpha + B^2 \right)^{\frac{1}{2}}, \end{aligned} \quad (12)$$

where  $B$  , the baseline length, is an input parameter. The angle,  $\theta$  , measured in parallel coordinate system at site 2 would be

$$\theta = \tan^{-1} \frac{R_1 \sin \alpha}{R_1 \cos \alpha - B} \quad (13)$$

Because of the curvature of the earth, the true elevation angle,  $\beta$  , at site 2 is given by

$$\left. \begin{aligned} \beta &= \theta + \frac{B}{3440} & \theta &\leq \frac{\pi}{2} - \frac{B}{3440} \\ \beta &= (\pi - \theta) - \frac{B}{3440} & \theta &> \frac{\pi}{2} - \frac{B}{3440} \end{aligned} \right\} \quad (14)$$

The elevation angle,  $\Gamma$  , at site 1 is

$$\left. \begin{aligned} \Gamma &= \alpha & \alpha &\leq \frac{\pi}{2} \\ &= \pi - \alpha & \alpha &> \frac{\pi}{2} \end{aligned} \right\} \quad (15)$$

The base of the ionosphere is considered to be at a height of 35 n. m.

Thus, the elevation angle at the point of ionospheric penetration from site 1 is

$$\gamma_1 = \cos^{-1} \frac{3440 \cos \Gamma}{3475} \quad (16)$$

From site 2, the elevation angle is given by

$$\gamma_2 = \cos^{-1} \frac{3440 \cos \beta}{3475} \quad (17)$$

The range measured at site 1 will be

$$R_{1M} = R_1 + K_1 \csc \Gamma + K_2 \csc \gamma_1 \quad (18)$$

and the range measured at site 2 will be



$$R_{2M} = R_2 + K_1 \operatorname{csec} \beta + K_2 \operatorname{csec} \gamma_2 , \quad (19)$$

where

$K_1$  = mean range error at vertical incidence for the troposphere, and

$K_2$  = mean range error at vertical incidence for the ionosphere.

The measured range difference will be

$$\Delta R_M = R_{1M} - R_{2M} . \quad (20)$$

Thus the measured angle will be

$$\alpha_M = \cos^{-1} \left[ \frac{1}{B} \left( \Delta R_M + \frac{B^2 - \Delta R_M^2}{2R_{1M}} \right) \right] , \quad (21)$$

and the angle error will be

$$\Delta \alpha = \alpha_M - \alpha . \quad (22)$$

The target angular rate,  $\dot{\alpha}$ , about site 1 is an input parameter. In the model for target motion,  $\dot{R}_1 = 0$ ; thus

$$\dot{R}_2 = \frac{R_1 B \sin \alpha}{R_2} \dot{\alpha} , \quad (23)$$

$$\dot{\beta} = \frac{1}{\cos \theta} \left[ \frac{R_1 \cos \alpha}{R_2} \dot{\alpha} - \frac{R_1 \sin \alpha}{R_2^2} \dot{R}_2 \right] \theta \leq \frac{\pi}{2} - \frac{B}{3440} ,$$

$$= -\frac{1}{\cos \theta} \left[ \frac{R_1 \cos \alpha}{R_2} \dot{\alpha} - \frac{R_1 \sin \alpha}{R_2^2} \dot{R}_2 \right] \theta > \frac{\pi}{2} - \frac{B}{3440} , \quad (24)$$

$$\dot{\gamma}_1 = \frac{3440 \sin \Gamma}{3475 \sin \gamma_1} \dot{\Gamma} \quad , \quad (25)$$

$$\dot{\gamma}_2 = \frac{3440 \sin \beta}{3475 \gamma_2} \dot{\beta} \quad . \quad (26)$$

The measured range rate at site 1 will be

$$\dot{R}_{1M} = -K_1 \csc \Gamma \tan \Gamma \dot{\Gamma} - K_2 \csc \gamma_1 \tan \gamma_1 \dot{\gamma}_1 \quad . \quad (27)$$

It has been assumed that  $K_2$  is a constant. This is only true for targets above the ionosphere or for targets at a constant height. In the general case, the expression for  $\dot{R}_{1M}$  would be

$$\begin{aligned} \dot{R}_{1M} = & K_1 \csc \Gamma \tan \Gamma \dot{\Gamma} - \frac{4 \times 10^7}{f^2} \csc \gamma_1 \tan \gamma_1 \dot{\gamma}_1 \int_0^{h_T} N_e(h) dh \\ & + \frac{4 \times 10^7}{f^2} \csc \gamma_1 N_e(h_T) \dot{h}_T \quad , \end{aligned}$$

where it is assumed that the electron density at the target height  $N_e(h_T)$  is constant over the time interval of the measurement. This differs in form from Equation (25) only by the last term. The maximum value of  $N_e(h_T)$  at winter noontime is  $2 \times 10^6$  (e/cm<sup>3</sup>), so that for the model to be accurate to  $10^{-3}$  for angles above 10 degrees,  $\dot{h}_T$  must be less than 40 meters/second (at 1280 megacycles/second). Thus, this model is restricted to targets at heights of more than 500 nautical miles and to targets between 35 and 500 nautical miles with altitude rates of less than 40 meters/second. The restrictions can be removed by including the appropriate electron density profile and determining target altitude rate.

At the second site, the measured range rate will be

$$\dot{R}_{2M} = \dot{R}_2 - K_1 \csc \beta \cotan \beta \dot{\beta} - K_2 \csc \gamma_2 \cotan \gamma_2 \dot{\gamma}_2, \quad (28)$$

and the range difference rate measured will be

$$\Delta \dot{R}_M = \dot{R}_{1M} - \dot{R}_{2M}. \quad (29)$$

Thus, the measured angular rate will be

$$\dot{\alpha}_M = - \frac{1}{B \sin \alpha_M} \left[ \left( 1 - \frac{\Delta R_M}{R_{1M}} \right) \Delta \dot{R}_M + \frac{1}{2R_{1M}^2} \left( \Delta R_M^2 - B^2 \right) \dot{R}_{1M} \right]. \quad (30)$$

and the angular rate error will be

$$\Delta \dot{\alpha} = \dot{\alpha}_M - \dot{\alpha}. \quad (31)$$

The propagation medium also introduces noiselike errors into the measurements. Differentiation of Equation (6) and letting  $d\Delta R = dR_1 - dR_2$  gives

$$d\alpha = - \frac{1}{B \sin \alpha} \left[ \left( 1 - \frac{\Delta R}{R_1} + \frac{\Delta R^2 - B^2}{2R_1^2} \right) dR_1 - \left( 1 - \frac{\Delta R}{R_1} \right) dR_2 \right]. \quad (32)$$

From this, the variance of  $\alpha$  is

$$\begin{aligned} \sigma_{\alpha}^2 = & \left( \frac{1}{B \sin \alpha} \right)^2 \left[ \left( 1 - \frac{\Delta R}{R_1} + \frac{\Delta R^2 - B^2}{2R_1^2} \right)^2 \sigma_{R_1}^2 + \left( 1 - \frac{\Delta R}{R_1} \right)^2 \sigma_{R_2}^2 \right. \\ & \left. - 2\rho_{R_1 R_2} \sigma_{R_1} \sigma_{R_2} \left( 1 - \frac{\Delta R}{R_1} + \frac{\Delta R^2 - B^2}{2R_1^2} \right) \left( 1 - \frac{\Delta R}{R_1} \right) \right], \quad (33) \end{aligned}$$

where  $\rho_{R_1 R_2}$  is the correlation of the noise in the two range measurements. It will be assumed that the variances of the two range measurements are equal:  $\sigma_{R_1}^2 = \sigma_{R_2}^2 = \sigma_R^2$ . Thus,

$$\begin{aligned} \sigma_\alpha^2 = & \left( \frac{\sigma_R}{B \sin \alpha} \right)^2 \left[ 2 \left( 1 - \frac{\Delta R}{R_1} \right)^2 + 2 \left( 1 - \frac{\Delta R}{R_1} \right) \left( \frac{\Delta R^2 - B^2}{2R_1^2} \right) + \left( \frac{\Delta R^2 - B^2}{2R_1^2} \right)^2 \right. \\ & \left. - 2 \left( 1 - \frac{\Delta R}{R_1} \right) \left( 1 - \frac{\Delta R}{R_1} + \frac{\Delta R^2 - B^2}{2R_1^2} \right) \rho_{R_1 R_2} \right] \\ = & \left( \frac{\sigma_R}{B \sin \alpha} \right)^2 \left[ \left( \frac{\Delta R^2 - B^2}{2R_1^2} \right)^2 + 2 \left( 1 - \rho_{R_1 R_2} \right) \left( 1 - \frac{\Delta R}{R_1} \right) \left( 1 - \frac{\Delta R}{R_1} + \frac{\Delta R^2 - B^2}{2R_1^2} \right) \right]. \end{aligned} \quad (34)$$

The noise error in angular rate is obtained from differentiating Equation (7):

$$\begin{aligned} d\dot{\alpha} = & -\dot{\alpha} \tan \alpha \, d\alpha - \frac{1}{B \sin \alpha} \left[ \left( 1 - \frac{\Delta R}{R_1} \right) d\dot{\Delta R} + \left( \frac{\Delta R^2 - B^2}{2R_1^2} \right) d\dot{R}_1 \right. \\ & \left. + \left( \frac{\dot{R}_1 \Delta \dot{R}}{R_1^2} - \frac{\Delta \dot{R}}{R_1} \right) d\Delta R + \left( \frac{\Delta \dot{R} \Delta R}{R_1^2} - \frac{\dot{R}_1 (\Delta R^2 - B^2)}{R_1^3} \right) d\dot{R}_1 \right]. \end{aligned} \quad (35)$$

The  $d\dot{R}$  terms could be expressed as functions of the geometry for the target motion used in the model; however, since the  $\dot{R}$ 's are obtained from the coefficients of the curve fitted to the range measurements, there is a relationship between the variance of the  $\dot{R}$ 's and the corresponding  $R$ 's. This relationship will be used in order to avoid restricting the equations to the target motion of the model.



Substitution of Equation (32) into Equation (35) and letting  $d\Delta R = dR_1 - dR_2$  and  $d\Delta\dot{R} = d\dot{R}_1 - d\dot{R}_2$  gives

$$\begin{aligned} d\dot{\alpha} = & \frac{\dot{\alpha} \tan \alpha}{B \sin \alpha} \left[ \left( 1 - \frac{\Delta R}{R_1} + \frac{\Delta R^2 - B^2}{2R_1^2} \right) dR_1 - \left( 1 - \frac{\Delta R}{R_1} \right) dR_2 \right] \\ & - \frac{1}{B \sin \alpha} \left\{ \left[ 1 - \frac{\Delta R}{R_1} + \frac{\Delta R^2 - B^2}{2R_1^2} \right] d\dot{R}_1 - \left[ 1 - \frac{\Delta R}{R_1} \right] d\dot{R}_2 \right. \\ & + \left[ \frac{\dot{R}_1 \Delta R}{R_1^2} + \frac{\Delta\dot{R} \Delta R}{R_1^2} - \frac{\Delta\dot{R}}{R_1} - \dot{R}_1 \frac{(\Delta R^2 - B^2)}{R_1^3} \right] dR_1 \\ & \left. + \left[ \frac{\Delta\dot{R}}{R_1} - \frac{\dot{R}_1 \Delta R}{R_1^2} \right] dR_2 \right\} . \end{aligned} \quad (36)$$

To simplify the remaining equations, the following quantities are used:

$$\begin{aligned} \ell &= \left( 1 - \frac{\Delta R}{R_1} + \frac{\Delta R^2 - B^2}{2R_1^2} \right) , \\ m &= \left( 1 - \frac{\Delta R}{R_1} \right) , \\ n &= \left[ \frac{\dot{R}_1 \Delta R}{R_1^2} + \frac{\Delta\dot{R} \Delta R}{R_1^2} - \frac{\Delta\dot{R}}{R_1} - \dot{R}_1 \frac{(\Delta R^2 - B^2)}{R_1^3} \right] , \text{ and} \\ p &= \left( \frac{\Delta\dot{R}}{R_1} - \frac{\dot{R}_1 \Delta R}{R_1^2} \right) . \end{aligned}$$

Equation (36) can be rewritten as

$$\begin{aligned} d\dot{\alpha} = -\frac{1}{B \sin \alpha} \left[ \ell d\dot{R}_1 - m d\dot{R}_2 + (n - \dot{\alpha} \tan \alpha \ell) dR_1 \right. \\ \left. + (p + \dot{\alpha} \tan \alpha m) dR_2 \right] . \end{aligned} \quad (37)$$

The variance of  $\dot{\alpha}$  will be

$$\begin{aligned} \sigma_{\dot{\alpha}}^2 = \left( \frac{1}{B \sin \alpha} \right)^2 \left[ \ell^2 \sigma_{\dot{R}_1}^2 + m^2 \sigma_{\dot{R}_2}^2 + (n - \dot{\alpha} \tan \alpha \ell)^2 \sigma_{R_1}^2 \right. \\ + (p + \dot{\alpha} \tan \alpha m)^2 \sigma_{R_2}^2 - 2\ell m \sigma_{\dot{R}_1} \sigma_{\dot{R}_2} \rho_{\dot{R}_1 \dot{R}_2} \\ + 2\ell(n - \dot{\alpha} \tan \alpha \ell) \sigma_{\dot{R}_1} \sigma_{R_1} \rho_{\dot{R}_1 R_1} + 2\ell(p + \dot{\alpha} \tan \alpha m) \sigma_{\dot{R}_1} \sigma_{R_2} \rho_{\dot{R}_1 R_2} \\ - 2m(n - \dot{\alpha} \tan \alpha \ell) \sigma_{\dot{R}_2} \sigma_{R_1} \rho_{\dot{R}_2 R_1} - 2m(p + \dot{\alpha} \tan \alpha m) \sigma_{\dot{R}_2} \sigma_{R_2} \rho_{\dot{R}_2 R_2} \\ \left. + 2(n - \dot{\alpha} \tan \alpha \ell) (p + \dot{\alpha} \tan \alpha m) \sigma_{R_1} \sigma_{R_2} \rho_{R_1 R_2} \right] . \end{aligned} \quad (38)$$

In the experimental system,  $R$  and  $\dot{R}$  would be obtained from the coefficients of the curve fitted to a time sequence of range measurements. Parameter estimation theory<sup>[2]</sup> shows that  $\sigma_{\dot{R}}^2 = k^2 \sigma_R^2$  and, furthermore, that the estimates of range and range rate are uncoupled; i. e.,  $\rho_{RR} = 0$ . Therefore, Equation (38) can be rewritten as

$$\begin{aligned} \sigma_{\dot{\alpha}}^2 = & \left( \frac{1}{B \sin \alpha} \right)^2 \left\{ \left[ \ell^2 k^2 + (n - \dot{\alpha} \tan \alpha \ell)^2 \right] \sigma_{R_1}^2 \right. \\ & + \left[ m^2 k^2 + (p + \dot{\alpha} \tan \alpha m)^2 \right] \sigma_{R_2}^2 - 2 \ell m k^2 \sigma_{R_1} \sigma_{R_2} \rho_{R_1 R_2} \\ & \left. + 2(n - \dot{\alpha} \tan \alpha \ell)(p + \dot{\alpha} \tan \alpha m) \sigma_{R_1} \sigma_{R_2} \rho_{R_1 R_2} \right\} \quad (39) \end{aligned}$$

Once again it is assumed that  $\sigma_{R_1} = \sigma_{R_2} = \sigma_R$ ; then

$$\begin{aligned} \sigma_{\dot{\alpha}}^2 = & \left( \frac{\sigma_R}{B \sin \alpha} \right)^2 \left[ \ell^2 k^2 + (n - \dot{\alpha} \tan \alpha \ell)^2 + m^2 k^2 + (p + \dot{\alpha} \tan \alpha m)^2 \right. \\ & \left. - 2 \ell m k^2 \rho_{R_1 R_2} + 2(n - \dot{\alpha} \tan \alpha \ell)(p + \dot{\alpha} \tan \alpha m) \rho_{R_1 R_2} \right] \quad (40) \end{aligned}$$

If it is assumed that  $\dot{R}$  is determined from the second coefficient of a third order polynomial, Reference [2] gives  $k = (2\sqrt{3} / \sqrt{n} T)$ . For a prf of 33-1/3 and a measurement interval of 3 seconds,  $k = 0.11547$ .

## RESULTS

The results are contained in Figures 2 through 15. Most of the data plotted is applicable to a target at a range of 1000 nautical miles, with an angular rate of 0.1 degree/second.

Plots of the range and range rate bias errors introduced by the propagation medium are shown in Figures 2 and 3. It is assumed that the residual range error after correction is 2 percent of the mean value for the troposphere and 25 percent of the mean value for the ionosphere. This is a reflection of the emphasis placed on determining the tropospheric effects, not a physical limitation.

The computed angle bias errors are compared in Figure 4, with those computed by the National Bureau of Standards (NBS)<sup>[3]</sup> for a 10-nautical mile baseline interferometer. It can be seen that for a target range of 1000 nautical miles, the errors computed by the program are greater than the NBS errors. This is to be expected, since the NBS calculation assumes that the "nearness" term,

$$\left(1 + \frac{B^2 - \Delta R^2}{2R_1 \Delta R}\right),$$

is equal to one. This is equivalent to assuming that the target range is infinite and that the elevation angles at the two sites differ by a constant (the earth central angle subtended by the two sites). The results obtained with the program indicate this assumption is not valid for a range-to-baseline ratio of 100 (range of 1000 nautical miles). For a target range of 10,000 nautical miles, however, the program figures agree well with the NBS data.

Figure 5 shows a plot of the total propagation angular rate bias error magnitude, and Figure 6 contains a plot of the total propagation angle bias error magnitude as a function of elevation angle. The mean value of the error is greater when the elevation angle is determined by coarse range rather than by phase measurements. This occurs because the range error caused by the ionosphere is of the same sign as the error caused by the troposphere when group delay rather than phase delay is measured. The magnitude of the residual error after correction is caused by the large uncertainty (25 percent) encountered in predicting the ionospheric effects.

Figures 7 and 8 provide plots of angle and angular rate noise errors based on phase errors of 3- and 20-degrees root-mean-square. While the computed bias errors are believed to be reasonably accurate, the computed noise errors are accurate only within an order of magnitude since the ratio of



noise-to-bias error can change unpredictably. In order to estimate the accuracy of the program, the 3-degree root-mean-square phase error was scaled by the  $(1/f^2)$  relationship to 53 and 108 megacycles, and compared with measured data<sup>[4]</sup> in Figure 9. The computed data is about four times the measured data. For a phase error of 20 degrees root-mean-square, the computed data would be thirty times greater.

These results are within the expected accuracy of the program since the phase errors represent total error measured in the experimental system (tropospheric, ionospheric, machine and target scintillation). The scaling process assumed that the entire error was ionospheric and, therefore, the resultant errors are larger than would be expected.

The contributions of the troposphere and the ionosphere to the total bias errors are shown in Figures 10 through 15.

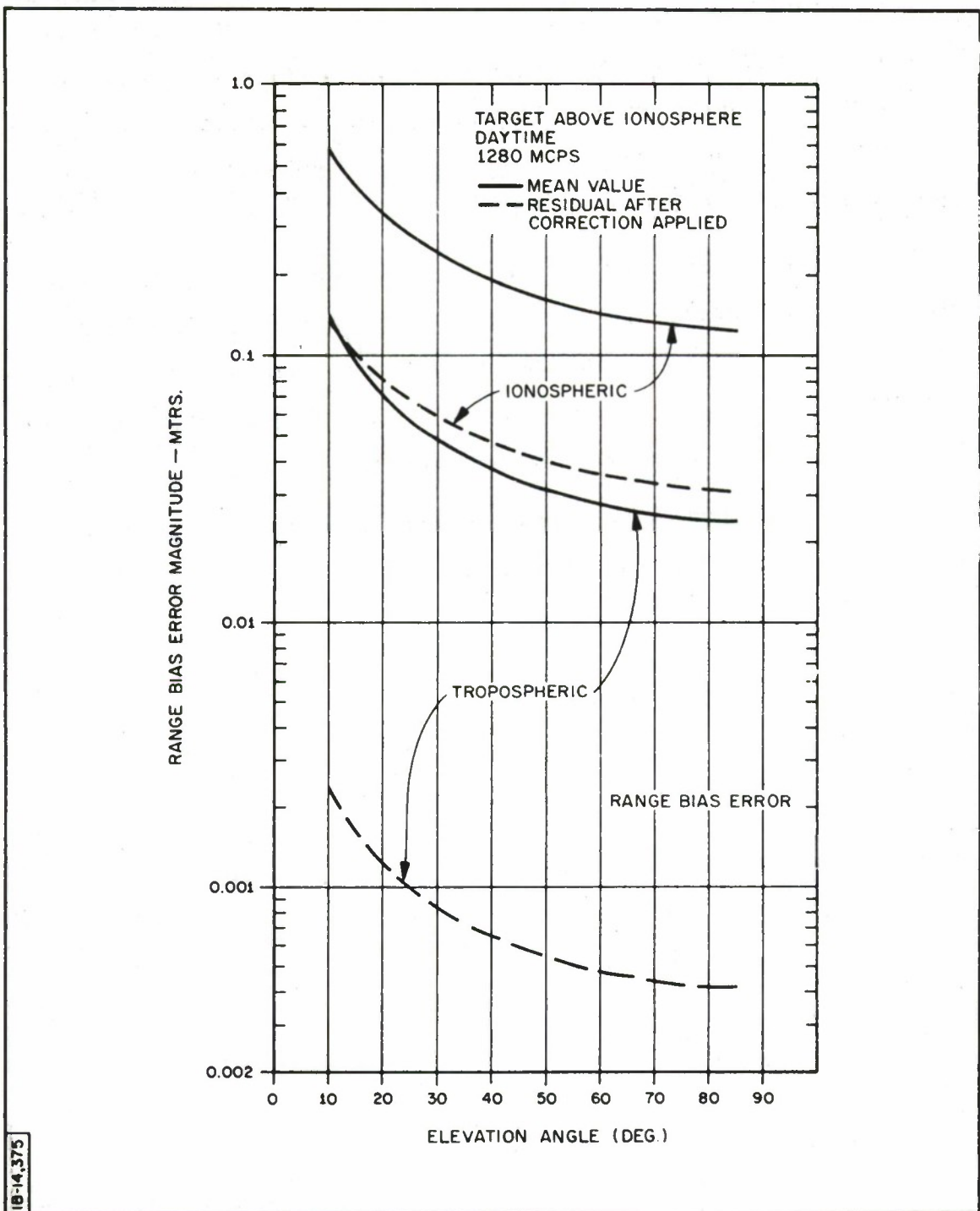


Figure 2. Magnitude of Range Bias Error

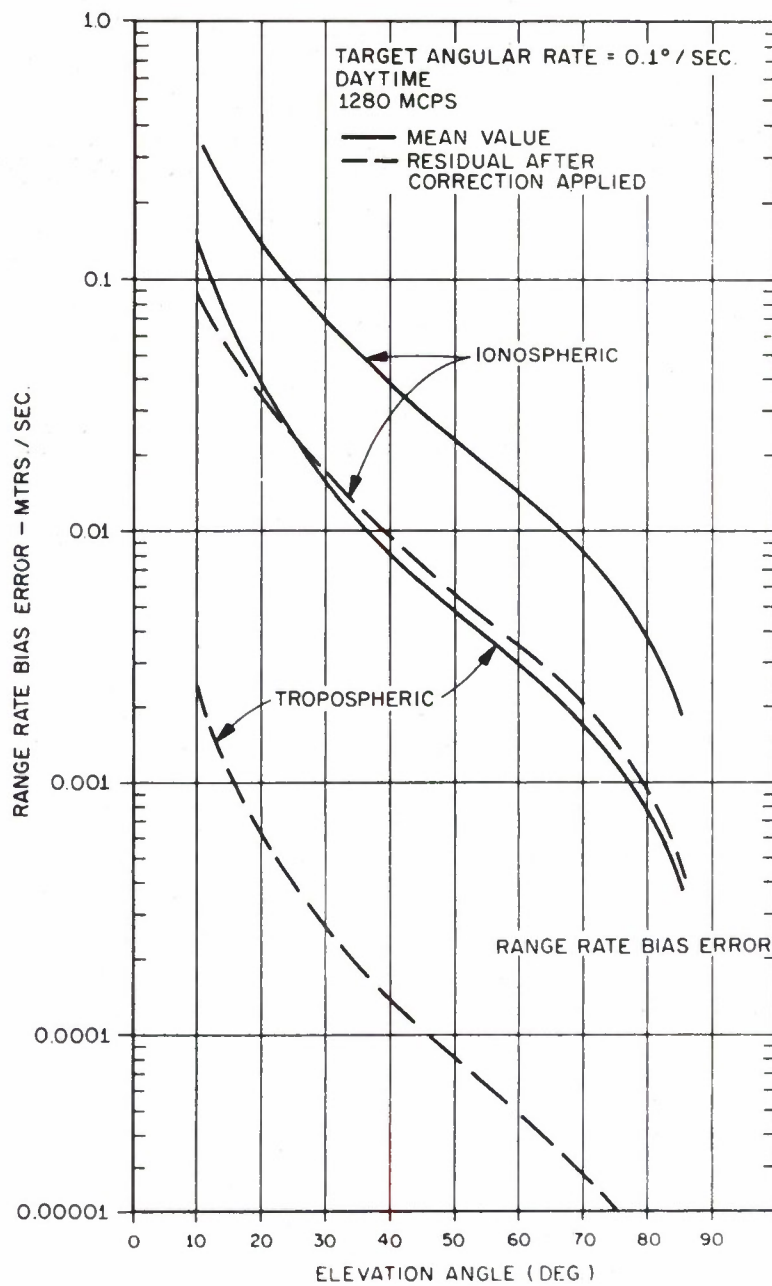


Figure 3. Magnitude of Range Rate Bias Error

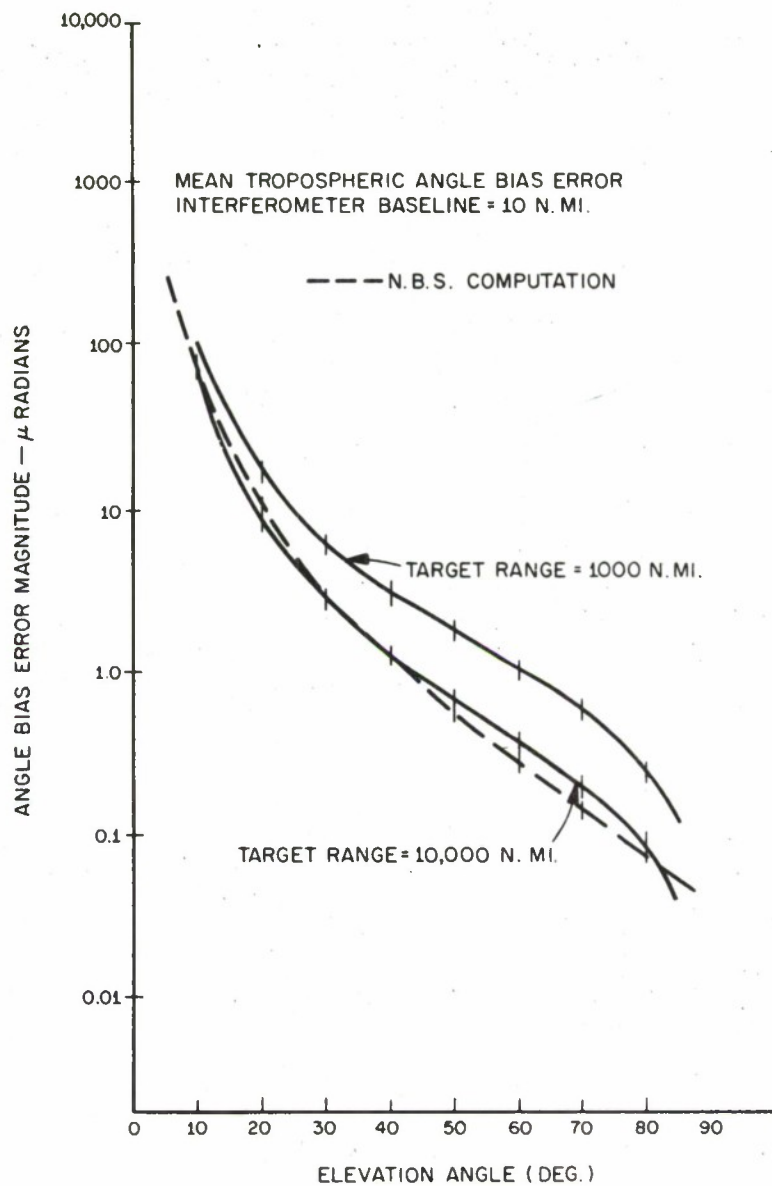
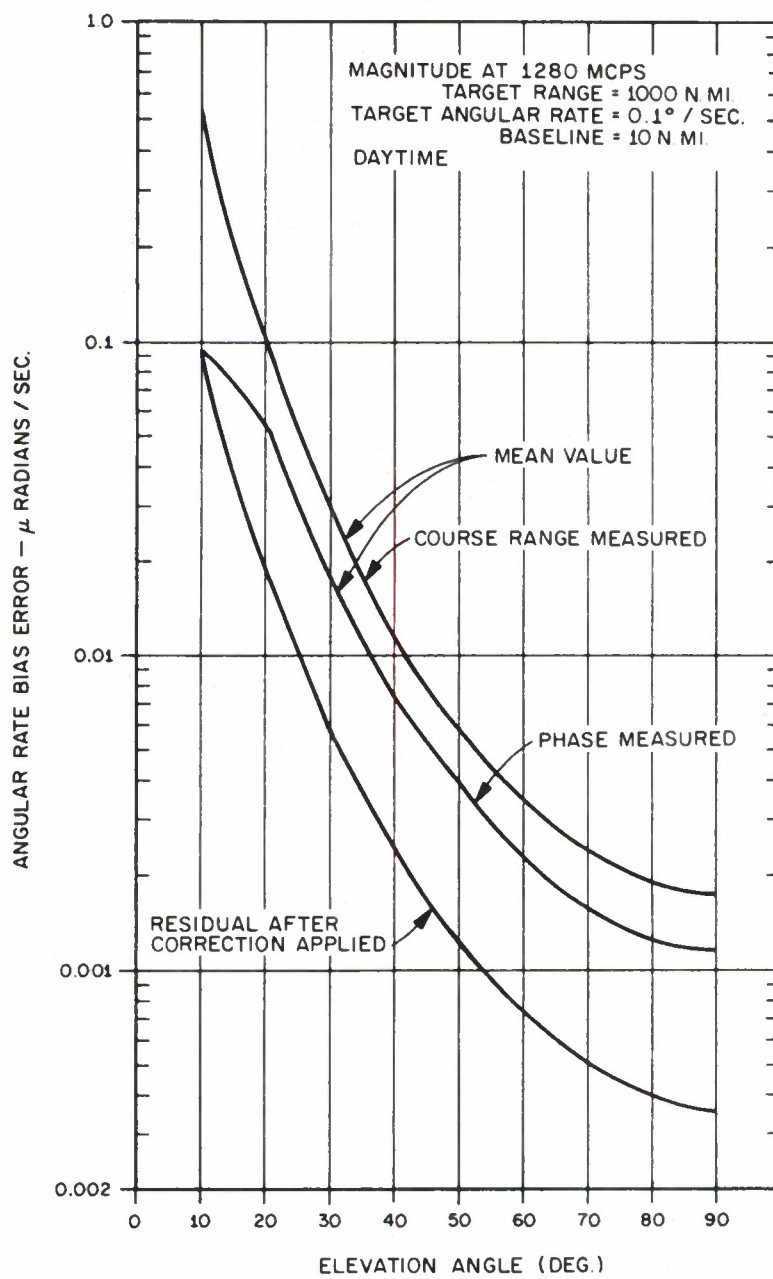


Figure 4. Comparison of Results





IB-14,371

Figure 5. Total Propagation Angle Bias Error

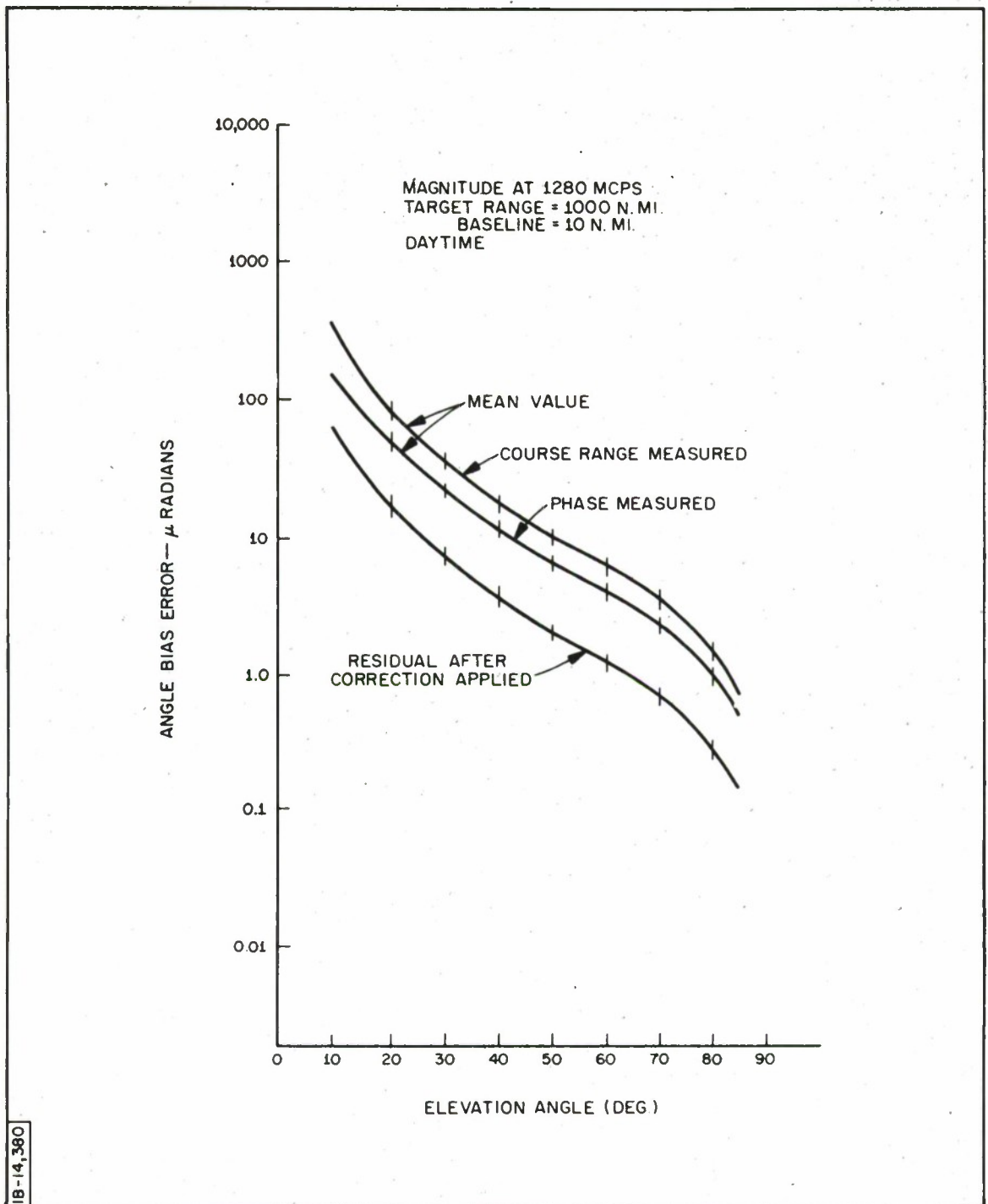
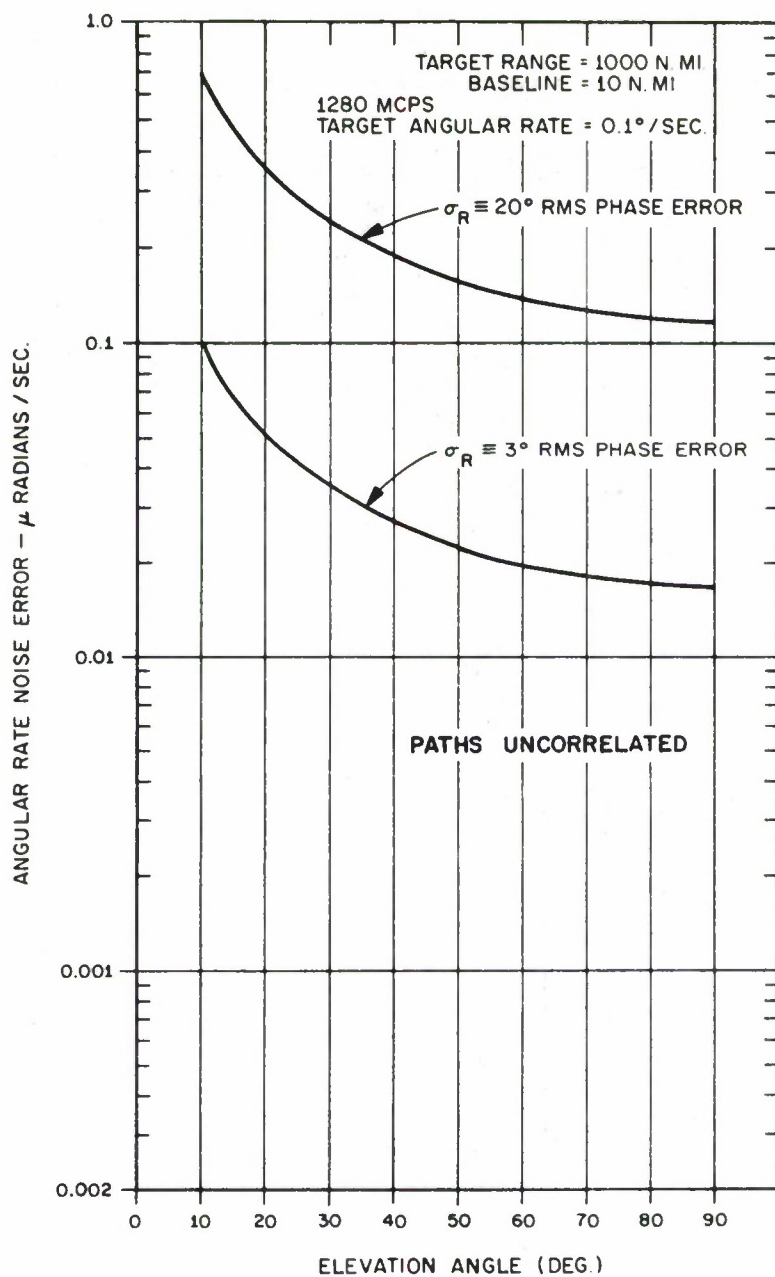


Figure 6. Total Propagation Angle Rate Bias Error



18-14,372

Figure 7. Angular Noise Error

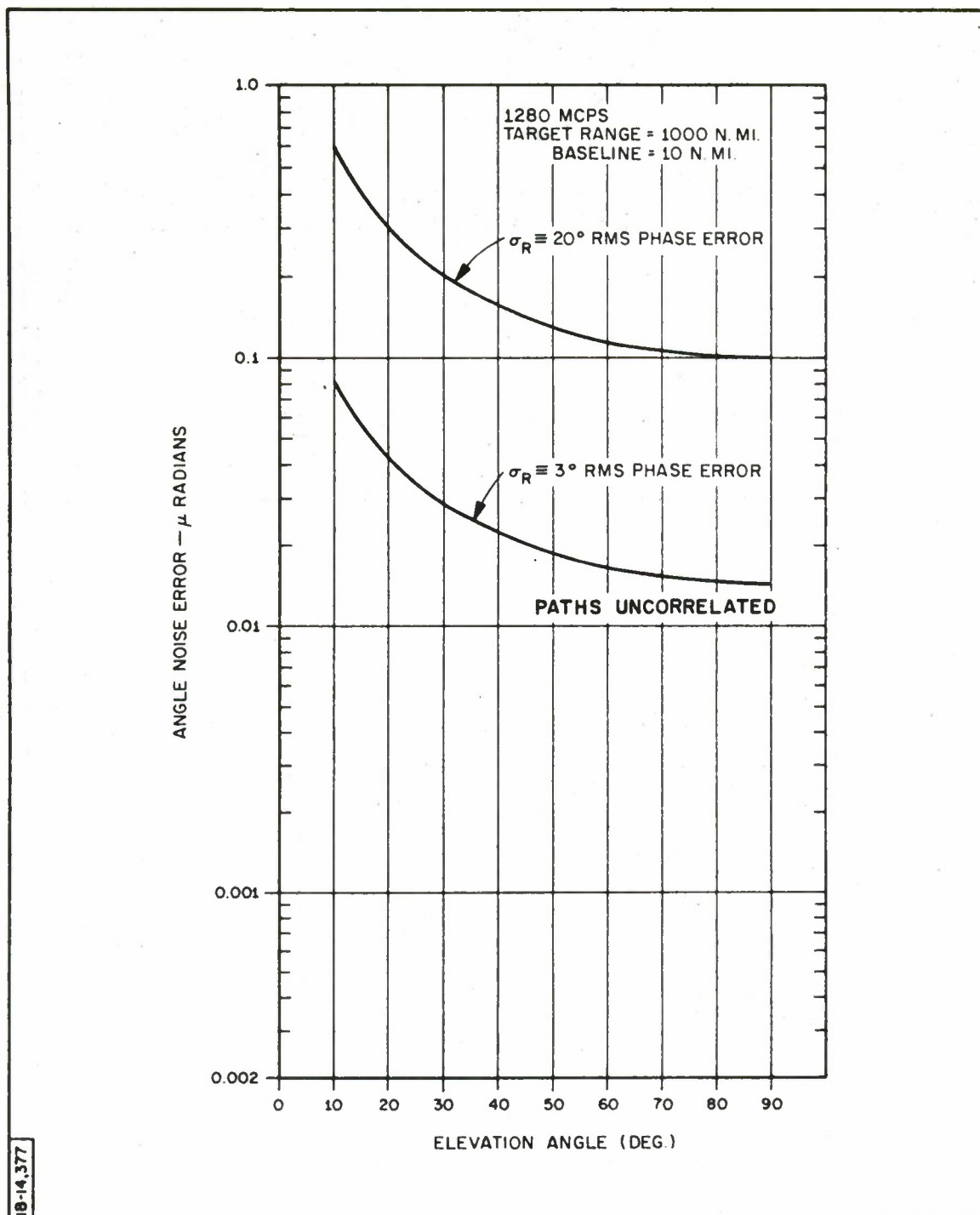


Figure 8. Angular Rate Noise Error



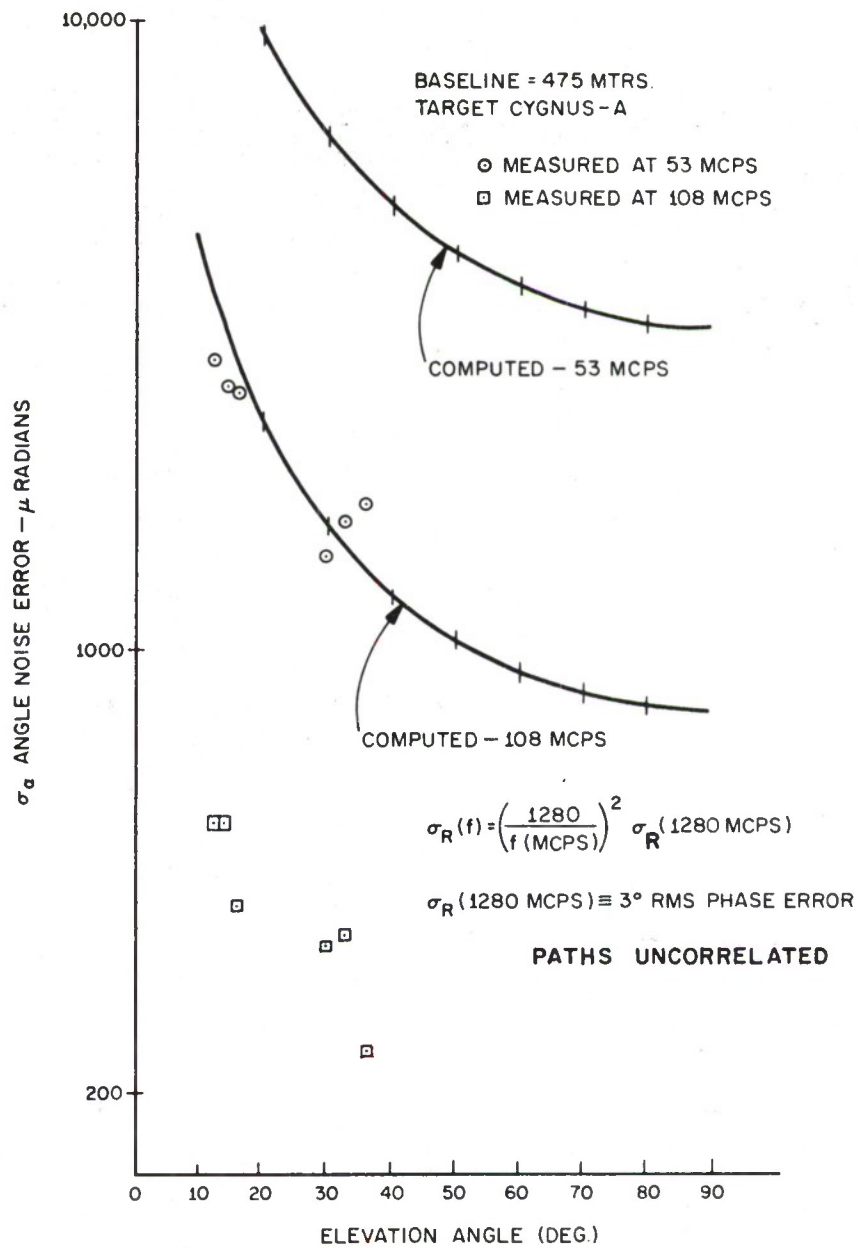
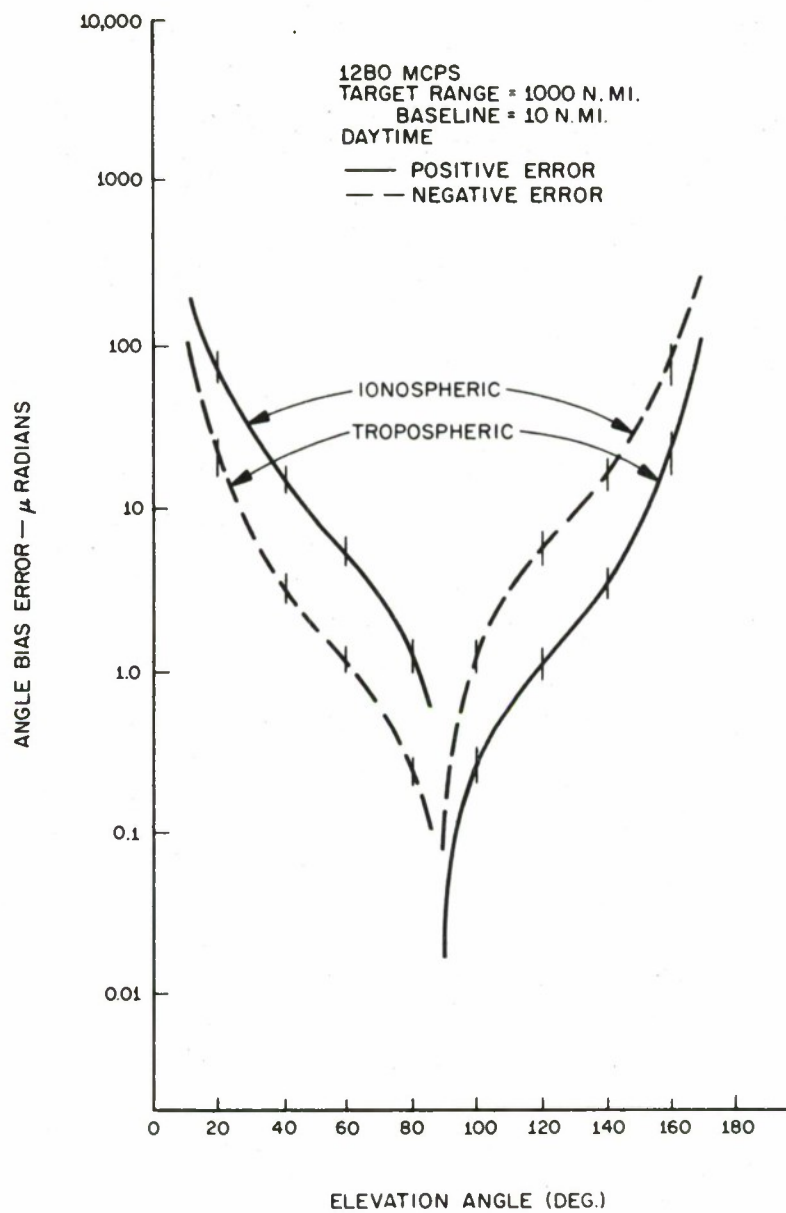
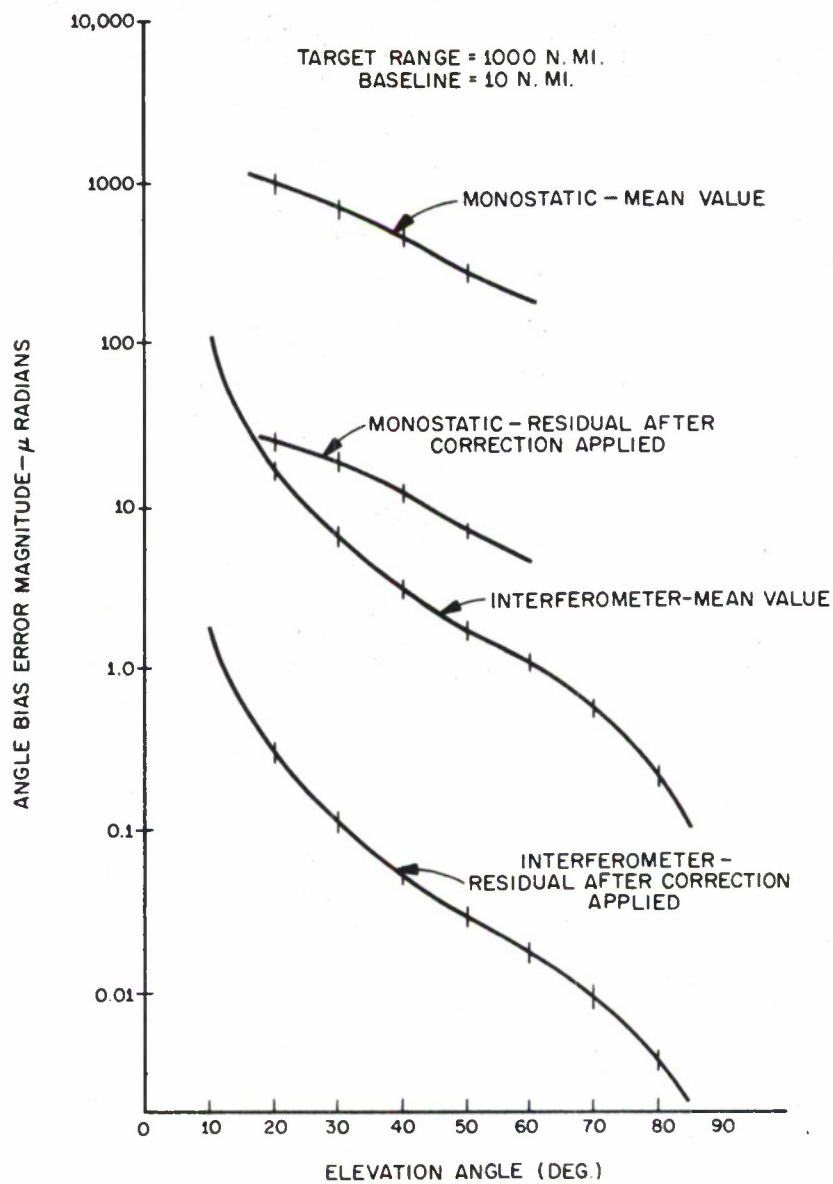


Figure 9. Comparison of Computed and Measured Data



118-14,379

Figure 10. Mean Value — Angular Bias Error



18-14,378

Figure 11. Tropospheric Angular Bias Error

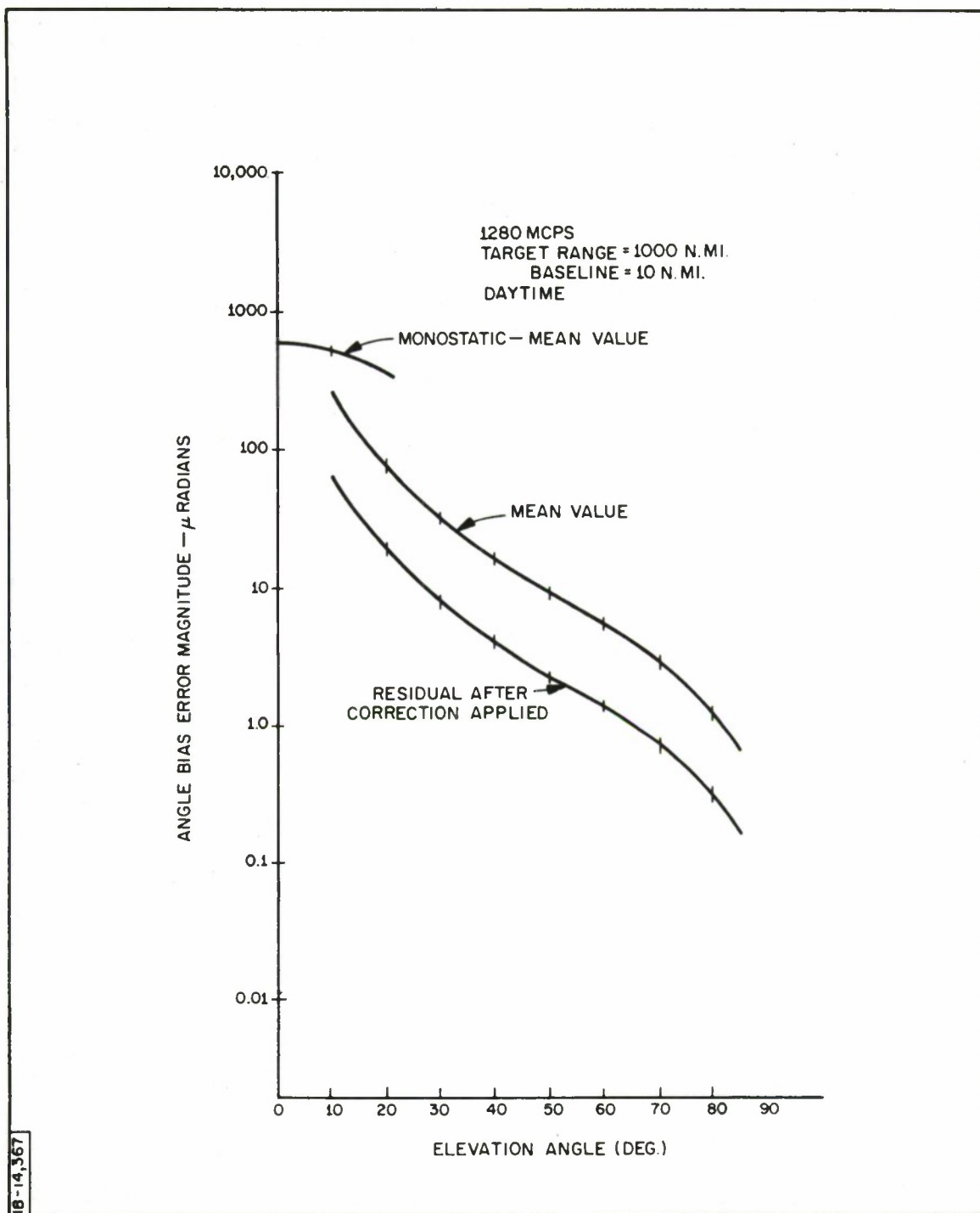
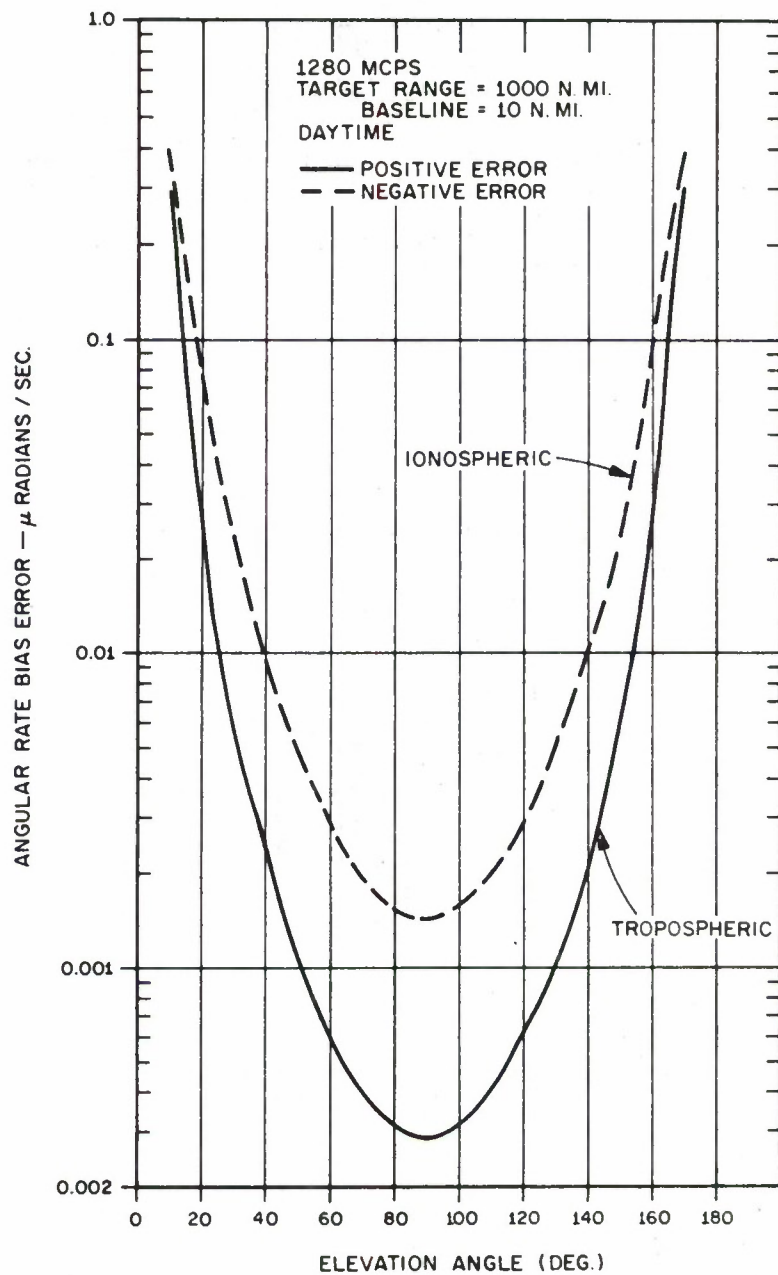


Figure 12. Ionospheric Angular Bias Error



18-14,373

Figure 13. Mean Value — Angular Rate Bias Error



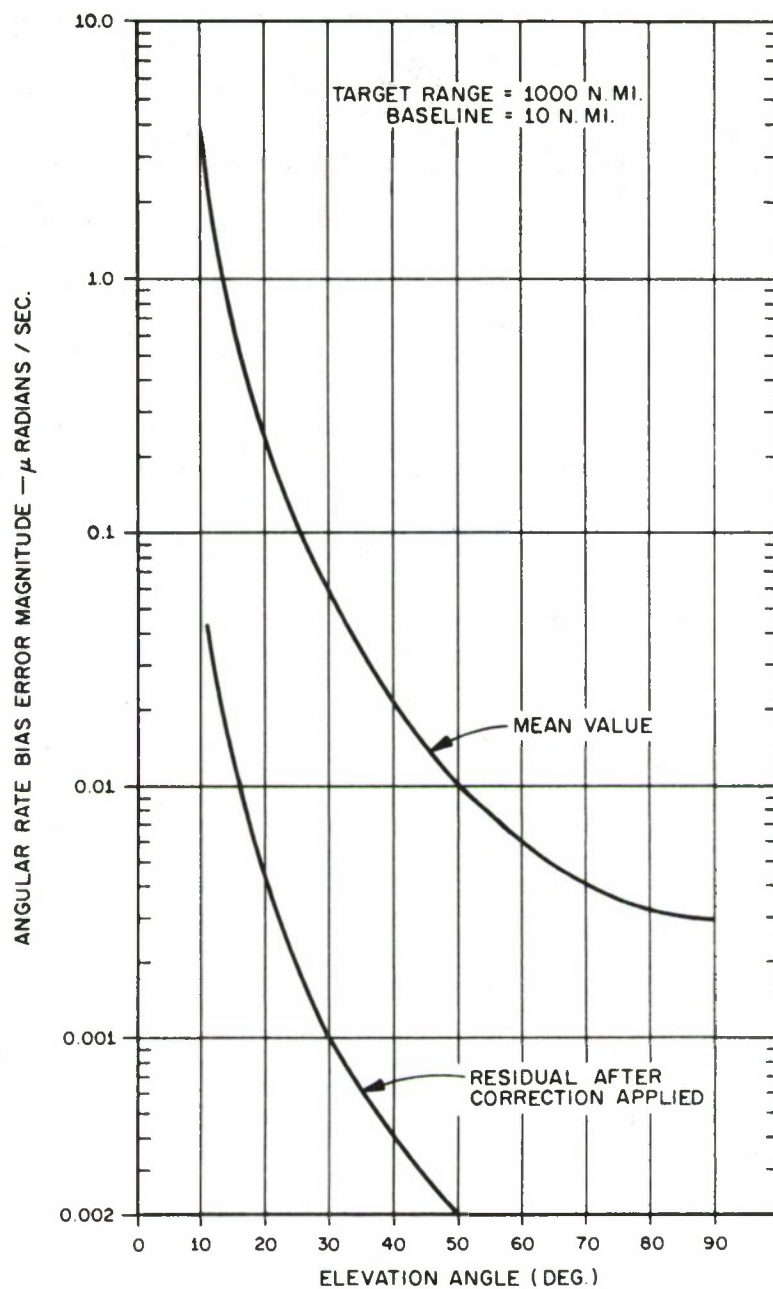


Figure 14. Tropospheric Angular Rate Bias Error

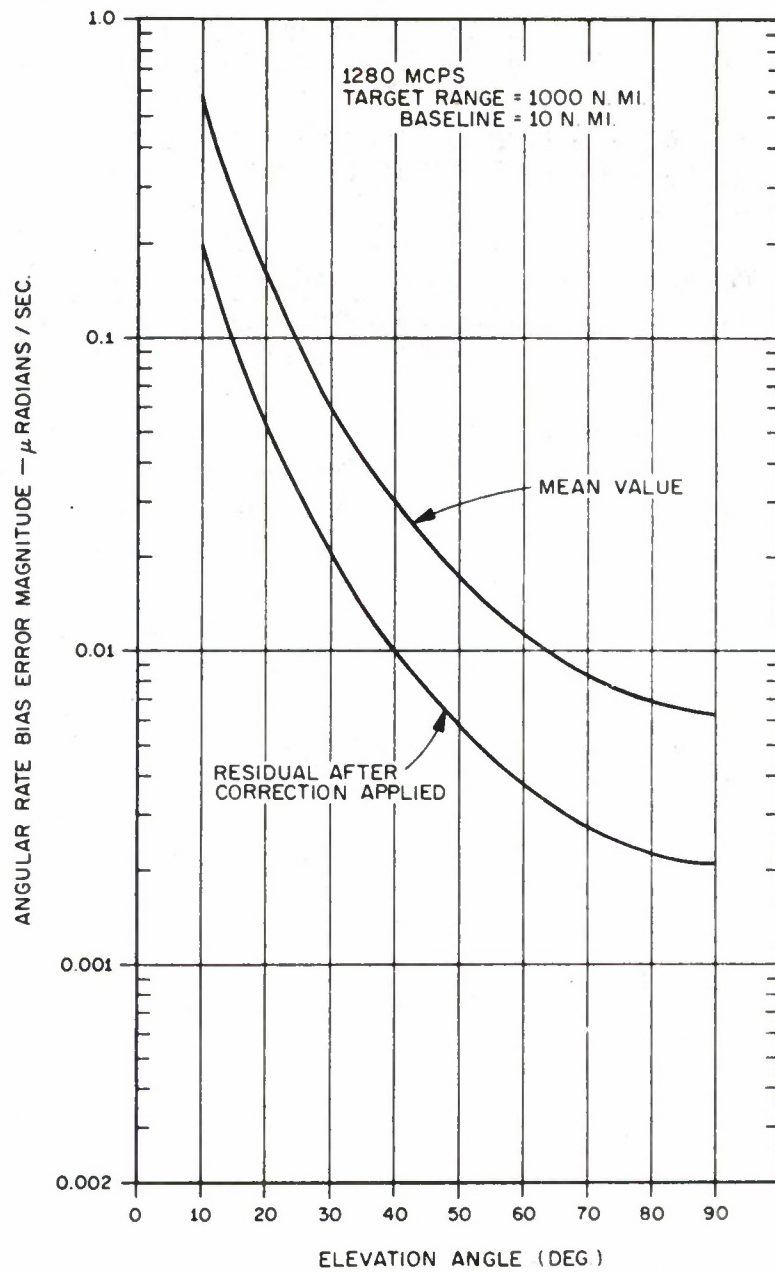


Figure 15. Ionospheric Angular Rate Bias Error

## REFERENCES

1. S. M. Newman, On Propagation Effects in the Interferometer System, The MITRE Corporation, W-07192, June 1964 (UNCLASSIFIED).
2. R. Manasse, Summary of Maximum Theoretical Accuracy of Radar Measurements, The MITRE Corporation, MTS No. 2, April 1960 (UNCLASSIFIED).
3. G. D. Thayer, and B. R. Bean, An Analysis of Atmospheric Refraction Errors of Phase Measuring Radio Tracking Systems — Part 1, National Bureau of Standards, Report 7254, June 5, 1962 (UNCLASSIFIED).
4. R. S. Lawrence, J. L. Jespersen, and R. C. Lamb, "Amplitude and Angular Scintillations of the Radio Source Cygnus-A Observed at Boulder, Colorado," NBS J. Res. 65D, July-August 1961.

## ATMOSPHERIC REFRACTION STUDIES AT FORT HUACHUCA

A. V. Carlson\*

The atmospheric refraction studies\*\* are being conducted to furnish data for the correction of tracking radar measurements of the position of various airborne targets which may be under test on the Electronic Proving Ground Ranges.

A typical test operation, requiring radar support, is the evaluation of an aircraft navigation system which requires that the position of the aircraft be accurately known, so that there is a standard for comparing the performance of the system being tested. Since such tests usually involve drones and Army aircraft as targets, flight altitudes are ordinarily less than 20,000 feet. Ranges may exceed 100 miles, however, so that radar elevation angles are often 1 degree or less and atmospheric refraction becomes an important factor. The test engineer may require an over-all accuracy of  $\pm 25$  feet in measuring the target position, which does not provide much allowance for error in computing refraction corrections.

The task of the meteorologist is to decide what meteorological observations are necessary, with what frequency these observations must be taken, and at what spacing over the test area they must be made, so that the correction computed for atmospheric refraction is reliable within the limits of accuracy specified by the test engineer.

---

\* Army Electronics Research and Development Activity, Fort Huachuca, Arizona.

\*\*This research is being performed under the Army inhouse Independent Laboratory Program, using the USAEPG Operation as a vehicle.

Studies thus far have been mainly an effort to learn more about the time and space variability of atmospheric refractivity in the lower atmosphere in Arizona, and to determine how this variability relates to the accuracy of target position error computations.

During November and December of 1963, over 100 radiosonde soundings were made at several sites in southeastern Arizona in support of an evaluation test of several airborne aircraft navigation systems. Many of these soundings were spaced 1 hour apart in time, and some were simultaneous soundings from different sites 40 to 50 miles apart. Highlights of the detailed analysis of these data are summarized in the remainder of this report.

The time variability of the gradient in atmospheric refractivity versus height ( $N$  units/1000 feet/hour) is, on the average, three to four times greater in the first 1000 feet above the surface than it is at higher levels. Figure 1 shows the average variability in  $N$  for each 1000-foot level as derived from the data obtained in November - December - 1963. Note that the average variability above the first 1000 feet is quite constant at approximately 2  $N$  units/1000/feet/hour (this includes the random instrument error in the radiosonde measurements).

Considering these variabilities or uncertainties in determining the refractivity, and considering the geometry of computing target position errors due to refractive bending of the radar ray, the average uncertainty in the computation of the position correction and the contribution of each 1000-foot layer to this uncertainty was computed. The Weisbrod Anderson ray-tracing technique was programmed for a G-15 Computer and used for these computations. From this analysis, it becomes evident that the first 1000 feet above the radar contributes approximately 70 percent of the total uncertainty in the position correction.



Assuming that uncertainty in measuring the refractive gradient in the first 1000 feet can be reduced to the same value as in the upper layers by making more frequent low-level observations, Figure 2 shows the cumulative contribution of the layers to the overall uncertainty in computing the target position error produced by atmospheric refraction.

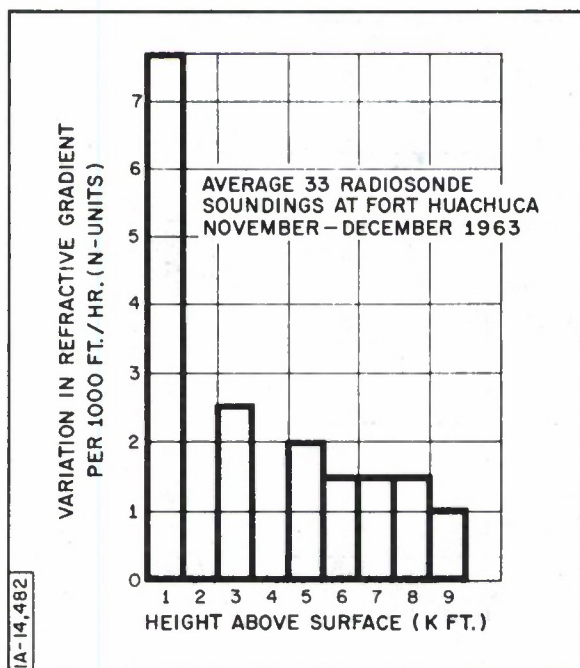


Figure 1. Time Variability of Atmospheric Refractive Gradient

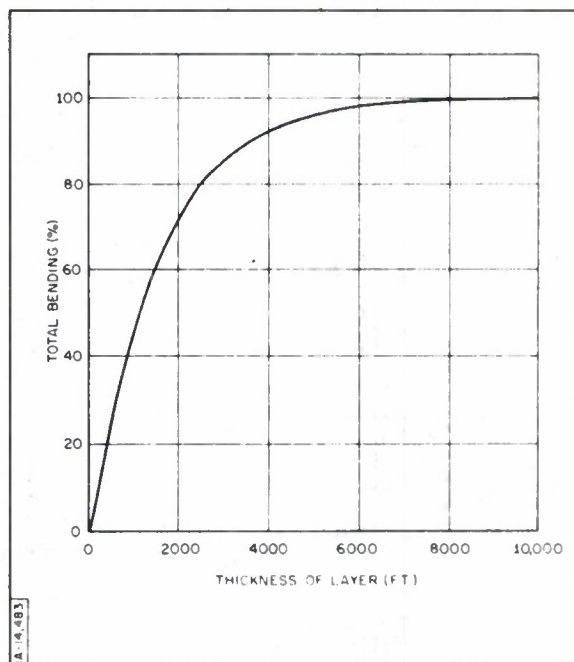


Figure 2. Cumulative Contribution of Atmospheric Layers

The chart in Figure 3 carries this analysis further. It provides an estimate of the reliability of target position error computations, based upon the assumption that the gradient in atmospheric refractivity can be determined to within  $\pm 2N$  units/1000 feet. This provides a planning guide in estimating the limits of ranges and altitudes at which a target can be flown and still meet the

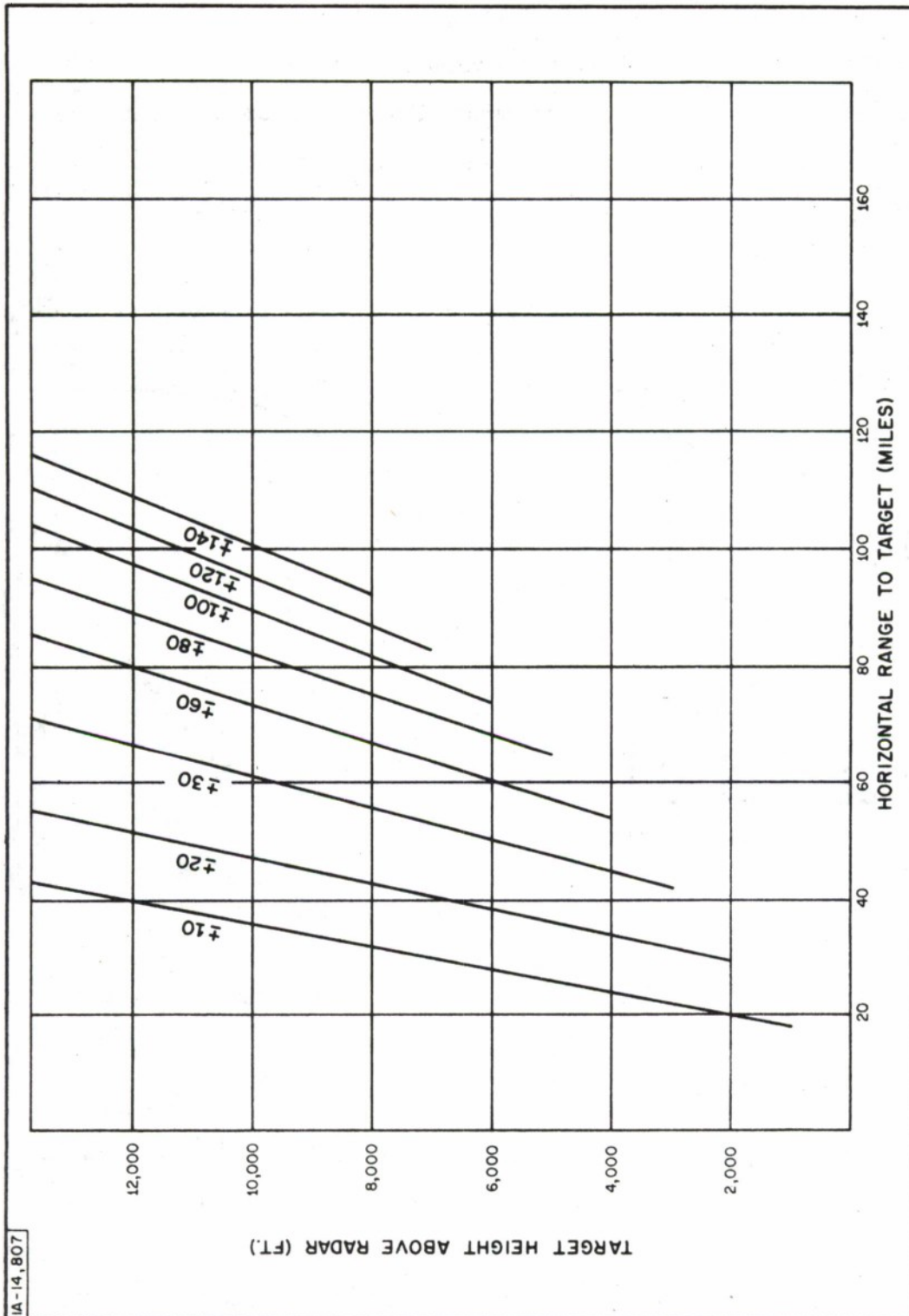


Figure 3. Precision of Atmospheric Correction

test engineer's requirements for accuracy of position measurements. For example, if he requires a position accuracy of  $\pm 40$  feet and is flying the target at 10,000 feet, the range should not exceed 60 miles. A report on this investigation has been published.<sup>[1]</sup>

As an extension of this preliminary study, several years of radiosonde, wiresonde, and surface data were gathered for several locations in Southern Arizona. Detailed objective procedures were then developed for estimating the type, spacing, and frequency of observations which would be needed to provide the atmospheric data to the precision required for radar-tracking corrections. Because of the greater variability in the lowest level, and the need, therefore, for more precise and more frequent observations in this level, these objective procedures are based on dividing the atmosphere into two parts: (1) the first 1000 feet above the radar, and (2) the atmosphere above 1000 feet. Several charts were developed for the meteorological planner.

From the chart shown in Figure 4, the operations planner can divide the total allowable error in position correction into two parts: (1) that which is contributed by the first 1000 feet, and (2) that which is contributed by the layers above 1000 feet.

The upper section of the chart shown in Figure 5 relates the error to the precision of measurement of refractive gradient in the lower 1000 feet for various ranges and altitudes of the target. The lower section relates the precision of refractive gradient measurement to the spacing of observation sites and frequency of observations.

Similarly, the chart shown in Figure 6 relates position error, refractive gradient precision, and the spacing and frequency of observations for the layers of the atmosphere above 1000 feet. Details of the development of these objectives procedures are contained in a report.<sup>[2]</sup>

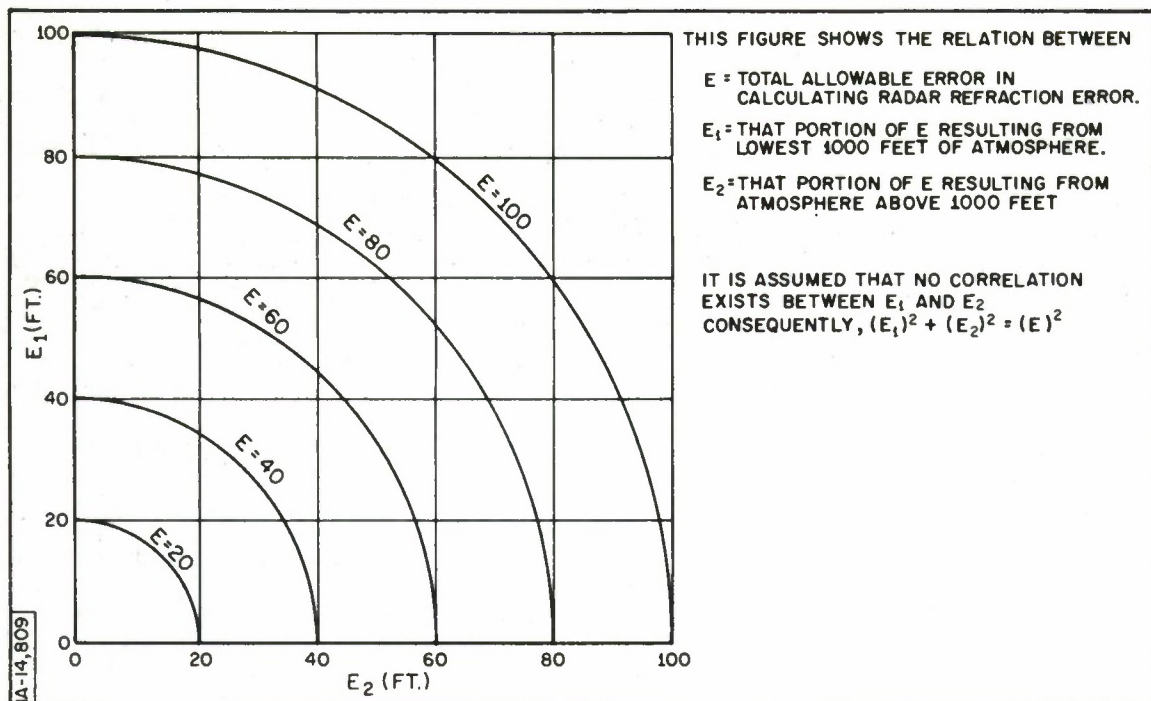
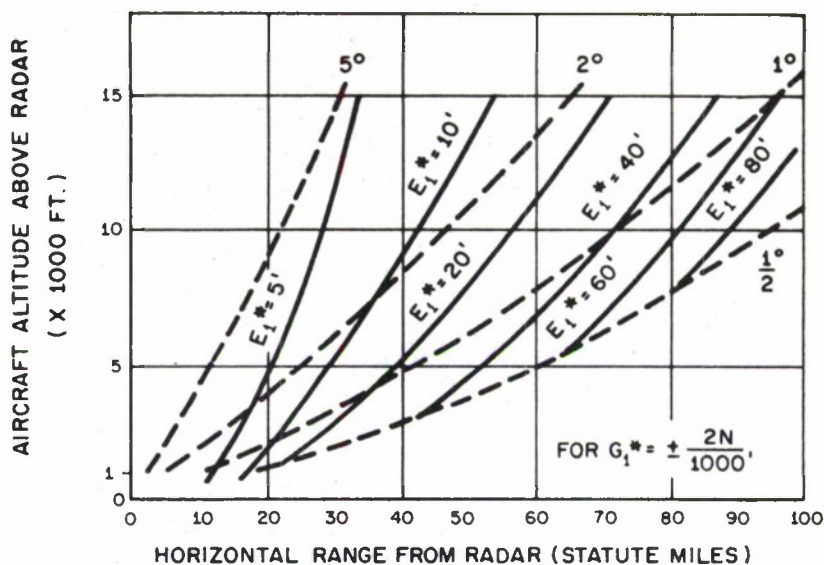


Figure 4. Radar Refraction Error

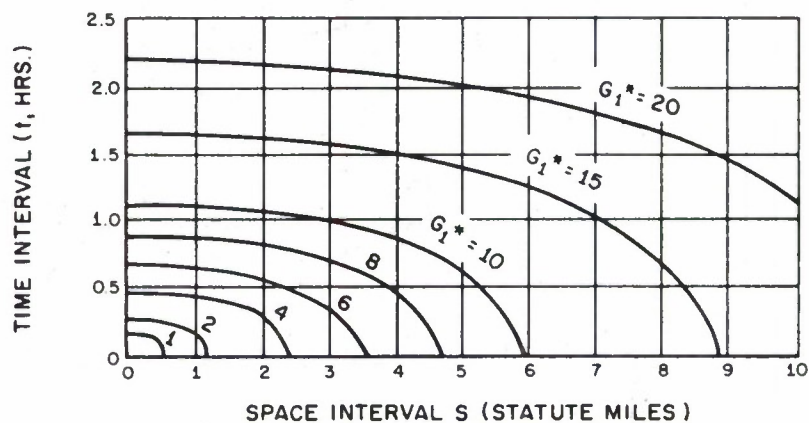
It has been noted, upon examination of tracking radar angle and range data, that frequent spurious excursions of the target appear to occur, with the occasional appearance of position displacements of several hundred feet. It is not known whether or not this is an atmospheric effect. Two field tests, designed to determine the effect of small-scale, short-lived atmospheric refraction anomalies on radar tracking performance, have been started. One test is essentially a repeat of the White Sands experiment of tracking a fixed beacon on a mountain, except that position and range data will be recorded at 0.1-second intervals. In the second test, the frequency and size of atmospheric "angels" within the beam of the tracking radar will be measured with an X-band vertical pointing radar operating simultaneously with the tracking radar. The University of Arizona is providing assistance in obtaining this angel data. The frequency and intensity of radar angels will be compared with the tracking





RELATION OF TOLERANCE IN CALCULATING RADAR REFRACTION ERROR  $E_1$  TO TOLERANCE IN OBSERVING VERTICAL GRADIENT OF REFRACTIVE INDEX  $G_1$  IN LOWEST 1000 FEET.

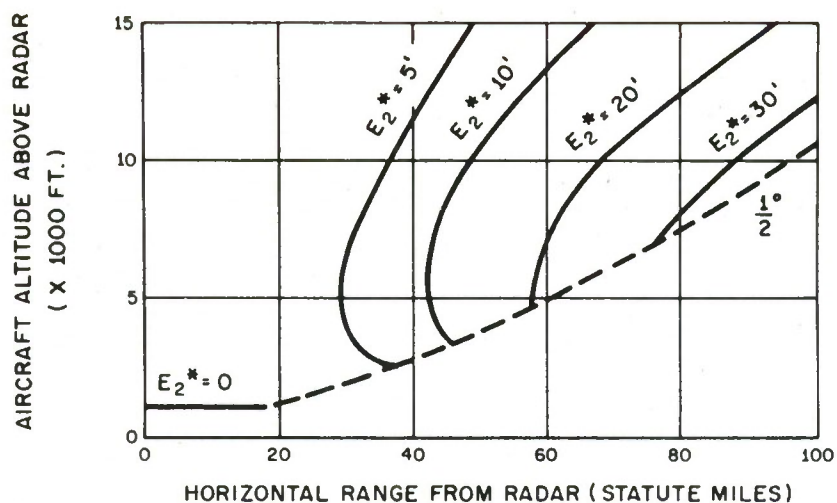
$$[G_1^*]^2 = \left[ \frac{N}{1000'} \right]^2 = \left[ \frac{9.1 N}{1000' \text{ HR.}} t \right]^2 + \left[ \frac{1.7 N}{1000' \text{ MILE}} S \right]^2$$



MAXIMUM TIME AND SPACE INTERVAL BETWEEN LOW LEVEL OBSERVATIONS FOR MEASURING  $G_1$  BELOW 1000 FT. TO PROVIDE CALCULATION OF RADAR REFRACTION ERROR TO  $\pm E_1^*$ .

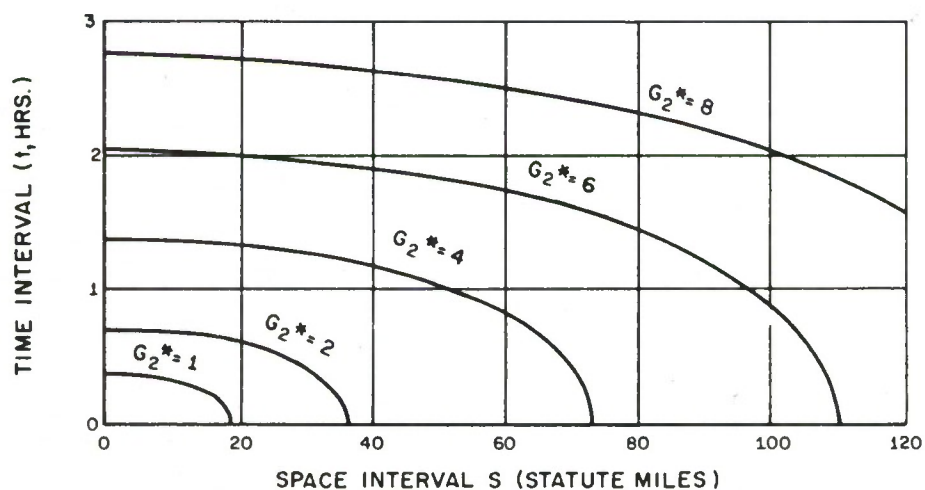
Figure 5. Low-Level Observations Required to Provide Necessary Data





RELATION OF TOLERANCE IN CALCULATING RADAR REFRACTION ERROR  $E_2$  TO TOLERANCE IN OBSERVING REFRACTIVE INDEX VERTICAL GRADIENT  $G_2$  ABOVE 1000 FEET.

$$[G_2^*]^2 = \left[ \frac{N}{1000'} \right]^2 = \left[ \frac{2.9 N}{1000' \text{ HR.}} t \right]^2 + \left[ \frac{0.54 N}{1000' \text{ MILE}} S \right]^2$$



MAXIMUM TIME AND SPACE INTERVAL BETWEEN RADIOSONDE OBSERVATIONS FOR MEASURING  $G_2$  ABOVE 1000 FEET TO PROVIDE CALCULATION OF RADAR REFRACTION ERROR TO  $\pm E_2^*$ .

1A-14,382

Figure 6. Radiosonde Observations Required to Provide Necessary Data

radar position data to determine what, if any, correlation exists between spurious excursions of the target and the presence of angels.

In summary, the current program in atmospheric refractivity research at Fort Huachuca consists of:

- (1) an analysis of the variability of atmospheric refractivity in the lower levels.
- (2) an attempt to correlate angel activity with Fluctuation in the radar position measurements; and
- (3) the development of objective techniques for planning meteorological observations to assure that accuracy requirements for refractive corrections for radar operation are met.

#### REFERENCES

1. A. V. Carlson, Report USAERDRA, met 8-64, July 1964, "Analysis of the Precision of Atmospheric Refractivity Corrections to Radar Tracking Measurements."
2. K. M. Barnett, Interim Report USAERDRA, met 9-64, June 1964, "An Objective Procedure for Planning Meteorological Observations Needed to Calculate Radar Refraction Errors."

## REFRACTION CORRECTIONS TO ELECTRICAL RANGE MEASUREMENTS

K. A. Norton\*

At the Fifth Joint AFMTC Range Users Data Conference, Dr. Charles L. Carroll, the Manager of the PAA Technical Staff, indicated that the most significant refraction problems are:

- (1) the determination of the ultimate limitations imposed by nature on electronic tracking systems;
- (2) the determination of optimum methods for correcting data from electronic tracking systems for the effects of tropospheric refraction;
- (3) the estimation of the magnitude of residual errors after using various correction procedures;
- (4) the development of methods for forecasting the magnitude of uncorrectable residuals for specific meteorological conditions; and
- (5) the development of real-time methods of correcting for the effects of tropospheric refraction.

This paper will provide answers to most of these problems. It will describe methods believed preferable to those currently being used, and will indicate how improved answers can be obtained in the future. The discussion will be confined to the problem of correcting a measurement of the electrical range  $R_e$  to a true geometrical range  $R_o$ :

$$R_o = R_e - R_e \Delta \cdot 10^{-6} \pm R_e \sigma \cdot 10^{-6} \quad (1)$$

---

\* Central Radio Propagation Laboratory, National Bureau of Standards, Boulder, Colorado.

Note that the correction  $\Delta$  and its standard deviation  $\sigma$  are expressed as dimensionless quantities: parts per million.

We are given an electrical range measurement antenna near the earth's surface and a target point somewhere above the radio horizon of the range measurement antenna at an apparent elevation angle  $\theta_o$ , and wish to determine methods of correcting the measured electrical range  $R_e$  to find the best available approximation to the true distance  $R_o$  between the centers of radiation of the range measurement antenna and the target antenna. It is assumed that the measured electrical range  $R_e$  is free of measurement error. Note that  $R_e(t_o) \equiv c\delta t(t_o)$ , where  $c$  is the free space velocity of light, and  $\delta t(t_o)$  is the transit time between the two antennas of a particular crest of the radio wave which leaves the target antenna at the time  $(t_o - R/v)$  and arrives at the range measurement antenna at the time  $t_o$ . The true distance along the slightly curved ray path followed by the radio wave is given by  $R$ , and  $v$  is the mean value of the velocities of the crest averaged along the curved ray path  $R$ .

By introducing the ray path  $R$ , it is implicitly assumed that ray tracing and geometrical optics will provide a satisfactory solution to the problem of estimating  $R_o$  from  $R_e$ . It is known that geometrical and wave optics theories yield somewhat different variance estimates for  $R_e$  in propagation through a turbulent atmosphere, but these differences occur at the larger fluctuation frequencies, and the difference  $\sigma_o^2(\theta_o, R_e)$  between these two variances certainly represents a negligible component of the residual variance of  $R_o$  after the best available ray-tracing corrections have been made to  $R$ .

There is no currently known wave optics method for estimating  $R_o$  from  $R_e$ , and it seems likely that this difference  $\sigma_o^2$  in the variances of  $R_e$ ,



determined by geometrical optics and by wave optics, may be a good measure of the minimum residual variance of  $R_o(t_o)$  which can be achieved by any electrical range measurement system in real time.

It is interesting to note that the residual phase noise<sup>\*</sup> of the MITRE Line Integral Refractometer is somewhat larger than  $\sigma_o^2$ . Whether or not  $\sigma_o^2$  does prove to be a lower bound to the residual variance of electrical measurements of the true range  $R_o(t_o)$  in real time, it will provide a convenient reference value for comparing the residual variances  $\sigma^2$  obtainable by various correction methods. Thus, we may write

$$\sigma^2 = k^2 \sigma_o^2 \quad (2)$$

It is evident that the smaller the value of  $k^2$ , the better the prediction method, and it may turn out that the best possible method will correspond to  $k = 1$ , although at present this is conjecture. It is anticipated that the dependence on  $\theta_o$ ,  $R_e$  and the general turbulence conditions in the atmosphere will be about the same for both  $\sigma^2$  and  $\sigma_o^2$ , so that  $k$  may be expected to be very nearly independent of  $\theta_o$ ,  $R_e$ , and the turbulent conditions of the atmosphere.

The reference variance  $\sigma_o^2$  can be calculated by using Gene Barrows' theory as discussed and illustrated graphically in his summary paper.<sup>[1]</sup> It will be convenient to determine the reference variance  $\sigma_o^2$  for the hypothetical case of the propagation between infinitesimally short dipole antennas. Although, none of the graphs in Barrows' paper gives the wave optics spectrum for this case, the method for calculating  $\sigma_o^2$  can be illustrated by means of Figure 1 in Ref. [1].

---

<sup>\*</sup> See Ref. [1], pp. 1-143 to 1-153 for Barrows' determination of the residual phase noise; see also pp. 1-107 to 1-III for Norton's discussion.



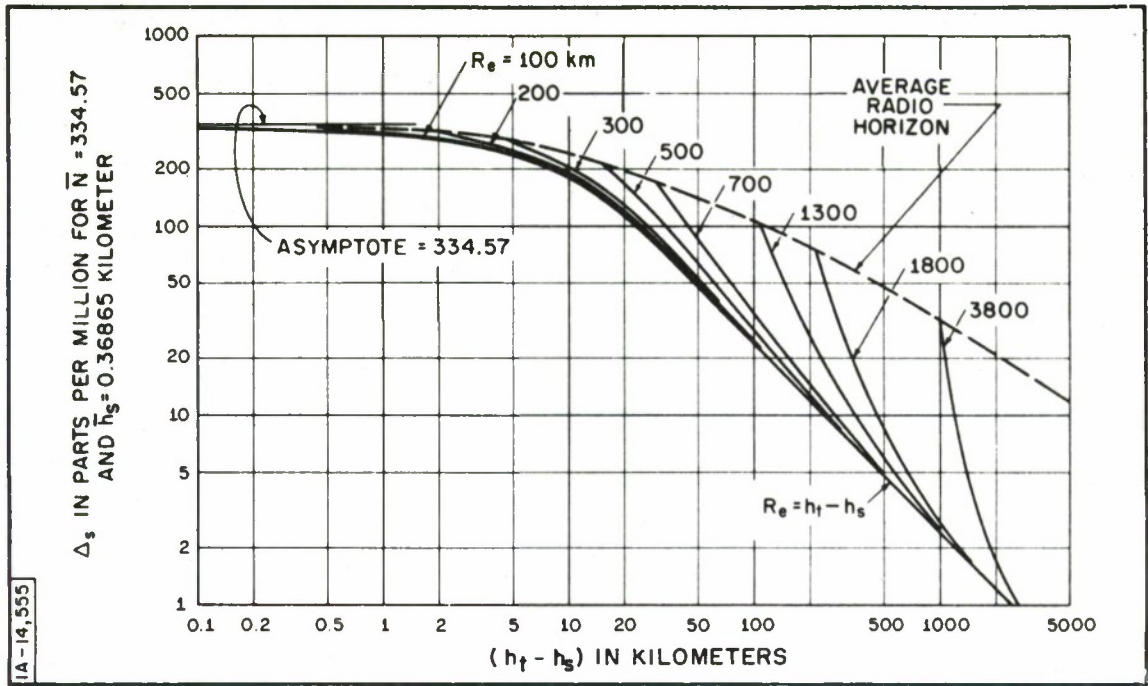


Figure 1. Regression Statistics of the CRPL Standard Sample of 77 Refractive Index Profiles:  $\Delta_s = \bar{\Delta}_s + b_s (N_s - 334.57) - c_s (h_s - 0.3685) \pm \sigma_s$

Let  $W_g(f)$  and  $W_w(f)$  denote the expected spectra of the variances of  $R_e$  as determined by geometrical and by wave optics, respectively, and expressed in parts per million squared per hertz. Now

$$\sigma_o^2 = \int_0^{\infty} \left\{ W_g(f) - W_w(f) \right\} df \quad (3)$$

With reference to Figure 1 in Ref. [1], let  $f_o$  denote the fluctuation frequency ( $f_o \approx 10^{-2}$  hertz) at which the solid and dashed curves converge. For  $f < f_o$ ,  $W_w(f) \approx W_g(f)$ ; and for  $f > f_o$ ,  $W_g(f)$  is given by the dashed curve.  $W_w(f)$  would be given by the solid curve in Figure 1 for  $f > f_o$ , except for the fact that this curve contains antenna filter factors for parabolic antennas with radii  $a_t = a_r = 1$  meter, whereas  $\sigma_o^2$  is defined for propagation between infinitesimal antennas. For infinitesimal antennas,  $W_w(f)$  approaches

$0.5 W_g(f)$  when  $f \gg f_0$ . Barrows has found that  $W_g(f) \cong W_w(f)$  at the frequency  $f_0$  given by

$$f_0 = U_{\perp} \sqrt{\frac{\nu}{10 c R_e}}, \quad (4)$$

where  $U_{\perp}$  is the effective velocity of the path through the turbulent atmosphere in a direction normal to the path; in the case of a fixed path, i. e., a path between terminals which have fixed locations,  $U_{\perp}$  is the component of the value of the wind velocity normal to the path, averaged along the path.

The geometrical optics spectrum  $W_g(f)$  of the electrical range between two infinitesimal antennas may be expressed as follows:

$$W_g(f) = W(f_0) (f_0/f)^{m+1}, \quad f < 0.1 f_0; \quad (5)$$

Similarly,

$$W_w(f) = W(f_0) F(f/f_0), \quad f > 0.1 f_0; \quad (6)$$

where  $F(f/f_0)$  varies from  $(f_0/f)^{m+1}$  when  $f \ll f_0$ , down to  $0.5 (f_0/f)^{m+1}$  for  $f \gg f_0$ . The parameter  $m$  is approximately equal to  $5/3$ . Now Equation (3) may be expressed in the following manner:

$$\sigma_o^2 = W(f_0) \int_0^{\infty} \left\{ (f_0/f)^{m+1} - F(f/f_0) \right\} df \cong f_0 W(f_0) H(m) (\text{ppm})^2, \quad (7)$$

$$H(m) = \int_0^{\infty} \left\{ X^{-(m+1)} - F(X) \right\} dX = \left( \frac{\pi}{20} \right)^{m/2} \frac{\pi^2 \Gamma[(m+2)/2]}{8(m+1) \Gamma^2[(m+1)/2] \sin(m\pi/4)}. \quad (8)$$

The following listing gives  $H(m)$  for several values of  $m$ :

$m$	$H(m)$
3/3	0.306414
4/3	0.186431
5/3	0.120817
6/3	0.082246
7/3	0.058714
8/3	0.036145
9/3	0.033467

For the typical example shown on Figure 1, (Ref. [1]),  $R_e \cong R_o = 100$  kilometers,  $\nu = 10^{10}$  Hz,  $U_{\perp} = 0.002$  kilometers per second,  $f_o = 0.011551$  Hz, and  $f_o W(f_o) \cong 10^{-4}$  (parts per million)<sup>2</sup>, so that  $\sigma_o^2 \cong 12 \times 10^{-6}$  (parts per million)<sup>2</sup> for  $m = 5/3$ . Thus  $\sigma_o \cong 0.003464$  parts per million, i. e., 0.03464 cm for this 100-kilometer path.

For other values of  $U_{\perp}$ ,  $R_e$  and  $\nu$ , the minimum variance  $\sigma_o^2$  may be determined with  $m = 5/3$  from the following:

$$\sigma_o^2 \sim U_{\perp}^{-5/3} R_e^{-1/6} \nu^{-5/6} \quad (9)$$

Note that the difference between geometrical and wave optics approaches zero as  $\nu$  is allowed to increase without limit. The above results are applicable where the target height  $h_t$  is the same as the height  $h_s$  of the range measurement antenna; the way in which  $\sigma_o^2$  is expected to decrease with  $(h_t - h_s)$  will be discussed in a later paper.

Using ray-tracing methods and the CRPL Standard Profile Sample, Thayer and Bean<sup>[2]</sup> have found the following regression relations involving the "surface" refractivity  $N_s$  measured at the height  $h_s$ , expressed in kilometers, above sea level:

$$R_e - R_o = a' + b'N_s - c'h_s \pm \sigma' . \quad (10)$$

The coefficients  $a'$ ,  $b'$ , and  $c'$  are functions of  $R_e$  and of the height,  $h_t$ , of the target antenna above sea level. If both sides of the above expression are divided by  $R_e$  and multiplied by  $10^6$ , the following normalized correction factor, expressed in parts per million, is obtained:

$$\Delta_s \equiv \frac{(R_e - R_o) \cdot 10^6}{R_e} = \bar{\Delta}_s + b_s (N_s - 334.57) - c_s (h_s - 0.36865) \pm \sigma_s . \quad (11)$$

where

$$\bar{\Delta}_s = (a' + b' \cdot 334.57 - c' \cdot 0.36865) \cdot 10^6 / R_e ;$$

$$b_s = b' \cdot 10^6 / R_e ;$$

$$c_s = c' \cdot 10^6 / R_e ; \text{ and}$$

$$\sigma_s = \sigma' \cdot 10^6 / R_e .$$

Figures 1 through 4 show  $\Delta_s$ ,  $b_s$ ,  $c_s$ , and  $\sigma_s$  versus  $(h_t - h_s)$  and  $R_e$ .

Thayer and Bean<sup>[2]</sup> have also given the following regression relation, using 84 Cape Kennedy profiles for all of which  $h_s = 0.008$  kilometers:

$$\Delta_k = \bar{\Delta}_k + b_k (N_s - 357.83) \pm \sigma_k . \quad (12)$$

Figures 5, 6 and 7 show  $\Delta_k$ ,  $b_k$ , and  $\sigma_k$  versus  $(h_t - h_s)$  and  $R_e$ .

For a 100-kilometer path,  $\sigma_s < 8.03$ , so that, as defined by Equation (2),  $k < 2.23 \times 10^3$  using Equation (11) and  $\sigma_s < 8.93$ , so that  $k < 2.58 \times 10^3$  using Equation (12).

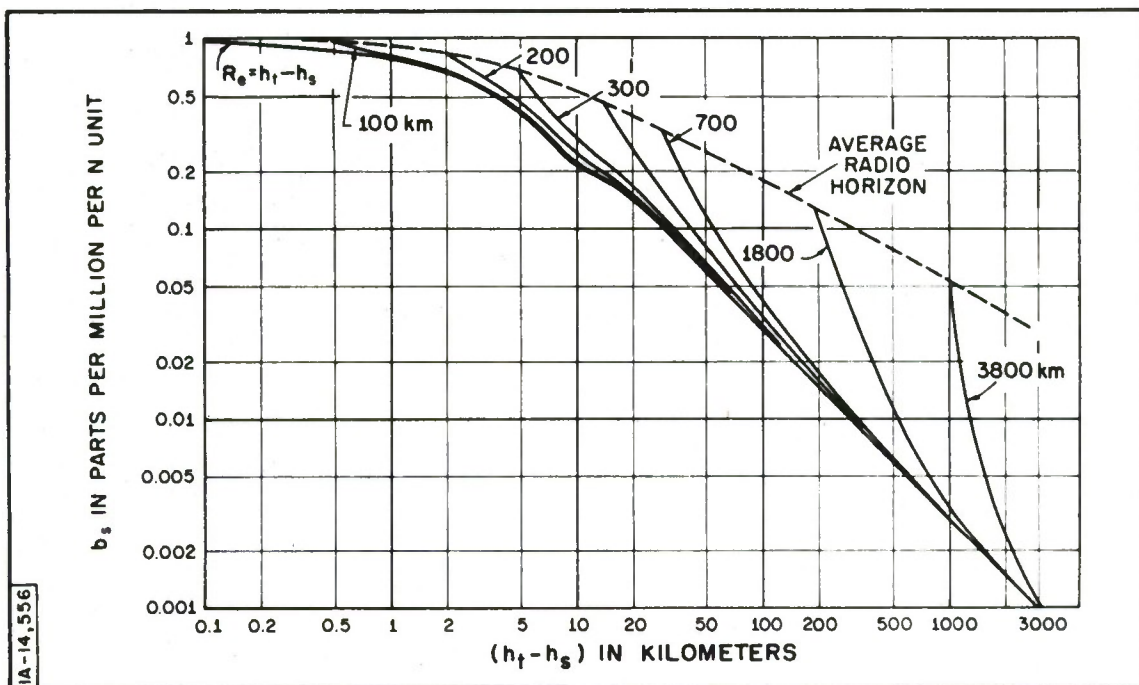


Figure 2. Regression Statistics of the CRPL Standard Sample of 77 Refractive Index Profiles:  $\Delta_s = \bar{\Delta}_s + b_s(N_s - 334.57) - c_s(h_s - 0.36865) \pm \sigma_s$



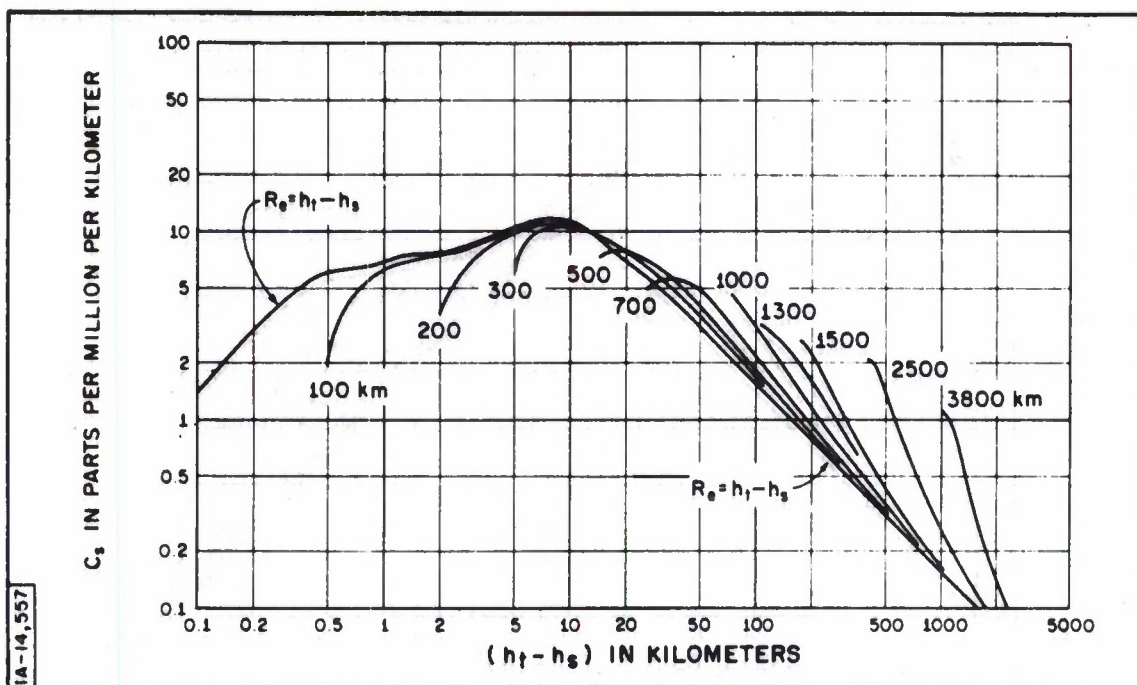


Figure 3. Regression Statistics of the CRPL Standard Sample of 77 Refractive Index Profiles:  $\Delta_s = \bar{\Delta}_s + b_s(N_s - 334.57) - c_s(h_s - 0.36865) \pm \sigma_s$

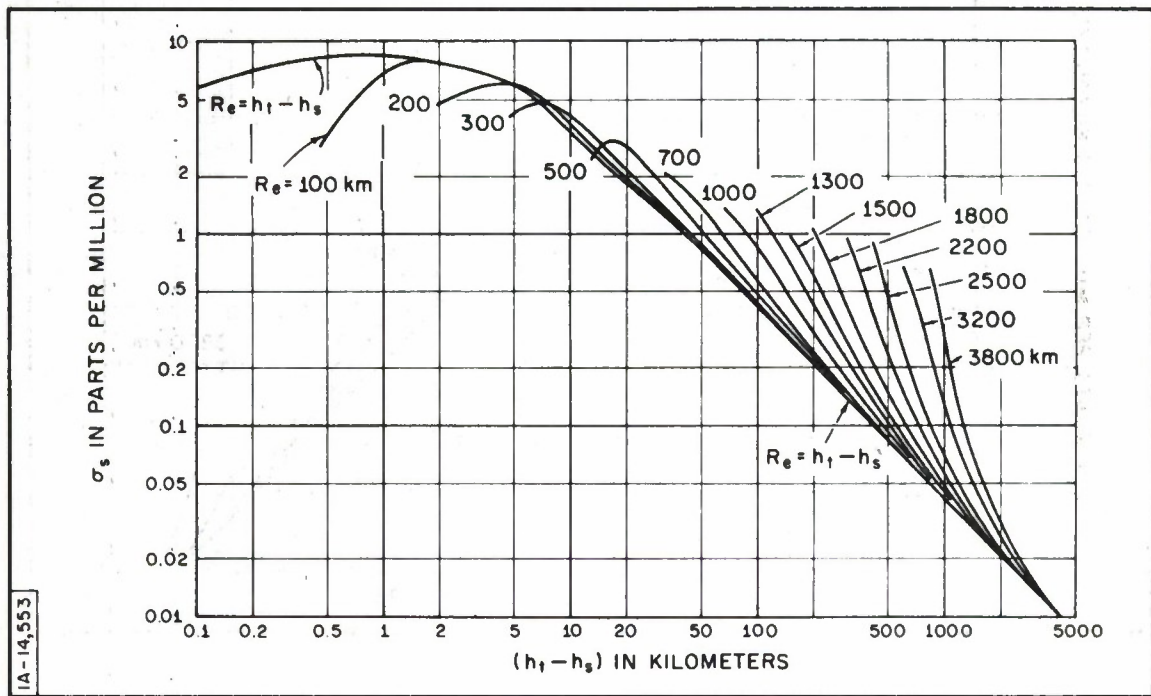


Figure 4. Regression Statistics of the CRPL Standard Sample of 77 Refractive Index Profiles:  $\Delta_s = \bar{\Delta}_s + b_s (N_s - 334.57) - c_s (h_s - 0.36865) \pm \sigma_s$

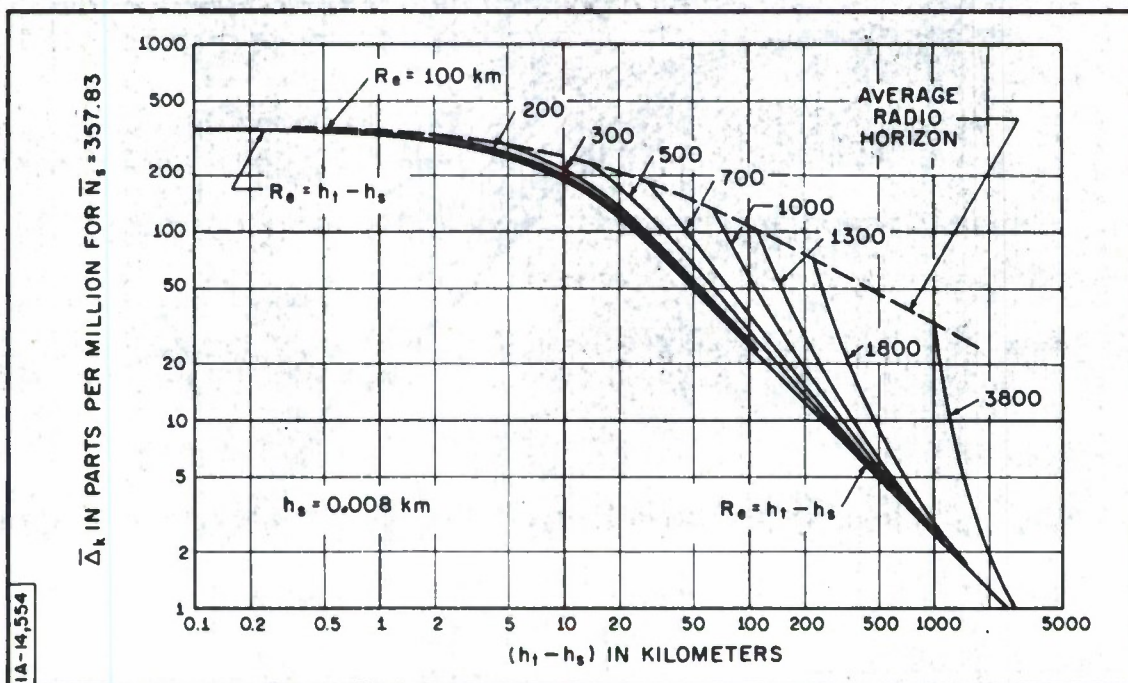


Figure 5. Regression Statistics for 84 Refractive Index Profiles Obtained at Cape Kennedy, Florida:  $\Delta_k = \bar{\Delta}_k + b_k(N_s - 357.83) \pm \sigma_k$

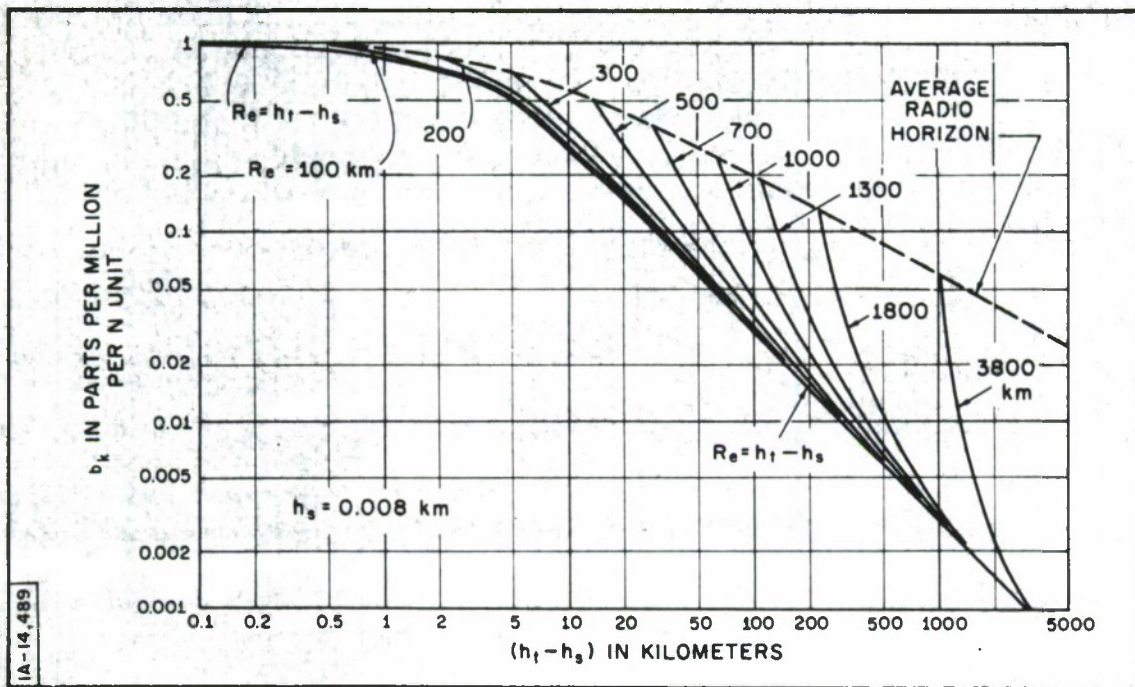


Figure 6. Regression Statistics for 84 Refractive Index Profiles Obtained at Cape Kennedy, Florida:  $\Delta_k = \bar{\Delta}_k + b_k (N_s - 357.83) \pm \sigma_k$



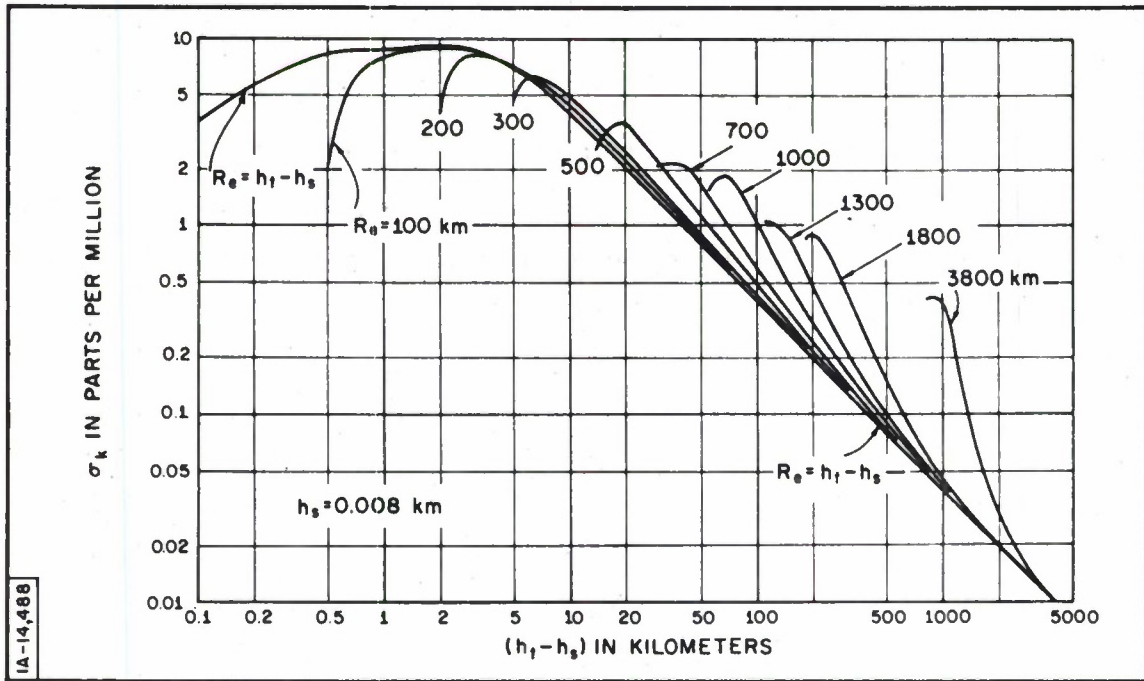


Figure 7. Regression Statistics for 84 Refractive Index Profiles Obtained at Cape Kennedy, Florida:  $\Delta_k = \bar{\Delta}_k + b_k (N_s - 357.83) \pm \sigma_k$



A more approximate correction,  $\Delta_n$ , [similar to (11) or (12)] may be derived in order to more clearly define the problem and to determine the optimum method for averaging  $N_s$  before it is used in Equation (11) or (12) in order to determine  $\Delta$  in real time. A simplified model for the refractive index in the troposphere will be employed. Using the right-handed set of unit vectors  $\vec{i}$ ,  $\vec{j}$ ,  $\vec{k}$ , let a point in the troposphere be denoted by  $\vec{r} = x\vec{i} + y\vec{j} + (z - h_s)\vec{k}$ , where  $\vec{i}$  is chosen so that it is parallel to the wind velocity; i.e.,  $\vec{U} \cdot \vec{i} = U$  and  $\vec{k}$  is vertical.

It is assumed that the surface refractivity  $N_s(\vec{r}, t)$  depends on  $t$  and  $x$  only as a function of the variable  $[t - (x/U)]$  and is independent of  $y$  for a fixed time,  $t$  and that  $N(\vec{r}, t)$  varies exponentially from its surface value as a function of  $z$  and the scale length  $h_o$  as follows:

$$N(\vec{r}, t) = N_s\left(t - \frac{x}{U}\right) \exp\left[-(z - h_s)/h_o\right]. \quad (13)$$

Given these assumptions and a fixed time,  $t$ ,  $N(\vec{r}, t)$  will not vary randomly with  $z$  and will not vary at all with  $y$ . Note that these assumptions are consistent with Taylor's hypothesis, but random variations with  $y$  and  $z$  at a fixed time could also be consistent with Taylor's hypothesis; however, the suppression of such random variations should not make my analysis substantially more unrealistic than it already is by virtue of the assumption that Taylor's hypothesis is applicable; i.e., that  $N_s$  depends on  $x$  and  $t$  only through the variable  $[t - (x/U)]$ .

A refractometer near the surface at the ground-based antenna of the ranging system at  $\vec{r} = 0$ , [which location will also be chosen to be the origin of coordinates at a height  $h_s$  above sea level,] would be expected to vary as a function of time in accordance with

$$N_s(\vec{r} = 0, t) = N_s(t). \quad (14)$$

It will be assumed that the frequency spectrum  $W_{N_s}(f)$  of  $N_s$  for any fixed value of  $\vec{r}$  is the same as its observed spectrum and that, its one dimensional wave-number spectrum in the direction  $(\vec{i} \cos \gamma + \vec{j} \sin \gamma)$  will be given by  $W_{N_s}(kU \cos \gamma / 2\pi)$ , i. e., by identifying the wave-number  $k$  with  $2\pi f / U \cos \gamma$ . If  $\ell_p$ ,  $\ell_n$ , and  $\ell_v$  denote the characteristic scales of anisotropic turbulence in the  $\vec{i}$ ,  $\vec{j}$ , and  $\vec{k}$  directions, respectively, then the dependence of  $N(\vec{r}, t)$  described by Equation (13) would correspond to a finite value for  $\ell_p$ , but to infinite values for  $\ell_n$  and  $\ell_v$ . There is some experimental evidence (Bull [3]), that  $\ell_p > \ell_v > \ell_n$ , but it does not appear that such data appreciably affect the conclusions reached in the following discussion.

Now consider a path through the troposphere between the antenna at the origin  $\vec{r} = 0$  and a target point  $\vec{R}_0 = x \vec{i} + y \vec{j} + (z_0 - h_s) \vec{k}$ . Let  $h_t$  be the height of the target point  $\vec{R}_0$  above sea level;  $h_t$  will usually be different from  $z_0$  because of the curvature of the earth. The electrical range at time  $t_0$  at which the radio waves arrive at the range measurement antenna at  $\vec{r} = 0$  is given by the following:

$$R_e(t_0) \equiv c \delta t(t_0) = c \left[ t_0 - \left( t_0 - \frac{R}{v} \right) \right] = \frac{cR}{v} \cong \int_0^R n\left(\vec{r}, t_0 - \frac{r}{v}\right) dr \quad (15)$$

The integral on the right of Equation (15) is approximate by virtue of the assumption that geometrical optics may be used, but as already shown, any error arising from this approximation will be of negligible importance.

Equation (15) may be rewritten as follows:

$$R_e(t_0) \cong \int_0^R [1 + n - 1] dr = R + \int_0^R (n - 1) dr \quad (16)$$

$$\left[ R_e(t_o) - R_o \right] \cong (R - R_o) + \int_0^R (n - 1) dr \quad (17)$$

Note that the distance along the ray path  $R$  differs slightly from that of  $R_o$ . It has been shown by Bean and Thayer<sup>[4]</sup> that for most tropospheric paths  $(R - R_o)$  is less than 27 percent of  $(R_e - R_o)$  for  $\theta_o > 0$  degrees; less than 2.3 percent for  $\theta_o > 50$  milliradians (2.86 degrees); and less than 0.8 percent for  $\theta_o > 100$  milliradians (5.73 degrees).

The present analysis neglects the transit time  $(r/v)$  through the troposphere (since  $v \gg U$ ) and assumes that  $t_o - (r/v) \cong t_o$ ; that is, that the time of arrival of a radio wave at  $\vec{r} = 0$  is not significantly different from its time of departure from the point  $\vec{R}_{oo}$  at which  $N \cong 0$ . This assumption is reasonable to the extent that the atmosphere does not change appreciably during the transit time  $\delta t = R_{oo}/c$ . Since  $R_{oo} \cong 1020$  kilometers for a ray at a 0-degree elevation angle ( $\theta_o = 0$ ) out to the point  $R_{oo}$  at a height  $h_t = 70$  kilometers, at which  $N \cong 0$ , we find that the transit time through the troposphere is  $\delta t < 0.0034$  second for any elevation angle. Changes in the atmosphere which occur during this short interval of time will be negligible in the context of the present discussion.

Now let  $N = (n - 1) \cdot 10^6$ , to obtain

$$\Delta_n t_o \cong \frac{(R - R_o) \cdot 10^6}{R_e} + \frac{1}{R_e} \int_0^R N(\vec{r}, t_o) dr \quad (18)$$

The  $x$ ,  $y$ , and  $(z - h_s)$  components of  $r$  may be expressed as

$$x \equiv r \cos \theta \cos \gamma ; \quad (19)$$

$$y \equiv r \cos \theta \sin \gamma ; \quad \text{and} \quad (20)$$

$$(z - h_s) \equiv r \sin \theta . \quad (21)$$

Substitution of Equation (13) into (18) gives:

$$\Delta_n(t_o) \cong \Delta_g + \frac{1}{R_e} \int_0^R dr N_s \left( t_o - \frac{x}{U} \right) \exp \left[ - \left( z - h_s \right) / h_o \right], \quad (22)$$

where

$$\Delta_g \equiv \frac{(R - R_o) \cdot 10^6}{R_e} .$$

The integration variable is given by

$$t = t_o - \frac{x}{U} = t_o - \frac{r \cos \theta \cos \gamma}{U} .$$

As  $r$  varies from 0 to  $R$ ,  $x$  varies from 0 to  $x_o \equiv R_o \cos \theta \cos \gamma$ ;  $z$  varies from  $h_s$  to  $z_o$ ;  $h$  varies from  $h_s$  to  $h_t$ ; and  $t$  varies from  $t_o$  to  $t_o - (x_o/U)$ . Equation (22) now becomes

$$\Delta_n(t_o) \cong \Delta_g + \frac{U}{x_o} \int_{t_o - \frac{x_o}{U}}^{t_o} dt N_s(t) \exp \left[ \frac{U \tan \theta (t - t_o)}{h_o \cos \gamma} \right] . \quad (23)$$

It is evident from Equation (23) that the appropriate value of  $N_s$  to use in Equations (11) or (12) is the weighted time value:



$$\bar{N}_s(t_o) = \frac{\int_{t_o - \frac{R_e \cos \theta \cos \gamma}{U}}^{t_o} dt N_s(t) \exp \left[ \frac{U \tan \theta (t - t_o)}{h_o \cos \gamma} \right]}{\int_{t_o - \frac{R_e \cos \theta \cos \gamma}{U}}^{t_o} dt \exp \left[ \frac{U \tan \theta (t - t_o)}{h_o \cos \gamma} \right]} \quad (24)$$

Equation (24)  $x_o$  is replaced by  $R_e \cos \theta \cos \gamma$  since  $R_e$ ,  $\theta$ , and  $\gamma$  are quantities which can be determined in real time by the electronic tracking system and by measurements of the wind direction at  $\vec{r} = 0$ . This expression for  $\bar{N}_s(t_o)$  should prove useful except for the special case in which the wind is blowing exactly normal to the path;  $\gamma$  is then equal to zero, and Equation (24) would indicate that at no time averaging is necessary. The above approximate analysis fails in this case because of the assumption that  $N_s$  does not vary with  $y$  at a fixed time  $t$ . Work is continuing on this problem with the object of developing a solution more generally applicable.

Note that  $\cos \gamma$  is positive for targets which are downwind and, in such cases,  $\bar{N}_s(t_o)$  can be determined strictly in real time. For targets lying in one of the quadrants from which the wind is blowing,  $\cos \gamma$  will be negative and  $N_s$  must then be averaged over the time interval from  $t_o$  to  $t_o + (R_o \cos \theta |\cos \gamma|/U)$  to determine  $\bar{N}_s(t_o)$ .

The way in which Equations (1), (11) and (24) may be used for correcting measured electrical ranges so that they approximate the true geometrical range  $R_o$  can now be illustrated. For this purpose, some measurements of the



electrical range  $R_e(t_o)$  over a 15.5 kilometer path from Boulder Creek to Green Mountain in Colorado will be used, together with measurements of  $N_s(t_o)$  made simultaneously near the Boulder Creek terminal of the path. These data were obtained and analyzed by personnel in Dr. M. C. Thompson's Lower Atmosphere Physics Section in CRPL. These data used were measured relative values of  $\Delta R_e(t_o)$  and absolute values of  $N_s(t_o)$  at 1-minute intervals over the 50-hour period of time from 1200 Jan. 3 to 1400 Jan. 5, 1962.\*

Because of the difficulty of determining the true range  $R_o$  over that path with an accuracy better than a few parts per million, it was not considered necessary to measure the absolute value of the electrical range  $R_e$ . Thus, only relative values of the electrical range  $\Delta R_e(t_o)$  were measured, and these relative values are believed to be accurate to better than 0.01 part per million over this 50-hour period.

Let  $\bar{R}_e$  denote the mean value of  $R_e(t_o)$  and  $\bar{N}_s$  the mean value of  $N_s(t_o)$  over the 50-hour period of the observations. If the absolute values of both of these quantities and of  $R_o$  were known, it would be possible to determine the bias  $B_s$  of Equation (11) for this period as follows:

$$B_s = \frac{(\bar{R}_e - R_o) \cdot 10^6}{\bar{R}_e} - \Delta_s - b_s(\bar{N}_s - 334.57) + c_s(1.56 - 0.36865) \quad (25)$$

For this particular propagation path and the observed data for this period of time,  $\bar{\Delta}_s + b_s(\bar{N}_s - 334.57) - c_s(1.56 - 0.36865) \cong 226$  (parts per million), but since neither  $\bar{R}_e$  nor  $R_o$  was known with sufficient accuracy, it was not possible to determine  $B_s$ . The data that were available, however, did permit a check on the utility of Equation (24). The results of preliminary analysis encourage a more complete study in the near future.

---

\* See Ref. [1], p. 1-171 for graphic presentation of these data.

Let  $y(t_o) \equiv (10^{+6}/R_o) \Delta R_e(t_o)$  denote a relative electrical range measurement expressed in parts per million, and let  $x(t_o) \equiv b_s \bar{N}_s(t_o)$  denote a surface refractive index correction determined by the formula

$$\bar{N}_s(t_o) = \frac{1}{n} \sum_{i=0}^n N_s(t_o + i \Delta). \quad (26)$$

A running average value of  $\bar{N}_s(t_o)$  was determined for the 50 hours of data, using  $n = 0, 15, 30, 45, 60$ , etc., up to 420. With  $n = 0$ , the variance of  $N_s(t_o)$  was found to be equal to  $36.5$  (parts per million)<sup>2</sup>. Similarly, the variance of  $y(t_o)$  was found to be  $27.1$  (parts per million)<sup>2</sup>. Note that the exponential weighting factor in Equation (24) was not used in Equation (26).

Figure 8 shows the variance  $\sigma_m^2$  of  $[y(t_o) - x(t_o)] \equiv [(10^{+6}/R_o) \cdot \Delta R_e(t_o) - \bar{N}_s(t_o)]$ , with  $b_s$  arbitrarily set equal to 1 and with  $\Delta$  set equal to +1 and -1 minute, corresponding to upwind and downwind targets, respectively. The predominant direction of the wind was toward Green Mountain over this 50-hour data period, although it was observed to change its direction over the entire 360 degrees at various times. Using the Thayer-Bean regression analysis, it appears that  $b_s$  should have been set equal to 0.830, and the use of this value would probably have resulted in a still greater reduction of variance, since the variance of  $x(t_o)$  with  $b_s = 0.83$  would have been equal to 25.1 which is nearer to the variance 27.1 of  $y(t_o)$ .

An analysis of the data obtained in Hawaii will use the following, more refined procedures. Equation (24) rather than Equation (26) will be used to determine  $N_s(t_o)$ , and the values of the wind speed  $U$  and wind direction  $\gamma$  will be determined as a function of  $t_o$  to obtain the appropriate averaging interval  $\tau(t_o) \equiv R_e \cos \theta \cos \gamma / U$  in real time. The use of these procedures should result in an even larger reduction of variance.

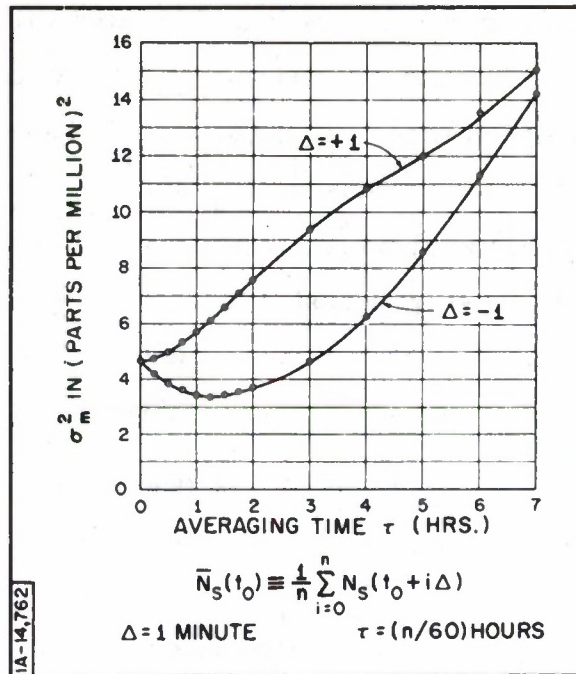


Figure 8. Variance  $\sigma_m^2$  of  $\left[ \left( 10^{+6}/R_o \right) \Delta R_e(t_0) - \bar{N}_s(t_0) \right]$  for the Period 1200 Jan. 3 to 1400 Jan. 5, 1962 Boulder Creek to Green Mountain Path:  $R_o = 15.5 \text{ km}$ ,  $h_s = 1.56 \text{ km}$ ,  $h_t = 2.22 \text{ km}$ ;  $N_s(t_0)$  Measured at Boulder Creek

An analysis will also be made of  $N_s(t_0)$  data measured at various heights above the surface in order to determine the height yielding the best correction to electrical range measurements. It appears that the optimum height will be much greater than the heights currently used because of the additional turbulence near the ground. Both the electrical range measurement antennas and the refractometers should be at much larger heights above the surface, but obviously there are practical difficulties involved. The  $N_s(t_0)$  measurements need not be made at exactly the same heights and locations as the range measurement antennas, but the data processing is simplified when these locations are the same. The instruments used to determine  $N_s(t_0)$  may advantageously have a time constant of a few minutes.



It appears from Figure 8 that the use of Equations (11) or (12), with  $\bar{N}_s(t_o)$  determined by Equation (24) and with  $\tau(t_o) = R_e \cos \theta \cos \gamma / U$  determined as a function of time, may make possible the provision of corrections to  $R_e(t_o)$  which have a precision  $\sigma_m$  of, say, 1 or 2 parts per million. It is important to emphasize, however, that the results shown in Figure 8 were obtained over a relatively short period of time\* and over a single 15.5-kilometer path, so that final judgment on the precision to be expected should await analysis of additional data samples over many diverse propagation paths.

The accuracy of the correction  $\Delta_s$  is given by  $\sqrt{B_s^2 + \sigma_m^2}$ . The values of  $\sigma_s^2$  and of  $\sigma_k^2$  shown on Figures 4 and 7, respectively, represent good estimates of the expected values of  $B_s^2 + \sigma_m^2 - b_s^2 \sigma_N^2$  and of  $B_k^2 + \sigma_m^2 - b_k^2 \sigma_N^2$ , respectively. Here  $\sigma_N$  denotes the standard error of a measurement of  $N_s$ . Finally, if  $\sigma^2$  denotes the variance of determinations of the true geometrical range  $R_o$  determined by Equation (11) or (12) and if  $\sigma_e^2$  denotes the variance of errors in the measurement of the electrical range  $R_e$ , then

$$\sigma^2 = \sigma_e^2 + \sigma_s^2 + b_s^2 \sigma_N^2 \text{ (ppm)}^2, \quad (27)$$

or

$$\sigma^2 = \sigma_e^2 + \sigma_k^2 + b_k^2 \sigma_N^2 \text{ (ppm)}^2. \quad (28)$$

Note that  $\sigma_e^2$  will vary with the type of system used for the electrical range measurement;  $\sigma_s^2$  or  $\sigma_k^2$  will vary slightly from range to range; and  $\sigma_N^2$  will vary with the types of instruments used to measure  $N$ .

Recent progress at the Air Force Eastern Test Range indicates that  $R_e \sigma_e \cdot 10^{-6}$  is occasionally as large as 1 meter for the better range

---

\* If this period of time were increased without limit, then it would be expected that the minimum value of  $\sigma_m^2$  would approach  $\sigma_e^2 + b_s^2 \sigma_N^2$ , and in this case,  $\sigma_c^2 < 10^{-4}$ .

measurement systems such as MISTRAM, but is usually much smaller than this. As a consequence, the terms  $\sigma_k^2$  and  $b_k^2 \sigma_N^2$  in Equation (28) are ordinarily the controlling factors in the over-all accuracy. Note that although the values of  $\sigma_s^2$  and  $\sigma_k^2$  given in this report are quite large, they nevertheless represent realistic estimates of the accuracy likely to be realized, using currently known techniques.

Since the ultimate in accuracy is seldom required in real time, it is often possible to use much more elaborate methods of determining  $\Delta$  than Equations (11) or (12). All of these methods involve some kind of ray tracing and differ only in the extent of the meteorological data used. It is believed that those methods which depend upon the assumption of an exponential profile will not yield results as accurate as those obtained by the use of Equations (11) or (12). It is not yet clear whether the use of corrections  $\Delta$  based simply on careful ray tracing through profiles obtained near the time-of-flight will yield better results than Equations (11) or (12); this is because of (a) the large errors currently present in most meteorological measurements, and (b) the changes in the atmosphere between the times that the measurements of  $R_e$  and those of the refractive index structure  $N(\vec{r})$  are made. Such errors tend to be averaged out in the processes leading to Equations (11) or (12) and to Equation (24).

It is recommended that the following steps be taken to reduce the magnitude of  $\sigma^2$ :

- (1) Methods for meteorological measurements of the three-dimensional refractive index structure should be improved.
- (2) Equations (11) or (12) should be used for correcting electrical range measurements. (Note that Equation (11) may be expected to give good results at any geographical location\*.)

---

\* See footnote on page 298



- (3) Instrumentation and procedures should be developed so that Equation (24) may be used in connection with all electrical range measurements with separate  $N_s(t_o)$ , and wind velocity measurements made near each range measurement antenna and, if feasible, at more than one height above the surface.
- (4) Ray tracings should be made at each test range\* using the best available three-dimensional meteorological refractive index data obtained near the time of each electrical range measurement mission in order to obtain pertinent corrections.
- (5) Efforts should be continued to reduce the variance  $\sigma_c^2$  in electrical range measurements; in particular, improvements should be made in the uniformity of the phase responses of the space vehicle antennas with direction in space over the entire range of directions involved on such flights.
- (6) Redundant measurements should be used to check the accuracy of the above methods of correction and to determine, if possible, whether it is better to follow 4, above, or 2 and 3.
- (7) The data obtained under 4, above, should be used to develop improved statistics at each test range\* for use in an equation similar to Equation (12).
- (8) The systematic influence of time of day, season of the year and geographical location on  $\Delta$ ,  $b$ ,  $c$ , and  $\sigma$  should be determined using the growing sample of data obtained under recommendation 7, above. As adequately large improved data samples become available in the future, the older profile data should be removed from the statistical analysis.
- (9) Consideration should be given to increasing the heights of the ground-based measurement antennas.

---

\* The large percentage of the time that ducts are present at the Pacific Missile Range emphasizes the gain to be expected from the use of statistics derived from refractive index profiles obtained at this particular location.

- (10) The  $N_s$  "surface" refractive index measurements should be made at various heights in order to determine an optimum height, with appropriate consideration given to the practical operational problems involved.
- (11) Continued support should be given to various research programs to develop
  - a) better methods for determining  $\Delta(t_o)$  at all frequencies  $\nu$ , including the optical range;
  - b) more accurate methods for measuring the refractive index and its statistics in the troposphere; and
  - c) better analytical methods for using these data.

Finally, it is recommended that  $\Delta$ ,  $\sigma$ ,  $\sigma_e$ , and  $\sigma_N$  be expressed in parts per million to facilitate intercomparisons and that the metric system be used at all ranges. Such standardization seems particularly appropriate for global ranging systems and is clearly the responsibility of the Air Force National Range Division.

#### REFERENCES

1. E. C. Barrows, "Residual Range and Range Rate Errors due to the Troposphere;" in Proceedings of the Second Tropospheric Refraction Effects Technical Review Meeting, I, Bedford, Massachusetts, The MITRE Corporation, ESD-TDR-64-103, March 1964 (AD435973), 1-143, 1-153 (U).
2. G. D. Thayer and B. R. Bean, private communication with author, June 15, 1962.
3. G. Bull, Hertz Institute Berlin-Aldershof.
4. B. R. Bean and G. D. Thayer, "Comparison of Observed Atmospheric Radio Refraction Effects with Values Predicted Through the Use of Surface Weather Observations," J. Research Natl. Bureau Standards, 670, 3, May-June 1963, 273-85.

# THE RESPONSE OF MICROWAVE REFRACTOMETER CAVITIES TO ATMOSPHERIC VARIATIONS

R. O. Gilmer,\* R. E. McGavin\* and B. R. Bean\*

## Authors' Preface

The material covered deals with both the measurement phase of the program and the results obtained. The presentation, therefore, comprises two papers. The first\*\* (see title above) deals with a test conducted on the National Bureau of Standards refractometers. The subsequent paper, "Observed Vertical Wave Number Spectra of Refractivity Near the Ground," by K. A. Norton and E. C. Barrows, presents the results of the measurements.

---

\* National Bureau of Standards.

\*\*This paper was also published in the Proceedings of the 1964 World Conference on Radar Meteorology.

## INTRODUCTION

The microwave refractometer (Crain<sup>[1]</sup> and Birnbaum<sup>[2]</sup>) has been used extensively to measure directly the radio refractive index of air (Bean<sup>[3]</sup>).

Although these instruments have been in use for many years, little information is available on their limitations as probes of atmospheric variations. Recently, a test on the National Bureau of Standards (NBS) refractometers was conducted. The results are presented in this report.

## THE NBS REFRACTOMETERS

In both the NBS absolute (Vetter<sup>[4]</sup>) and relative refractometers (Birnbaum<sup>[2]</sup>), the sampling cavity, placed in the free atmosphere, is the source of most of the inaccuracy of the instrument. Although the sampling cavity should be capable of indicating the true variations of the refractive index of air, the variations are influenced by changes in cavity temperature, wind speed, and direction, and by limitations due to the finite size of the cavity.

### The Temperature Coefficient of the Sampling Cavity

The resonant frequency of the sampling cavity is a function of its dimensions. Present-day cavities are made of Invar, having a temperature coefficient of approximately 1N unit per degree centigrade. Temperature compensation reduces this to 1 or 0.2 of an N unit/degree centigrade; coefficients as low as 0.03 N/C<sup>0</sup> have been achieved (Crain and Williams,<sup>[5]</sup> Vetter and Thompson<sup>[6]</sup>). Errors of this kind are serious only when a slowly varying temperature over a considerable range is encountered. Although the statically determined temperature coefficient cannot yield an exact correction, it does permit a fair estimate of the error. The possibility of improving the cavity performance by the use of special ceramics has been investigated (Thompson, Freethey and Waters<sup>[7]</sup>).



### Aspect Sensitivity of the Sampling Cavity

The sampling cavity is a cylindrical barrel with ventilated end plates. When used on an aircraft, the air sample enters along the axis of the barrel. However, in a typical ground-based location, the air sample may arrive at any angle with respect to the cavity axis. To determine any effect caused by the "aspect" of the cavity relative to the direction of the mean wind, multiple cavities were mounted at fixed angles relative to the air flow in each of the tests conducted.

### Velocity Sensitivity of the Sampling Cavity

The intrusion of the sampling cavity into the airstream generates turbulence which increases with the air speed, with a consequent reduction in pressure within the cavity. To determine the pressure effect, a plastic duplicate of the cavity was tested in a wind tunnel. The pressure inside the cavity and that of the undisturbed airstream outside were measured by a differential manometer to determine any sensitivity to velocity in the range up to 68 miles/hour. (Thermocouples were used to measure temperature changes: within the experimental accuracy, the temperature changes were negligible.) These differential pressure measurements were made for various aspect angles relative to the air flow. The data were used to compute a pressure coefficient defined as

$$C_p = \frac{\Delta P}{1/2 \rho u^2},$$

where

- $\Delta P$  = difference between the pressure inside the cavity and that in the unobstructed tunnel,
- $\rho$  = air density in the wind tunnel, and
- $u$  = wind velocity in the wind tunnel.



Hence, when  $C_p$  is a constant at any aspect angle for an entire range of velocity, the flow is turbulent. It can be seen in Figure 1 that from 0.447 to and including 2.24 meters/second (curves A, B, and C),  $C_p$  varies with velocity.

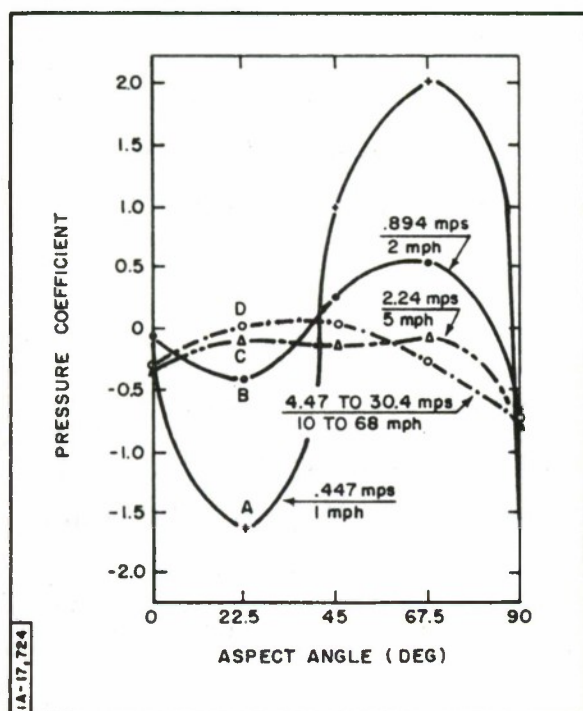


Figure 1. Pressure Coefficient of NBS Microwave Sampling Cavity as a Function of Aspect Angle for Varying Wind Velocity

However, in the velocity range of 4.47 to 30.4 meters/second (curve D),  $C_p$  is a constant for any particular aspect angle. Below 4.47 meters/second, the flow through the cavity is in the laminar or transitional region between laminar and turbulent flow; above 4.47 meters/second, the flow is turbulent. The error of refractivity caused by the velocity of the air as a function of aspect angle is illustrated in Figure 2. The error was calculated from the measured pressure drop in the cavity. The 45-degree aspect offers the minimum induced error in refractivity caused by the pressure drop, while the value increased for aspect angles greater and less than 45 degrees. Apparently, the location of the minimum is caused by the shape of the temperature-compensating disks within the cavity.

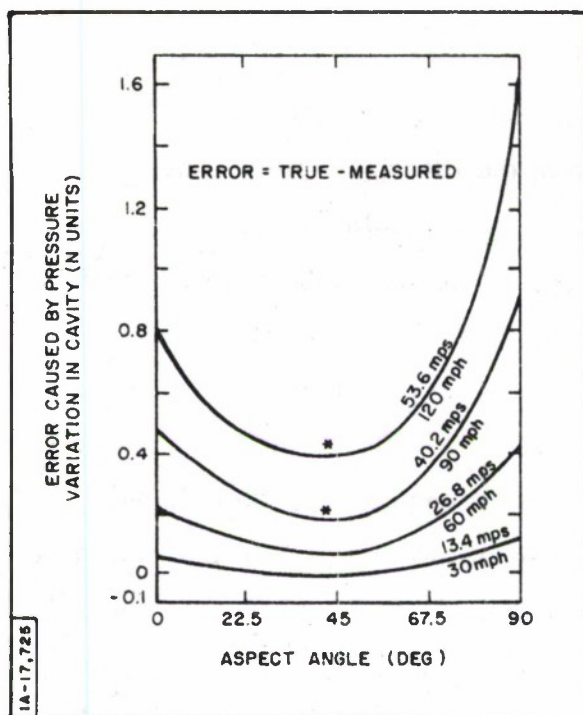


Figure 2. Calculated Error in Refractivity Measurements. (The curves for 40.2 and 53.6 meters/second are extrapolated from data.)

### Spatial Resolution of the Sampling Cavity

Because of its finite size and the external electric field, the cavity measures a weighted average of the variations of a volume of air somewhat larger than its dimensions. The configuration of the end plate and the compensating disks inhibits flushing time and thus further limits the ability of the refractometer to resolve the differences between the refractive index of air parcels passing through the cavity.

In a slowly moving atmosphere, which is homogeneous at least over the dimension of the cavity, the cavity will resolve differences of refractivity separated by a distance comparable to the dimensions of the cavity (Hartman<sup>[8]</sup>). However, at velocities where the flow through the cavity becomes turbulent, further filtering occurs. The cavity so conditions the air sample that the practical limit of resolution is further restricted.

As pointed out, when the air velocity is greater than 4.47 meters/second, the flow through the cavity is turbulent, and some filtering effect is to be expected. An experimental determination of the filtering action of the NBS cavity was conducted by using a transparent plastic duplicate of the sampling cavity immersed in a water flow tunnel, with Reynolds numbers approximately the same as those encountered in the free atmosphere during conditions of fully developed turbulence. Blobs of colored dye were injected upstream from the cavity and permitted to flow through it. Colored motion pictures were taken of the flow around and through the cavity for aspect angles of 0, 22-1/2, 45, 67-1/2, and 90 degrees, relative to the direction of the water flow. The time required for the dye to completely flush from inside the cavity for several flow velocities was obtained from visual inspection of the motion pictures. From the measured flushing time and velocity of the water, the estimated minimal spatial resolution of a count oriented into the air flow was found to be 0.75 meter, whereas the cavity oriented 90 degrees to the air flow indicated a resolution 2.2 times as long. This, however, was found under static conditions where the direction of the air flow was constant.

#### Spectral Characteristics of the Sampling Cavity as a Function of Aspect

Tests were conducted in a wind tunnel and in the free atmosphere. Spectral analysis was performed on the refractivity obtained from three sampling cavities oriented at 0, 45, and 90 degrees to the wind. Wind tunnel tests indicated that the sampling cavity whose axis was 90 degrees to the direction of the air flow lowered the spectral density of all frequency components which were measured. In the free atmosphere, a different effect was noted. Many spectral samples were analyzed and, in all cases, little spectral difference was noted for the cavity whose axis is parallel to the direction of the air flow and for that at 45 degrees to the direction of the wind. In all samples investigated, the

cavity oriented 90 degrees to the prevailing wind indicated a significantly higher spectral density at all frequencies for which measurements were made. Repeated samples indicated similar results.

As a result of these tests a modified cavity (Figure 3) was developed, with slots cut into the side of the barrel (where the field would be little effected), with essentially no loss of  $Q$  ( $Q_L = 11,500$ ) or transmission characteristics. This cavity was mounted with its axis parallel to the axis of a conventional cavity and normal to the axis of a second conventional cavity. Several samples were procured with the mean wind direction normal to the first conventional cavity, then normal to the second conventional cavity (Figure 4).

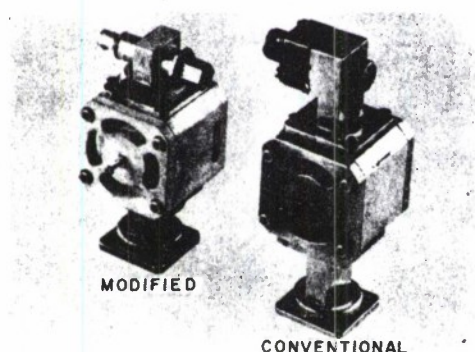


Figure 3. NBS Microwave Sampling Cavities

The spectra of the two conventional cavities exactly reversed when the mean direction of the air flow changed by 90 degrees (Figure 5). The spectra of the cavity of 90 degrees to the wind is higher in both cases, apparently indicating that the variable wind at extremely oblique angles pumps the cavity, inducing an error in the refractive index spectrum at all frequencies. However, the position of the spectra of the "omnidirectional cavity" remains unchanged. Figure 6 shows the comparison between the wind direction and the cavities oriented approximately at 0 and 90 degrees relative to the mean wind. A



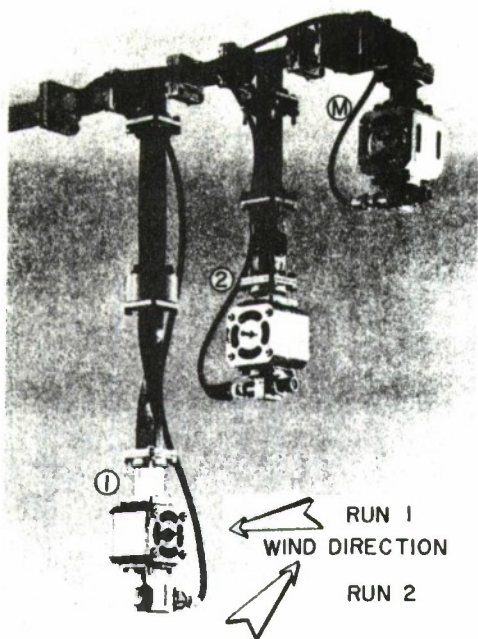


Figure 4. Experimental Comparison of NBS Microwave Cavities

surprising correlation is apparent between the direction of the wind and the response of the 90-degree cavities. There is no apparent correlation between the wind direction and the 0-degree cavities.

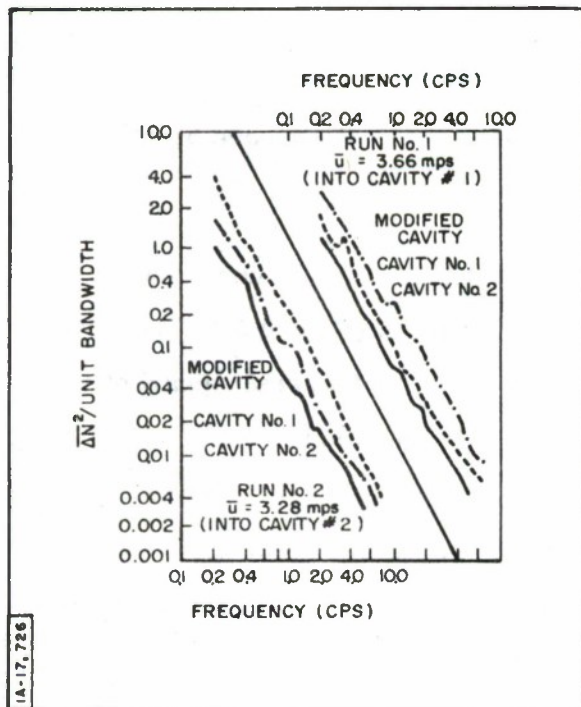


Figure 5. Comparison of Spectra of the NBS Sampling Cavities for Winds Parallel to and Normal to the Axis of the Cavities



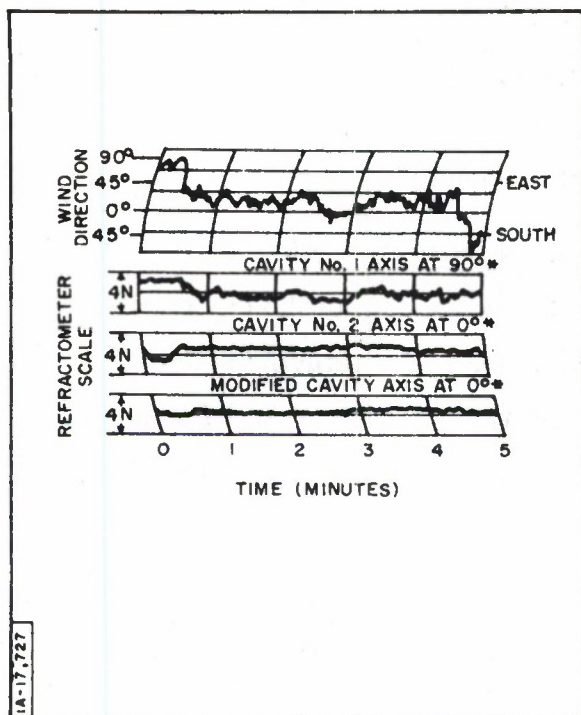


Figure 6. Comparison of Measured Refractive Index and Wind Variations in Run No. 2 of Figure 5. (Relative to Mean Wind Direction of 14.4 degrees)

## CONCLUSIONS

Results of these tests indicate the following characteristics of the NBS sampling cavity as a probe of the atmospheric variations.

1. The cavity is slightly velocity-sensitive. Figure 2 gives an indication of the error in the measured refractivity as a function of wind speed and direction. On ground-based applications, if the wind speed is less than 13.4 meters/second, the error is less than 0.1 N, and may be neglected. For airborne operations, a correction for wind speed may be made using the results shown in Figure 2.
2. When placed into static air flow in excess of 4.47 meters/second, the NBS cavity will resolve with essentially no mutual contamination variations separated by 0.75 meter. Variations separated by 0.3 meter may be in error by as much as 20 percent, and for

separations of less than 0.3 meter, the resolution falls off rapidly.

Preliminary estimates on the "omnidirectional" cavity indicate an improvement of approximately 40 percent.

3. Refractometer cavities are aspect-sensitive, particularly when the mean air flow is at right angles to the axis of the cavity. In the free atmosphere, considerable spectral energy is added because of a "pumping" of the cavity by the variable wind. An "omnidirectional" cavity now developed appears to be relatively insensitive to this limitation.

#### REFERENCES

1. C. M. Crain, "Apparatus for Recording Fluctuations in the Refractive Index of Atmosphere at 3.2 Centimeter Wavelength," Rev. Sci. Instr., 21, 5, (1957) 456-457.
2. G. Birnbaum, "A Recording Microwave Refractometer," Rev. Sci. Instr., 21, 2 (1950), 169-176.
3. B. R. Bean, "The Radio Refractive Index of Air," Proc. IRE, 50, 3 (1962) 260-273.
4. M. J. Velter, private communication, 1962.
5. C. M. Crain and C. E. Williams, "Method of Obtaining Pressure and Temperature Insensitive Microwave Cavity Resonators," Rev. Sci. Instr., 28, 8 (1957) 620-623.
6. M. J. Vetter and M. C. Thompson, Jr., "An Absolute Microwave Refractometer," Rev. Sci. Instr., 33, 6 (1962) 656-660.

## REFERENCES (Cont'd)

7. M. C. Thompson, Jr., F. E. Freethey, and D. M. Waters, "Fabrication X Techniques for Ceramic X-Band Cavity Resonator," Rev. Sci. Instr., 29, 10 (1958) 865-868.
8. W. J. Hartman, "Limit of Spatial Resolution of Refractometer Cavities," J. Res. of NBS, 64D 1 (1960) 65-72.

# OBSERVED VERTICAL WAVE NUMBER SPECTRA OF REFRACTIVITY NEAR THE GROUND

K. A. Norton and E. C. Barrows<sup>\*</sup>

## SUMMARY

By determining the cross correlations between the radio refractivity  $N_i$ , expressed in parts per million and measured as a function of time, with refractometers at heights above the ground  $h_1 = 7.62$ ,  $h_2 = 8.53$ ,  $h_3 = 10.97$ ,  $h_4 = 19.05$ , and  $h_5 = 45.72$  meters (m), it was found that the correlation for a period  $T = 200$  seconds varied with  $\Delta_{ij} = (h_j - h_i)$  approximately in accordance with a normalized correlation function having the form

$$C(\rho, \mu) = \frac{2^{1-\mu}}{\Gamma(\mu)} \left[ \alpha(\mu)\rho \right]^\mu K_\mu \left[ \alpha(\mu)\rho \right] \quad (1)$$

where

$$\begin{aligned} \rho &= \Delta / \Lambda_V(\mu) \quad , \\ \Lambda_V(\mu) &= \int_0^\infty C(\rho, \mu) d\Delta \quad , \\ \alpha(\mu) &= \frac{\Gamma(0.5)\Gamma(\mu + 0.5)}{\Gamma(\mu)} \quad . \end{aligned}$$

In the preceding,  $\Gamma$  denotes the gamma function,  $K_\mu$  denotes the modified Bessel function (Basset's function) of order  $\mu$ ,  $\alpha(\mu)$  is a constant for a given  $\mu$ , and  $\Lambda_V(\mu)$  is the integral scale of the turbulence in the

---

<sup>\*</sup>National Bureau of Standards. Central Radio Propagation Laboratory. Boulder, Colorado.

vertical direction expressed in meters. The correlation function has been normalized so that  $C(0, \mu) = 1$  and the integral

$$\int_0^{\infty} C(\rho, \mu) d\rho = 1.$$

The model agrees best with the data when  $\mu$  lies within the range  $1/4 < \mu < 1/3$ . Note that the use of  $\mu = 1/3$  yields a spectrum which is in agreement in the inertial subrange with the Obukov-Kolmogorov model for locally homogeneous isotropic turbulence.

In this inertial subrange, the wave number spectral density  $W_p(q, \mu)$  of  $N_i$  along a horizontal line parallel to the mean direction of the wind would be expected to have the form

$$\begin{aligned} W_p(q, \mu) &= s_{N_i}^2 (dq/dk) \frac{2}{\pi} \int_0^{\infty} d\rho \cos [q\rho] C(\rho, \mu) \\ &= (dq/dk) s_{N_i}^2 \frac{2}{\pi} \left\{ 1 + [q/\alpha(\mu)]^2 \right\}^{-(\mu + 0.5)}, \end{aligned} \quad (2)$$

where  $s_{N_i}^2$  denotes the sample variance  $\langle (N_i - \bar{N}_i)^2 \rangle$  and the dimensionless variable  $q$  is given by

$$q = \Lambda_p(\mu)k = \Lambda_p(\mu)(2\pi/\lambda) = \Lambda_p(\mu)(2\pi f/U). \quad (3)$$

Here the wave number  $k = 2\pi/\lambda$ , where  $\lambda$  is a scale of the turbulence,  $f$  is the fluctuation frequency in hertz (cycles per second) and  $\Lambda_p(\mu)$  is the integral scale of the turbulence in meters in a direction parallel to that of the mean wind which has a magnitude equal to  $U$  meters per second. If the



subscript  $p$  is replaced by  $v$  in Equation (2) and in the middle members of Equation (3) then these equations give the expected wave number spectral density along a vertical line.

The identification of  $\lambda$  with  $U/f$  in the third expression for  $q$  shown in Equation (3) implies the applicability of Taylor's hypothesis for the inertial subrange and provides a predicted form for the frequency of  $N_i$ . Thus an approximation to the frequency spectral density  $W_p(f, \mu)$  may be obtained from Equation (2) simply by replacing  $(dq/dk)$  by  $(dq/df)$ .

A modification of Equation (1) is used (see independent method for determining  $\mu$  and the integral scales  $\Lambda_v(\mu)$ , later in this report) which makes allowance for the finite ( $T = 200$  seconds) data samples used and this analysis indicates that  $\mu$  varies in successive 200-second samples from 0.17 to 0.42 with a median value of 0.28; the corresponding vertical wave number spectrum varies as  $k^{-\nu}$  in the inertial subrange where  $\nu = 2\mu + 1$  so that  $\nu$  varies from 1.34 to 1.84 with a median value of 1.56. This variation of  $\nu$  in successive 200-second data samples is comparable to that of the corresponding parameter for the horizontal wave number spectrum as inferred from an analysis of the frequency spectra of refractivity so we conclude that the turbulence of refractivity near the ground is approximately isotropic as regards the parameter  $\nu$ .

Note that  $\nu = 5/3$  for the Kolmogorov-Obukov model and this lies well within the range of our observed values. Estimates of  $\nu$  were obtained for three 1/2-hour periods by using the method of least squares and these varied from 1.62 to 1.65 as determined from the three shortest scales  $\Delta = 0.91$ , 2.44 and 3.35 meters.

It is observed that these results are incompatible with the observed carrier frequency dependence of the transmission loss in forward scatter

radio propagation if it is assumed that this same  $\nu$  power will be found at much larger heights above the surface. This suggests, pending the expected confirmation of these radio meteorological observations at much larger heights above the surface, that some mechanism such as reflection from sharp vertical gradients of refractivity rather than anisotropic turbulence is probably responsible for most of the radio frequency energy observed in tropospheric forward scatter propagation at points well beyond the radio horizon.

A brief discussion is also given of the significance of these results for the prediction of the variance of electrical range measurements made by means of radio waves propagated through the troposphere. A re-examination is also made of some earlier work on this subject. Thus Birnbaum and Bussey<sup>[1]</sup> observed the refractivity as a function of time using cavities spaced both vertically and horizontally on a tower in Long Island, New York. Since their measurements were not made on enough cavities simultaneously, it is difficult to draw definitive conclusions. However the analysis made does not indicate any significantly different behavior of these Long Island data.

Thompson, Janes and Kirkpatrick<sup>[2]</sup> as well as Thompson and Janes<sup>[3]</sup> have reported data on the shape  $\nu$  of the wave number spectrum in the horizontal direction determined by invoking Taylor's hypothesis and using the frequency spectra of refractivity observed with single refractometers in Colorado and in Hawaii. These data indicate that the slope of the wave number spectra in the horizontal direction depends on the wind speed and that  $\nu$  is apparently larger at the top of Mt. Haleakala at an altitude of 3050 meters.

## INTRODUCTION

The correlation  $C(\vec{r})$  between the fluctuations with time of the refractive index measured at two points in the troposphere is known to depend upon the vector separation  $\vec{r}$  between the two points; i. e. , the direction of the second

point relative to the first point and the magnitude  $r$  of their separation. This three-dimensional correlation function provides a description of tropospheric turbulence which is useful for predicting many important aspects of radio wave propagation at the higher radio frequencies, e. g. , 30 megahertz and above. In particular, Booker and Gordon,<sup>[4]</sup> Villars and Weisskopf,<sup>[5]</sup> Norton,<sup>[6,7]</sup> and Wheelon<sup>[8]</sup> have discussed the relevance of this correlation function to the forward scattering of radio waves and Muchmore and Wheelon,<sup>[9]</sup> Norton,<sup>[10]</sup> and Barrows<sup>[11]</sup> have discussed its relevance to the problem of predicting the expected variance of the measured electrical range between two points in the troposphere.

Let  $n_i(t)$  denote the refractive index at a point  $\vec{r}_i$  as a function of the time  $t$ ; then its refractivity  $N_i(t) \equiv [n_i(t) - 1] \cdot 10^6$  is conveniently expressed in parts per million. The normalized correlation function for two points  $\vec{r}_i$  and  $\vec{r}_j$  separated by the vector distance  $\vec{r}_{ij} \equiv \vec{r}_j - \vec{r}_i$  may be expressed:

$$C(\vec{r}_{ij}, T, t) = \frac{\langle [N_i(t) - \bar{N}_i] [N_j(t) - \bar{N}_j] \rangle_T}{\left\{ \langle [N_i(t) - \bar{N}_i]^2 \rangle_T \langle [N_j(t) - \bar{N}_j]^2 \rangle_T \right\}^{\frac{1}{2}}}, \quad (4)$$

where  $\bar{N}_i$  denotes the mean value of  $N_i(t)$  over the time interval of length  $T$  from  $t - (T/2)$  to  $t + (T/2)$ , and the symbol  $\langle \rangle$  indicates that an average value of the enclosed quantity is taken for this interval of time. Note that the correlation function  $C(\vec{r}_{ij})$  will, in general, depend upon the time  $t$ , the time interval  $T$ , and the locations  $\vec{r}_i$  and  $\vec{r}_j$  of the two cavities.

If the parameters describing the correlation function for a fixed time interval  $T$  depend upon the direction of  $\vec{r}_{ij}$ , the turbulence is anisotropic, and if these parameters depend upon either the location  $\vec{r}_i$  of the reference

point or the time  $t$ , the turbulence is said to be inhomogeneous. The refractive index turbulence of the troposphere is known to be both anisotropic and inhomogeneous.

In the studies reported, the direction of  $\vec{r}_{ij}$  is vertical and its magnitude in meters is designated  $\Delta_{ij} = h_j - h_i$ .

### Experimental Procedure

The refractivity  $N_i(t)$  was measured with the National Bureau of Standards relative refractometer (Thompson and Vetter<sup>[12]</sup>) at five heights above the local terrain as listed in the summary and illustrated in Figure 1. The refractometer cavities at these five heights were referenced to a common cavity (Birnbaum<sup>[13]</sup>). The data sample analyzed was chosen at a period of time during which the wind was blowing approximately into the sampling cavities so as to avoid the spurious fluctuations arising from the sensitivity to wind direction of the conventional cavities which were used (Gilmer, McGavin and Bean,<sup>[14]</sup>).

A 3-hour data sample (0900-1200 August 13, 1963) was selected for analysis. From this sample six 30-minute samples were chosen for comparison. These six samples represent somewhat different turbulent atmospheric motions, the first sample corresponding to the least turbulent conditions.

Figure 2 shows a 10.5-minute sample of the five refractometer responses which are representative of the basic data on which the conclusions in this report are based.

Using the National Bureau of Standards Correlation Analyzer, ten different cross correlations were obtained in an analog fashion between the refractivity observations at the various levels. Figure 3 shows three samples



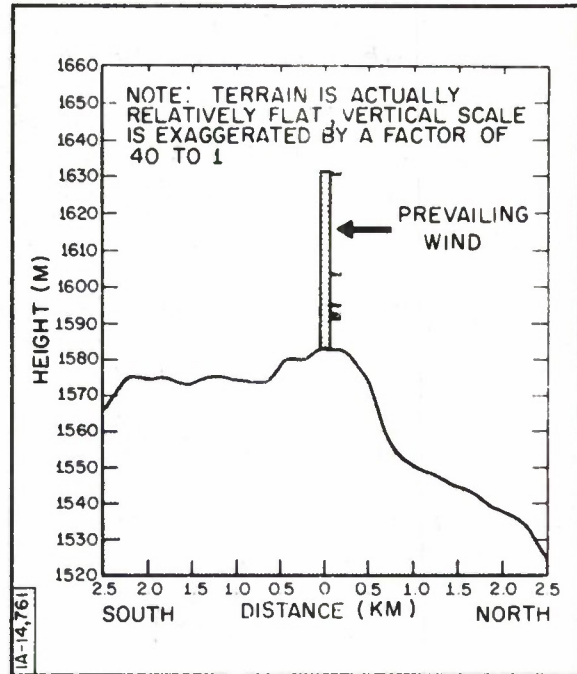


Figure 1. Refractivity at Various Heights

of the output of this correlation analyzer with  $\Delta_{ij} = 3.35$  meters for the period 0900 to 1000, using averaging times  $T = 10, 50$  and  $200$  seconds. Note that the mean value of the correlation was about the same for the  $50$ - and  $200$ -second averaging times, which suggests that the data are very slowly varying for sampling intervals  $T$  in excess of  $100$  seconds. For convenience, all of the subsequent analysis was done using  $T = 200$  seconds. By choosing  $T$  as small as  $200$  seconds, the effects of any long-term relative drifts in the absolute calibrations of the several refractometer cavities were essentially eliminated. Note in this connection that  $C(\vec{r}_{ij})$  is independent of the absolute values of  $N_i(t)$ . For each minute, values of  $C(\Delta_{ij})$  were determined from records like those shown in Figure 3 for the ten different values of  $\Delta_{ij}$ . Since it is known that the are hyperbolie tangent of a sample correlation function tends to be a normally distributed random variable, <sup>[15, 16]</sup> each of these one minute values was converted to  $z(\Delta_{ij})$  by means of the following transformation:



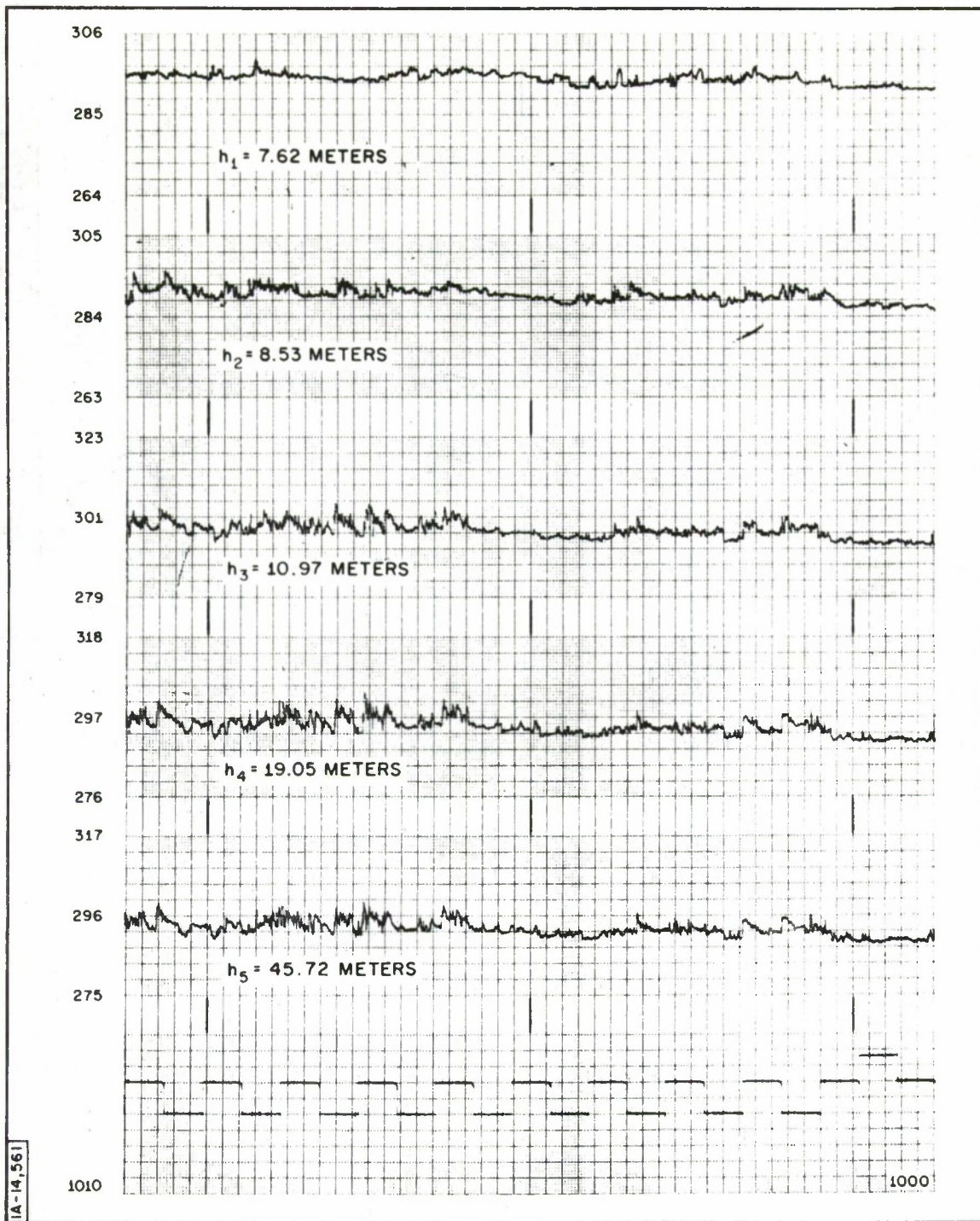


Figure 2. Refractometer Response

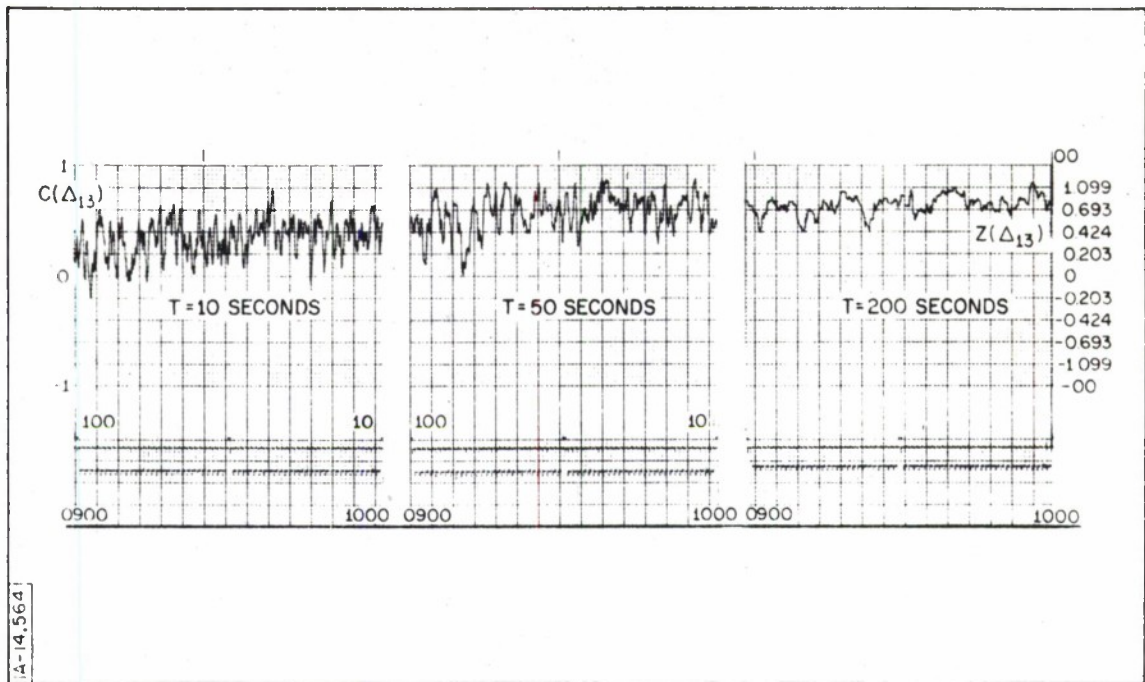


Figure 3. Correlation Analyzer Output

$$z(\Delta_{ij}) = \tanh^{-1} C(\Delta_{ij}) . \quad (5)$$

Convenient tables for determining a value of  $z$  corresponding to an observed  $C$  have been published by the Staff of the Harvard University Computation Laboratory.<sup>[17]</sup> These 1-minute values of  $z(\Delta_{ij})$  have been analyzed in several different ways, as discussed in the following sections of this paper.

#### DETERMINATION OF $\mu$ AND INTEGRAL SCALES $\Lambda_V(\mu)$

The points on Figure 4 show the variations from the minute to minute of the analog cross correlations  $C(\Delta_{1j})$  for the period of time 1000 to 1029; the dashed lines are digital correlations and will be discussed in the following pages, using the Bessel correlation model defined by Equation (1) in the summary. A discussion of this model, together with tables and series expansions is available in a paper by Norton;<sup>[7]</sup> Figure 5 shows  $C(\rho, \mu)$  and  $z(\rho, \mu)$  as

of  $\Lambda_{vk}(\mu)$  and the means  $\bar{\delta}$  of  $\delta_k(\Delta_{ij}, \mu)$  for  $\mu = 1/4, 1/3, 1/2$ , and 1 for the three 29-minute periods 0900-0928; 1000-1028; and 1100-1128. If we define the inertial subrange as those values of  $\Delta_{ij} < \Lambda_v$ , i.e.,  $\rho < 1$ , then it appears from Table I that  $\Delta_{12}$  and  $\Delta_{13}$  are in the inertial subrange only for  $\mu = 1/4$ .

Figures 6, 7, and 8 show these mean deviations  $\bar{\delta}$  plotted as a function of  $\Delta_{ij}$ . It is evident from these figures that the data appear to fit the Bessel correlation model best when  $1/4 < \mu < 1/3$ . In order to establish whether the observed mean deviations  $\bar{\delta}$  represent statistically significant departures from zero, the following analysis was made for each value of  $\Delta_{ij}$  of the variance of  $z_k$  about its running mean values  $z_{mk}$  over a 29-minute sample:

$$z_{mk} = \frac{1}{29} \sum_{j=k-14}^{j=k+14} z_j \quad (k = 15 \text{ to } n-14) \quad (5)$$

Note that only  $n-28$  values of  $z_{mk}$  are available from a sample of  $n$ . Now define the covariance function

$$\gamma(k) \equiv \frac{1}{n-28-k} \sum_{i=15}^{n-14-k} (z_i - z_{mi})(z_{i+k} - z_{mi+k}), \quad (6)$$

and autocorrelation function

$$\rho_k \equiv \gamma(k)/\gamma(0). \quad (7)$$

Three different values of  $\gamma(k)$  and  $\rho(k)$  were determined: (a) using the first half of the sample of  $n-48$ , (b) using the second half of this sample, and (c) using all of this sample; a representative sample of these values is given in Table II.

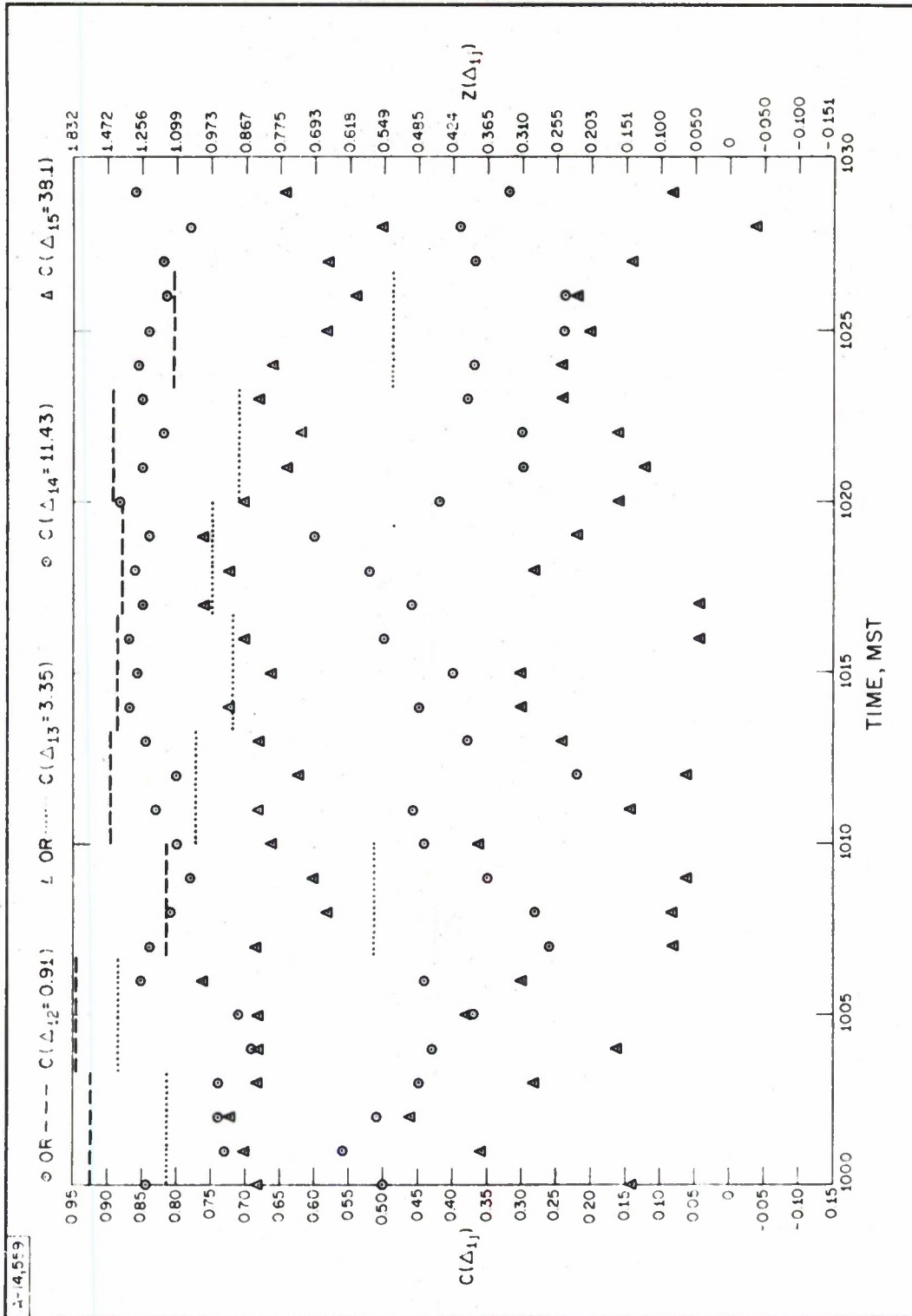


Figure 4. Time Variations of Cross-Correlations



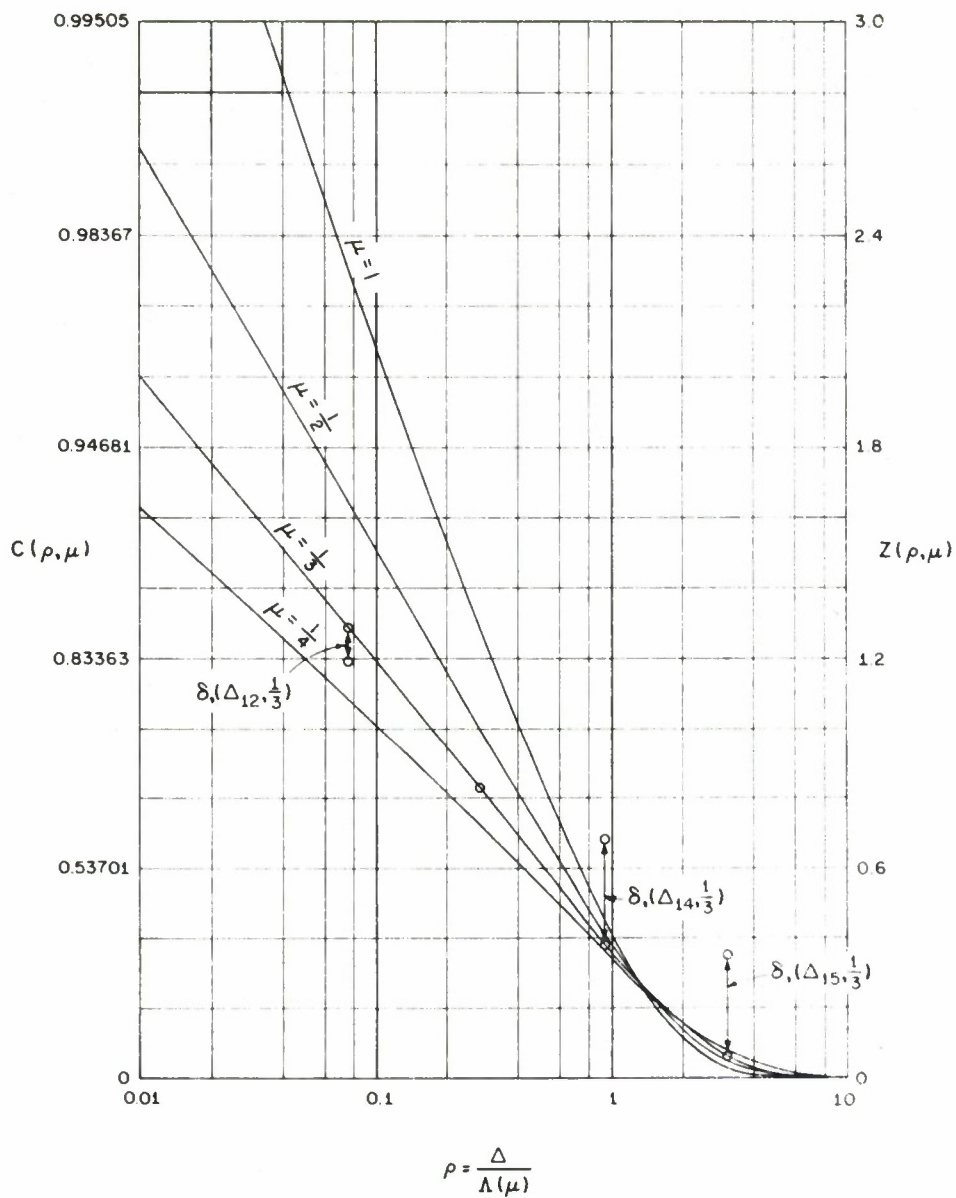


Figure 5. Relationship of  $C(\rho, \mu)$  and  $Z(\rho, \mu)$  with  $\rho = \Delta/\Lambda(\mu)$



a function of  $\rho = \Delta/\Lambda(\mu)$ , using linear  $z$  and logarithmic  $\rho$  scales, for  $\mu = 1/4, 1/3, 1/2$ , and  $1$ . Note that  $C(\rho, 1/2) = \exp[-\rho]$ , the correlation model used by Booker and Gordon;<sup>[4]</sup> and  $C(\rho, 1) = (\pi\rho/2)K_1(\pi\rho/2)$ , the correlation model which yields in the inertial subrange the turbulent mixing spectrum proposed by Villars and Weisskopf<sup>[5]</sup> and later discussed in more detail by Wheelon.<sup>[18]</sup>

The following procedure was used to determine how well the observed data fit the correlation functions shown in Figure 5. Let  $z_k(\Delta_{13})$  denote the value of  $z(\Delta_{13})$  corresponding to the  $k^{\text{th}}$  minute in the observed sample  $k = 1$  to  $n = 176$  between 0900 and 1200, with the four values missing at 1056, 1057, 1058, and 1059. Each of these  $n$  values was used to determine  $\rho_k(\Delta_{13}) = 3.35/\Lambda_{vk}(\mu)$  and thus  $\Lambda_{vk}(\mu)$  for each of the four values of  $\mu$ . For example,  $z_1(3.35) = 0.83$ , and with  $\mu = 1/3$  it follows that  $\rho_1(\Delta_{13}) = 0.275$  and  $\Lambda_{v1}(1/3) = 12.18$  meters. For this same minute and using this same value of  $\Lambda_{v1}(1/3)$ , values of  $z(\rho, 1/3)$  were determined from Figure 5 for  $\Delta_{12}$ ,  $\Delta_{14}$ , and  $\Delta_{15}$  and compared with the observed values  $z_1(\Delta_{12}) = 1.19$ ,  $z_1(\Delta_{14}) = 0.68$  and  $z_1(\Delta_{15}) = 0.35$ . For the same minute and  $\mu = 1/3$ :  $\rho_1(\Delta_{12}) = 0.0747$ ,  $z_1(\Delta_{12}, 1/3) = 1.29$ ;  $\rho_1(\Delta_{14}) = 0.938$ ,  $z_1(\Delta_{14}, 1/3) = 0.38$ ;  $\rho_1(\Delta_{15}) = 3.128$ ,  $z_1(\Delta_{15}, 1/3) = 0.06$ . Finally, the deviations

$$\delta_k(\Delta_{ij}, \mu) \equiv z_k(\Delta_{ij}) - z_k(\Delta_{ij}, \mu) \quad (5)$$

were determined: for example, with  $\mu = 1/3$ , we find  $\delta_1(\Delta_{12}, 1/3) = -0.10$ ;  $\delta_1(\Delta_{13}, 1/3) \equiv 0$ ;  $\delta_1(\Delta_{14}, 1/3) = 0.30$ ; and  $\delta_1(\Delta_{15}, 1/3) = 0.29$ . The points on Figure 5 correspond to the data observed for  $k = 1$  at 0900 and illustrate the method used for determining  $\Lambda_{v1}(1/3)$  and  $\delta_1(\Delta_{ij}, 1/3)$  for  $\mu = 1/3$  and  $\Delta_{12} = 0.91$  meters,  $\Delta_{13} = 3.35$  meters,  $\Delta_{14} = 11.43$  meters and  $\Delta_{15} = 38.1$  meters. Table 1 gives the means and sample standard deviations

Table I

(Values of  $P(\Delta_{ij}) < 10^{-5}$  are set equal to 0)

$\mu$	Time	0900-0928	1000-1028	1100-1128
$\frac{1}{4}$	$\Lambda_v$ (meters)	13.32	17.09	27.99
$\frac{1}{4}$	$s\Lambda_v$ (meters)	5.66	6.56	15.39
$\frac{1}{4}$	$\bar{\delta}(\Delta_{12})$	0.090138	- 0.010759	0.013815
	n''	29.27	29.27	29.27
$\frac{1}{4}$	$s_{\bar{\delta}}(\Delta_{12})$	0.020407	0.030234	0.019032
$\frac{1}{4}$	$P(\Delta_{12})$	0.000011	0.72	0.47
$\frac{1}{4}$	$\bar{\delta}(\Delta_{14})$	- 0.037138	- 0.003414	- 0.024593
	n''	29.425	29.425	29.425
$\frac{1}{4}$	$s_{\bar{\delta}}(\Delta_{14})$	0.029783	0.016919	0.027960
$\frac{1}{4}$	$P(\Delta_{14})$	0.21	0.84	0.38
$\frac{1}{4}$	$\bar{\delta}(\Delta_{15})$	- 0.000931	0.071000	- 0.002037
	n''	29.29	29.29	29.29
$\frac{1}{4}$	$s_{\bar{\delta}}(\Delta_{15})$	0.031179	0.021992	0.037708
$\frac{1}{4}$	$P(\Delta_{15})$	0.98	0.0013	0.96
$\frac{1}{3}$	$\bar{\Lambda}_v$ (meters)	9.33	10.89	16.83
$\frac{1}{3}$	$s\Lambda_v$ (meters)	3.29	3.45	7.13
$\frac{1}{3}$	$\bar{\delta}(\Delta_{12})$	- 0.010034	- 0.113276	- 0.088741
$\frac{1}{3}$	$s_{\bar{\delta}}(\Delta_{12})$	0.021080	0.030122	0.019605

Table I (cont.)

$\mu$	Time	0900-0928	1000-1028	1100-1128
$\frac{1}{3}$	$P(\Delta_{12})$	0.63	0.00017	0
$\frac{1}{3}$	$\bar{\delta}(\Delta_{14})$	0.042276	0.079517	0.065704
$\frac{1}{3}$	$s_{\bar{\delta}}(\Delta_{14})$	0.028900	0.016052	0.027527
$\frac{1}{3}$	$P(\Delta_{14})$	0.1415	0	0.017
$\frac{1}{3}$	$\bar{\delta}(\Delta_{15})$	0.055241	0.145310	0.111889
$\frac{1}{3}$	$s_{\bar{\delta}}(\Delta_{15})$	0.030540	0.022304	0.033008
$\frac{1}{3}$	$P(\Delta_{15})$	0.071	0	0.0007
$\frac{1}{2}$	$\bar{\Lambda}_v$ (meters)	7.20	8.36	10.91
$\frac{1}{2}$	$s\bar{\Lambda}_v$ (meters)	1.81	1.89	3.37
$\frac{1}{2}$	$\bar{\delta}(\Delta_{12})$	- 0.174103	- 0.292138	- 0.278926
$\frac{1}{2}$	$s_{\bar{\delta}}(\Delta_{12})$	0.023635	0.030950	0.020243
$\frac{1}{2}$	$P(\Delta_{12})$	0	0	0
$\frac{1}{2}$	$\bar{\delta}(\Delta_{14})$	0.127069	0.182172	0.191852
$\frac{1}{2}$	$s_{\bar{\delta}}(\Delta_{14})$	0.028501	0.015770	0.025810
$\frac{1}{2}$	$P(\Delta_{14})$	0	0	0

Table I (concl'd)

$\mu$	Time	0900-0928	1000-1028	1100-1128
$\frac{1}{2}$	$\bar{\delta}(\Delta_{15})$	0.050414	0.189517	0.196370
$\frac{1}{2}$	$s_{\bar{\delta}}(\Delta_{15})$	0.032475	0.023276	0.027547
$\frac{1}{2}$	$P(\Delta_{15})$	0.12	0	0
1	$\bar{\Lambda}_v$ (meters)	5.62	6.28	7.53
1	$s\Lambda_v$ (meters)	1.06	1.04	1.63
1	$\bar{\delta}(\Delta_{12})$	- 0.526241	- 0.609862	- 0.639111
1	$s_{\bar{\delta}}(\Delta_{12})$	0.026535	0.038710	0.021873
1	$P(\Delta_{12})$	0	0	0
1	$\bar{\delta}(\Delta_{14})$	0.231345	0.293138	0.345963
1	$s_{\bar{\delta}}(\Delta_{14})$	0.025937	0.016995	0.025862
1	$P(\Delta_{14})$	0	0	0
1	$\bar{\delta}(\Delta_{15})$	0.090586	0.202103	0.230889
1	$s_{\bar{\delta}}(\Delta_{15})$	0.030317	0.023476	0.025483
1	$P(\Delta_{15})$	0.0028	0	0

1A-14,763

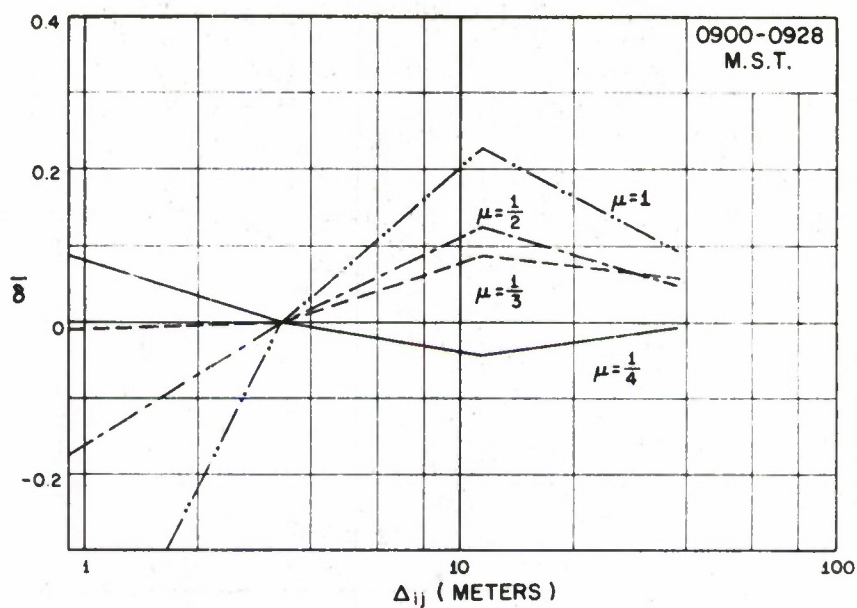


Figure 6. Mean Deviations of  $\bar{\delta}$  at 0900

1A-14,750

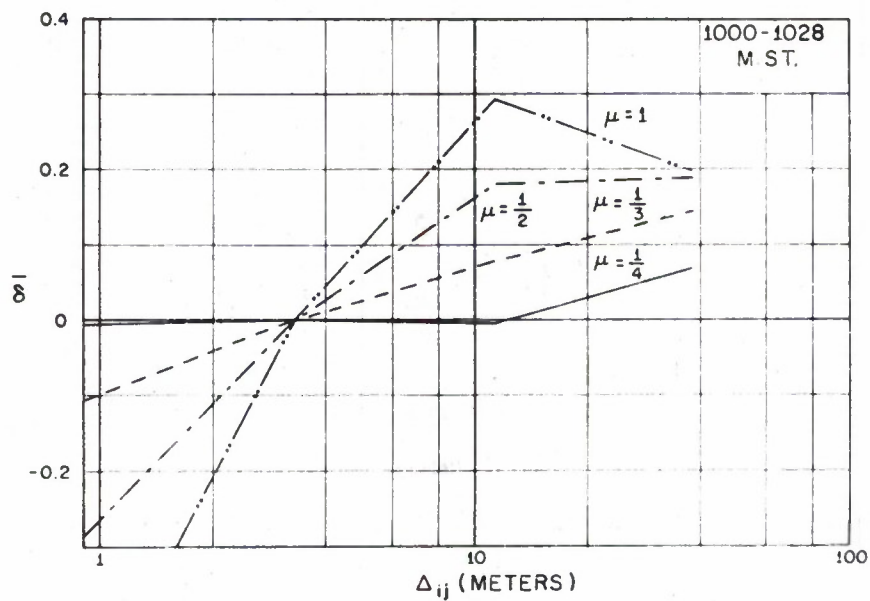


Figure 7. Mean Deviations of  $\bar{\delta}$  at 1000



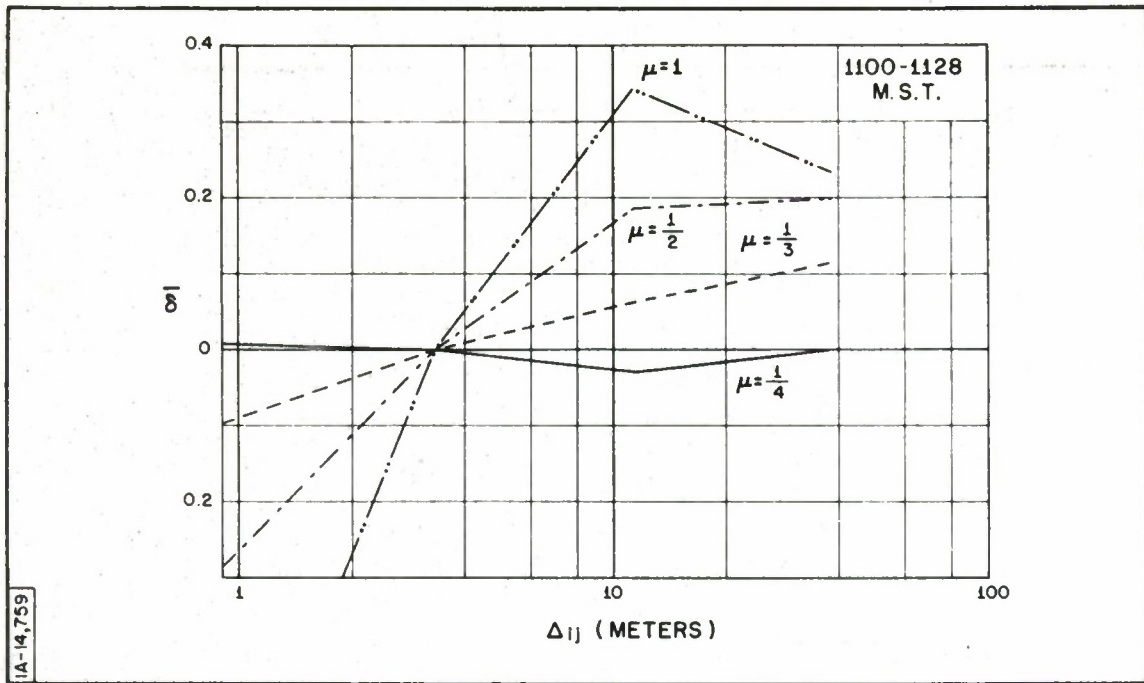


Figure 8. Mean Deviation of  $\bar{\delta}$  at 1100

Following Siddiqui, [19] the sample variance of the mean  $s_{zm}^2$  may be estimated by:

$$s_{zm}^2 = s_z^2/n' = \gamma(0)/n', \quad (8)$$

where

$$\frac{1}{n'} \cong \frac{1}{29} \left\{ 1 + 2 \sum_{k=1}^{28} \left( 1 - \frac{k}{29} \right) \rho_k \right\}. \quad (9)$$

Table III gives  $n'$  for the ten different values of  $\Delta_{ij}$  used in our present analysis and based on the three sets of values of  $\rho(k)$  described above. It appears from these values that the statistic  $n'$  is relatively stationary during this interval of time.

Table II  
Autocorrelation,  $\rho_k$

k	0900-1030	1030-1200	0900-1200
1	0.564787	0.527370	0.543792
2	0.283739	0.170381	0.220132
3	0.014406	-0.118390	-0.060108
4	-0.048807	-0.174545	-0.119361
5	-0.163448	-0.135988	-0.148040
6	-0.105636	-0.107324	-0.106583
7	-0.191730	-0.035557	-0.104099
8	-0.189924	-0.095245	-0.136798
9	-0.097046	-0.108347	-0.103387
10	0.012165	-0.164755	-0.087107
11	-0.116273	-0.181828	-0.153057
12	-0.179293	-0.180521	-0.179982
13	-0.181209	-0.059544	-0.112941
14	-0.097219	0.012205	-0.035820
15	-0.031343	-0.000589	-0.014086
16	0.016166	0.101716	0.064169
17	-0.021814	0.071043	0.030289
18	-0.139698	-0.003359	-0.063196
19	-0.180114	-0.054545	-0.109655
20	-0.057097	-0.015208	-0.033592
21	-0.104788	0.124368	0.023794
22	-0.072307	0.068901	0.006927
23	0.015841	0.164749	0.099396
24	0.107258	-0.001429	0.046272
25	0.018932	-0.062685	-0.026865
26	0.032777	-0.041643	-0.008981
27	0.001883	-0.069908	-0.038400
28	0.005297	-0.119027	-0.064463

Table III

n' for Ten Values of  $\Delta_{ij}$ 

i	$h_i$ Meters	j	$h_j$ Meters	$\Delta_{ij}$ Meters	(a) 0900-1030	(b) 1030-1200	(c) 0900-1200
1	7.62	2	8.53	0.91	28.99	29.24	29.13
1	7.62	3	10.97	3.35	29.52	29.34	29.41
1	7.62	4	19.05	11.43	29.57	29.28	29.44
1	7.62	5	45.72	38.10	29.48	28.72	29.17
2	8.53	3	10.97	2.44	29.32	29.13	29.21
2	8.53	4	19.05	10.52	29.70	29.66	29.68
2	8.53	5	45.72	37.19	29.87	29.15	29.45
3	10.97	4	19.05	8.08	29.44	29.57	29.49
3	10.97	5	45.72	34.75	29.49	28.89	29.21
4	19.05	5	45.72	26.67	28.88	29.23	29.07

The estimates  $s_{\bar{\delta}}(\Delta_{ij})$  of the standard errors of  $\bar{\delta}(\Delta_{ij})$  given in Table 1 were determined by using  $n''_{ij} = (n'_i + n'_j)/2$  in the formula:

$$s_{\bar{\delta}}^2(\Delta_{ij}) = s_{\bar{\delta}}^2(\Delta_{ij})/n''_{ij} . \quad (10)$$

If we now assume that  $\bar{\delta}$  is a normally distributed random variable and that  $s_{\bar{\delta}}$  is a good estimate of its standard deviation, then we can determine the probabilities  $P(\Delta_{ij})$  that  $\bar{\delta}(\Delta_{ij})$  are sampling errors. These probabilities are given in Table 1 and several conclusions may be drawn from these data:

- (a) Since these probabilities for all three values of  $\Delta_{ij}$  are near zero for  $\mu = 1/2$  and  $\mu = 1$ , we conclude that our data are

inconsistent with the one-dimensional wave number spectrum in the vertical direction as determined from either of these Bessel correlation models.

- (b) Our data are consistent with the Bessel correlation model only for values of  $\mu$  lying within the range  $1/4 < \mu < 1/3$ .

It is of interest to refer to a somewhat similar analysis by Birnbaum and Bussey<sup>[1]</sup> of refractivity data taken on a 128-meter tower in New York in August. They obtained values for the correlation function for vertical separations first of 114 meters and then of 17 meters, taken at different times and for sample lengths ranging from 16 to 53 minutes. Converting their sample correlations to  $z \equiv \tanh^{-1} C$  and averaging, one finds  $\bar{z}_1 = 0.22$  for the 114 meter separation and  $\bar{z}_2 = 0.75$  for the 17 meter separation. Referring to Figure 5 it is evident that the Bessel model  $z(\rho, \mu)$  is very nearly independent of  $\mu$  for  $\bar{z}_1 = 0.22$  and  $\rho_1 = 1.6$  and thus we find  $\Lambda_v = 71$  meters. Assuming that this same integral scale characterized the data at the 17 meter separation, even though they were taken at a different time, it follows that  $\rho_2 = 0.24$  and thus, since  $\bar{z}_2 = 0.75$ ,  $\mu \cong 1/4$ . Although this estimate of  $\mu$  obtained from an analysis of Birnbaum and Bussey's earlier data is consistent with the values determined above, the integral scale is very much larger. This may be due to the longer data samples involved or to the higher tower used.

In the next section a different method will be used for determining both  $\mu$  and  $\Lambda_v(\mu)$  which makes appropriate allowance for the effects of the finite sampling time  $T$ .

It may be useful to comment further on the method that was used to determine the equivalent random sample size  $n'$  for estimating the standard deviation of the mean value of a random variable known only as a function of the time. In some cases the analyst may not have had a sample of data having a size



$n > m$ , the number of values used in determining the mean. In such cases it is tempting to hypothesize the model  $\gamma_k = \gamma_0 \rho^{|k|}$  and to estimate  $\rho$  and  $m'$  by:

$$\rho = \gamma(1)/\gamma(0) \quad (11)$$

$$m' = m(1 - \rho^2)/(1 + \rho^2) . \quad (12)$$

From column (c) in Table II we find  $\rho = 0.543792$  so that, as determined by Equation (12),  $m' = 15.76$ . This value is very much smaller than the more accurate estimate of 29.13 determined by Equation (9); when estimating  $m'$ , therefore, it is important to determine  $\rho_k$  for all of the lags up to  $(m - 1)$ , whenever feasible. In the example given,  $m'$  is nearly equal to  $m$ , a value that would be appropriate for determining the mean of  $m$  independent of and thus uncorrelated to values of  $z$ ; however, it would be erroneous to infer from this that our samples of  $m$  are uncorrelated.

#### INDEPENDENT METHOD FOR DETERMINING $\mu$ AND THE INTEGRAL SCALES $\Lambda_v(\mu)$

In this section an independent analysis will be made of the same basic data used in the preceding section. Since frequency spectra are to be determined for another part of the analysis, the  $N_i(t)$  data were digitized using a sampling interval,  $\tau$ , of 1/30 second and cross correlations  $C(\Delta_{ij})$  were determined digitally from these data with  $T = 200$  seconds. Some samples of these digital cross correlations are shown by the dashed and dotted horizontal lines on Figure 4 where they can be compared with the corresponding analog cross correlations indicated by the circles and triangles. Although  $T = 200$  seconds in both cases, the analog data on Figure 4 appear to lie a little



below the digitized cross correlations. This is very probably caused by the fact that a high-pass filter was used with the analog correlation analyzer in order to eliminate the effects of low frequency trends with periods of the order of  $T/2$  seconds and longer.

The effect on the frequency spectrum of using a finite time interval  $T$  is to introduce the filter  $\left\{1 - \sin[\pi f T] / \pi f T\right\}^2$  as a factor in the expression for the spectrum with a corresponding effect on the correlation for the larger values of  $\rho$ . We have already seen in Figure 3 that  $C(\Delta_{13})$  increases with  $T$ . This suggests that it is desirable to determine a correlation function which corresponds to the vertical wave number spectrum:

$$W_v(q, \nu) = s_{N_i}^2 A(\nu) q^{-\nu} \left(1 - \frac{\sin q}{q}\right)^2, \quad (13)$$

where

$$A(\nu) = \frac{\Gamma(\nu + 2) \cos\left(\frac{2 - \nu}{2} \pi\right)}{\pi (\nu + 1 - 2^{\nu - 1})} \quad (1 \leq \nu < 3)$$

$$q = ka = a 2\pi f / U = \pi T f$$

$$a = TU/2 = 100 \text{ U meters}$$

$$\nu = 2\mu + 1.$$

The correlation function  $C(\rho', \nu)$  is related to the wave number spectrum by:

$$W_v(q, \nu) = s_{N_i}^2 a \frac{2}{\pi} \int_0^\infty d\rho' \cos(q\rho') C(\rho', \nu). \quad (14)$$

It can be shown that Equation (13) is the solution of Equation (14) for the normalized correlation function

$$C(\rho', \nu) = \frac{\nu(\nu+1)}{2\nu+2-2^\nu} \left\{ -\rho'^{\nu-1} + \frac{(\rho'+1)^\nu + (1-\rho')|1-\rho'|^{\nu-1}}{\nu} + \frac{2\rho'^{\nu+1} - (\rho'+2)^{\nu+1} - |\rho'-2|^{\nu+1}}{4\nu(\nu+1)} \right\}, \quad (15)$$

where

$$\rho' = \Delta/a = 2\Delta/TU = b(\nu)\rho$$

$$b(\nu) = \Lambda_v(\nu)/a$$

$$b(\nu) = \Lambda_v(\nu)/a \quad .$$

The arc hyperbolic tangent  $z(\rho', \nu)$  of this correlation function is shown by the solid curves on Figure 9. The dashed curves on Figure 9 are the  $z$  transform of the Bessel correlation function defined by Equation (1) in the summary after

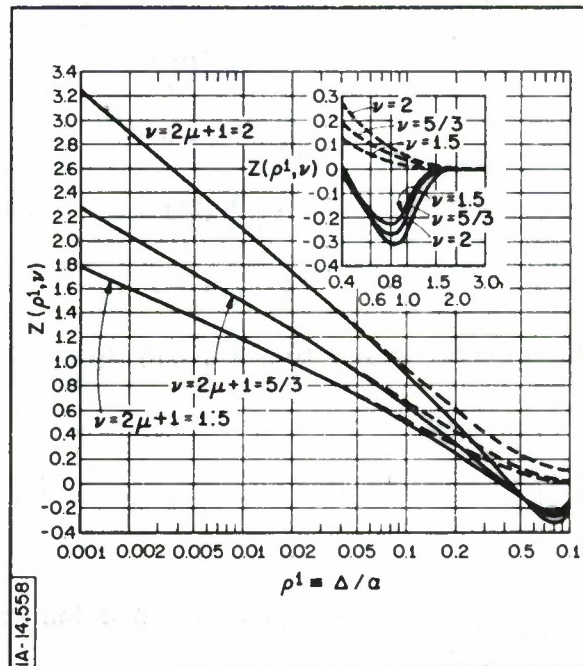


Figure 9. Z-Transform of Bessel Function

multiplying by the normalizing factor  $b(\nu)$ . For  $\mu = 1/2$ ,  $\nu = 2$ , and  $b(2) = 1/3$ ; for  $\mu = 1/3$ ,  $\nu = 5/3$  and  $b(5/3) = 0.236009$ ; for  $\mu = 1/4$ ,  $\nu = 3/2$  and  $b(3/2) = 0.183594$ . It is evident from Figure 9 that the finite sampling time  $T$  has a large effect on the form of the correlation function for  $\rho' > 0.05$  and  $z(\rho', \nu)$  actually becomes negative for  $\rho' > 0.4$ .

If we set  $q = 0$  in Equation (14) then the resulting integral is, in accordance with the definition

$$\Lambda_v(\mu) = \int_0^{\infty} C(\rho, \mu) d\Delta,$$

in the summary, just  $1/a$  times the integral scale  $\Lambda_v(\mu)$ . Since,  $W_v(0, \nu) = 0$  as determined by Equation (13) it follows that a non-zero integral scale can not be determined from a finite sample of data unless one restricts himself to the smaller values of  $\rho$  not affected by the sample size and postulates some arbitrary, non-negative form for the larger  $\rho$  values. The natural scale to use for describing the effect of the sample size is  $a = TU/2$ . This is related to the integral scale which would be obtained if a Bessel correlation model were fitted to the data for smaller  $\rho$  values by the relation  $b(\nu) = \Lambda_v(\nu)/a$ , where  $b(\nu)$  depends only on  $\nu$ .

Table IV gives  $a = 100 U$ ,  $s_{N_i}^2$  and  $z(\Delta_{ij})$  for those 200-second samples for which reliable data were available. Unfortunately, after the data were analyzed by the method given in the preceding section, the  $N_2(t)$  data for the period 0900 to 0930 were inadvertently erased from the magnetic tape on which they were recorded.

Since  $z_j(\Delta_{ij})$  is a normally distributed random variable and since  $\rho'_{ij} = \Delta_{ij}/a$  may be considered to be known for each 200-second data sample, it was possible to use the method of least squares to fit the observed  $(z_j, \Delta_{ij})$

TABLE IV

Calculated Values as  $\nu$  and  $\Lambda_\nu(\nu)$ 

Time	j	a = 100 U	$s_{N1}^2$	$s_{N2}^2$	$s_{N3}^2$	$z(\Delta_{12})$	$z(\Delta_{23})$	$z(\Delta_{13})$	$\nu$	$\Lambda_\nu(\nu)$
0900 -0903 $\frac{1}{2}$	1	67.0561	1.325291		1.43958			0.707273	1.492352	12.17
0903 $\frac{1}{2}$ -0906 $\frac{1}{2}$	2	82.7026	2.644550		3.33341			1.02982	1.697822	20.26
0906 $\frac{1}{2}$ -0910	3	106.3958	1.664908		1.41381			0.842283	1.490836	19.26
0910 -0913 $\frac{1}{2}$	4	57.2212	3.418075		1.94626			0.682208	1.513075	10.76
0913 $\frac{1}{2}$ -0916 $\frac{1}{2}$	5	113.9954	4.00701		3.05522			0.922298	1.532221	22.06
0916 $\frac{1}{2}$ -0920	6	123.3833	2.974557		2.70710			0.988227	1.560647	24.96
0920 -0923 $\frac{1}{2}$	7	96.1138	4.426780		3.34970			0.881384	1.540958	18.84
0923 $\frac{1}{2}$ -0926 $\frac{1}{2}$	8	78.2322	6.974701		6.60376			1.23809	1.897253	23.77
1000 -1003 $\frac{1}{2}$	9	116.2307	2.954985	2.96453	2.84792	1.62046 (1.654687)	1.34768 (1.289714)	1.13696 (1.169175)	1.703865	28.59
1003 $\frac{1}{2}$ -1006 $\frac{1}{2}$	10	116.2307	3.301291	3.63713	3.61448	1.78788 (1.894694)	1.51306 (1.473425)	1.39198 (1.335295)	1.827944	32.92
1006 $\frac{1}{2}$ -1010	11	122.9363	3.561383	3.73418	3.25935	1.13918 (1.051499)	0.806186 (0.8232880)	0.568362 (0.7465834)	1.401036	19.04
1010 -1013 $\frac{1}{2}$	12	129.6419	3.507187	4.39721	4.20422	1.45609 (1.533834)	1.31168 (1.206056)	1.02186 (1.097499)	1.624540	28.85
1013 $\frac{1}{2}$ -1016 $\frac{1}{2}$	13	118.4659	2.228400	2.60675	2.39932	1.40629 (1.378069)	1.09552 (1.077222)	0.901618 (0.9770117)	1.561859	24.02
1016 $\frac{1}{2}$ -1020	14	121.5951	2.847284	2.79552	2.33407	1.36959 (1.418376)	1.18334 (1.110744)	0.970350 (1.008431)	1.577816	25.27
1020 -1023 $\frac{1}{2}$	15	125.1715	3.428030	3.81943	2.86133	1.42484 (1.372946)	1.06967 (1.077562)	0.887569 (0.9792163)	1.551391	24.97
1023 $\frac{1}{2}$ -1026 $\frac{1}{2}$	16	160.9348	1.853697	1.72294	1.19120	1.11205 (0.9872803)	0.691178 (0.7868775)	0.530958 (0.7196714)	1.347251	22.55
1100 -1103 $\frac{1}{2}$	17	122.9363	4.625374	4.85188	4.46532	1.58118 (1.700963)	1.38820 (1.330781)	1.25290 (1.208744)	1.716913	30.86
1103 $\frac{1}{2}$ -1106 $\frac{1}{2}$	18	102.8194	7.201927	6.40543	6.68768	1.51616 (1.478147)	1.14954 (1.142444)	0.947991 (1.030814)	1.635038	23.25
1106 $\frac{1}{2}$ -1110	19	93.8786	3.286588	3.50363	3.26630	1.31064 (1.346059)	1.09177 (1.032862)	0.897869 (0.9281347)	1.581535	19.65
1110 -1113 $\frac{1}{2}$	20	119.8070	2.941458	2.92021	2.47004	1.30120 (1.319411)	1.10185 (1.032312)	0.859042 (0.9365175)	1.531518	23.15
1113 $\frac{1}{2}$ -1116 $\frac{1}{2}$	21	111.7602	1.496424	1.64597	1.57177	1.22633 (1.169716)	0.931131 (0.9100749)	0.668345 (0.8277384)	1.467888	19.47



to  $z(\rho', \nu)$  and thus to determine the most likely value for  $\nu$  for each sample. These  $\nu$  values as well as the associated  $\Lambda_V(\nu)$  values given by  $b(\nu) = \Lambda_V(\nu)/a$  are given in Table 4. The most likely  $\nu$  values as obtained by the least squares method for all samples  $j$  in the first, second, and third hours were found to be 1.641557, 1.651151 and 1.615090, respectively. The most likely  $\nu$  value for all 21 samples was found to be 1.638562. For  $j = 9$  to 21, the values of  $z_j(\Delta_{ij})$  shown in parentheses are those determined by the least squares curve fit. Note that the values of  $\Lambda_V(\nu)$  in Table 4 are comparable to those in Table 1 for  $\mu = 1/3$  (i. e.,  $\nu = 5/3$ ).

Returning to Equation 13, it is evident that it involves a mixture of the vertical and horizontal turbulence structure, since the effect of the time constant  $T$  will affect the vertical scales in the precise way implied only when it is assumed that the turbulence is homogeneous and isotropic as regards its  $\nu$  dependence, and that Taylor's hypothesis,  $q = k a = a \, 2\pi f/U = \pi \tau f$ , is applicable. It is probable that all of these conditions are reasonably well satisfied in the inertial subrange; further study of the validity of these assumptions, and of the extent to which the variance of  $z_j(\Delta_{ij})$  indicated in Table 4 may be due to errors in the measurement of  $U$ , is being made.

It is expected that ultimately the data at each height will be used to determine frequency spectra; values of  $\nu$  can then be determined, by invoking Taylor's hypothesis, along a horizontal line. Until these values have been obtained using this data, reference may be made to values of  $\nu$  determined in this way by Thompson, Janes and Kirkpatrick<sup>[2]</sup> and by Thompson and Janes;<sup>[3]</sup> their Colorado observations were obtained near the ground and indicated that  $\nu$  tends to decrease with increasing wind speed, varying from 1 to 2.3 with a mean value of 1.6. They also reported measurements of  $\nu$  made in this way for the horizontal direction in Maui, Hawaii, near the top of Mt. Haleakala at an altitude of 3050 meters; in this case  $\nu$  varied somewhat more erratically



with wind speed over a range from 1.6 to 3.1 with a mean value of 2.2. These mountain-top measurements of  $\nu$  in the horizontal direction appear to show that  $\nu$  tends to increase with increasing altitude but it is not known whether similarly large values of  $\nu$  would be observed at similar heights above level terrain.

## CONCLUSIONS

The analysis thus far indicates that the turbulence of refractivity near the ground is approximately isotropic as regards the parameter  $\nu$  and that this parameter is of the order of  $5/3$ , the value predicted by Obukov and Kolmogorov for the inertial subrange. Pending the expected confirmation of these conclusions at higher heights above the surface, these results would appear to have far-reaching implications as regards the mechanisms responsible for tropospheric forward scatter propagation. In an earlier paper, Norton, Rice and Vogler<sup>[20]</sup> showed that the observed dependence of the basic transmission loss in tropospheric beyond-the-horizon propagation was on the average proportional to  $f^{-\nu}$  where  $\nu = 2.956 \pm 0.244$ . This dependence was found consistent with the assumption that refractivity turbulence was the mechanism responsible for the forward scattered energy, if it is also assumed that the vertical wave number spectrum of refractivity varies as  $k^{-\nu}$ . Phase results on transmission loss variability are clearly inconsistent with the measured values of  $\nu$  given in this paper.

Later Norton<sup>[7]</sup> analyzed some Lincoln Laboratory data on the carrier frequency dependence of beyond-the-horizon transmission loss which indicated a median value of  $\nu$  of 2.75 and values of  $\nu$  less than 2 were observed for 8% of the time. while values of  $\nu < 5/3$  were observed for less than 4% of the time. This paper (published in 1960) also showed the large observed variations in the carrier frequency dependence were inconsistent with the

assumption that tropospheric turbulence is the mechanism responsible for tropospheric forward scatter; a proposal was made that meteorological measurements of the kind described above should be made to determine the conditions for which the turbulence of refractivity may be considered to be the mechanism responsible for the large fields observed in beyond-the-horizon propagation.

The paper on the "Frequency Dependence of the Seasonal Variation of Transmission Loss in Tropospheric Beyond-the-Horizon Propagation at VHF and UHF by Hirai and Kurihara<sup>[21]</sup> on page 454 of the Proceedings of the 1964 World Conference on Radio Meteorology indicates that  $\nu$  varies in Japan between 1.6 in February to 2.8 in July and August. These data suggest that refractivity turbulence may be responsible for much of the forward scatter of radio waves in the winter months in Japan.

The above evidence leads us to conclude that some mechanism other than refractivity turbulence is responsible most of the time for the observed beyond-the-horizon propagation over most of the propagation paths for which transmission loss data are available. Many experimenters have suggested that this other mechanism is the reflection of radio waves by sharp vertical gradients of refractivity. Thus Englund, Crawford and Mumford<sup>[22]</sup> and Friend<sup>[23]</sup> discussed this mechanism from somewhat different points of view and Diamond<sup>[24]</sup> commented extensively on the results obtained by Friend. Somewhat later Norton<sup>[25]</sup> concluded that the tropospheric waves received in beyond-the-horizon propagation were often "reflected at various levels in the troposphere at which there are assumed to be more or less abrupt discontinuities in the distribution with height of the index of refraction" and that the observed fields could not be explained by any of the other mechanisms under consideration at that time.

One of the most definitive papers on the sharp vertical gradient mechanism is by Friis, Crawford and Hogg;<sup>[26]</sup> in this paper it is shown that the basic

transmission loss in beyond-the-horizon propagation via sharp vertical gradients would be expected to be proportional to  $f^{-\nu}$  with  $\nu \approx 3$  most of the time, but varying from 2 to 4 depending upon the nature and extent of the layers involved.

A recent summary of the role of the layer structure of the troposphere in explaining tropospheric propagation was published by Saxton, Lane, Meadows and Mathews<sup>[27]</sup> and in this paper extensive references are given to the relevant literature.

Tropospheric turbulence is the mechanism usually used<sup>[10]</sup> for explaining the observed variations in the electrical lengths of line-of-sight propagation paths at the higher radio frequencies. However, this phase noise is sometimes much larger at the lower elevation angles than would be predicted from tropospheric turbulence theories, and the sharp vertical gradients, which we now believe are in large measure responsible for most of the beyond-the-horizon propagation, may also be the origin of much of this excessive variance in the electrical lengths of line-of-sight propagation paths.



## ACKNOWLEDGMENTS

This paper would not have been possible without the very extensive assistance provided by B. R. Bean, R. E. McGavin and the other personnel in the Radio Meteorology Section of the Troposphere and Space Telecommunication Division of CRPL. The data we are here interpreting were obtained primarily for another purpose as is discussed in a paper by Bean and McGavin<sup>[28]</sup> given at the 1963 World Conference on Humidity and Moisture in Washington, D. C.

Much of the work in gathering these data, obtaining the appropriate calibration factors, and cataloging it was done by R. W. Krinks, M. E. Robinson and C. B. Emmanuel.

Acknowledgment is also made of the careful and extensive data reductions carried out in the Data Reduction Instrumentation Section under the direction of Walter E. Johnson. Particular credit is due to Robert E. Hubbard who developed the National Bureau of Standards Analogue Correlation Analyzer.

Finally, acknowledgment should be made of the programming for the digital computer done by Judd Payne, William B. Sweezy and Mrs. Carolen M. Jackson.



## REFERENCES

1. G. Birnbaum, and H. E. Bussey, "Amplitude, Scale, and Spectrum of Refractive Index Inhomogeneities in the First 125 Meters of the Atmosphere," Proc. IRE, 43, No. 10, 1412-1418, Oct. 1955.
2. M. C. Thompson, Jr., H. B. Janes, and A. W. Kirkpatrick, "An Analysis of Time Variations in Tropospheric Refractive Index and Apparent Radio Path Length," J. of Geophys. Res., 65, No. 1, 193-201, Jan. 1960.
3. M. C. Thompson, Jr., and H. B. Janes, "Radio Path Length Stability of Ground-to-Ground Microwave Links," NBS Tech. Note 219, 1964.
4. H. G. Booker, and W. E. Gordon, "A Theory of Radio Scattering in the Troposphere," Proc. IRE, 38, No. 4, 401-412, Apr. 1950.
5. F. Villars, and V. F. Weisskopf, "On the Scattering of Radio Waves by Turbulent Fluctuations of the Atmosphere," Proc. IRE, 43, No. 10, 1232-1239, Oct. 1955.
6. K. A. Norton, "Point-to-Point Radio Relaying Via the Scatter Mode of Tropospheric Propagation," IRE Trans. Commun. Systems, CS-4, No. 1, 39-49, Mar. 1956.
7. K. A. Norton, "Carrier-Frequency Dependence of the Basic Transmission Loss in Tropospheric Forward Scatter Propagation," J. of Geophys. Res., 65, No. 7, 2029-2045, July 1960; published in somewhat more detail as NBS Tech. Note 53, May 1960.
8. A. D. Wheelon, "Radio Scattering by Tropospheric Irregularities," J. of Atmos. Terrest. Phys., 15, 185-205, 1959.
9. R. B. Muchmore, and A. D. Wheelon, "Line-of-Sight Propagation Phenomena. I. Ray Treatment. II. Scattered Components," Proc. IRE, 43, No. 10, 1437-1458, Oct. 1955.
10. K. A. Norton, "Effects of Tropospheric Refraction in Earth-Space Links" (paper presented at the XIVth General Assembly of USRI in Japan, Sept. 1963); published in the Proceedings of the Second Tropospheric Refraction Effects Technical Review Meeting, Tech. Doc. Rept. ESD-TDR-64-103, I, 155-193, The MITRE Corporation, Bedford, Mass., Mar. 1964.

## REFERENCES (Cont.)

11. E. C. Barrows, "Residual Range and Range Rate Errors Due to the Troposphere" (paper presented at the Second Tropospheric Refraction Effects Technical Review Meeting), Nov. 1963; published in the Proceedings, Tech. Doc. Rept. ESD-TDR-64-103, 1, 143-153, The MITRE Corporation, Bedford, Mass., Mar. 1964.
12. M. C. Thompson, Jr., and M. J. Vetter, "Compact Microwave Refractometer for Use in Small Aircraft," Rev. Sci. Instr., 29, No. 12, 1093-1096, Dec. 1958.
13. G. Birnbaum, "Fluctuations in the Refractive Index of the Atmosphere at Microwave Frequencies," Phys. Rev., 82, 110-111, Apr. 1951.
14. R. O. Gilmer, R. E. McGavin, and B. R. Bean, "The Response of Microwave Refractometer Cavities to Atmospheric Variations," Proceedings of the 1964 World Conference on Radio Meteorology Incorporating the Eleventh Weather Radar Conference, 244-247, Sept. 1964.
15. R. A. Fisher, "On the Probable Error of a Coefficient of Correlation Deduced from a Small Sample," Metron, 1, 4, 1921.
16. A. Hald, Statistical Theory with Engineering Applications, John Wiley & Sons, New York, 1952.
17. H. H. Aiken, Tables of Inverse Hyperbolic Functions, Harvard University Press, Cambridge, Mass., 1949.
18. A. D. Wheelon, "Spectrum of Turbulent Fluctuations Produced by Convective Mixing of Gradients," Phys. Rev., 105, No. 6, 1706-1711, 1957.
19. M. M. Siddiqui, "Some Statistical Theory for the Analysis of Radio Propagation Data," J. Res. NBS, 66D, No. 5, 571-580, Sept.-Oct. 1962.
20. K. A. Norton, P. L. Rice, and L. E. Vogler, "The Use of Angular Distance in Estimating Transmission Loss and Fading Range for Propagation through a Turbulent Atmosphere over Irregular Terrain," Proc. IRE, 43, No. 10, 1488-1526, Oct. 1955.

# REFERENCES (Cont.)

21. M. Hirai and Y. Kurihara, "Frequency Dependence of the Seasonal Variation of Transmission Loss in Tropospheric Beyond-the-Horizon Propagation at VHF and UHF," Proceedings of the 1964 World Conference on Radio Meteorology Incorporating the Eleventh Weather Radar Conference, 454-457, Sept. 1964.
22. C. R. Englund, A. B. Crawford, and W. W. Mumford, "Ultra-Short-Wave Transmission and Atmospheric Irregularities," Bell System Tech. J., 17, 489-519, 1938.
23. A. W. Friend, "Developments in Meteorological Sounding by Radio Waves," J. Aeron. Sci., 7, No. 8, 347-352, June 1940.
24. H. Diamond, Letter to the Editor Commenting on Paper by A. W. Friend, J. Aeron. Sci., 7, No. 8, June 1940.
25. K. A. Norton, "Propagation in the FM Broadcast Band," Advan. Electron., 1, 381-421, 1948.
26. H. T. Friis, A. B. Crawford, and D. C. Hogg, "A Reflection Theory for Propagation Beyond the Horizon," Bell System Tech. J., 36, 627-644, May 1957.
27. J. A. Saxton, J. A. Lane, R. W. Meadows, and P. A. Matthews, "Layer Structure of the Troposphere," Proc. IEE, 111, No. 2, 275-283, Feb. 1964.
28. B. R. Bean and R. E. McGavin, "The Use of the Radio Refractometer to Measure Water Vapor Turbulence," Proceedings of the 1963 World Conference on Humidity and Moisture (to be published by Reinhold Publishing Co.).



# COMPARISON OF REFRACTION EFFECT CORRECTION TECHNIQUES

C. Gardner\*

## INTRODUCTION

This paper summarizes a preliminary study conducted to compare differences in tracking data corrections resulting from various atmospheric refractive data inputs.

Trajectory corrections were computed for each of two basically different atmospheric conditions. broadly typical of West Coast and East Coast launch environments, using the same hypothetical launch based on three different representations of the vertical refractive-index profile.

## CORRECTION COMPUTATIONS

### Refractive Profiles

Two sites were selected as representative of different atmospheric soundings more or less typical of East and West Coast missile launch environments —

West Coast: San Nicolas Island, Calif. , 1600Z 23 June 1964.

(Strong low-level temperature inversion with a 60 N-unit decrease between 1500 and 1700 feet. )

East Coast: Patrick AFB, Fla. , 0013Z 25 November 1961.

(Refractive-index variation with altitude typical for the Patrick AFB, Florida area. )

---

\* Headquarters, Pacific Missile Range, Point Mugu, California.



In each case, two exponential profiles or quasi-exponential approximations to the detailed refractive profile were also adopted for comparisons. The Eastern Test Range (ETR) exponential profile is defined by a curve originating at the surface with a refractive-index value of  $N_s$  and decreasing exponentially to 4 N-units at 100,000 feet. The National Bureau of Standards (NBS) profile is defined (Bean and Thayer<sup>[1]</sup>) by a curve that originates at the surface with a value  $N_s$  and decreases exponentially through the value of  $N_s$  and  $\Delta N$  at a height of 1 kilometer above the surface, where  $\Delta N = -7.32 \exp(0.005577 N_s)$ . Figures 1 and 2 show refractive profiles for the two basic soundings and the corresponding exponential profiles. Table I lists the several profiles by number as they are identified on accompanying figures throughout this paper.

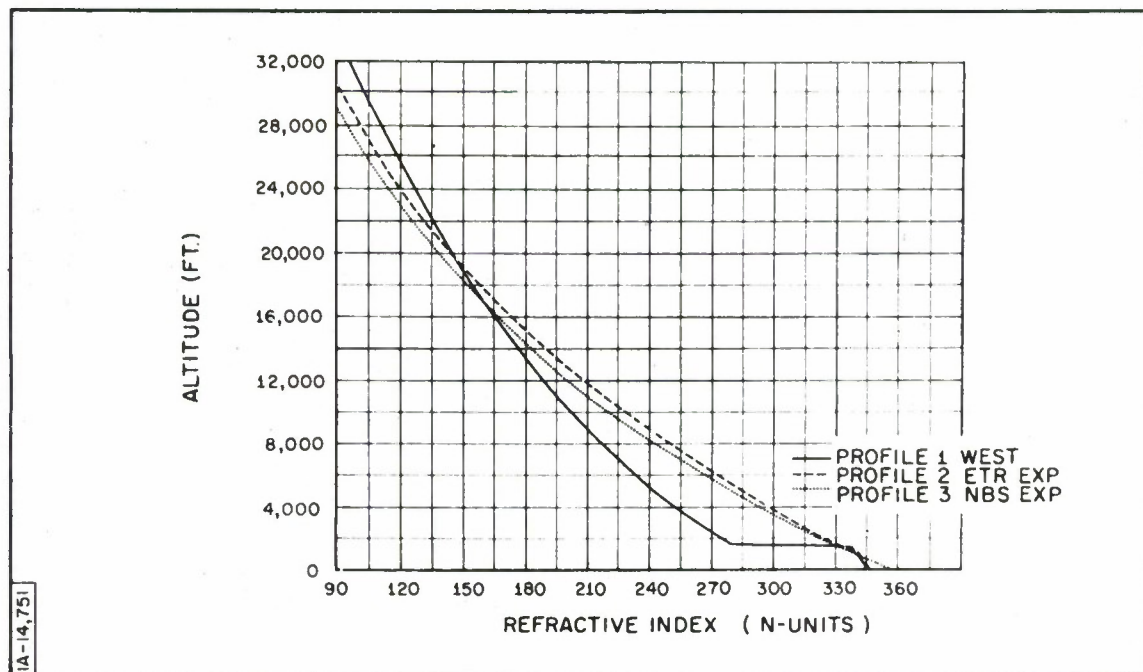


Figure 1. Refractive Profiles 1, 2 and 3

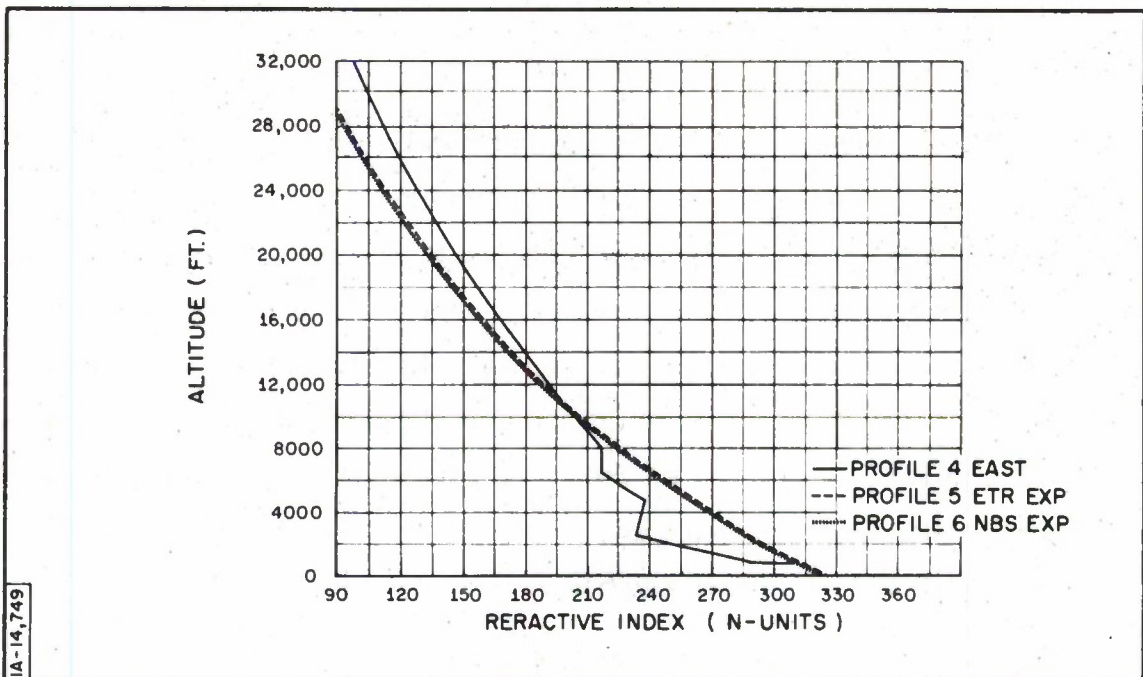


Figure 2. Refractive Profiles 4, 5 and 6

Table I

Guide to Profile Identification

Profile No.		Profile - Identification
West Coast	1	Refractometer + Rawinsonde: 1600Z 23 June 1964
	2	ETR exponential approximation of (1)
	3	NBS quasi-exponential approximation of (1)
East Coast	4	Rawinsonde: 0013Z 25 November 1961
	5	ETR exponential approximation of (4)
	6	NBS quasi-exponential approximation of (4)

### Trajectory Data

The programmed trajectory of a hypothetical missile launch provided the theoretical (in the absence of refraction effects) elevation angles and slant ranges to Radars 1 and 2, which were assumed to be located approximately 55 nautical miles apart and at elevations of 1000 feet and 44 feet, respectively. Radar 1 was located approximately 81 nautical miles downrange of the launch site and 57 nautical miles to the left of the line-of-flight. Radar 2 was located 29 nautical miles downrange of the launch site and 77 nautical miles to the left of the line-of-flight. (This configuration corresponds to the placement of San Nicolas and Point Mugu Radars relative to a Point Arguello launch.)

The missile trajectory as a function of time is described in Figures 3, 4 and 5. The altitude, which is independent of the radars, is given in Figure 3. The elevation angles and slant ranges are shown in Figures 4 and 5, respectively, for each radar. The maximum elevation angle for Radar 1, not shown in Figure 4, was about 48.6 degrees at 145 seconds of flight time.

### Method of Computation

Refraction corrections in this study are defined as the differences between the theoretical data of Figures 3 - 5 and the data determined for the several refractive index profiles. It is possible, through iterative ray-tracing processes, to determine the unique ray path between the radar and the target for any flight time with a given refractive profile.

All refraction corrections were calculated by the Pacific Missile Range (PMR) refraction correction method (Gardner<sup>[2,3]</sup>) on an IBM 7094 computer. This is the PMR standard ray-tracing technique for determining bending effects produced by any horizontal stratified refractive medium. It should be noted that this study considers only the corrections derived from ray-tracing

equations. The correlation between these corrections and residual errors has not been determined. Each of the exponential profiles used a preset table of altitudes for N-unit computations, with 250 feet as the initial altitude above the surface. This initial gradient, between the surface and 250 feet, is about 10 to 12 N-units per 1000 feet (close to measured values).

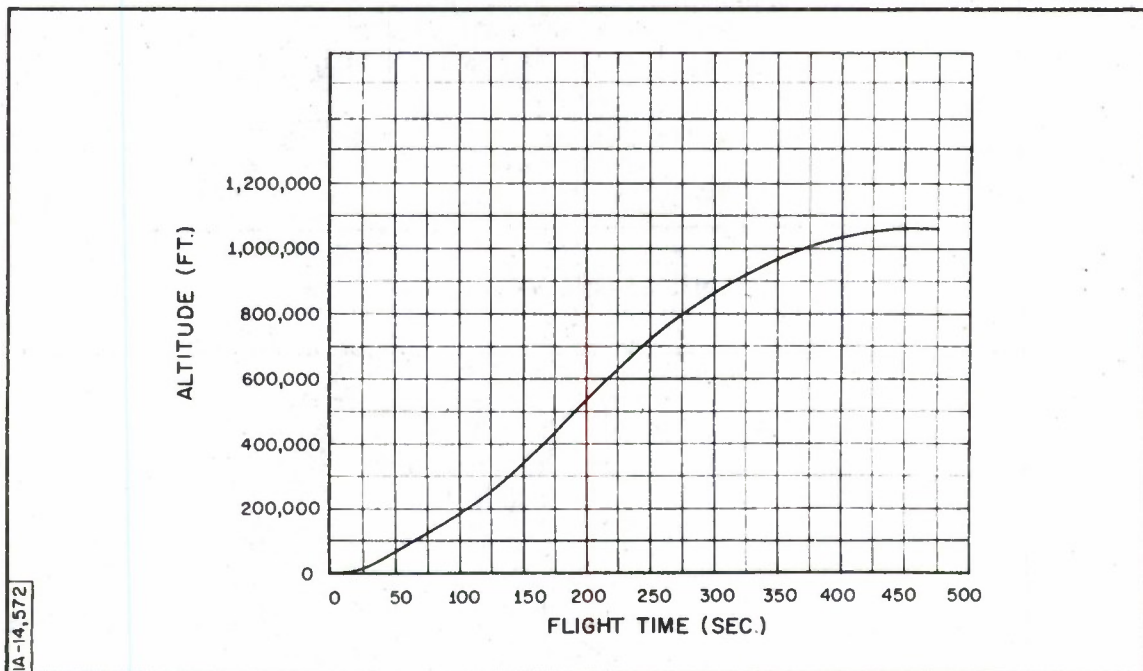


Figure 3. Altitude Versus Flight Time



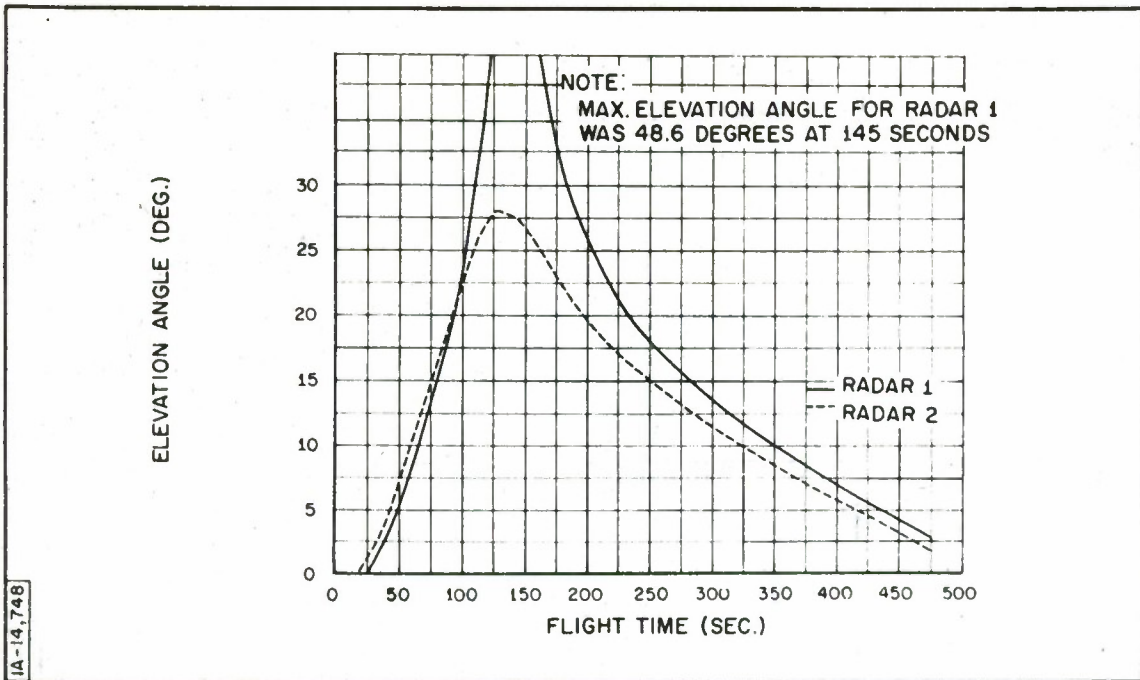


Figure 4. Elevation Angle Versus Flight Time

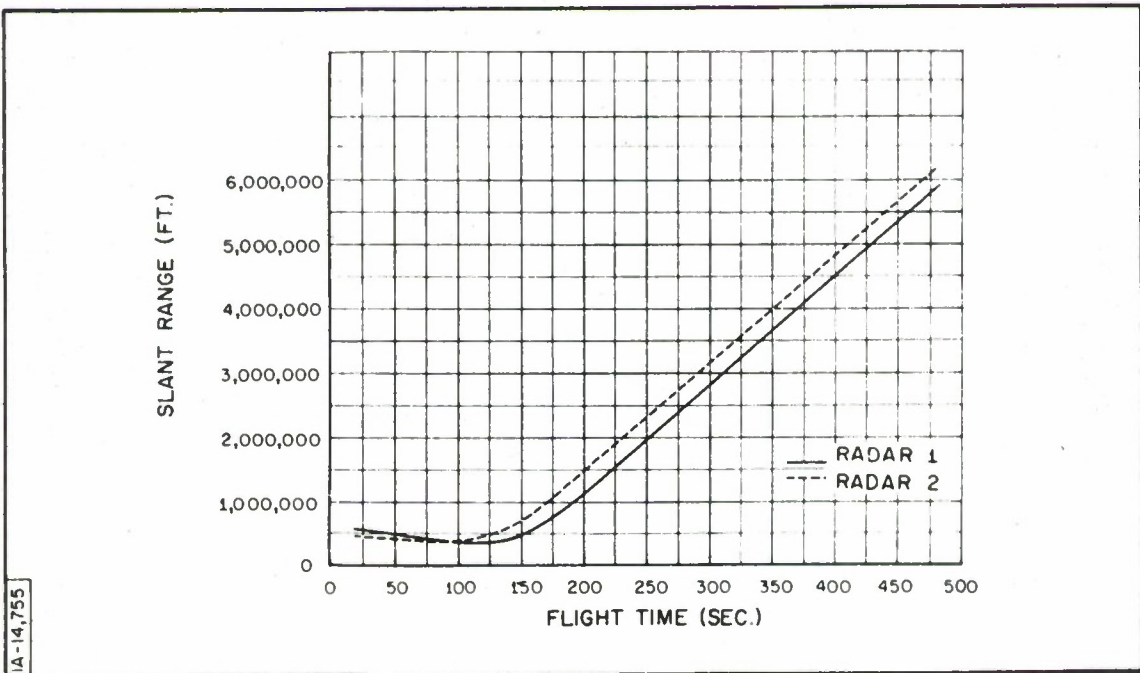


Figure 5. Slant Range Versus Flight Time

## DISCUSSION OF RESULTS

### West Coast Case

The West Coast refractive case selected is a typical low-level inversion condition. This combined rawinsonde and refractometer-determined refractive index profile was recorded at San Nicolas Island, California, at 1600Z on 23 June 1964. It is referred to hereafter as the rawinsonde-refractometer profile, and is identified as Profile 1 in Figure 1. The ETR and NBS exponential approximations of Profile 1 are given by Profiles 2 and 3, respectively.

### Altitude

The computed altitude corrections for Radars 1 and 2, using the rawinsonde-refractometer profile, is shown in Figure 6. The altitude corrections for Radar 2 are greater than those for Radar 1 after about the first 100 seconds. This is because of the lower elevation angle of Radar 2 for all but the early portion of the flight (see Figure 4)).

A comparison between the altitude corrections for the ETR and NBS exponential profiles and the rawinsonde-refractometer profile for Radar 1 is shown in Figure 7. The differences in altitude corrections for combinations of the above profiles are generally very small compared to the total corrections. The total difference in altitude correction is always less than 100 feet whenever the elevation angle is greater than 5 degrees (between 50 and 435 seconds for Radar 1, between 40 and 415 seconds for Radar 2). However, as the elevation angle decreases below 5 degrees, the differences increase very rapidly. A similar comparison of altitude corrections for Radar 2 is given by Figure 8. Again, the difference in altitude correction is always less than 100 feet whenever the elevation angle is greater than 5 degrees.

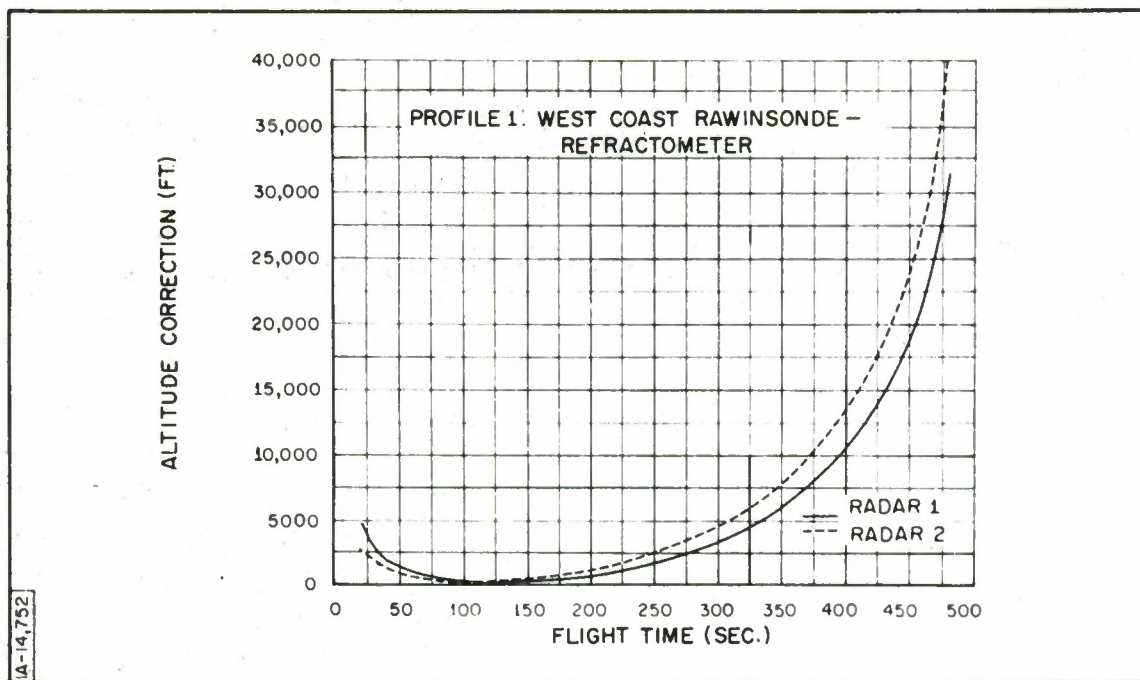


Figure 6. Altitude Correction for Profile 1

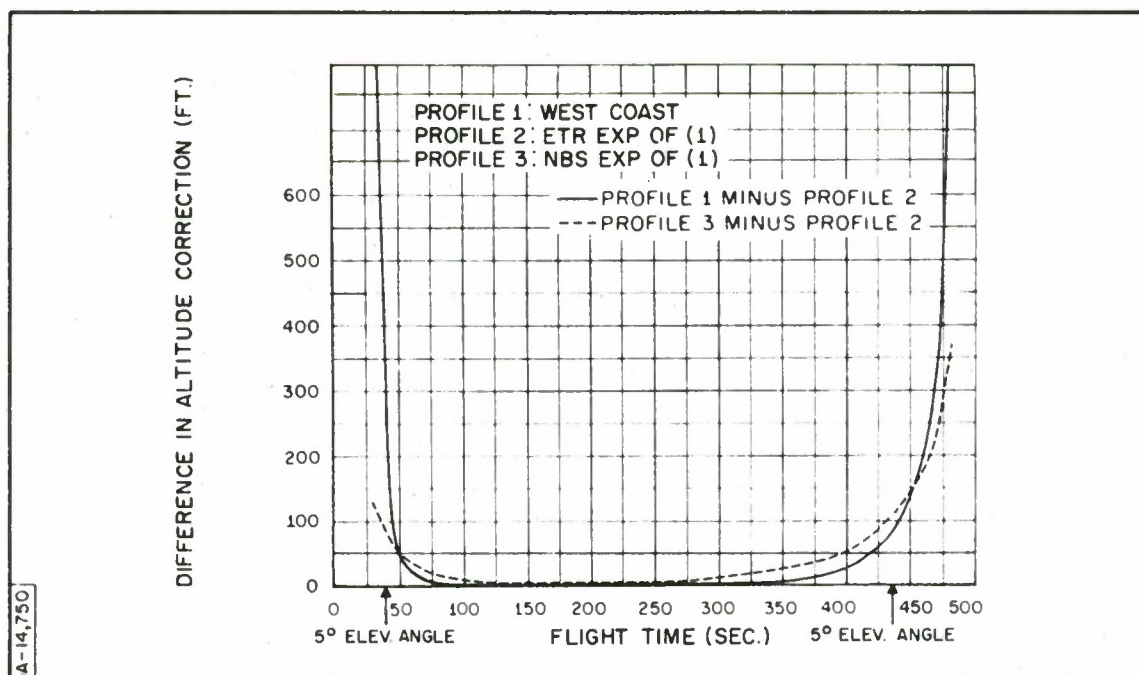


Figure 7. Radar 1: Difference in Altitude Correction as Computed for Refractive Profiles 1, 2 and 3

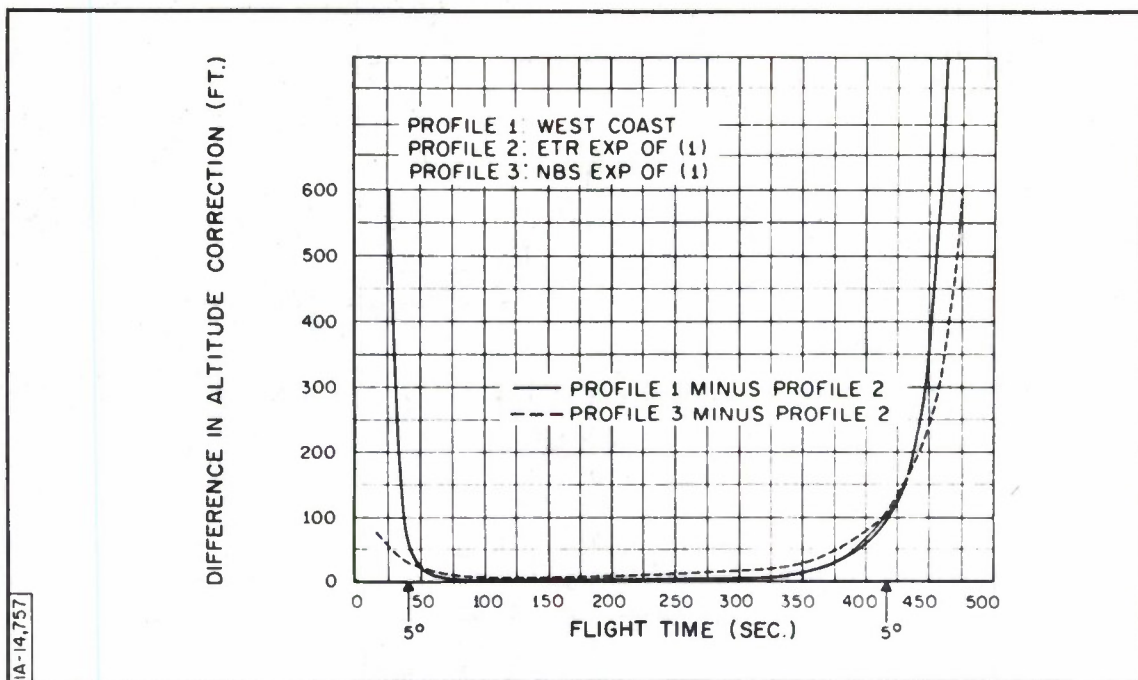


Figure 8. Radar 2: Difference in Altitude Correction as Computed for Refractive Profiles 1, 2 and 3

### Elevation Angle

The elevation angle corrections for Radars 1 and 2, using Profile 1, are given in Figure 9. The difference between the two correction curves changes sign; i. e., the curves cross at approximately 90 seconds. This coincides with the corresponding cross-over of the theoretical elevation angles in Figure 4, and results from the geometry of the two radar locations with respect to the launch site and subsequent trajectory. Immediately after launch, Radar 2, because it is closer to the launch site, tracks a higher elevation angle and shorter range. As the missile proceeds downrange, it nears Radar 1, and thereafter Radar 1 tracks at a higher elevation angle and shorter slant range than Radar 2.



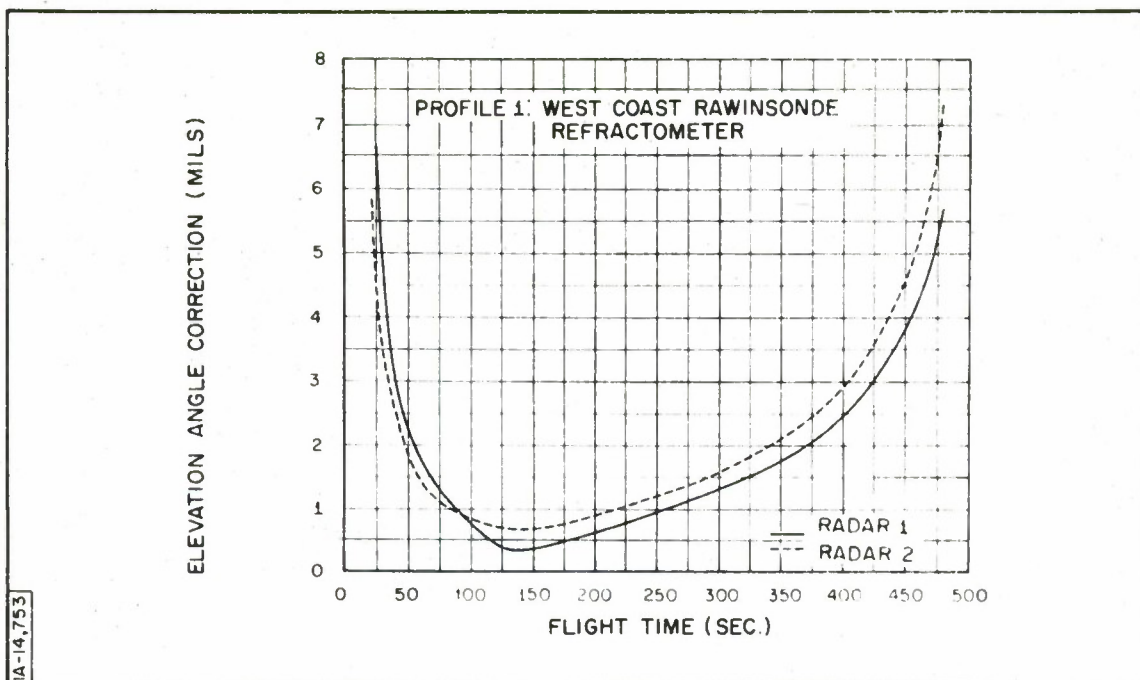


Figure 9. Elevation Angle Correction for Profile 1

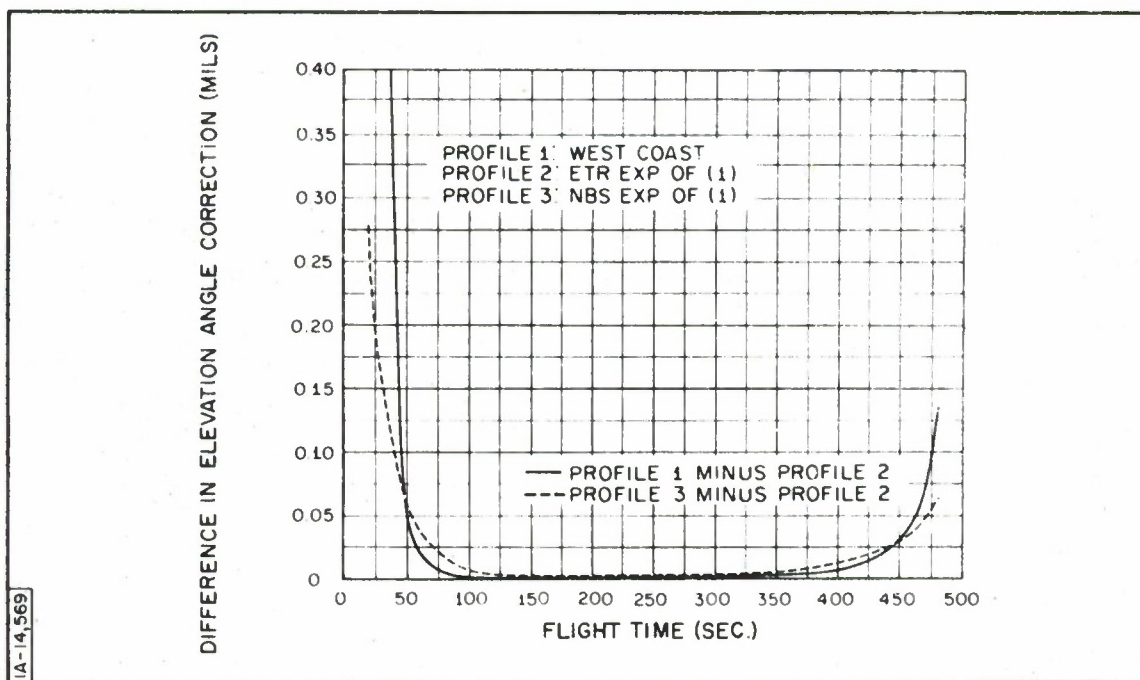


Figure 10. Radar 1: Difference in Elevation Angle as Computed for Refractive Profiles 1, 2 and 3

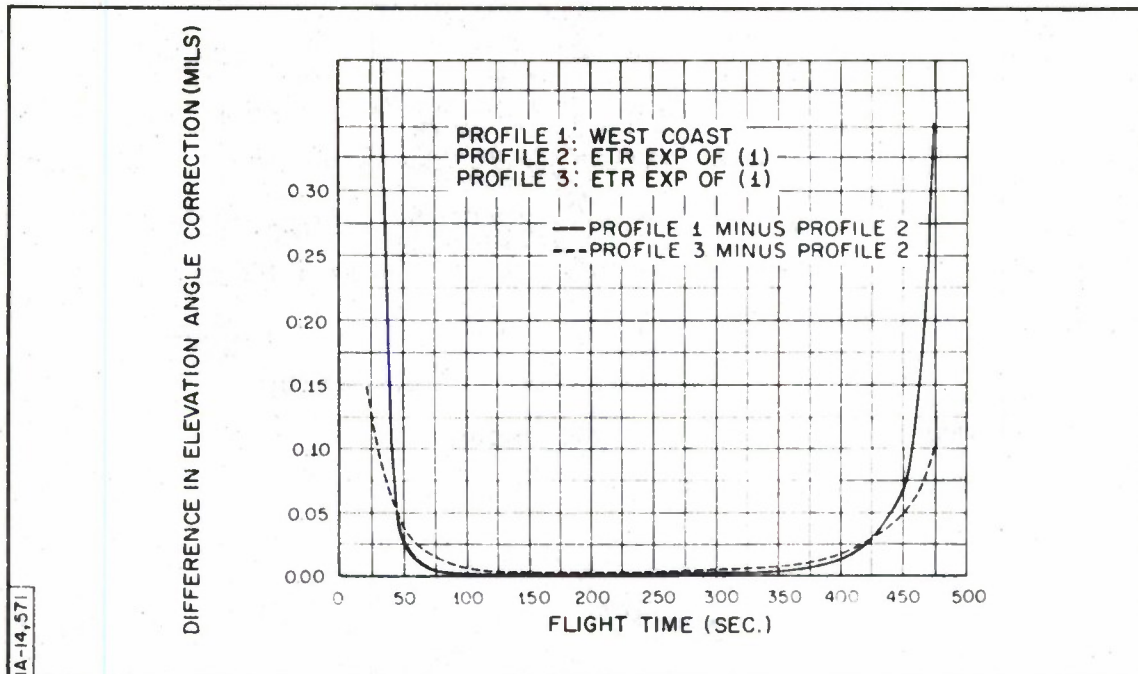


Figure 11. Radar 2: Difference in Elevation Angle Correction as Computed for Refractive Profiles 1, 2 and 3

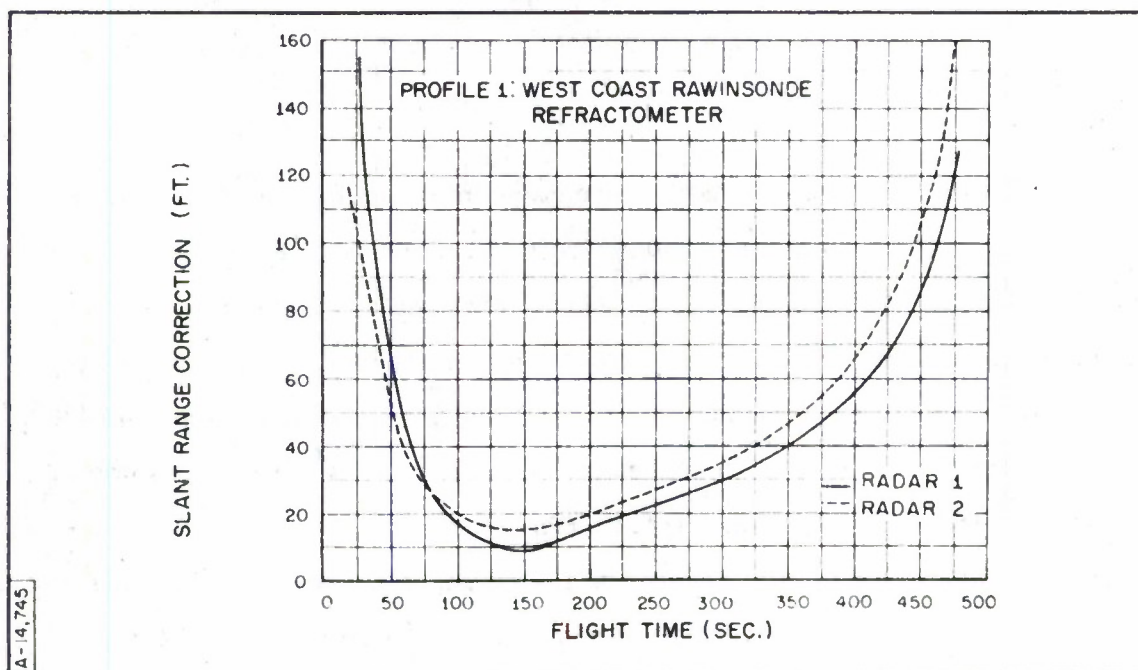


Figure 12. Slant Range Correction for Profile 1

A comparison between the elevation angle corrections for the ETR and NBS exponential profiles and the rawinsonde-refractometer profiles for Radar 1 is given by Figure 10. The greatest differences, occurring within the first 50 seconds and after 480 seconds of flight time, result from the greater bending effect for lower elevation angles. This effect is also shown for Radar 2 in Figure 11. It is noted that larger differences in elevation angle corrections are observed between the rawinsonde-refractometer and the ETR exponential profiles (Profiles 1 and 2) than between the ETR and NBS exponential profiles (Profiles 2 and 3).

#### Slant Range

The slant range corrections for Radars 1 and 2, using the rawinsonde-refractometer profile, are given in Figure 12. As shown in the figure, a cross-over of corrections at about 80 seconds of flight time produced by the geometry of radar locations.

A comparison between the slant range corrections for the ETR and NBS exponential profiles and the rawinsonde-refractometer profiles for Radar 1 is given by Figure 13. These differences in corrections are more pronounced during the first 45 seconds of flight time. The differences in slant range corrections between the two types of exponential profiles (Profiles 2 and 3) are about twice as large as the differences between the rawinsonde-refractometer profile and the ETR exponential profiles (Profiles 1 and 2). Figure 14 illustrates the same effect for Radar 2. The maximum at about 40 seconds of flight time may be caused by differences between the refractive index gradients of Profiles 2 and 3 (Figure 1) near the surface.

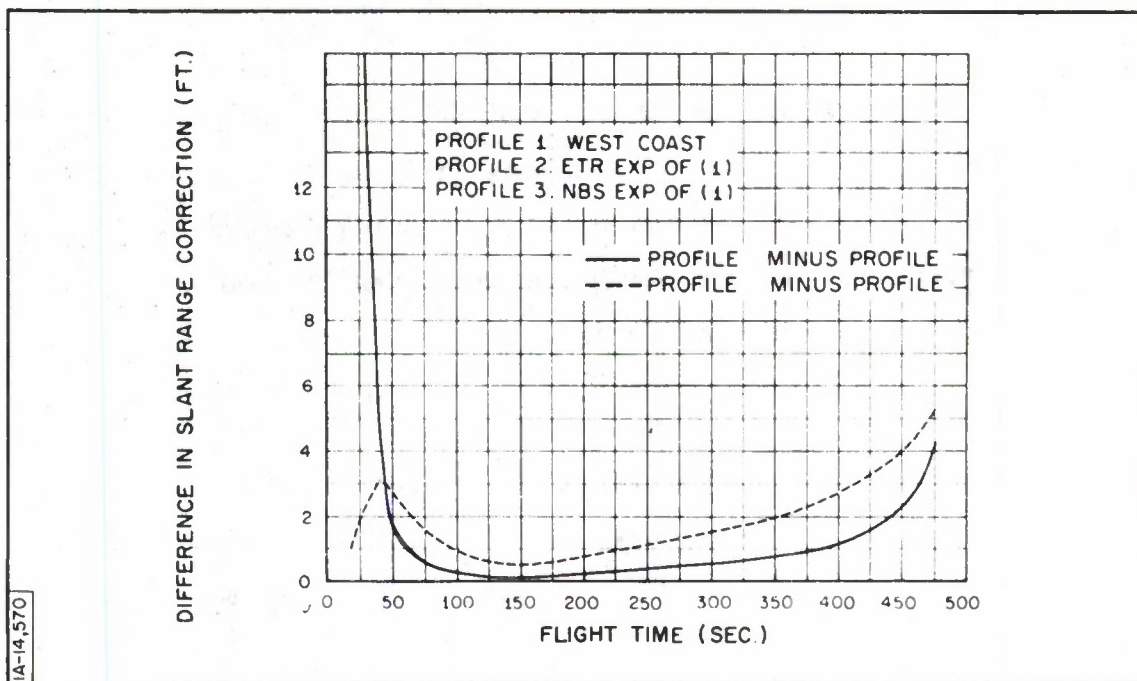


Figure 13. Radar 1: Difference in Slant Range Correction as Computed for Refractive Profiles 1, 2 and 3

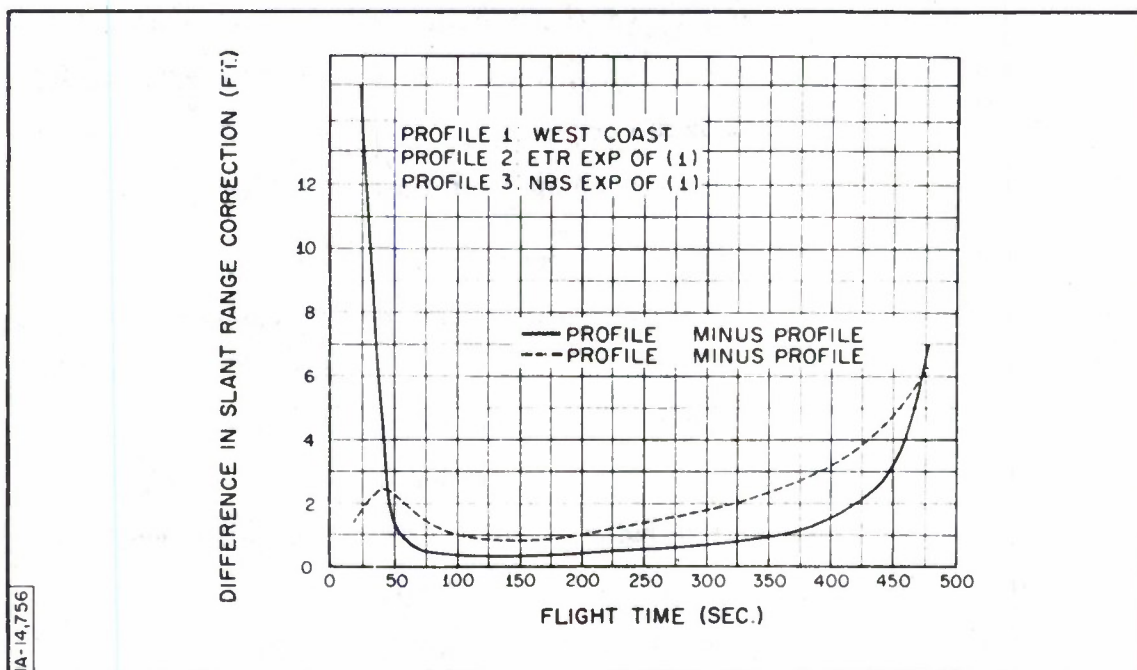


Figure 14. Radar 2: Difference in Slant Range Correction as Computed for Refractive Profiles 1, 2 and 3



### East Coast Case

The foregoing was an analysis for a typical PMR summer low-level inversion. The effect of an ETR inversion as recorded by rawinsonde at 1300Z on 25 November 1961 on the same missile trajectory is considered next. This is identified as Profile 4 in Figure 2; the corresponding ETR and NBS exponential approximations are given by Profiles 5 and 6, respectively.

### Altitude

The altitude corrections for Radars 1 and 2 are given by Figure 15. A comparison between the altitude correction for the ETR and NBS exponential profiles and the rawinsonde profile, as computed for Radar 2, is given by Figure 16.

As indicated by Figures 6 and 15, Radar 2 corrections were larger than Radar 1 corrections for both East and West Coast cases. Figure 16 shows that Profile 1 with the pronounced inversion resulted in larger corrections than Profile 4. Thus, the presentation of Radar 1 data for the East Coast case would add little in the illustration of correction differences due to radar position, and no Radar 1 corrections were computed for Profiles 5 and 6.

It is significant that the differences between the altitude corrections computed for the ETR exponential profile (Profile 5) and the NBS exponential profile (Profile 6) as shown in Figure 16 is much smaller for the East Coast case than for the similar West Coast comparison (Figure 8). This is a result of the difference between the two exponential profiles which is greater for larger values of surface refractive index  $N$ -unit due to the manner in which each profile is defined. This can be seen by comparing the exponential profiles of Figures 1 and 2, between which there is a surface  $N$ -unit difference of 20.

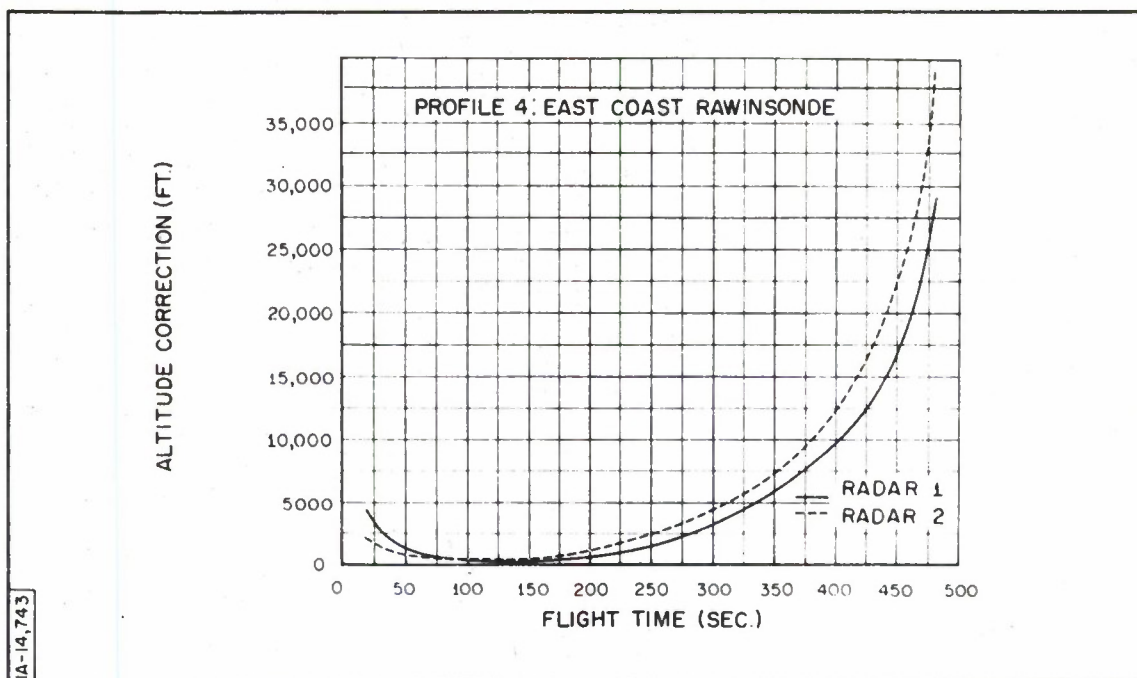


Figure 15. Altitude Correction for Profile 4

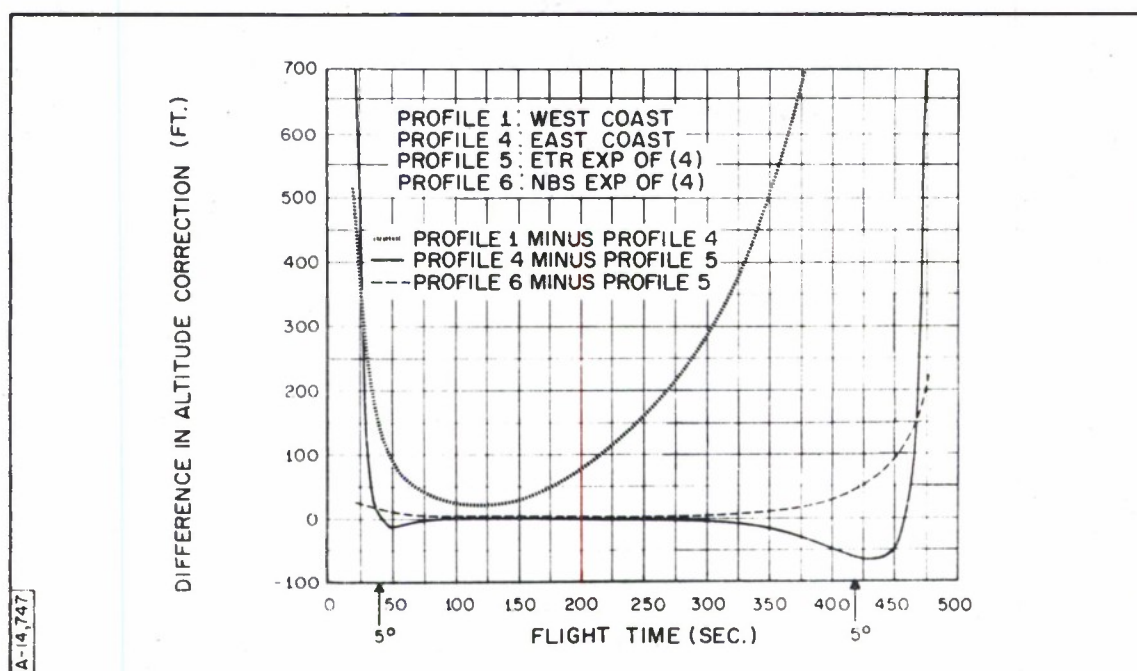


Figure 16. Radar 2: Difference in Altitude Correction as Computed for Refractive Profiles 4, 5, and 6, and for Refractive Profiles 1 and 4

### Elevation Angle

The elevation angle corrections for Radars 1 and 2, using Profile 4, are given by Figure 17. Comparisons between the elevation angle corrections for the ETR and NBS exponential profiles and the rawinsonde profiles for Radar 2 are given by Figure 18. The pronounced difference between these and corresponding comparisons for the West Coast case (Figure 11) results from difference in refractive index structure for each case. Figure 18 also provides a comparison between elevation angle corrections for the PMR rawinsonde-refractometer and the ETR rawinsonde profiles, as computed for Radar 2.

### Slant Range

The slant range corrections for Radars 1 and 2, using Profile 4, are given by Figure 19. Comparisons between slant range corrections for the ETR and NBS exponential profiles and the rawinsonde profiles for Radar 2 are given by Figure 20. The changes in the curves of differences in slant range correction occurring at about 40-50 seconds of flight time appear to be caused by the difference in structure of the refractive profiles being considered. In addition, a comparison of the slant range correction for the ETR rawinsonde profiles, and the PMR rawinsonde-refractometer, as computed for Radar 2, is given in Figure 20.

## SUMMARY AND CONCLUSIONS

A comparison between actual extreme refractive conditions for the Eastern Test Range (ETR) and the Pacific Missile Range (PMR) in relation to ETR and NBS exponential atmospheres was made for a hypothetical satellite launch as seen by two widely separated radars. It has been shown that for tracking elevation angles greater than 5 degrees, either type of exponential atmosphere, originating from a measured surface refractive index, can be used

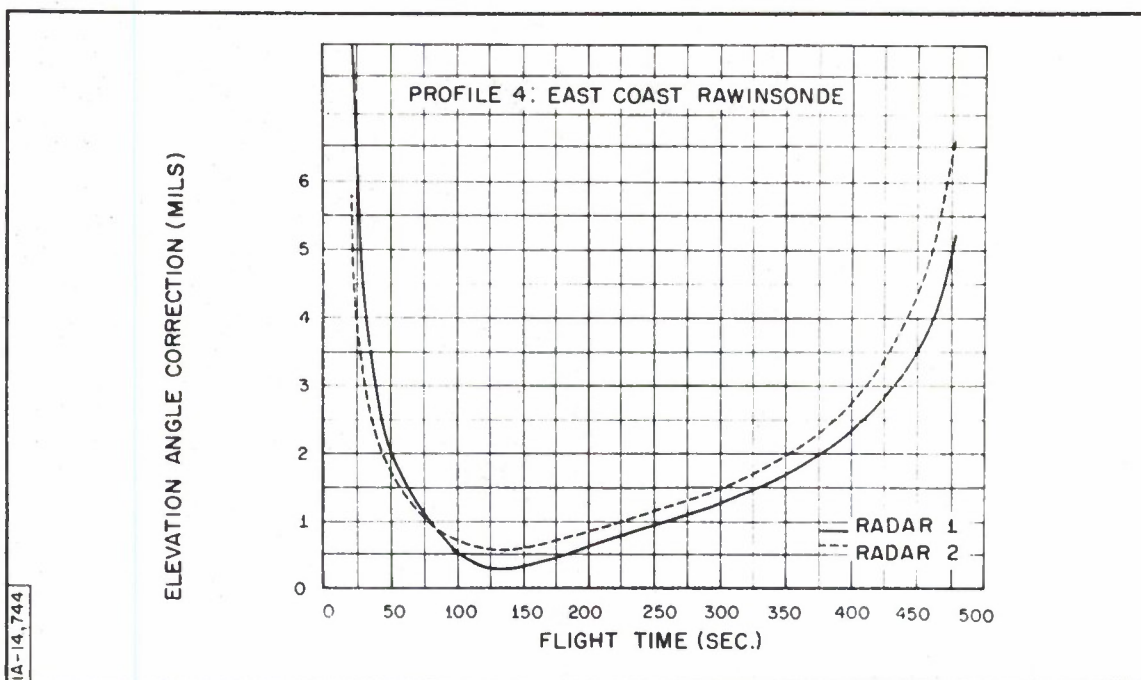


Figure 17. Elevation Angle Correction for Profile 4

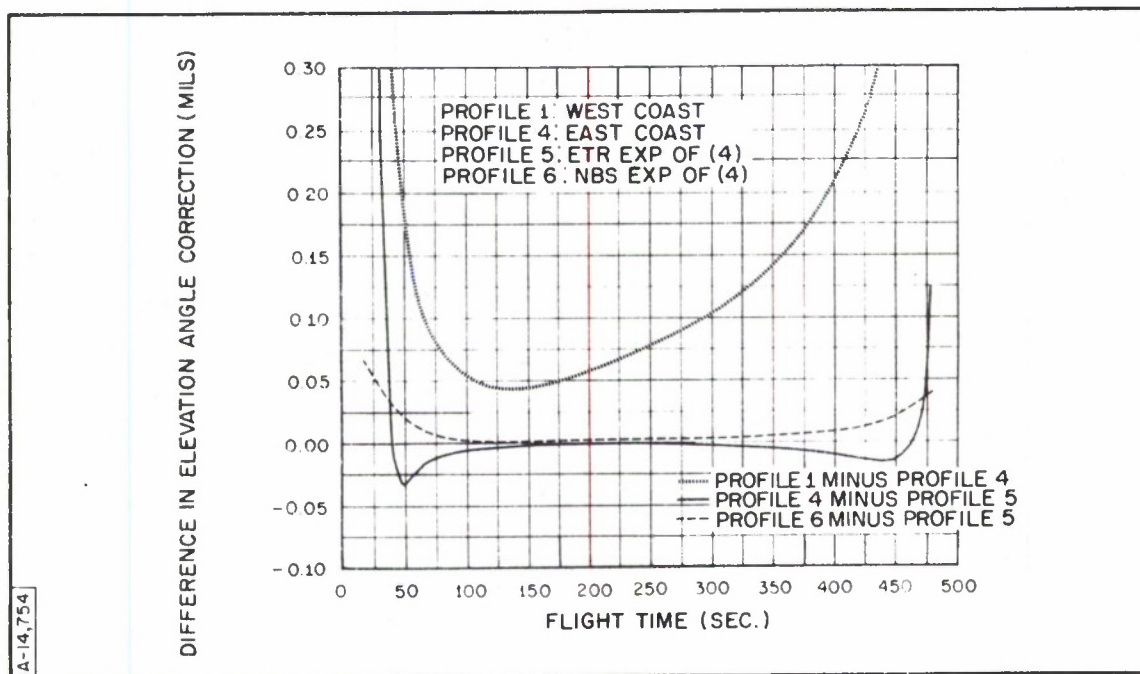


Figure 18. Radar 2: Difference in Elevation Angle Correction as Computed for Refractive Profiles 4, 5 and 6



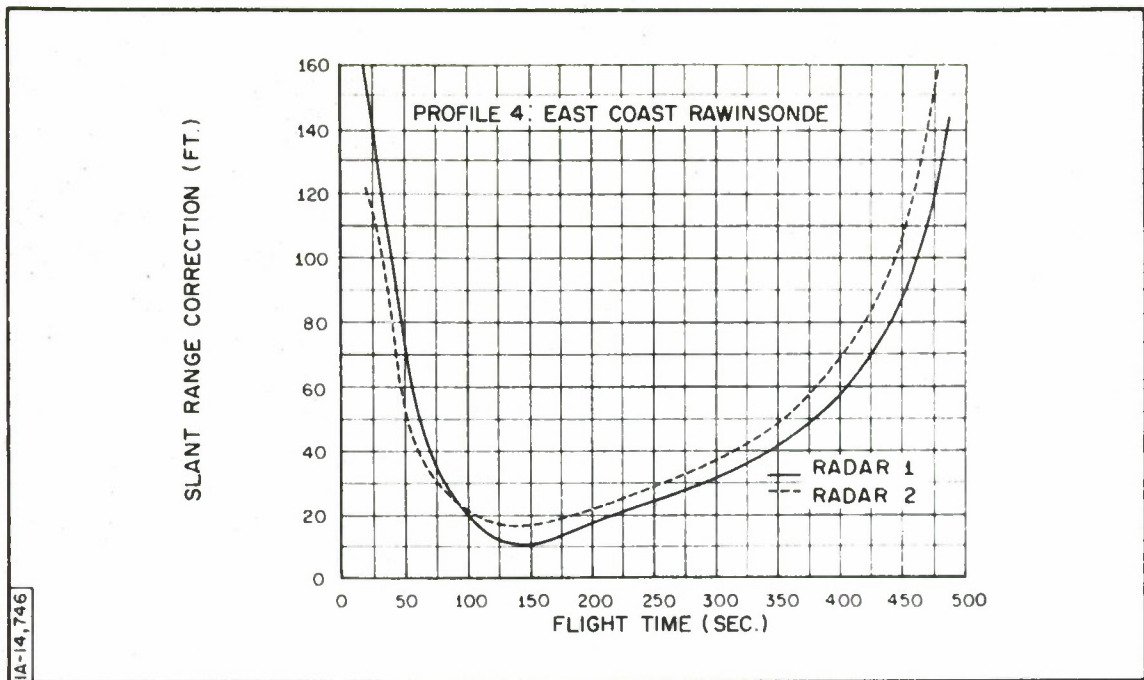


Figure 19. Slant Range Correction for Profile 4

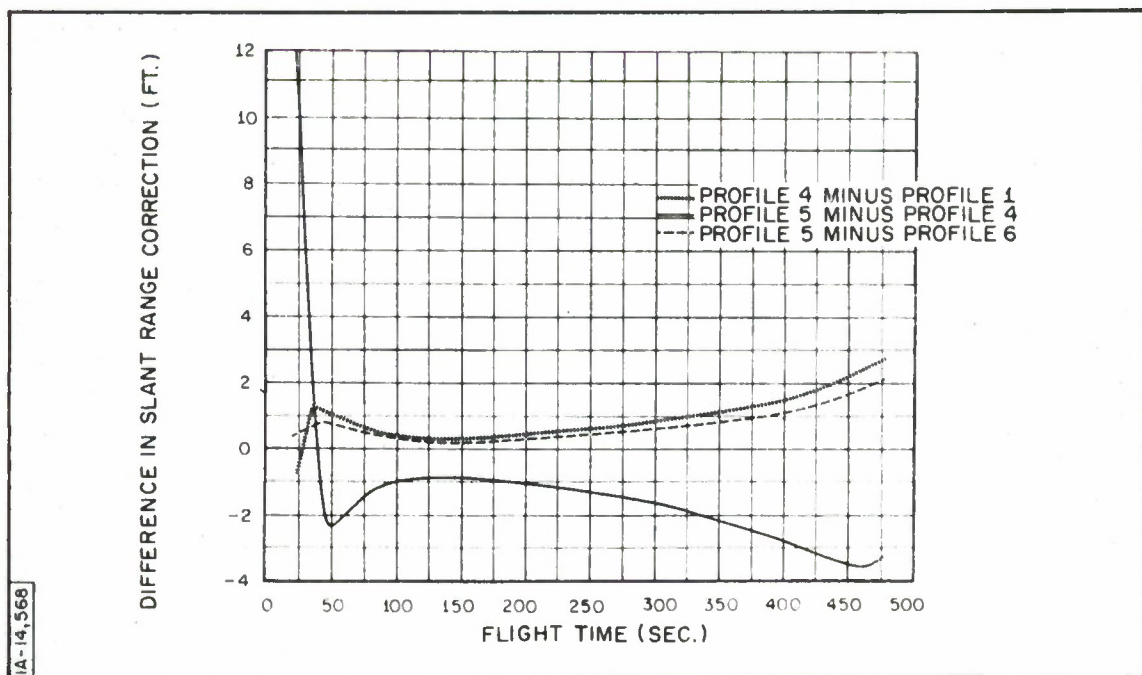


Figure 20. Radar 2: Difference in Slant Range Correction as Computed for Refractive Profiles 4, 5, and 6, and for Refractive Profiles 1 and 4

for position determination within 100 feet. Consequently, the only variable atmosphere input required for this accuracy is the current surface refractive index. Below a 5-degree elevation angle, refraction corrections should only be made with the use of detailed rawinsonde plus refractometer refractive index profiles, using standard ray-tracing techniques.

#### REFERENCES

1. B. R. Bean, and G. B. Thayer, NBS Monograph 4, 29 October 1959.
2. C. Gardner, "Determination of Elevation and Slant Range Errors Due to Atmospheric Refraction," PMR Technical Note No. 3280-6, Rev. December 1962.
3. C. Gardner, "Tracking Errors at Low Elevation Angles Due to Tropospheric Refractive Effects," Proceedings of the Second Tropospheric Refraction Effects Technical Review Meeting, Vol. II, FSD-TDR-64-103, April 1964.

## MULTIPATH PROPAGATION EXPERIMENTS

E. W. Heinzerling<sup>\*</sup>

### INTRODUCTION

This paper presents two separate subjects dealing with multipath propagation: (1) the results of the overwater multipath test performed at Eleuthera, B. W. I., during the fall of 1963, and (2) the description of a proposed test to determine the multipath characteristics produced by atmospheric anomalies.

### BACKGROUND

Multipath transmission may be defined as the transmission of a signal from transmitter to receiver via two or more paths as shown in Figure 1. The direct signal from transmitter to receiver is used as a reference. It has the shortest propagation path,  $R$ , and has a normalized magnitude of  $D = 1.0$ . The upper multipath signal is characterized by an additional propagation path  $\Delta_1$ , and has a relative magnitude of  $M_1$ . It may be produced by atmospheric anomalies. The lower multipath signal is characterized by an additional propagation path length  $\Delta_2$  and has a relative magnitude  $M_2$ . It is caused by reflection from the earth's surface. It differs from the atmospheric multipath case since a phase shift of 180 degrees occurs upon reflection at the grazing angles of reflection which are of interest.

The multipath signal may then be described by:

- (a)  $M$ , the relative magnitude of the multipath signal with respect to the direct signal;
- (b)  $\Delta$ , the additional propagation path length of the multipath signal with respect to the direct signal; and
- (c)  $\alpha$ , the angle-of-arrival of the multipath signal with respect to the direct signal.

---

<sup>\*</sup> General Electric Company, Syracuse, New York.

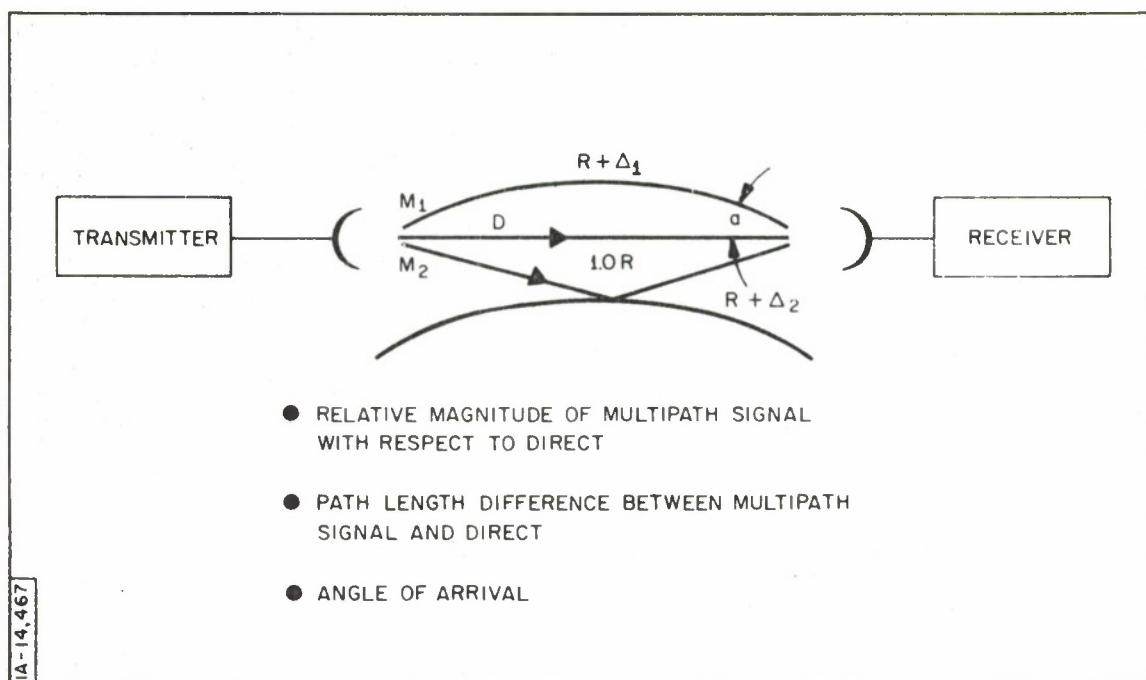


Figure 1. Multipath Characteristics

Several methods may be used to measure multipath propagation characteristics. In the narrow-pulse technique, a transmitter generates radio-frequency pulses with a duration of a few millimicroseconds. Multipath transmission is characterized by the reception of two or more pulses for each transmitted pulse. In the angle-of-arrival technique, a height-finding type of radar antenna with high vertical resolution is scanned in elevation about the normal elevation angle of reception. Multipath transmission is characterized by the reception of significant energy at two or more elevation angles. A third method of measuring multipath transmission is the swept frequency technique.

#### SWEPT FREQUENCY TECHNIQUE

In the swept frequency technique, illustrated in Figure 2, a transmitter is swept in frequency over a wide bandwidth; in our particular case, from 7.0 to 11.0 kilomegacycles. This signal is propagated over the path whose



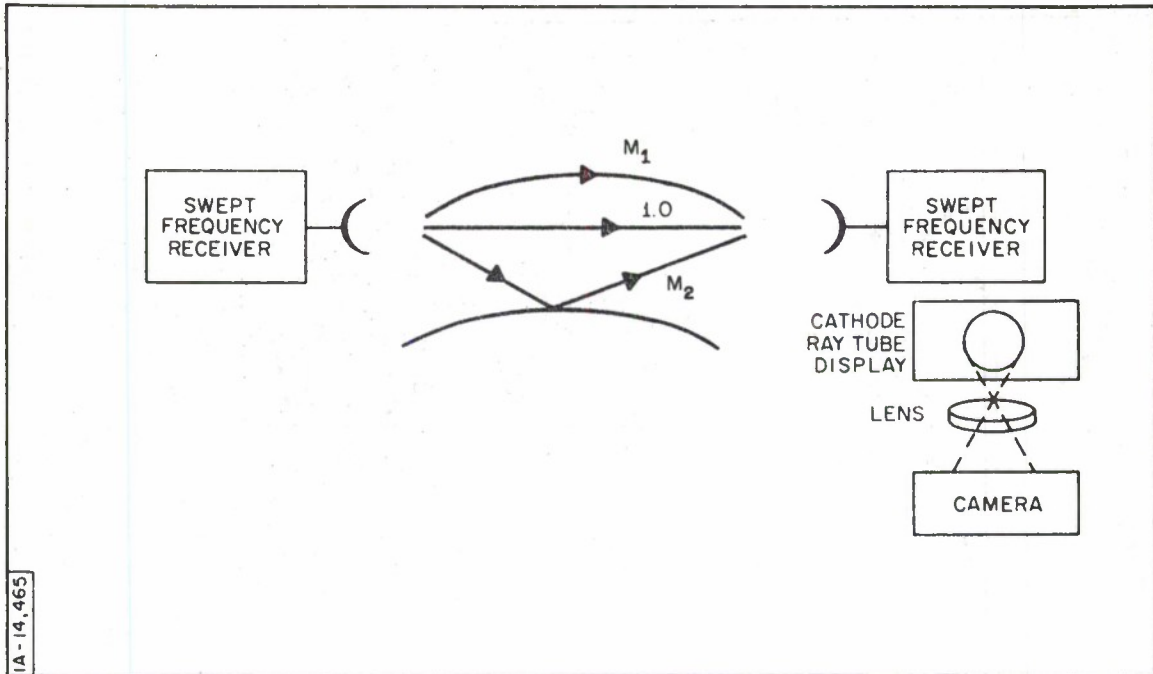


Figure 2. Swept Frequency Measuring Technique

characteristics are to be measured and is received by a swept frequency receiver. The receiver tracks the transmitted signal and displays, on its cathode ray tube, a plot of received amplitude versus received frequency. This is recorded by means of a camera for later analysis. In order to understand the operation of the swept frequency technique, let us consider the vector relationship between the direct and one multipath signal at the receiver. This is illustrated in Figure 3. The direct signal is represented by the large vertical vector drawn from the head of the direct vector. Because of the additional propagation path,  $\Delta$ , of the multipath signal, the multipath vector lags in phase behind the direct vector by an angle  $\theta$  which is given by the formula

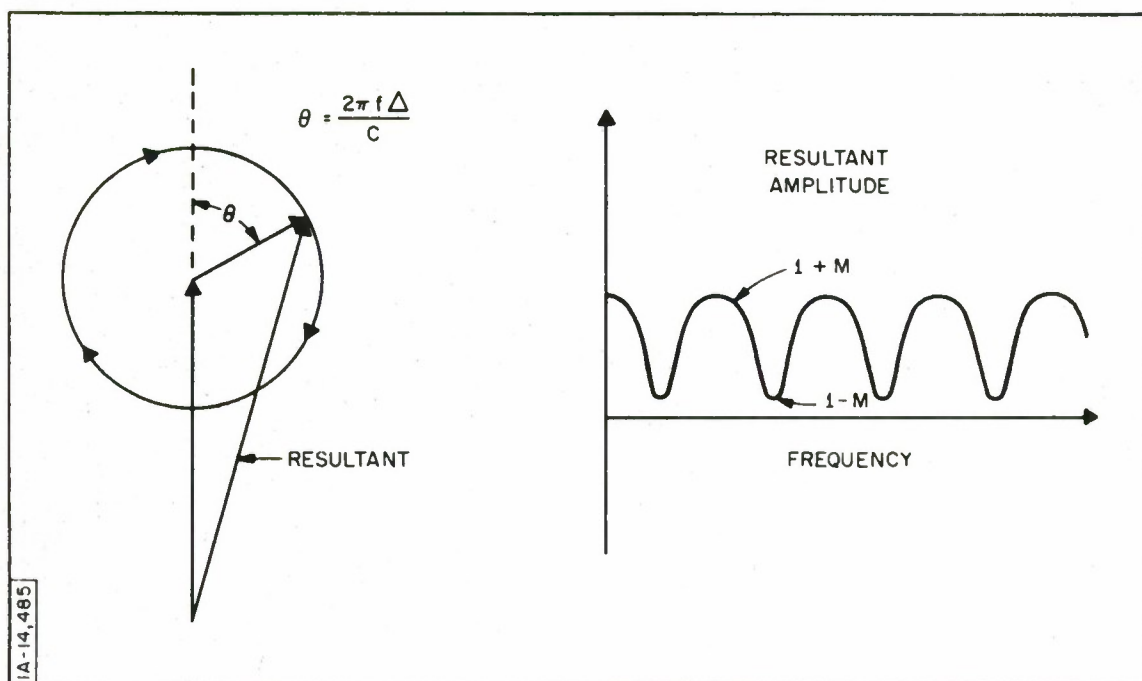


Figure 3. Zero-Degree Phase Reversal Upon Reflection

$\theta = (2\pi f\Delta/C)$ , where  $f$  is the instantaneous frequency and  $C$  is the velocity of light. The resultant of the two vectors is the amplitude of the signal seen by the receiver. From the formula for  $\theta$  it can be seen that, as the frequency is increased, the angle  $\theta$  will increase and the multipath vector will rotate about the direct vector. The resultant amplitude will vary from peak to null in a typical pattern which might be described as a multipath signature.

The peaks will correspond to those times when the multipath and direct vectors are in phase, and the nulls to those times when they are out of phase. By measuring the value of the peak and the null, the relative magnitude of the multipath vector may be calculated. By measuring the frequency separation between nulls, i. e., the frequency shift required to rotate the multipath vector through 360 degrees, the path length difference may be calculated. Figure 3 shows the typical amplitude pattern for a multipath signal which does not

undergo a phase reversal upon reflection. It is characteristic of reflection occurring at angles of incidence smaller than the Brewster angle and of atmospheric-produced multipath. It should be noted that a peak occurs at zero frequency.

Figure 4 is similar to Figure 3 except that a 180-degree phase shift is assumed upon reflection. It is characteristic of reflections occurring at grazing elevation angles above the earth's surface. Because of the phase reversal, a null occurs at zero frequency rather than a peak as in the previous case.

## EQUIPMENT

Figure 5 is a block diagram of the swept frequency transmitter. It consists of a backward wave oscillator which is swept between 7.0 and 11.0 kilomegacycles at a rate of 10 cycles per second by the sawtooth sweep voltage. The resulting radio frequency signal is amplified in a traveling wave tube and transmitted over the path to be measured. A sample of the transmitted power is compared with a reference and the error signal is used to control the amplitude of the backward wave oscillator. Thus, constant power is available at the sampler regardless of the rather violent fluctuation in power produced by the backward wave oscillator and the gain of the traveling wave tube as the frequency is scanned.

Figure 6 is the simplified block diagram of the receiver. It is a super-heterodyne receiver employing an automatic frequency control loop to obtain a 30-megacycle intermediate frequency. The incoming signal is mixed with the local oscillator signal in the broadband balanced mixer. The resultant intermediate frequency signal is amplified with fixed gain and then limited in order to remove any amplitude fluctuation. The limited signal is applied to a frequency discriminator where an error voltage proportional to deviation of

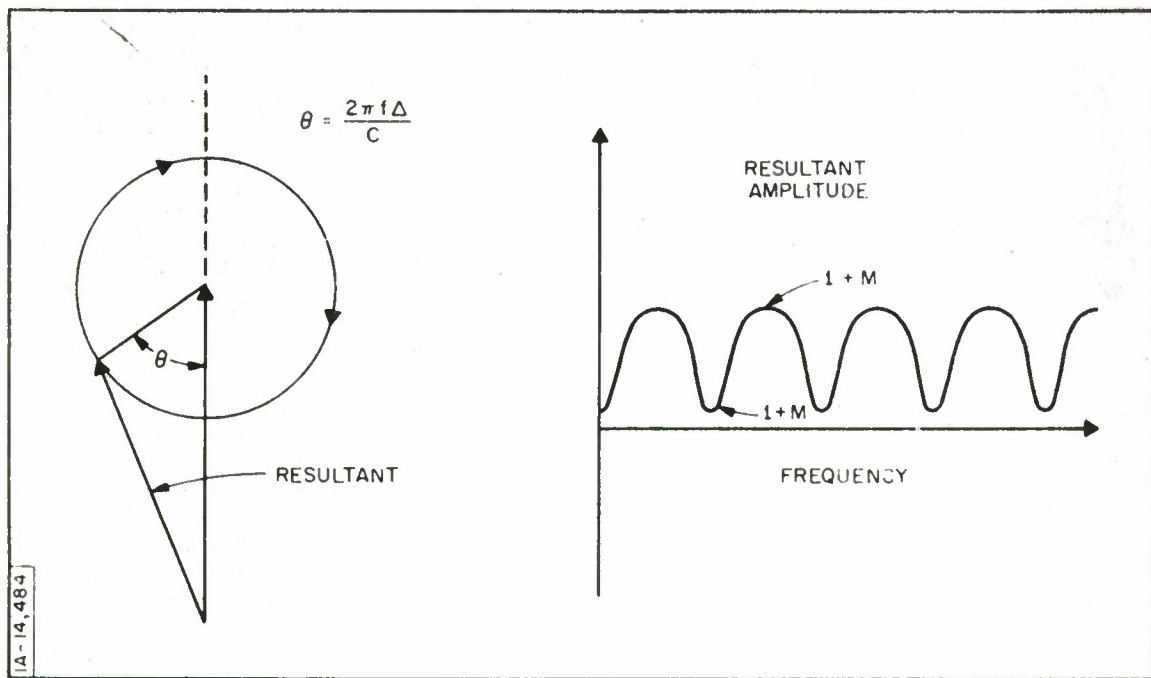


Figure 4. 180-Degree Phase Reversal Upon Reflection

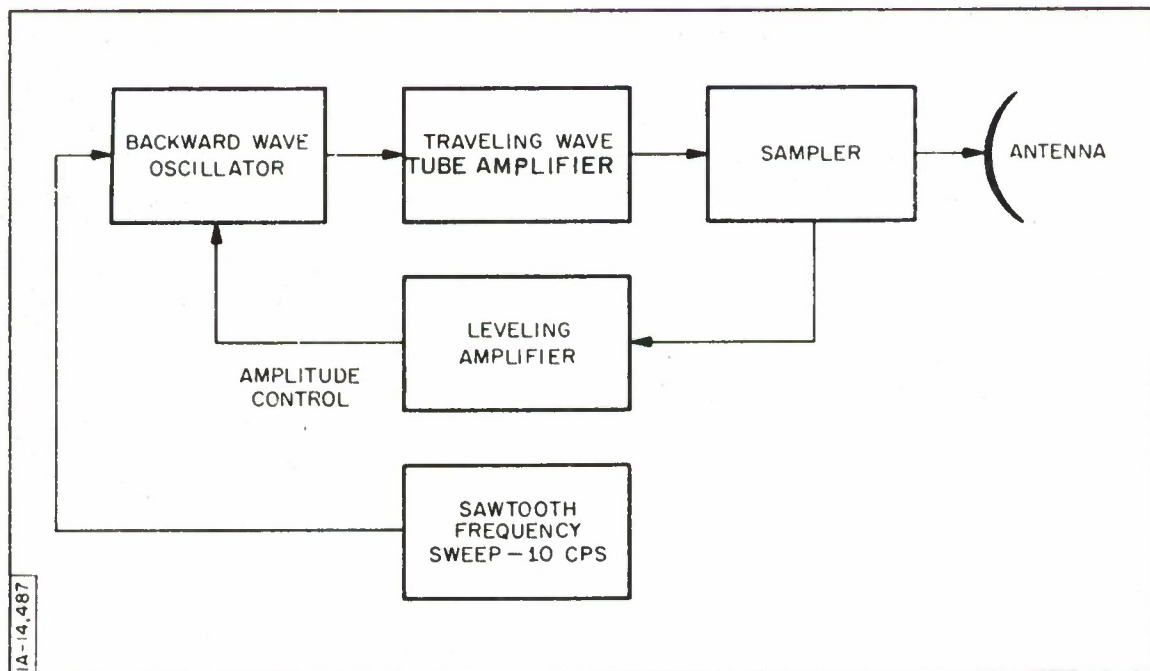


Figure 5. Block Diagram of Swept Frequency Receiver



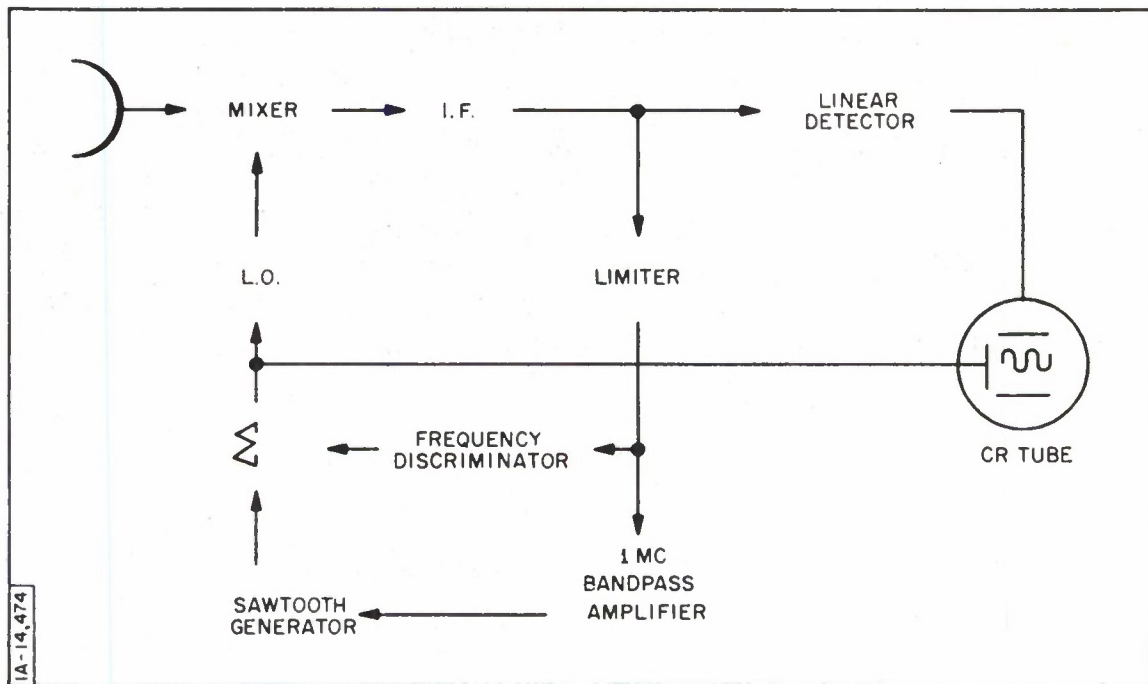


Figure 6. Simplified Block Diagram of Swept Frequency Receiver

the intermediate frequency from 30 megacycles is produced. This error voltage is amplified and applied to the backward wave oscillator helix to control its frequency.

In order to reduce the gain requirements of the frequency-locked loop, an auxiliary sawtooth generator is used to supply the majority of the local oscillator drive voltage. The sawtooth generator is triggered at the beginning of the sweep by a pulse which passes through the 1.0-megacycle bandpass amplifier. This pulse occurs when the transmitted signal is 30 megacycles below the present local oscillator signal. The output of the intermediate frequency amplifier contains the desired amplitude fluctuations. The intermediate frequency signal is detected in a linear detector and applied to the vertical deflection plates of the cathode ray tube. The horizontal deflection voltage is produced by linearizing the backward wave oscillator drive voltage.

The display on the cathode ray tube is then a plot of received signal amplitude versus received signal frequency.

#### ELEUTHERA EXPERIMENT

The purpose of the Eleuthera multipath experiment was to determine the characteristics of overwater multipath transmission. The sweep frequency transmitter was located at an elevation of about 100 feet above sea level. The antenna for the receiver was located about 30 overwater miles away at an elevation of 250 feet above sea level. Some of the results of this experiment are shown in Figures 7, 8, 9 and 10, which were chosen to represent a wide variety of conditions. However, each graph shows a frequency variation of 7 kilomegacycles at the right to 11 kilomegacycles at the left.

Figure 7 represents a multipath signal of relative amplitude of  $M = 0.81$  and a path length difference of  $\Delta = 0.265$  foot. The small ripples on the gross multipath pattern are predominately caused by multipath signals internal to the transmitter and should be neglected.

Figure 8 is typical of the signal received during a poor MISTRAM baseleg operation. The null is extremely deep, representing a multipath vector of about 0.95. The two little pips at the bottom of the null are interfering signals generated at the receiving site. During rapidly changing conditions, the null might change from that of Figure 7 to that of Figure 8 in 14 seconds.

Figure 9 is typical of the relatively rare multiple propagation paths. The figure represents two paths.

Figure 10 is typical of very small values of path length difference approaching the resolution capability of the equipment. It represents a path length difference of only 0.11 foot and a relative magnitude of 0.45.

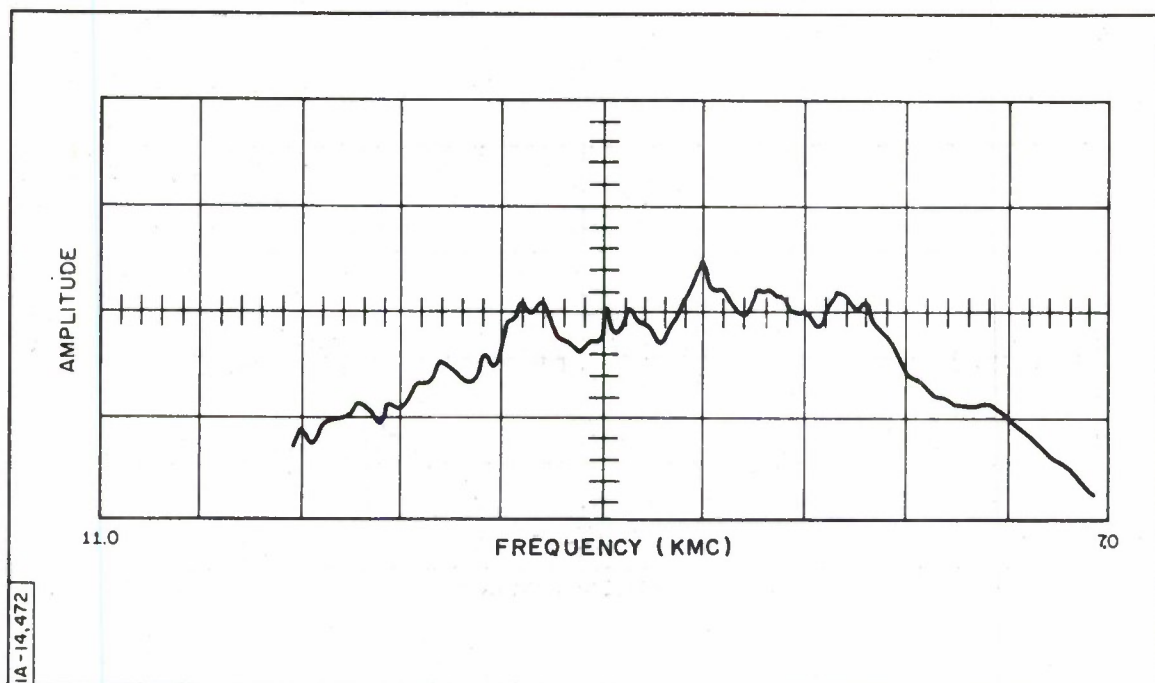


Figure 7. Eleuthra Multipath Experiment Results ( $M = 0.81$ ;  $\Delta = 0.265$ )

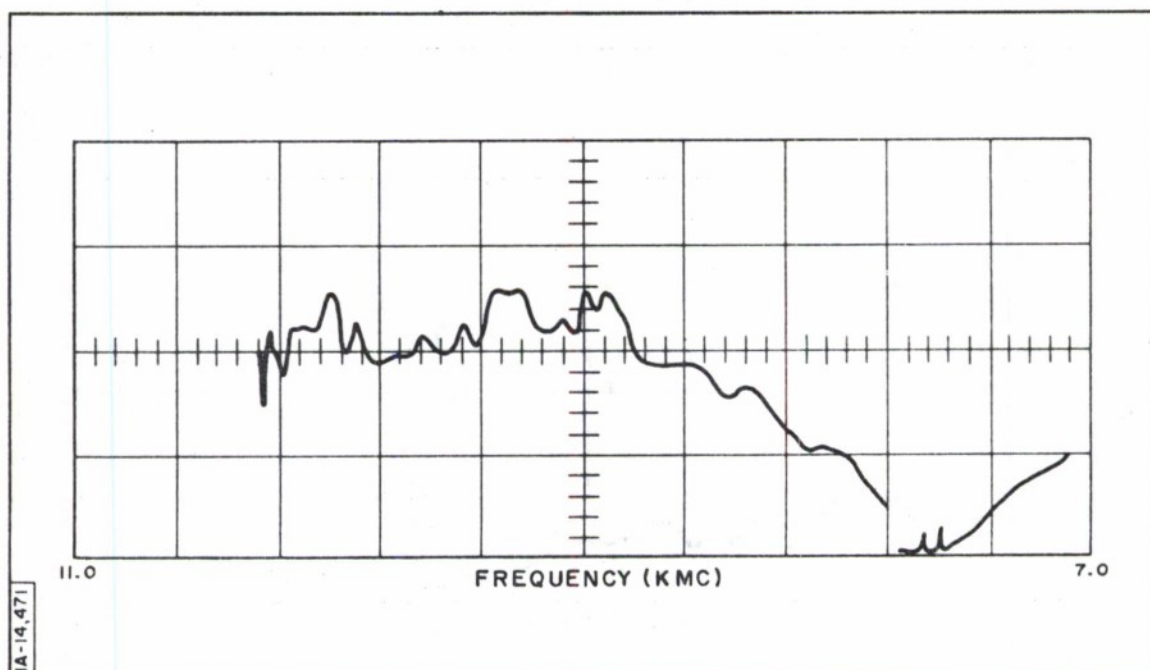


Figure 8. Eleuthra Multipath Experiment Results (Signal Received During Poor MISTRAM Baseleg Operation)

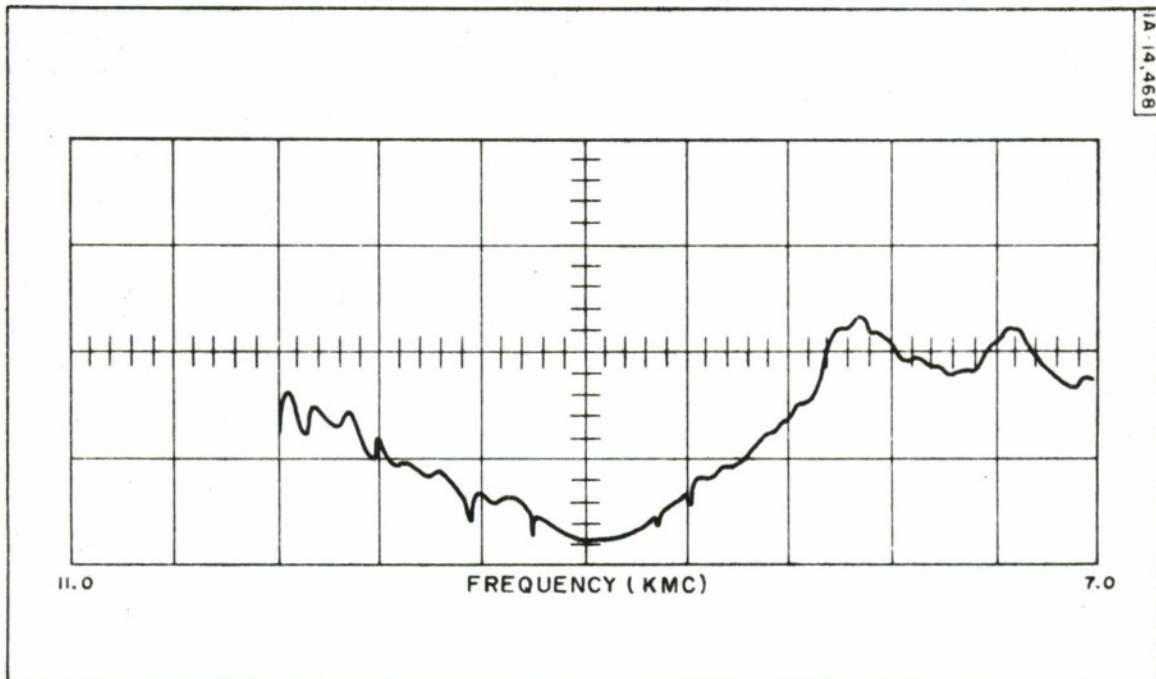


Figure 9. Eleuthra Multipath Experiment Results (Typical Example of Multiple Propagation Paths)

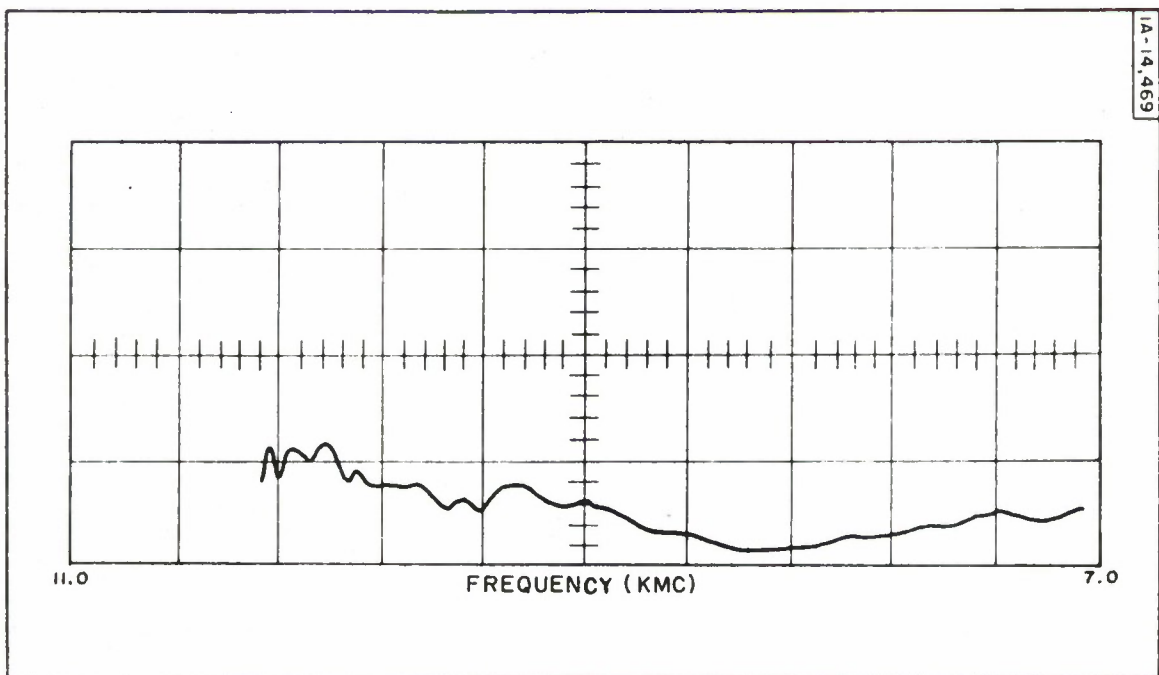


Figure 10. Eleuthra Multipath Experiment Results ( $M = 0.45$ ;  $\Delta = 0.11$ )



A chronological record of the path length difference and relative magnitude of the multipath signal indicated that the path length difference varied between about 0.1 and 0.4 feet. This is up to six times larger than the theoretically calculated path length difference, utilizing the  $4/3$  earth radius model. The relative magnitude of the multipath vector varied between 0.3 and approximately unity (a value approaching unity can represent infinite attenuation and is impossible to measure accurately with the equipment available). Reports of 20-to-40-decibel fades are fairly common on overwater paths, and indicate that the multipath vector may be significantly larger than the theoretical value of  $M = 0.52$  calculated from a consideration of the divergence produced by reflection from a spherical reflection surface.

#### APPLICATION

The results of this test may be readily applied in the optimization of a frequency-diversity overwater communication link, shown in Figure 11. Two frequencies are propagated over the multipath-plagued environment in the expectation that both signals will not simultaneously fade sufficiently to produce a complete system dropout.

As shown in Figure 12, the multipath-plagued propagation medium is inherently frequency-sensitive. It becomes readily apparent that to obtain the maximum diversity between channels, the two channels should be separated in frequency by an amount which will cause one signal to be in a null while the other is at a peak of the amplitude pattern. Under these conditions, shifts, expansion, or contraction of the amplitude pattern due to reasonable atmospheric changes will be incapable of producing simultaneous fading on both channels. This simple observation may be readily put on a more quantitative basis in order that suitable design numbers can be generated.

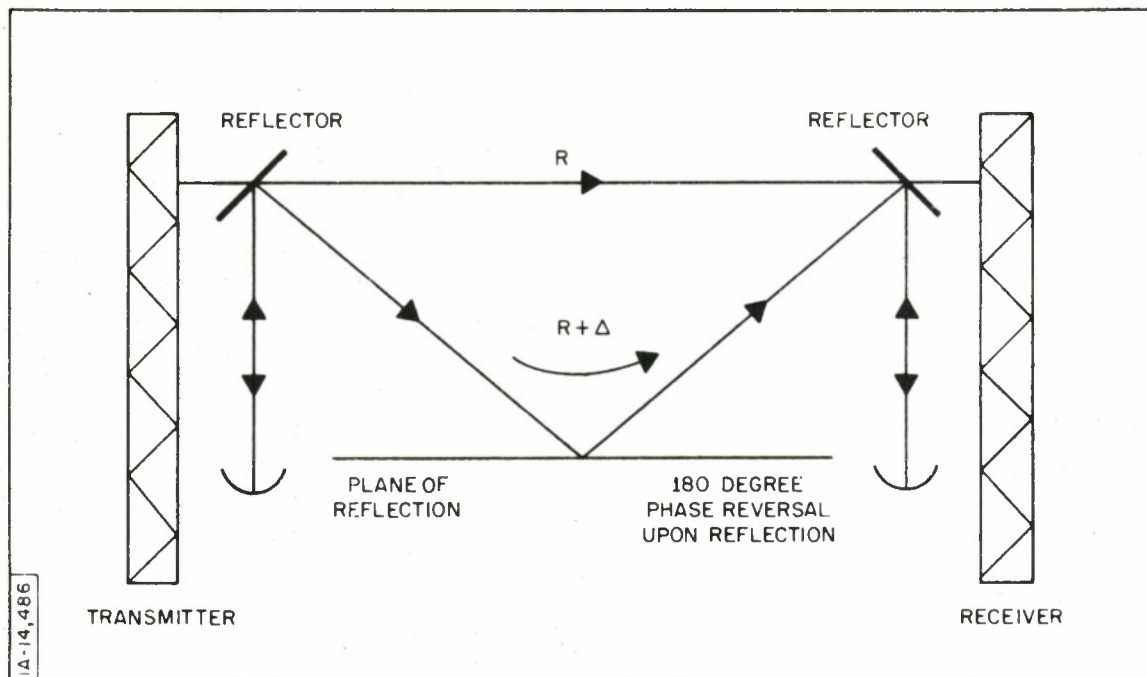


Figure 11. Frequency-Diversity Overwater Communication Link

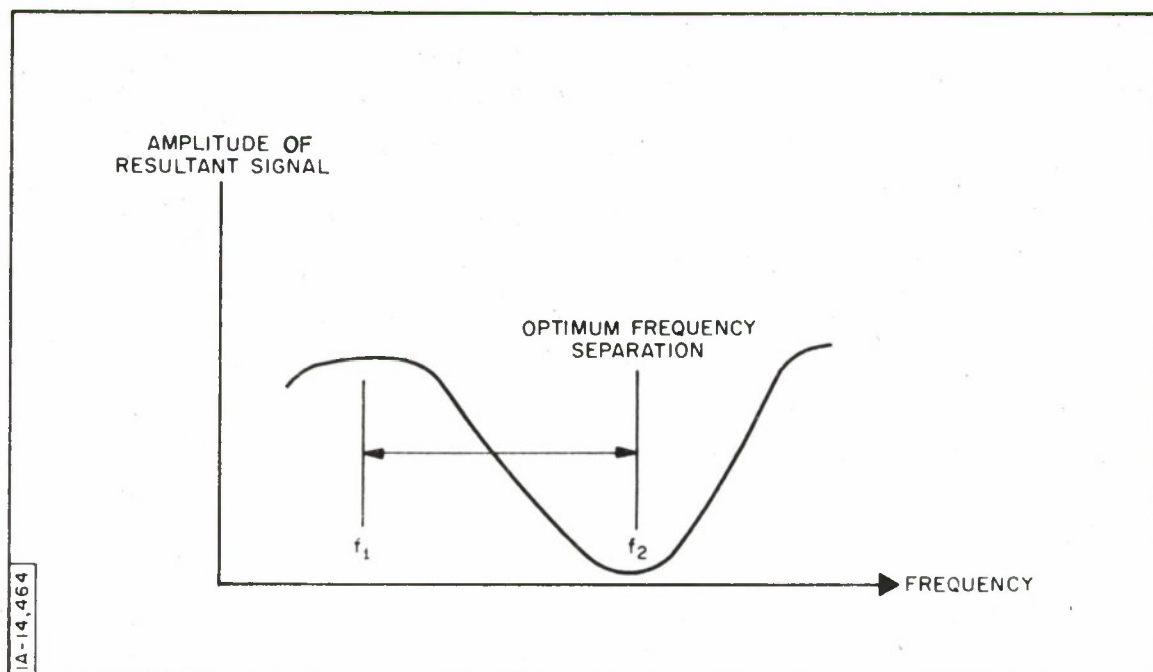


Figure 12. Typical Amplitude Versus Frequency Display

Let us now look at the same problem in terms of,  $\Delta$ , the path length difference. Figure 13 is a plot of the received amplitude of two signals of frequency,  $f_1$  and  $f_2$ , separated by 200 megacycles as a function of  $\Delta$ . It can be seen that for very low values of  $\Delta$ , the fading occurs almost simultaneously on both channels, but for higher values of  $\Delta$ , the fading of one

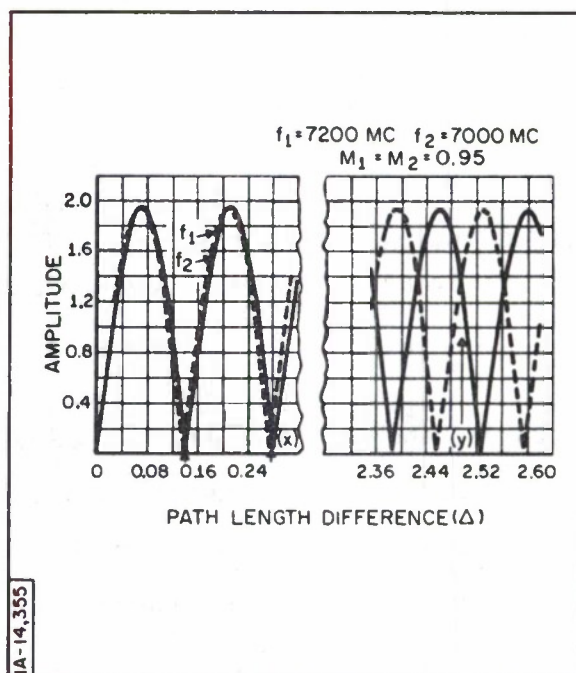


Figure 13. Signal Level Versus Path Length Difference

channel is interleaved between that of the other. This interleaving condition is considered to be the optimum condition. Simultaneous fading cannot occur in spite of rather violent variations in  $\Delta$ , and the integrity of the communication system will be maintained.

Let us now examine the vector diagrams of the received signals for our frequency diversity communication link as shown in Figure 14. The signals received over the direct path at each of the frequencies are represented by the

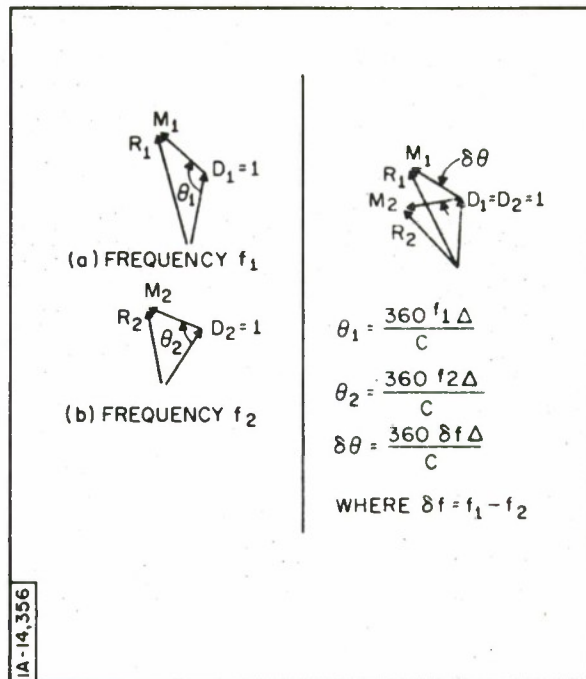


Figure 14. Vector Diagrams of Received Signals

vectors  $D_1$  and  $D_2$ , and are assumed to be of unity magnitude. There is a phase difference between the two direct vectors, produced by the difference in the direct-signal propagation range when expressed in terms of wavelengths. This is, however, of no significance in the following discussion.

The multipath vectors are labeled  $M_1$  and  $M_2$ , and are delayed in phase with respect to the related direct vector by the angles,  $\theta_1$  and  $\theta_2$ , due to the additional propagation distance  $\Delta$ . As expressed by the familiar formula at the lower right of Figure 14. The resultant vectors are, of course, given by the vector addition of the direct and multipath vectors in each case. The vector diagram to the right is obtained from the two on the left by superimposing the two direct-signal vectors. Of importance in Figure 14 is the differential angle  $\delta\theta$  between the two multipath vectors since it determines the "phase" relationship between the two fading patterns.



Now let us examine how these vectors behave as  $\Delta$ , the path difference changes. Since  $f_1$  and  $f_2$  are both much greater than  $\delta f = f_1 - f_2$ , the frequency difference between channels, it can be seen that the predominant effect of a change in  $\Delta$  will be to simultaneously rotate both multipath vectors about the direct vectors. If the differential frequency is small, the two multipath vectors will be close together and deep simultaneous fades may occur when the multipath vectors have rotated so as to be out-of-phase with their direct vectors. If, on the other hand, the frequency separation is large enough so that the two multipath vectors are 180 degrees apart, rotation of the multipath vectors will not produce deep simultaneous fades.

The maximum simultaneous fade vector relationship for insufficient frequency separation is shown on the left side of Figure 15. The vector relationship for optimum frequency separation is shown on the right side.

Now that we have determined the optimum multipath vector relationship, it would be desirable to determine the fading which is likely to be encountered for a typical system as the pathlength difference varies. Figure 16 is a plot of the maximum simultaneous multipath attenuation versus the (path length difference) (differential frequency) product. It can be seen that the optimum system is obtained for a product of about  $50 \times 10^7$ . For the path measured, a frequency separation of about 2 kilomegacycles would produce optimum results, with an average path length difference of 0.25 foot. Typical variation in path length of  $\pm 0.15$  foot will then produce a maximum attenuation of about 5 decibels.

#### PROPAGATION NOISE EFFECTS ON RADARS AT LOW ELEVATION ANGLES

In the radio tracking or guidance of a missile, the velocity parameters are of the utmost importance in accurately predicting the impact zone or the orbit of injection. If accurate velocity data can be obtained at low elevation

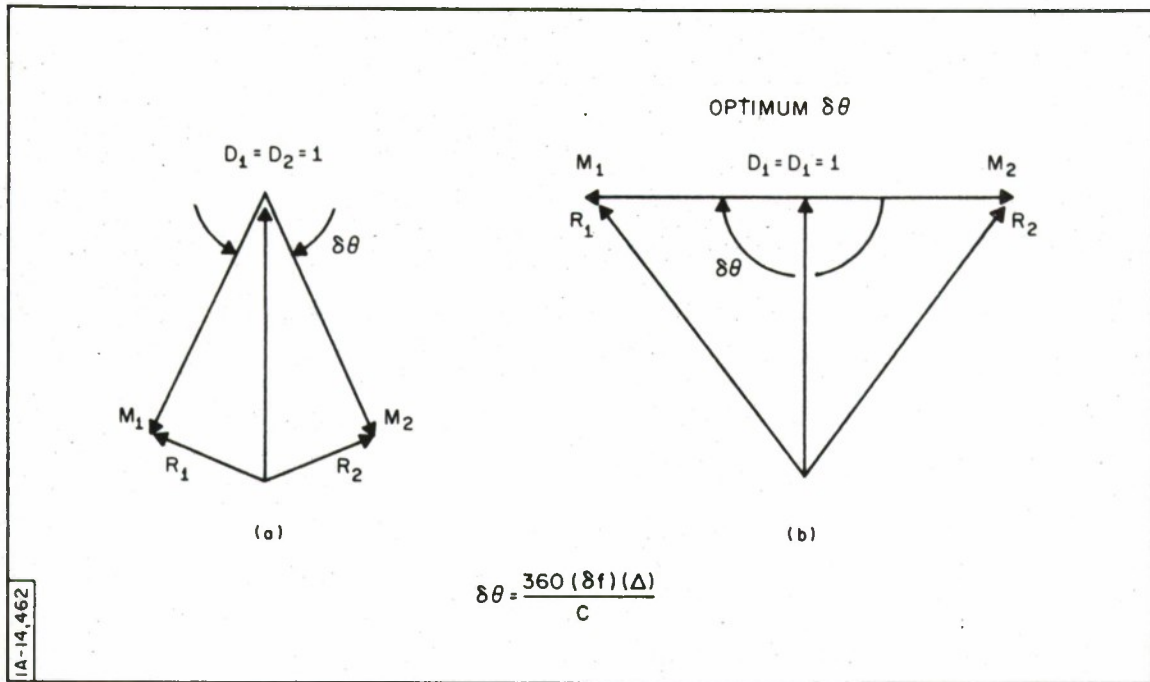


Figure 15. Maximum Simultaneous Fade Vector Relationship

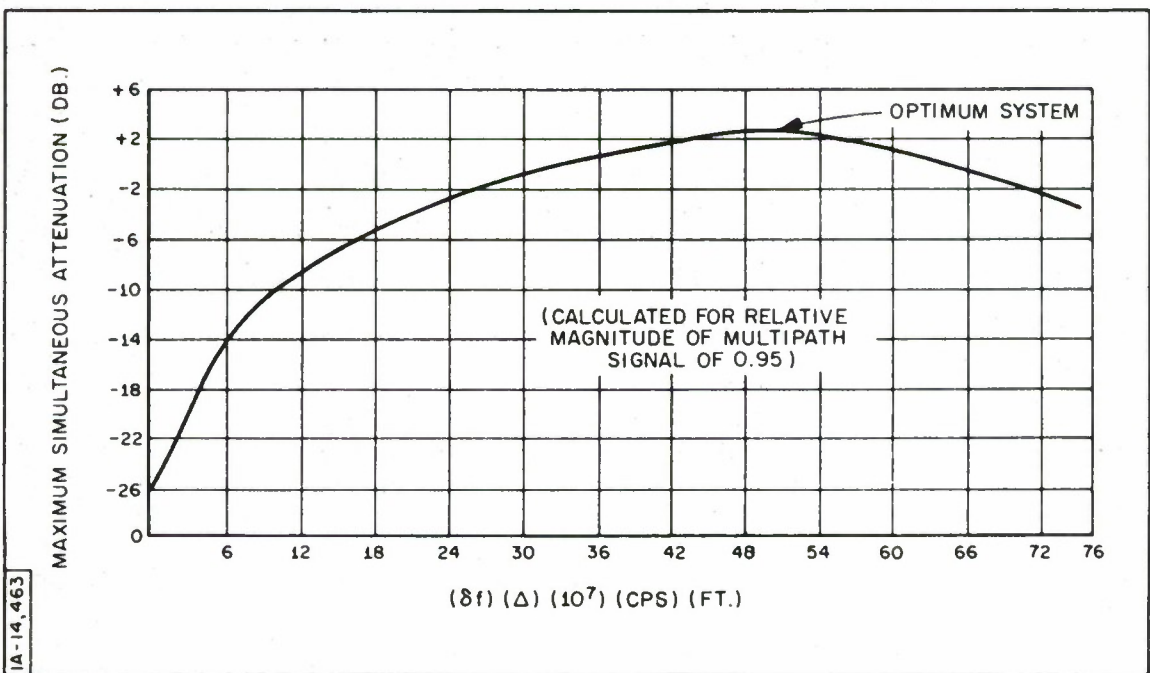


Figure 16. Minimum Signal Level Versus (Differential Frequency) (Path Length Difference) Product

angles with respect to the launch site, desirable trade-offs may be realized in terms of increased payload, less fuel load, increased accuracy of guidance or orbit determination. However, it has been noted that at low elevation angles, the accuracy of a given guidance or tracking system is often degraded because of the increase in system noise output. This noise is visible on both precision tracking radars and interferometer systems and is of concern because it contains noise components of sufficiently low frequency that effective filtering may not be used to discriminate between it and missile motion.

The noise to be discussed in this paper is produced by propagation through the atmosphere at a low elevation angle. It caused a great deal of concern and interest several years ago when a large increase in the lateral rate system noise output was observed on the G. E. Mod III missile guidance system. It was particularly noticeable on the "Lateral Rate System" and has often been referred to as: "Lateral Rate Noise."

Several characteristics of this noise are known. It is produced by propagation through the atmosphere. It is visible only at low elevation angles of, let us say, less than 15 degrees. It is roughly proportional to the cosecant of the elevation angle to some power  $n$  where  $n$  varies between 0.5 and 2.3 and the elevation angle is greater than about 2 degrees. It has a power density spectrum which contains very low frequencies; it peaks at about 0.2 cycle per second and then exponentially tapers at higher frequencies. It is capable of producing both amplitude and phase modulation of the incoming signal. The magnitude of the noise is unpredictable and may vary by a 10:1 ratio from one missile test to another.

Figure 17 shows the typical increase in lateral rate system noise output as the elevation angle is decreased for four missiles on which the noise was particularly prominent.

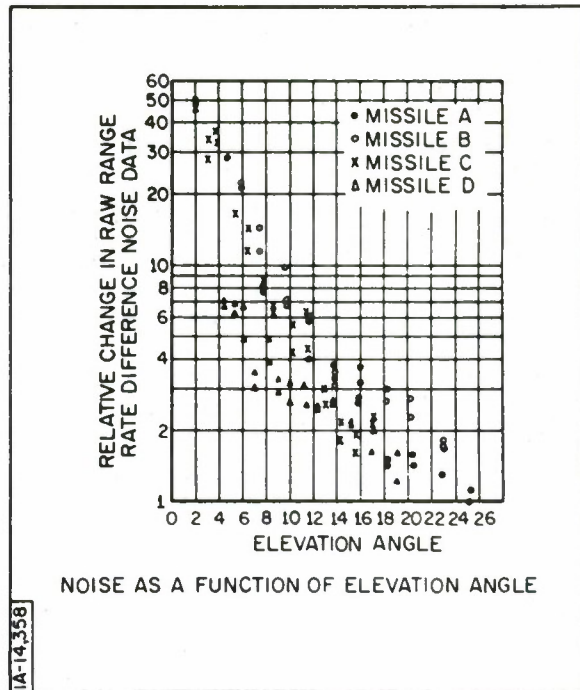


Figure 17. Typical Increase in Lateral Rate System

Figure 18 illustrates the characteristics of this propagation noise. It represents a small selected portion of the lateral rate output data near the end of a missile flight. A straight line drawn through the center of the noise points would represent the actual missile movement. Perturbations about this line represent lateral rate noise. The low frequency cyclical nature of this noise should be noted, since it is of primary concern. In this particular record, it has a period of about 4 seconds.

Several theories have been advanced to explain the cause of this noise. In this paper we will consider one theory, namely, that it is a noise produced by a multipath propagation environment which is produced by atmospheric anomalies.

The existence of an atmospheric-produced multipath has been studied before. In the 1950s, members of the Bell Telephone Laboratories found that multipath



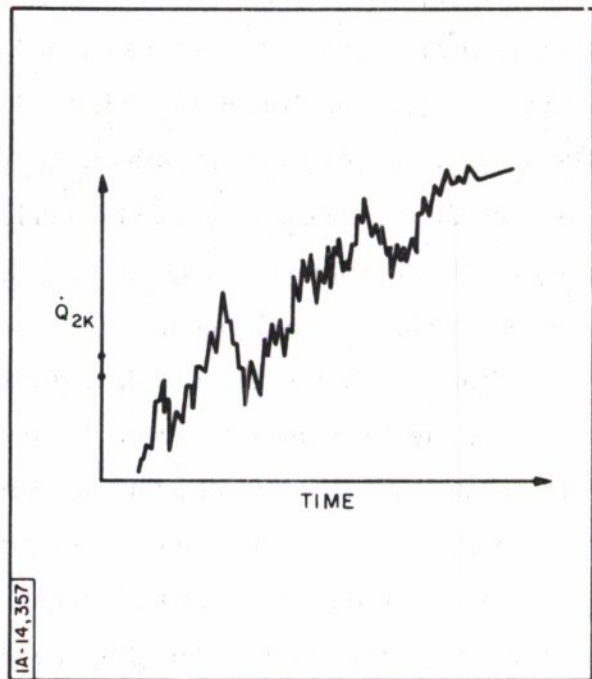


Figure 18. Lateral Rate Noise

transmission was, on occasions, capable of producing severe fading on their point-to-point microwave system. They measured path length differences of up to 10 feet for a 30-mile path and a relative amplitude of the multipath signal equal to, and at times greater than, the direct signal.

In addition to the Bell experiments other experimental data is available. For example, it is rather common knowledge that a radar site when tracking a single target at low elevation angles is, at times, capable of seeing multiple targets under certain meteorological conditions. An interesting experiment in this area was performed by Mr. Wong, who was working at Wright-Patterson at the time. By means of an aircraft, he collected vertical index of refraction records of the atmosphere. He utilized these records of the atmosphere in a ray tracking analog computer program to calculate the ray paths which would be taken by a signal from a ground station to an airborne receiver. His results

indicated that atmospheric index of refraction anomalies were capable of causing ray paths at the target for two rays which originated at slightly different elevation angles. Both the Telephone and the Wong experiments indicate the possible existence of atmospheric multipath as the possible cause for lateral rate noise. The theory can be checked, at least crudely, by postulating a multipath model and seeing if it is capable of explaining experimental data. The model must be capable of producing amplitude and phase perturbations, which is certainly possible with a multipath model. In addition, there should, at least for simple cases, be some correlation between the amplitude and phase data. As a matter of fact, if the multipath model could be applied to only one antenna of an interferometer system at a time, and if the multipath could be approximated by the simplest model of only one multipath signal and direct signal, a direct-amplitude phase correlation should be possible. Before proceeding along this line of reasoning further, let us go back one step and examine the interferometer system which was used to gather the lateral rate data.

Figure 19 is a simplified block diagram of the interferometer system to be considered. The signal from the missile is propagated to two receiving stations separated by 2000 feet. The outputs from the two receiving stations are mixed together to obtain their phase difference. This phase difference is multiplied by 256 in order to increase the sensitivity of the system. The number of cycles of the phase multiplied signal occurring within a 0.1-second gate is counted in the lateral rate counter. The number in the counter is then a measure of the rate of change of differential phase which has occurred during the 0.1-second counting interval.

In the absence of lateral rate noise, this number may be related to the rate of change of path length difference between the missile and each of the receiving stations. The presence of a multipath signal whose magnitude

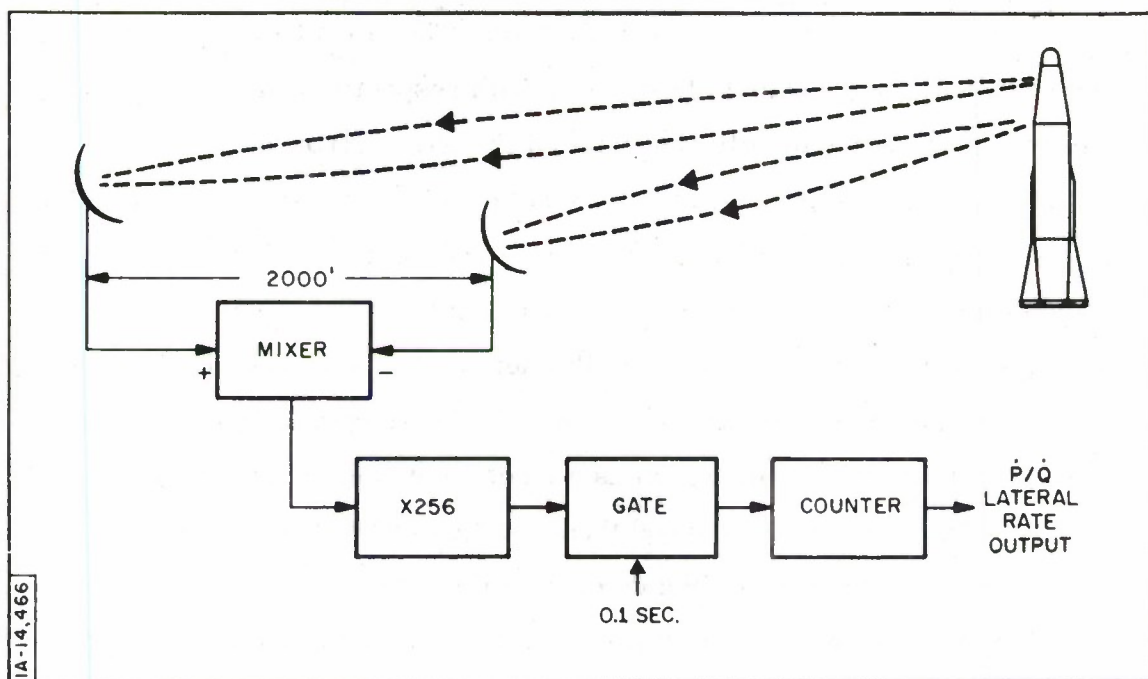


Figure 19. Lateral Rate System

and relative phase vary as a function of time serves to phase-modulate the received signal as a function of time, and produces a noise output.

Perhaps the most conclusive reason for suspecting that lateral rate noise is produced by a multipath mechanism is in the correlation which is, at times, possible between the received signal strength, as represented by the automatic gain control voltage, and the lateral rate output, labeled  $\dot{P}/\dot{Q}$ . Assume a simple example of multipath transmission and derive the relationship which must exist between the automatic gain control voltage and  $\dot{Q}$  lateral rate output, and that the multipath affects only one receiving station and that it is of the simplest variety consisting of only one direct signal and one multipath signal. If it is further assumed that the multipath vector rotates linearly with time, a 90-degree phase relationship between the amplitude of the resultant received signal strength and the phase error will be noted.



This is plotted in the top of Figure 20. The lateral rate system is sensitive to the rate of change of phase error with respect to time, and the  $\dot{Q}$  error may then be obtained by differentiation of the phase error with respect to time. The  $\dot{Q}$  error signal will then be in-phase or out-of-phase with respect to the automatic gain control voltage, depending upon which receiving station is assumed to be producing the noise. A similar line of reasoning may be employed to derive the  $\dot{Q}$  error from the automatic gain control fluctuations. This reasoning takes the following steps. If the automatic gain control voltage or resultant amplitude fluctuation as a function of time is known, the multipath vector configuration which caused these fluctuations can be estimated. From this vector configuration we can determine the phase error as a function of time and this in turn can be differentiated to produce the lateral rate error as a function of time.

These steps were taken in the analysis of one sample of noise as illustrated in Figure 21. The sample was chosen at a time when one receiving station automatic gain control voltage was relatively constant, but the other was quite noisy. The vector diagram corresponding to the east automatic gain control voltage was constructed, and the resultant phase error was plotted as a function of time. The phase error curve was differentiated to produce the calculated signal.

The comparison between the actual signal and the derived signal using the multipath model is shown in Figure 22. It can be seen that there is rather remarkable agreement. This same process was repeated for other portions of the lateral rate noise record but without the high degree of correlation noted here — perhaps because the model was too simple.

One other type of automatic gain control  $-\dot{P}/\dot{Q}$  correlation has been noted. From the simple multipath model it can be seen that the maximum rate of



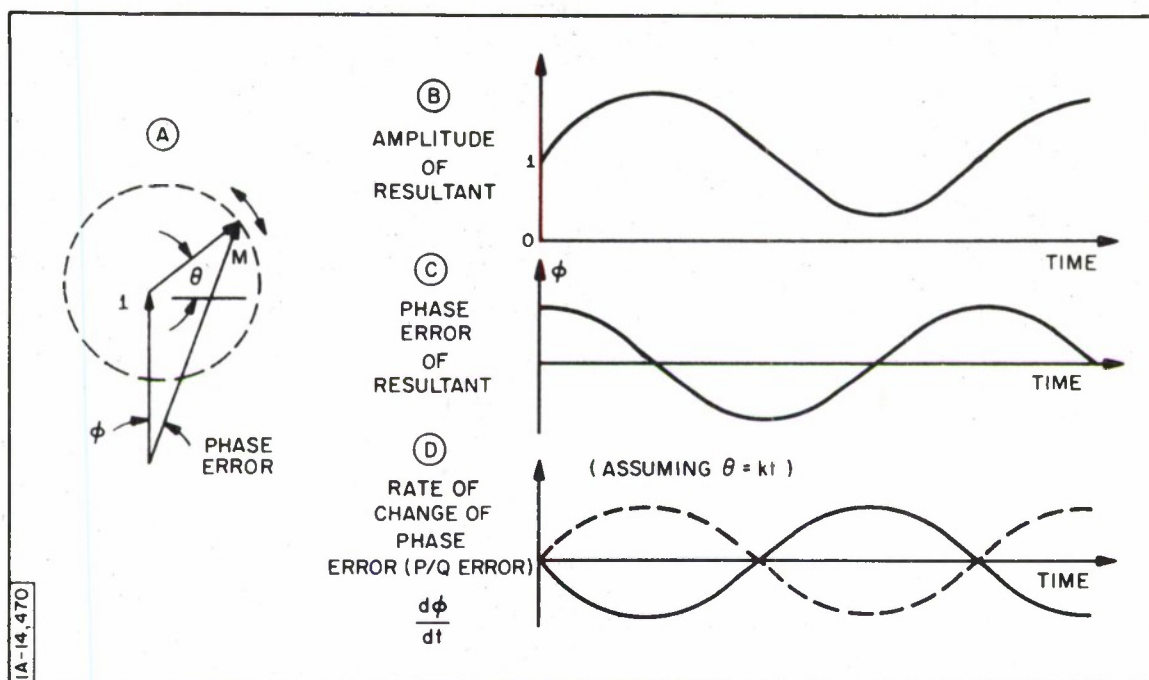
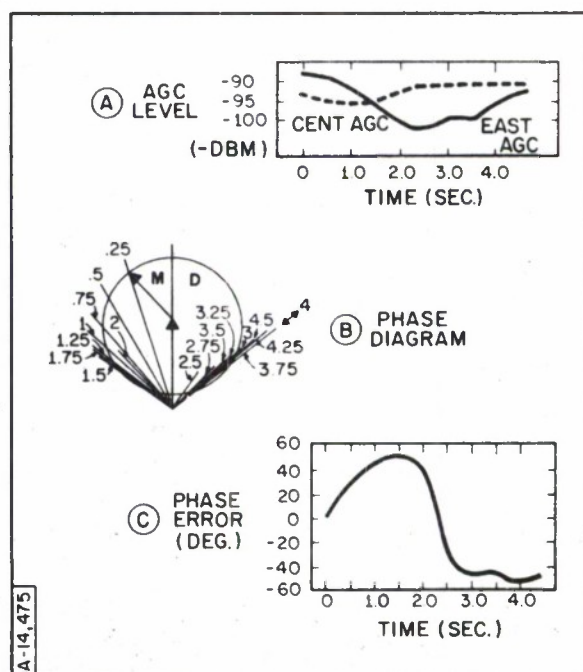
Figure 20. Calculation of  $\dot{P}/\dot{Q}$  Error For Linearly Varying Multipath Phase Error

Figure 21.  $\dot{P}/\dot{Q}$  Error -  $\dot{P}/\dot{Q}$  AGC Correlation

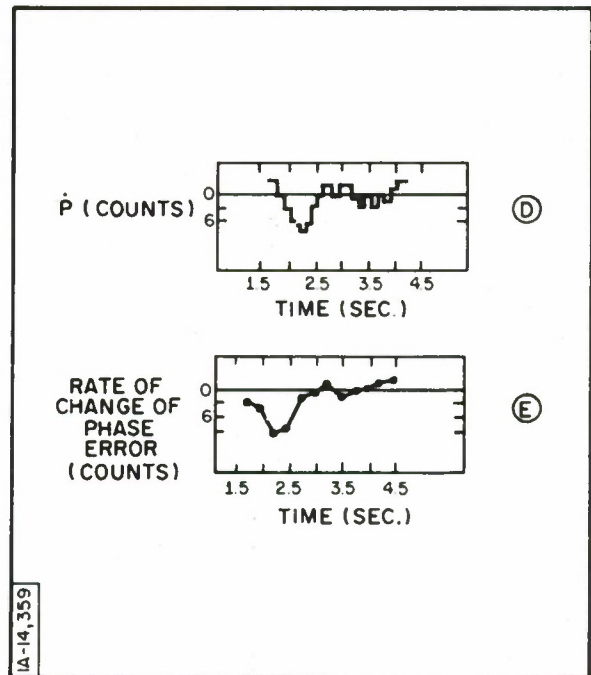


Figure 22.  $\dot{P}/\dot{Q}$  Error -  $\dot{P}/\dot{Q}$  AGC Correlation

change of phase error will occur at the time when nulls occur in the received signal strength. In another missile test which produced large propagation noise, the peaks of this noise with nulls in the automatic gain control record were correlated with good results.

In order to obtain a better quantitative understanding of the "multipath propagation noise" phenomena, General Electric is proposing that an atmospheric multipath test be conducted. The objectives of this test will be to confirm that the noise is produced by multipath, to obtain a valid real-time method of measuring the magnitude to be expected on a missile test; and to measure atmospheric multipath characteristics so that the performance of equipment in this environment be predicted.

The basic concepts of the proposed atmospheric multipath test are shown in Figure 23. A swept frequency transmitter is located in a high-performance

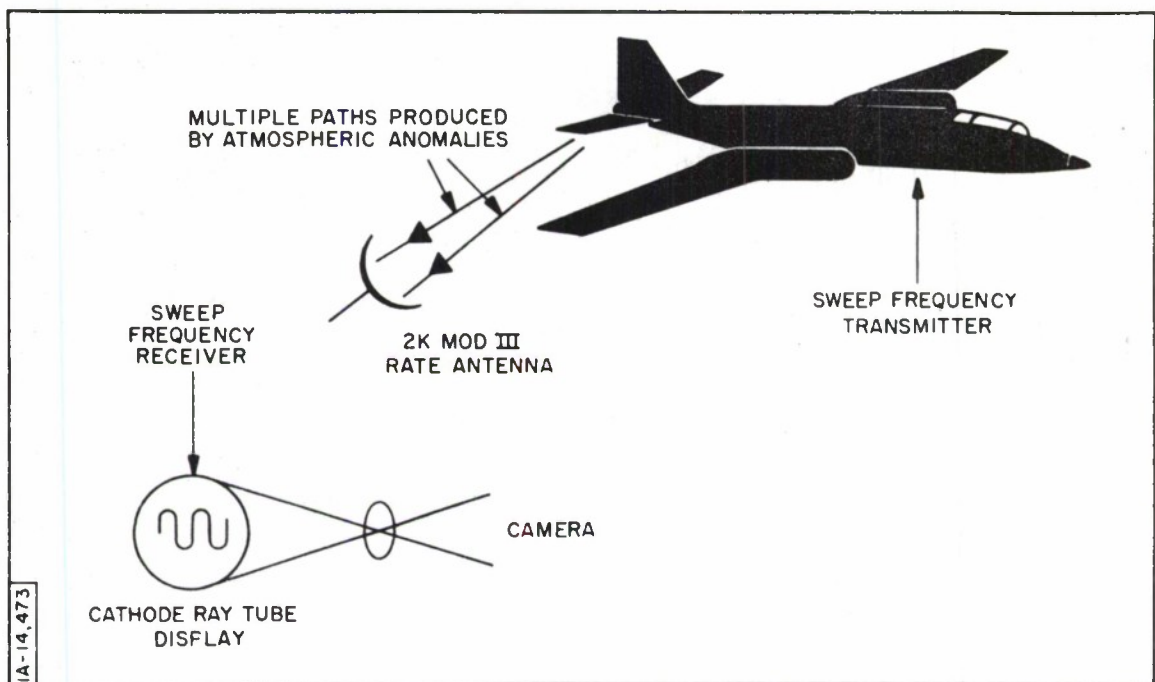


Figure 23. Proposed Atmospheric Multipath Test

aircraft which may be flown above the majority of the atmosphere to be measured. The signal which has been propagated through the medium to be measured is received by a swept frequency receiver on the ground, and the resultant amplitude versus frequency is displayed on a cathode ray tube.

It is hoped that the results of a test of this nature will permit determining the extent of which lateral rate noise is caused by multipath will provide a method of predicting the magnitude of the noise likely to be encountered before a missile launch, will allow atmospheric multipath's characteristics to be measured and, hopefully, will provide information about ways to minimize or circumvent the problem.

# THE BALLISTIC RESEARCH LABORATORIES' PROPAGATION RANGE

George J. Stiles \*

## INTRODUCTION

Measurements of the effects of the atmosphere on the propagation of light have been conducted at the Ballistic Research Laboratories since 1955. Most of the measurements have been obtained by means of horizontal optical paths within about 10 feet of the surface of the earth. The early measurements were made at night, but an examination of the meteorology of the problem has shown that the influence of the sun causes a great difference between daytime and nighttime characteristics of the optical path. Recent measurements have, therefore, been made in the daytime.

As a ray of light is propagated through the atmosphere, it is deviated by refraction and diffraction, which are caused by variations in the index of refraction of the air. It can be shown that the principal cause of the variations in index of refraction is caused by temperature variations. At optical wavelengths, the variation caused by water vapor and pressure can be shown to be negligible.

The application of meteorology in the prediction of the qualitative properties of temperature variations is discussed in the next section of this paper. The section "Optical Measurements." describes an experiment which illustrates a relationship between a physical measurement of the atmosphere and the effects of turbulence on a narrow beam of light. The final portion contains a description of the Ballistic Research Laboratories Electromagnetic Propagation Range.

---

\*Ballistic Research Laboratories, Aberdeen Proving Ground, Maryland.



## METEOROLOGY

Air is heated by absorbing sunlight or by sunlight absorbed by the surface of the earth. \* In the lower atmosphere, the latter process is dominant. One of the first considerations thus is how the temperature of the surface is determined. For simplicity, assume that the boundary between the atmosphere and the earth is of negligible thickness. This boundary will have a temperature which is determined by an inward heat flux from the sun and sky and four outward fluxes of heat: black-body radiation, heat conducted into the soil, heat used in evaporating water from the soil, and heat removed by the turbulent air.

The flux received by the surface comes from both the sun and the sky, and is determined by the reflectivity of the surface. The amount of flux received from the sun depends on its position in the sky and on the condition of the atmosphere. When clouds are present, a large percentage of the solar radiation is scattered into space, and the flux at the surface is reduced. Under these conditions, the reduced solar flux is augmented by black-body radiation from the lower side of the clouds, resulting in an increase in the relative amount of long-wave radiation received at the surface. The absorbed flux will then depend on the reflectance of the surface as a function of wavelength.

The reflectance of the surface depends on the material of which it is composed. Snow, for instance, may reflect nearly all of the radiation received from the sun at visual wavelengths, while asphalt will absorb nearly all of the radiation received from the sun, sky, and clouds. It is clear that the reflectance of the surface plays an important part in the heat flux balance at the surface of the earth.

---

\* This discussion is based principally on the excellent book cited as Reference [1].

The inward flux is absorbed by the surface and distributed among the outward fluxes. Figure 1 (from Reference [1] ) illustrates the heat exchange at

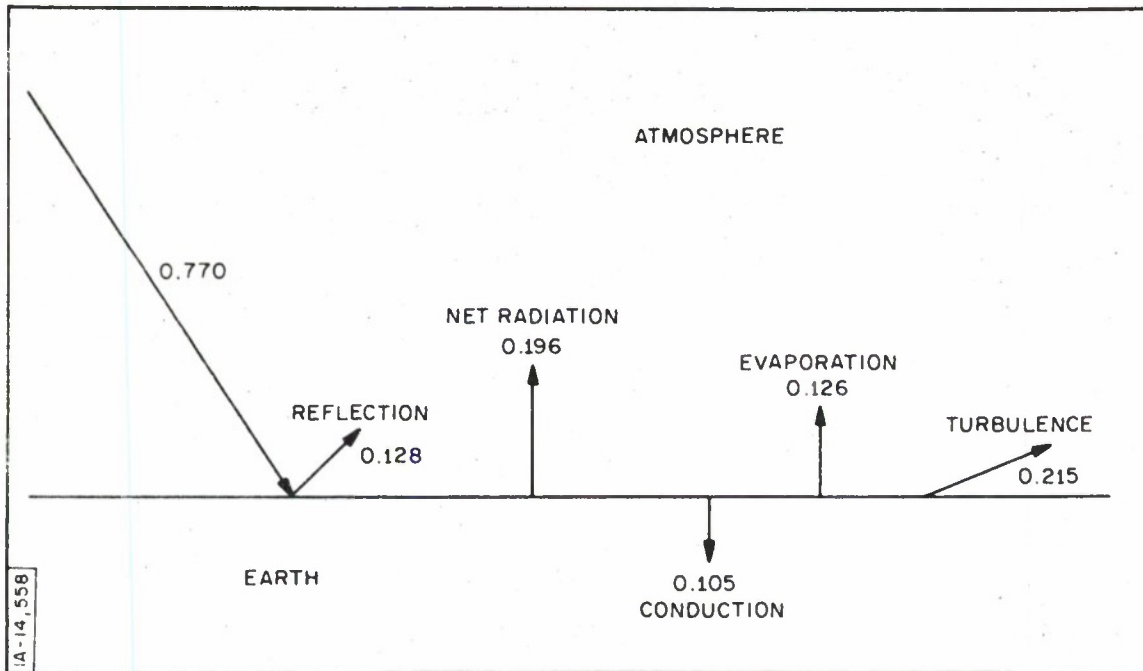


Figure 1. Heat Exchange at the Surface of the Earth in Gram-Calories per Square Centimeter per Minute (From Meteorology; see Reference [1].)

surface of the earth. It indicates that the four fluxes (considered separately in the following paragraphs) which remove heat from the surface are of approximately the same magnitude, and, in general, none of them can be neglected. The measurements were taken over a grassy field on a clear spring day in England shortly after noon.

Body-black radiation depends on the surface temperature and the emissivity of the surface. On a clear day, the surface temperature will rise to a maximum shortly after noon and then decrease. Since the emissivity of real surfaces is nearly constant with respect to changes in temperature and wavelength, the outgoing radiation is given by the Stefan-Boltzmann law.

The flux of heat into the soil depends on the thermal conductivity of the soil and its temperature distribution as a function of depth below the surface. On a clear day, there is a large downward flux in the morning, which decreases at midday, and reverses its direction in the late afternoon when the surface temperature decreases. The heat reaching the surface at night is primarily radiated to the sky.

The heat flux expended in evaporating water from the soil is limited by the rate at which water can reach the surface and the rate at which the atmosphere can remove it. The flow of water upward through the soil depends on the type of soil. Sandy soil can conduct water much more readily than can more dense soils. The water vapor can be transported away from the surface by convection resulting from a high surface temperature or by wind.

The heat removed by turbulence depends on the wind and the roughness of the surface, as well as the surface temperature. The turbulence of the wind, such as may be caused by a rough surface, has an important effect on removing heat.

The result of the balance of the heat fluxes is the determination of the surface temperature. The thin layer of air in contact with the surface is either heated or cooled by conduction from the surface. During the daytime, the air is usually warmed, and at night, it is usually cooled. Only the daytime case is considered.

The air in contact with the surface will be heated to a temperature determined by the air temperature, the surface temperature, and the length of time during which the air is in contact with the surface. If there is no wind, the time of heating will be greater, and the air will be heated to a higher temperature. The thickness of the layer has been estimated to be of the order of 1 centimeter over a surface with no vegetation. The heated air has a lower

density than the air above the sheet of heated air, so buoyant force, which tends to cause it to rise, is exerted on it. The mechanism by which it can be detached from the surface is considered next.

The buoyant force exerted on this sheet of air cannot result in upward movement of the air until the sheet is "torn" along some line to permit cooler air from above the sheet to flow under the sheet and replace it. It may be assumed that the "tear" would start at some irregularity in the surface and be propagated under the influence of the buoyant force and natural air motion. As soon as the sheet of warm air is separated from the surface and replaced by cooler air, it becomes a part of the atmosphere and is subjected both to bending, stretching, and tearing forces, which changes its shape, and to conduction, which changes its shape, and to conduction, which lowers its temperature. As the warm air rises, its temperature approaches that of the surrounding air, and its identity is lost. At higher elevations in the atmosphere, the temperature differences of importance will probably be caused by larger scale mechanisms than those described.

The effect of the small local variations of temperature on a beam of light propagated near the surface of the earth depends on the gradient of index of refraction or the gradient of temperature, since they are linearly related. Assume that boundary effects reduce the temperature of the warm air near its boundary with the cooler air so that the temperature gradient across the sheet of warm air is approximately proportional to the ratio of the temperature difference to the thickness of the sheet. The temperature gradient is given by:

$$\frac{dT}{dx} = \frac{a (T_2 - T_1)}{t} = \frac{a\Delta T}{t} ,$$



where

$a$  = constant of proportionality,

$T_2$  = air temperature within the sheet,

$T_1$  = air temperature outside the sheet, and

$t$  = thickness of the sheet.

As the warm air rises, its temperature gradually decreases. At the same time, however, the temperature outside the sheet decreases with height, according to the lapse rate. The difference in temperature across the boundary can either increase or decrease, so that the numerator in the temperature gradient will either increase or decrease. The term in the denominator will decrease with height as the sheet becomes stretched in the air flow. It is not clear from this analysis how the gradient of index of refraction varies with height. Additional studies of the behavior of air flow near the surface of the earth will be required to understand this problem. The variation of the index of refraction gradients with time of day is more simply explained.

On a clear day, the surface temperature increases to a peak at midday and then decreases. Under stable meteorological conditions, it would be expected that the change of temperature over periods of several minutes would show a consistent progression and that  $\Delta T$  would increase consistently to a peak value at midday. Since the air circulation increases from the typical calm at sunrise, especially in summer, it might be expected that the thickness of the warm layer would decrease during the morning. If this analysis is correct, in the morning  $\Delta T$  increases and  $t$  decreases; so the ratio increases with time, and it is reasonable to predict that the index of refraction gradient increases. The following section, presents the result of an optical measurement which agrees with this prediction.

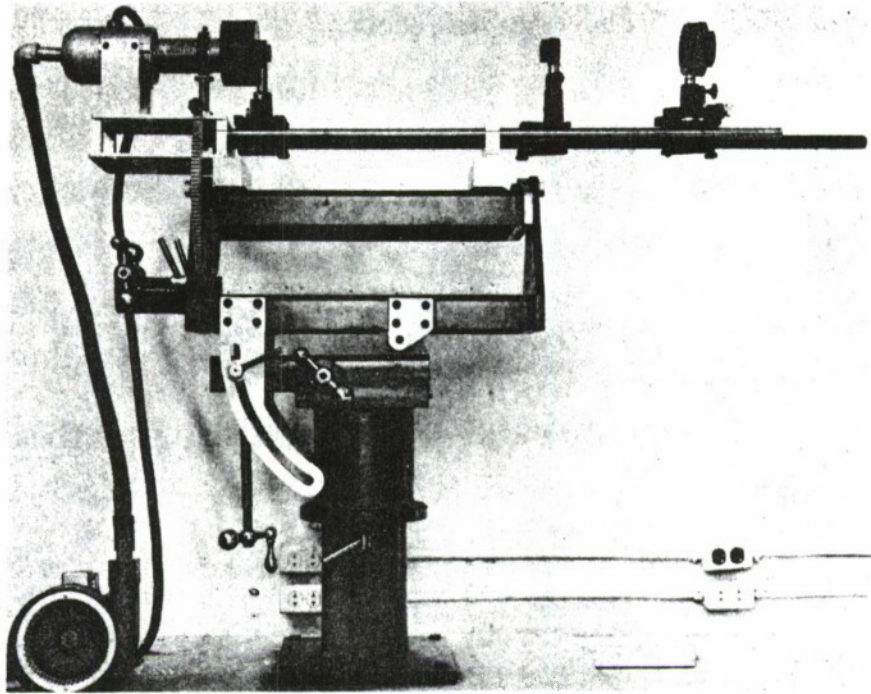
## OPTICAL MEASUREMENT

If a narrow, uniform beam of radiation is propagated through the atmosphere near the surface of the earth, irregularities in the intensity distribution over a cross section of the beam will occur as a result of refraction and diffraction caused by the irregularities in the atmosphere. The analysis in the previous section of this paper indicates that the irregularities in the radiation will become more severe with time during the morning of a clear day. The following experiment confirms that prediction.

The source of light was a ruby rod  $1/4$  by  $2-1/4$  inches, with an output of less than 0.1 watt-second. An optical projection system with a focal length of 3.8 meters and an aperture diameter of 4.0 centimeters was used to project all the radiation from the ruby onto the distant target.

The target was a white surface, with a black grid at 3-inch intervals in the vertical and horizontal directions. The target was located in the rear of a 28-foot van to reduce the incident daylight. A camera located to the front and side of the target was used to obtain photographs of the target when it was illuminated. A synchronization system permits the use of a shutter speed of  $1/100$  second. Figure 2 shows the laser and projector.

Figure 3 shows three typical beam patterns at a range of 1400 meters from the illuminator on a clear summer day. The beam had an average height of 8 feet above a grass-covered field. The left-hand photograph is typical of early morning while the air and surface are cool; the pattern is nearly uniform. By midmorning, the pattern generally resembles that of the center photograph, which shows small illuminated regions separated by large dark areas. By early afternoon, the pattern may resemble the right-hand photograph, where the light areas are lighter and the dark areas larger. Microdensitometer tracings of the original negatives showed that the variations of photographic



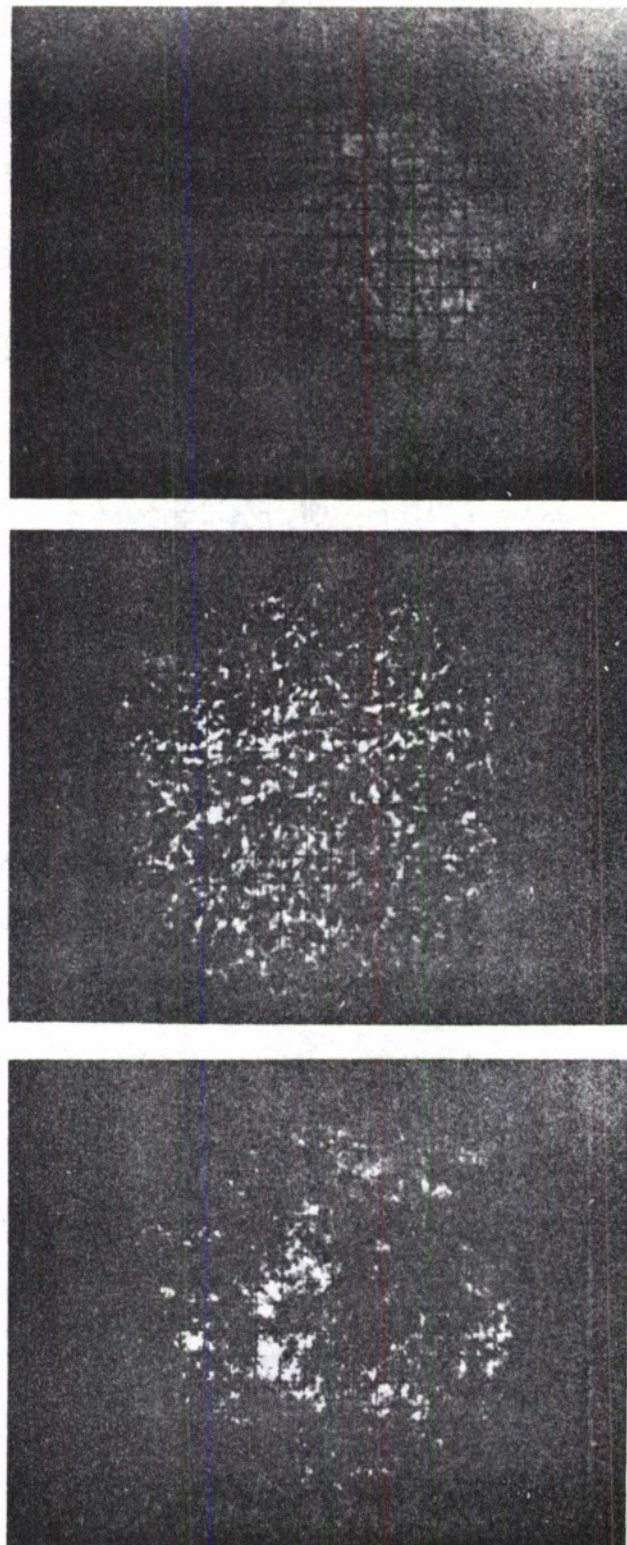
Laser head at upper left emits radiation which is focused on distant target by negative lens at upper center and positive lens at upper right.

Figure 2. Ruby Laser Illuminator Used in Optical Propagation Experiment

density across the photograph of the beam increased in magnitude during the morning and reached a peak at midday. No significant quantization of the size of the variations was possible.

Simultaneously with the photography of the beam on the target, measurements of the fluctuation of temperature in the atmosphere were made in the





The beam pattern during the early morning is shown in the left photograph; those for mid-morning and midday are shown in the center and right photographs, respectively.

Figure 3. Three Typical Beam Distribution Patterns (Range: 1400 Meters)



vicinity of the illuminator.\* The measurement technique employs a fine wire in a Wheatstone Bridge to sense the temperature of the air. By this means, air temperature can be measured with a time constant of a few milliseconds. The measured temperature records were classified according to the maximum change in temperature which occurred during a one-second interval at the approximate time of the photograph.

The photographs were divided into four groups according to the magnitude of the density variations, and averages were taken. The temperature fluctuation measurements were divided into four groups according to the corresponding photographs, and averages were taken. The results, listed in Table I, show

Table I

Relationship of  $\Delta T$  and  $\Delta D$

Group	Maximum $\Delta T$ ( $^{\circ}\text{C}$ )	Maximum $\Delta D$
1	0.75	0.75
2	0.50	0.55
3	0.30	0.30
4	0.10	0.15

that the groups of photographs obtained during periods of large temperature fluctuations have large density variations. Although the correlation between temperature and density is quite good, the method of grouping and averaging used is quite crude. Correlation between individual data points would be much more satisfactory; however, the data from this experiment are not suitable for such treatment.

---

\* These measurements were obtained by using the method described in Reference [2].

## ELECTROMAGNETIC PROPAGATION RANGE

A new facility, the electromagnetic propagation range, is intended to serve as a basic research facility, offering ground cover control and the measurement of atmospheric parameters by means of sensors and a data processing system. It should enable more uniform data to be obtained because of improvements in the uniformity of the conditions along the path and by providing additional meteorological data.

The surface of the range, a flat area 400-feet wide and 2400-feet long, is sufficiently distant from obstructions to provide nearly uniform meteorological conditions.

Six masts are being installed to support various meteorological sensors. (see Table II). At the present time, the 68 sensors can be connected to individual pre-amplifiers in the recording van. The outputs of the pre-amplifiers can be scanned at rates of 1/100, 1/10, 1, and 10 seconds for the entire array. Eventually, the system will be expanded to 150 channels. The output of the system is recorded on digital magnetic tape in a format compatible with the IBM 1401 computer. The system has been developed to maintain the accuracy of the sensors and to record at intervals within the sensor time constants.

A 50-foot tower at the end of the range is on order. A 50-foot tower with elevator platform, movable along tracks at the beginning of the range, is in the design stage. Plans to increase the length of the range are pending.

## REFERENCES

1. O. G. Sutton, Micrometeorology, New York, McGraw-Hill, 1953.
2. V. I. Tatarski, Wave Propagation in a Turbulent Medium, New York, McGraw-Hill, 1961.

Table II  
System Input, BRL Electromagnetic Propagation Range

Number of Channels		Sensor Type	Voltage Range		Sensor Output Impedance ( $\Omega$ )	Accuracy (% of full scale)
Immediate	Future		Full Range (v)	Nominal Operating Range (v)		
18	30	Thermistor BW-M327	1.2-5.5	1.4-2.2	30 K - 500 K	$\pm 0.31$
12	30	Vane and Generator BW-WS 101	0-1.4	0-0.56	1400	$\pm 0.25$
12	30	Vane and Generator BW-WS 101	0-1.4	0-1.4	1400	$\pm 0.83$
6	30	Dew Point Hygrometer Bendix	1.2-5.5	1.4-2.2	30 K - 500 K	$\pm 0.31$
6	6	Macreedy Bivane	0-1.6	0-1.6	1600	$\pm 0.13$
6	6	Macreedy Bivane	0-1.6	1.12-1.6	1600	$\pm 0.28$
6	6	Macreedy Bivane	0-1.6	1.12-1.6	1600	$\pm 0.28$
0	6	Not designed as yet	0-10	5.0 -10	600	$\pm 0.01$
2	6	Refractometer Colorado Res MR-100	0-10	7 -10	600	$\pm 0.025$

## REFRACTION MEASUREMENTS BY LUNAR TRACKING

H. I. Ewen and P. M. Kalaghan\*

### INTRODUCTION

The objective of this contract effort was to investigate the scientific and system engineering aspects which determine the efficacy of the actively illuminated moon as an exo-atmospheric target capable of precise tracking by existing range instrumentation radar receiving systems. The availability of such a target in a precisely known orbit affords opportunity for accurate measurement of refractive bending.

The suggested applicability of the illuminated moon to measurements of this type was based on the unusual nature of microwave lunar reflectivity characteristics, which demonstrate a pronounced specular component subtending a relatively small solid angle of the projected lunar surface, "apparently" centered on the subterrestrial point.

Though a number of experimenters have investigated microwave lunar reflective properties, the ephemeral position of the specular component relative to the optically observed disk of the moon has not been precisely measured nor is it possible to extract this information to the desired precision from measurements thus far reported. This situation was anticipated at the outset of the study effort, and, for this reason, our analysis has been directed primarily to establishing the feasibility of undertaking this measurement with maximum utilization of existing equipments and facilities.

It was assumed at the outset of the program that an FPQ-6 radar system would be used as the receiving terminal for the experiment since this system

---

\* Ewen Knight Corporation, East Natick, Massachusetts



represents perhaps the most advanced precision pointing range instrumentation instrument currently available. The analysis and derivation of illuminator requirements were therefore predicted on the assumption that the receiving terminal will be equivalent to, or meet, the stated performance specifications of an FPQ-6 radar receiving system.

## LUNAR SCATTERING CHARACTERISTICS

Radar studies of the moon have been under way since World War II. Results of observations at various wavelengths extending from 15 meters to .86 centimeters have been published in the literature. The characteristics of the lunar echo depend principally on the operational mode of the radar transmitter. By a combination of short pulse, coherent pulse, and CW techniques, observers have attempted to ascertain the reflection properties of the lunar surface at radio wavelengths. We shall summarize here the parameters characterizing these reflections.

### Lunar Range

From Table I, the mean distance of the moon from the earth is 384,405  $\pm$  4 kilometer. The two-way travel time over this distance produces an echo delayed 2.56 seconds. Since the orbit of the moon has an eccentricity of 0.0549, the actual range can vary from +7.7 to -5.4 percent of the mean range. As a result, the echo power (in systems utilizing transmitting and receiving beams comparable to and larger than 1/2 degree) will vary from 74 percent to 125 percent of the value observed at the mean distance.

### Lunar Doppler Shift

Since the moon moves in an elliptical rather than circular orbit, there will usually be a component of velocity directed toward the earth. The maximum value of this component is  $\pm$ 55 meters per second. In addition to this relative

Table 1

## Lunar Characteristics

Mean Range:	384,405 $\pm$ 4 km
Two-way Travel Time:	2.56 seconds
Orbital Eccentricity:	0.05490
Range Variation:	+7.7% to -5.4% of Mean Range
Uncertainty in Position	1 part in 10 <sup>5</sup>
Maximum Radial Velocity:	$\pm$ 55 m/sec
Equatorial Radius:	1738.0 km
Synodic Month:	29.530588 days
Mean Sidereal Motion:	548 arc second/sec.
Cross Section:	$7 \times 10^{11} \text{ m}^2$ ( $\pm$ 3 db)(C-band)

motion of the moon and earth, an observer on the surface of the earth will have a velocity component in the line of sight due to diurnal rotation of the earth. The maximum value of this velocity is  $\pm 464$  meters per second. These two components may be added vectorially to give the total velocity of the observer relative to the center of the moon. At a frequency of 6 Kmc, the maximum doppler shift resulting from the two motions discussed above amounts to  $\pm 20,760$  cycles per second.

#### Doppler Spread of Lunar Echoes: Lunar Libration

Although the moon seems to rotate with constant angular velocity with a period of rotation exactly equal to the period of its sidereal revolution around the earth, slight motions of surface features relative to the earth have been observed. These motions, generally referred to as optical librations, are grouped into three classes:

- (1) optical libration in longitude,
- (2) optical libration in latitude, and
- (3) diurnal libration.

#### Libration in Longitude

The optical libration in longitude results from the fact that the moon rotates in the course of a month uniformly and, at the same time, it revolves in its orbit around the earth with a variable angular velocity. The maximum angular displacement of lunar features caused by this libration amount to  $\pm 7.9$  selenocentric degrees. The rate of libration in longitude is direct at apogee and retrograde at perigee with a maximum value of about  $4 \times 10^{-7}$  radians per second.

#### Diurnal Libration

Displacements of the observer situated on the earth's surface enables him to see some additional portions of the moon, resulting from the rotation of the earth. This effect is called the diurnal libration and is in the direct sense when the moon is in transit, having a maximum rate at zero declination of  $12 \cos L \times 10^{-7}$  radians per second, where  $L$  is the geographic latitude of the observer.

The effect of the individual librational spins is to alter the path lengths of the various scattering centers on the lunar surface resulting in phase shifts of the various frequency components making up the echo. This causes the echo amplitude to fade at a rate depending on the resultant total librational velocity component parallel to the line of sight.

Since many different points on the lunar surface contribute to the returned signal, a point offset from the center will, due to the combination of the three librations mentioned above, be in motion relative to the center. Since this motion

will generally have a component along the line of sight, the doppler frequency shift of the return from the offset point will be slightly different than the shift of the return from the central point. This variation in returned frequency relative to the central point is referred to as the doppler spread of the echo. Noting that the maximum velocity of a lunar limb point relative to the center is about  $\pm 2$  megacycle per second, it follows that at C-band this velocity produces maximum frequency offsets of  $\pm 90$  cycles per second relative to returned frequency of the central portion of the lunar disc for an observer at 45 degree geographic latitude.

### The Lunar Radar Cross Section

The scattering cross section is given as:

$$\sigma = f(g, \rho, R_o, \lambda) \quad , \quad (1)$$

where  $g$  is the directivity of the target,  $\rho$  is the reflection coefficient, and  $R_o$  is the lunar geometric radius. Where the wavelength  $\lambda$  of the incident radio waves is very much shorter than the radius  $R_o$  of the target, a smooth perfectly conducting object will have a scattering cross section  $\sigma'$  equal to the actual area of the disc, i. e. ,  $\pi R_o^2$ . If, however, the sphere is made of dielectric materials having a reflection coefficient  $\rho$  , then:

$$\sigma' = \rho \pi R_o^2 \quad . \quad (2)$$

Senior and Siegel<sup>[1]</sup> have shown that for a smooth target the electrical constants of the surface may be determined by studying the wavelength dependence of  $\rho$  . Where the target is not smooth, but has irregularities which are greater in size than  $\lambda/8$  , the scattering cross section becomes:

$$\sigma = g \rho \pi R_o^2 \quad , \quad (3)$$

in which  $g$  is a directivity term which denotes the gain of the target over an isotropic radiator of the same size. Because a radar transmitter provides a coherent



source of radiation, the gain  $g$  will be a function of the wavelength  $\lambda$  and the aspect from which the target is viewed. The relative contribution to the intensity of the elements on the surface will depend upon the scattering mechanism — the law relating the power reflected per unit solid angle to the angular distance between the normal to the surface and the ray path.

Unfortunately, for a rough target such as the moon, a measurement of the echo intensity will provide only a determination of the product  $\rho g$ . Thus, precise experimental separation of  $g$  and  $\rho$  is currently not available and undoubtedly will require a bistatic experiment using a lunar probe. However, it may be said that the value of reflectivity appears not to be a function of wavelength between 15 meters and 3 centimeters, although indications are that the radar cross section is decreasing for  $\lambda < 20$  cm.

#### C-Band Lunar Model

Interpolating the lunar measurement data currently appearing in the literature, the pertinent features of C-band lunar echoes can be inferred. Relying mainly on the measurements of Evans and Pettengill,<sup>[2]</sup> an echo intensity versus time delay between the lines shown in Figure 1 will be the basic characteristic assumed. Taking an average value in the shaded area and replotting as a linear function of the fractional lunar radius  $k^*$ , the scattering characteristics of Figure 2 results. This is the basic "C-band Moon" assumed below.

The cumulative reflected energy can be obtained by integrating the scattering characteristic of Figure 2. It is apparent that most of the echo originates from the central portion of the disc; in particular, 80 percent of the return comes from the central region within the circle of fractional radius equal to 0.25, whereas 50 percent of the return comes from the central circle with 0.10 fractional radius.

---

\*  $k = (1 - \cos^2 \phi)^{1/2}$ ;  $\phi$  = the angle of incidence.

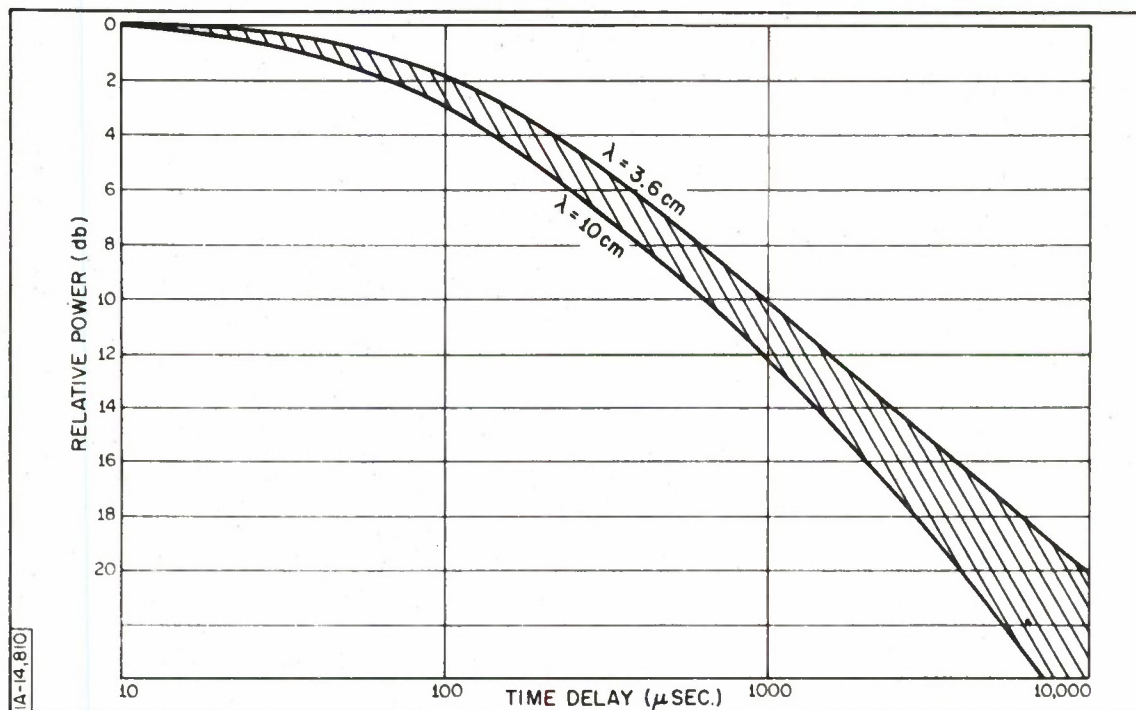


Figure 1. Echo Intensity Versus Time Delay

Since the foregoing intensity curve was based on uniform illumination of the entire lunar disc, the actual return when the disc is illuminated by a transmitting beam whose width is less than or comparable to the diameter of the disc will further "sharpen" the central response. The scattering distributions resulting from illuminator apertures of 85, 60, and 28 feet are given in Figure 3.

The other primary echo characteristic, the doppler spread, can also be estimated from data in the literature. The maximum libration rate causes a total frequency spread of  $\pm 90$  cycles per second from limb to limb, and the intensity of the various frequency components can be inferred from the recent S-band data by Muhleman<sup>[3]</sup> of JPL. In particular, it was found that the power spectrum of the returned signal could be represented as being of the form:

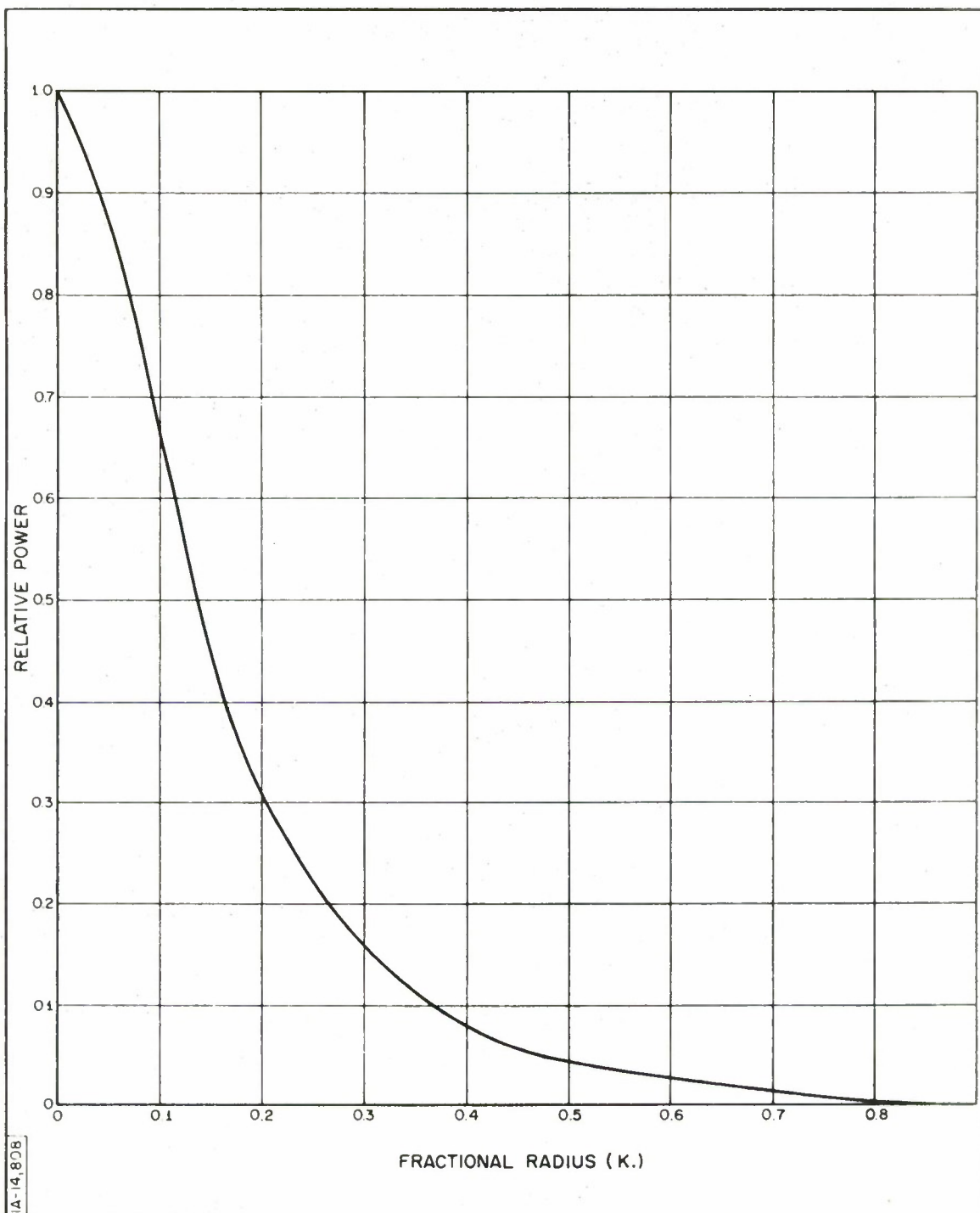


Figure 2. Scattering Characteristics

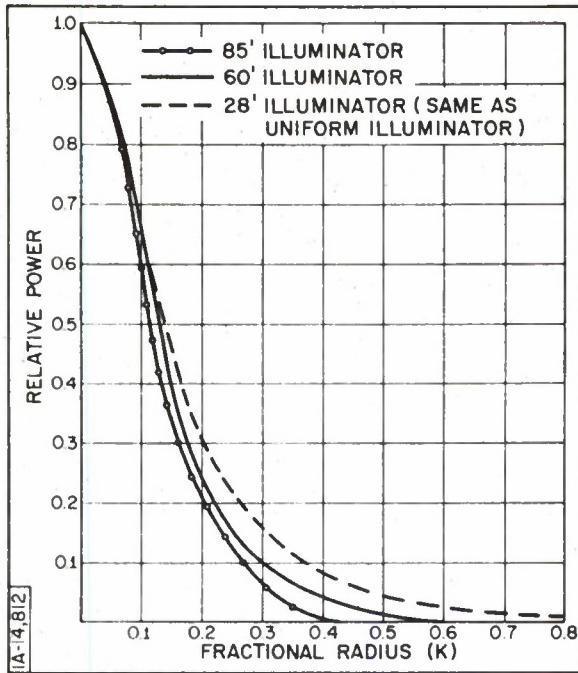


Figure 3. Effective Aperture Diameter

$$P(f) \sim \left[ 1 - \left( f/f_{\max} \right)^2 \right]^{50} , \quad (4)$$

where  $f_{\max}$  is the limb value of the frequency spread at the time of observation. Using this relation, an estimate of the power spectrum of the C-band return during a period of maximum librational motion is given in Figure 4. By integrating this spectrum over frequency, it can be shown that 50 percent of the returned power is within  $\pm 7$  cycles per second of the central value of 85 percent of the power is within  $\pm 13$  cycles per second of the central value.

In summary, the intensity and frequency distribution characteristics contained in Figures 2 and 4 appear to be a fair estimate of the actual scattering properties of the illuminated Moon. These characteristics will form the basis of the Systems Analysis of the overall utility of the Moon in measurement of pointing errors of current radar systems.



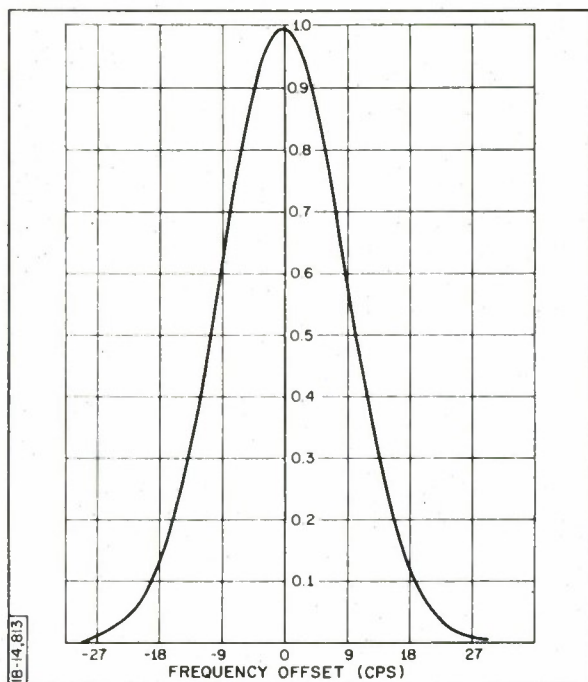


Figure 4. Frequency Spread

## SYSTEM ANALYSIS

Utilizing Manasse's general expression for the angular tracking accuracy capability of a monopulse radar, the rms angular tracking accuracy,  $\epsilon$ , can be written:

$$\epsilon = \frac{\theta}{K} \frac{(1 + S/N)^{1/2}}{(S/N)(M)^{1/2}}, \quad (5)$$

where

$\theta$  = receiving aperture beamwidth (3 db);

$k$  = geometrical constant relating slope of error, signal curve to beamwidth;

$S/N$  = predetection signal-to-noise ratio; and

$M$  = smoothing or integrating factor appropriate to system mode of operation, in particular  $M$  is  $B\tau$  for a CW system and  $R\tau$  for a pulsed system, where  $\tau$  is the servo integration time,  $B$  the predetection bandwidth, and  $R$  the system pulse repetition rate.

Various workers in the field have employed differing values of the constant. Manasse's original value was 2.2, while the Jet Propulsion Laboratory has found a value of 2.8 to be more accurate for their Goldstone Site. In analyzing the Polaris Program Radiometric Sextant, Ewen Knight arrived at a value of 3.1 for  $k$ . Finally, various analyses by RCA groups have been based on a value around 0.6, so that at present there is no universally accepted value.

Squaring Eq. (5), rearranging terms, and solving the resulting quadratic yields the following expression relating the signal-to-noise (S/N) ratio to the tracking accuracy:

$$S/N = \frac{\theta^2}{2k^2 \epsilon^2 M} \left[ 1 + \left( 1 + \frac{4k^2 \epsilon^2 M}{\theta^2} \right)^{1/2} \right] \quad (6)$$

In addition, another expression for (S/N) can be obtained from the normal radar equation, as:

$$S/N = \frac{P_T G_T \sigma A_R}{16 \pi^2 R^4 L k B [T_o (NF-1) + T_A]} \quad (7)$$

where

- $P_T$  = the transmitted power;
- $G_T$  = the gain of the transmitting antenna;
- $\sigma$  = the scattering cross section of the target;
- $R$  = the range of the target;
- $L$  = the overall system loss;
- $k$  = Boltzmann's constant;
- $(NF)$  = the receiving system noise figure;
- $B$  = the predetection receiver bandwidth;
- $T_O$  = the ambient temperature,  $290^\circ \text{K}$ ;
- $T_A$  = the antenna temperature due to the background around the target; and
- $A_R$  = the effective receiving aperture.

Now, noting that the product of  $G_T A_R$  can be written in terms of  $\theta$ , the 3-decibel beamwidth of the receiving antenna, and the efficiencies  $\rho_T$  and  $\rho_R$  of the transmitting and receiving antenna, Eq. (7) can be re-expressed as:

$$S/N = \gamma \frac{P_T}{B \theta^2}, \quad (8)$$

where

$$\gamma = \frac{1.44 \times 10^6 \rho_T \rho_R \sigma A_T}{16 R^4 L k [T_O (NF-1) + T_A]} \quad (9)$$

Since Eq. (8) defines an alternate expression for  $(S/N)$  in terms of  $\theta$ ,  $P_T$  and  $B$ , it can be equated to the expression in Eq. (6) so that the following expression for the transmitter power,  $P_T$ , results:

$$P_T = \frac{\theta^4 B}{2\gamma k^2 \epsilon^2 M} \left[ 1 + \left( 1 + \frac{4k^2 \epsilon^2 M}{\theta^2} \right)^{1/2} \right] \quad (10)$$

Thus Eq. (10) relates the required transmitter power  $P_T$  for a system having an accuracy  $\epsilon$  and beamwidth  $\theta$ . Writing the explicit form for the term  $M$ , the generalized System Equations may be obtained for the particular modes of operation considered; i. e., full, CW wherein both the receiver and transmitter are operated in a continuous fashion, and, alternatively, semi-CW, where the transmitter is operated on a CW mode but in which the receiver is operated in a "Gated" mode with a pulse or gate repetition rate  $R$ .

### Numerical Results

For more quantitative conclusions regarding Eq. (10), several system and target parameters must be specified. Since the program anticipated is the attempted tracking of an illuminated lunar surface with an FPQ-6 radar receiving system, the particular values of system parameters used for calculations are given in Table II.

Substituting these values in the appropriate System Equations, the values of the required transmitter power as a function of bandwidth  $B$ , tracking accuracy  $\epsilon$ , gate repetition rate  $R$ , and servo time constant  $\tau$ , may be calculated.

The results of such calculations indicate that for a tracking accuracy of 0.10 mil (rms), a 20-kilowatt illuminator would be quite suitable, being above the minimum level of 7.5 kilowatts required when the normal 500-kilocycle system bandwidth is employed. This indicates that 0.10 mils can be



Table 2

Values of System Parameters

Transmitting System: (CW)

Power:	$P_T$ (to be determined)
Reflector Diameter:	28 feet
Efficiency:	50%
Frequency:	5900 Mc

Receiving System:

Reflector Diameter:	29 feet
Receiving Beamwidth:	7 mils (at 5900 Mc)
Receiver Noise Figure:	7.5 db (without paramp)
System Loss:	3 db
Background Antenna Temperature:	$200^\circ \text{K}$
Bandwidth:	Variable (500 Kc minimum)
Gate Repetition Rate:	Variable (1700 cps maximum)
Geometrical Factor:	2.0 (nominal value)

Lunar Characteristics:

Range:	$3.84 \times 10^8$ meters
Total CW Reflectivity:	.078
CW Cross Section:	$7 \times 10^{11}$ meter <sup>2</sup>
Scattering Distribution:	Figure 2
Frequency Spectrum:	Figure 4

obtained without any modification or adaptation to the "stock" receiving system. Furthermore, under the constraint that no modifications be performed to the FPQ-6, the ultimate tracking accuracy possible is 0.05 mil when a 20-kilowatt illuminator is employed. If, however, RF and IF bandwidth reduction is possible, filters could be inserted in the front end of the receiver, and an illuminator of only a few hundred watts would be a possible solution yielding a 0.10 mil accuracy.

If the accuracy requirement is further increased to 0.01 mil, it becomes clear that the combination of a 20-kilowatt illuminator, and an unmodified FPQ-6 cannot supply the specified tracking accuracy when the minimum available system bandwidth is 500 kilocycles. However, if the IF bandwidth could be limited to 50 kilocycles, the system would be capable of 0.01 mil even when operating in the gated mode. On the other hand, if the gating could be disabled so that CW operation could be attained, then an accuracy better than 0.005 mil would be possible when the 500-kilocycle bandwidth is employed.

It should be noted that the FPQ-6 may also be operated in some cases with a parametric amplifier with a noise figure of 4 decibels. If this front end is employed, then the transmitter power requirements would drop by 3 decibels.

Since an experimental moon illumination setup in which no changes are required in the existing circuitry and operational modes of the FPQ-6 may be desirable, consideration has been given to augmenting the characteristics of the illuminating system. In particular, the diameter of the reflector was chosen as the most accessible parameter to be varied. Consideration of the effect of the size of the illuminator reflector on the required transmitter power as a function of the tracking accuracy indicates that if 20 kilowatts is considered as the maximum transmitter power practical on a CW basis, then a 28-foot reflector is sufficient to allow FPQ-6 tracking with 0.045-mil accuracy; a 60-foot reflector, a 0.016-mil accuracy; and a 85-foot reflector, a 0.01-mil accuracy.

The drawback to employing larger reflectors is that the pointing requirement becomes extremely severe. Implicit in this analysis is the assumption that the illuminating beam is centered on the lunar subterrestrial point. If this is not the case, then the lunar scattering function given in Figure 2 becomes distorted, with the result being that the apparent center of scattering function (also known as the brightness distribution) is shifted off to one side. Since a receiving system such as the FPQ-6 will track the "apparent center of brightness" rather than the true center of the lunar disc, significant errors will occur in the tracking data due to this asymmetric illumination. Assuming that such illuminator pointing errors are not the result of operator error, but rather are due to mount backlash, gear cogging, etc., then in order to perform the proposed experiment successfully, definite requirements must be imposed on the mechanical accuracy of the illuminator mount-and-drive system.

Recalling the basic lunar scattering function given in Figure 2, the effect of an offset in the illuminating pattern will be to modify this scattering function. In particular, the resultant scattering function will simply be the product of the antenna pattern function times the scattering function and will thus be a function of the offset  $\delta$  of the center of the antenna pattern relative to the center of the lunar disc. Integrating such "modified" scattering functions (brightness distributions) and calculating the shift in the apparent center of brightness due to an offset  $\delta$  in the illuminator beam, Figure 5 results. Assuming that such errors should amount to no more than  $1/2$  the desired measurement accuracy  $\epsilon$ , this figure indicates that an 85-foot illuminator requires a  $1/40$ -mil mount accuracy, a 60-foot illuminator requires a  $1/20$ -mil mount accuracy, and a 28-foot illuminator requires a  $1/2$ -mil mount accuracy when 0.01 mil is stated as the overall desired measurement accuracy. Since these figures, as well as those required of the receiving system, are all well within the state of the art at the present, the feasibility of performing the measurements is on firm ground.

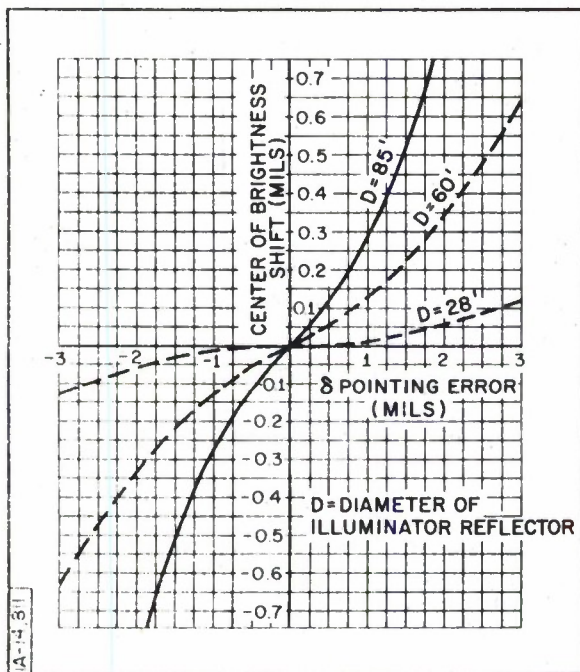


Figure 5. Effect of Offset in Illuminator Beam

#### MOON ILLUMINATION APPLICATION TO REFRACTIVE MEASUREMENT

Having established the feasibility of enhancing the radio brightness of the lunar surface by means of active illumination from an earth-based, C-band transmitter, highly accurate tracking of the subterrestrial point becomes possible for an earth-based receiving system such as the FPQ-6. Furthermore, since the ephemeris of the target, the lunar subterrestrial point, is known to less than 0.001 mil, it becomes possible to calibrate the quality of the tracking data by comparing the predicted position of the Moon to the known position given by an ephemeris. The resulting system errors can then be attributed to jitter in the center of brightness of the Moon and to refractive fluctuations and scintillations.

In order to calibrate the overall capability of the tracking system, the two effects of center of brightness wander and refractive bending must be separated.



This separation may be accomplished by a careful choice of observation times. In particular, the basic test of the lunar subterrestrial point as a stable target may be accomplished by confining initial observations to times when the Moon is above 40 degrees elevation. At these higher elevation angles, the total refractive bending (using a Bean and Cahoon<sup>[4]</sup> model with a surface refractivity of 350 N units) amounts to less than 0.5 mil and is both predictable and stable to within 0.02 mil (corresponding to a  $\pm 20$  N-unit variation) for observations lasting several minutes. Thus, the data from the tracking system whose "design-tracking accuracy" can be put at 0.01 mil (root mean square) is a true indicator of the jitter of the target to within a combined "system plus atmosphere" accuracy of less than 0.03 mil (root mean square). If the data then indicates tracking with root mean square errors comparable to 0.03 mil, then it may be inferred that the subterrestrial point has an inherent jitter less than the accuracy of the system and, as such, present no basic limitation to further atmospheric tests. However, if the resulting data indicates a tracking accuracy an order of magnitude worse than the calculated system capability, then high target jitter is implied and this jitter defines the ultimate accuracy of all future measurements.

Once this high elevation angle data is taken, the basic "system plus target" accuracy,  $\epsilon_0$ , may be determined and observations may then be taken at elevation angles down to the horizon. By tracking the lunar surface at these small angles, it becomes possible to determine directly the ray bending  $\tau$  due to the atmosphere to the accuracy  $\epsilon_\tau$ . With  $\tau$  so determined together with  $\epsilon_\tau$  the root mean square accuracy at lower elevation angles, it is possible to infer the values of  $N_s$ , the surface refractivity used by Bean and Cahoon.<sup>[4]</sup> By simultaneously measuring  $N_s$  with a radiosonde at the times of observation, further information can be obtained on the range of validity of many of the proposed analytical methods, as well as the Bean and Cahoon<sup>[4]</sup> regression analysis. Furthermore, what is important about this technique is that with this type of

measurement, the refractive bending can be observed directly and appropriate corrections applied to the system output data without having to assume or measure the atmospheric refractive profiles.

## REFERENCES

1. T. B. A. Senior and K. M. Siegel, "A Theory of Radar Scattering by the Moon," J. Res. NBS, 64D, 217, 1960.
2. J. V. Evans and G. H. Pettengill, "The Scattering Behavior of the Moon at Wavelengths of 3.6, 68 and 78 cm," J. Geophys. Res., 68, 423, 1963.
3. D. O. Muhleman, "Radar Investigation of Venus," Ph. D. Thesis, Harvard University, 1963.
4. B. R. Bean and B. A. Cahoon, "The Use of Surface Weather Observations to Predict Total Atmospheric Bending of Radio Rays at Small Elevation Angles," Proc. IRE, 45, 1545, 1957.

## BIBLIOGRAPHY

Bay, Z. , "Reflection of Microwaves from the Moon," Hungarian Physica Acta, 1, 1, 1946.

Blevis, B. C. , and J. H. Chapman, "Characteristics of 488 Megacycles Per Second Radio Signals Reflected From the Moon," J. Res. NBS, 64D, 331-334, 1960.

Bramley, E. N. , "A Note on the Theory of Moon Echoes," Proc. Phys. Soc. G.B. , 80, 1128, 1962.

Briggs, B. H. , G. J. Phillips, and D. H. Shinn, "The Analysis of Observations on Spaced Receivers of the Fading Radio Signals," Proc. Phys. Soc. (London), B, 63, 106-121, 1950.

Brown, W. E. , "A Lunar and Planetary Echo Theory," J. Geophys. Res. , 65, 3087-3095, 1960.

Browne, I. C. , J. V. Evans, J. K. Hargreaves, and W. A. S. Murray, "Radio Echoes from the Moon," Proc. Phys. Soc. (London), B, 69, 901-920, 1956.

Daniels, F. B. , "Radar Determinations of Scattering Properties of the Moon," Nature, 87, 399, 1960.

Daniels, F. B. , "A Theory of Radar Reflections from the Moon and Planets," J. Geophys. Res. , 66, 1781-1788, 1961.

Daniels, F. B. , "Author's Comments on the Preceding Discussion," J. Geophys. Res. , 67, 895, 1962.

Daniels, F. B. , "Radar Determination of the rms Slope of the Lunar Surface," J. Geophys. Res. , 68 (2), Jan. 15, 1963.

Daniels, F. B. , "Radar Determination of Lunar Slopes: Correction for the Diffuse Component," J. Geophys. Res. , 68, 2864, 1963.

DeWitt, J. M. , Jr. , and E. K. Stodola, "Detection of Radio Signals Reflected from the Moon," Proc. IRE, 37, 229-242, 1949.

Evans, J. V. , "The Scattering of Radio Waves by the Moon," Proc. Phys. Soc. London, B, 70, 1105-1112, 1957.



Evans, J. V. , "Radio Echo Observations of the Moon at 3.6 cm Wavelength," Lincoln Lab. MIT TR-256, 1962a.

Evans, J. V. , "Radio Echo Studies of the Moon," in Physics and Astronomy of the Moon, ed. Z. Kopal, Academic Press, New York, 1962b.

Evans, J. V. , S. Evans, and J. H. Thomson, "The Rapid Fading of Moon Echoes of 100 Mc/s," Paris Symposium on Radio Astronomy, ed. R. N. Bracewell, pp. 8-12, Stanford University Press, Stanford, 1959.

Evans, J. V. , and G. H. Pettengill, "The Scattering Properties of the Lunar Surface at Radio Wavelengths," in The Solar System, Vol. 4, ed. G. P. Kuiper and B. M. Middlehurst, University of Chicago Press, Chicago, 1963.

Evans, J. V. , "A Lunar Theory Reasserted - a Rebuttal," J. Res. NBS, (Radio Prop.) 67, 1, 1963.

Evans, J. , and Pettengill, G. H. , "The Scattering Behavior of the Moon at Wavelengths of 3.6, 68, 784 cm," J. Geophys. Res. , 68, 423, 1963.

Evans, J. V. , "Radio Echo Studies of the Lunar Surface," J. Geophys. Res. , 67, 3556, 1962.

Fischer, I. , "Parallax of the Moon in Terms of a World Geodetic System," Astronom. J. , 67, 373, 1962.

Fricker, S. J. , R. P. Ingalls, W. E. Mason, M. L. Stone, and D. W. Swift, "Computation and Measurement of the Fading Rate of Moon Reflected UHF Signals," J. Res. NBS, 64D, 455-465, 1960.

Grieg, D. D. , S. Metzger, and R. Waer, "Considerations of Moon-Relay Communication," Proc. IRE, 36, 652-663, 1948.

Hagfors, T. , "Some Properties of Radio Waves Reflected from the Moon and Their Relation to the Lunar Surface," J. Geophys. Res. , 66, 777-785, 1961.

Hargreaves, J. K. , "Radar Observations of the Lunar Surface," Proc. Phys. Soc. London, B, 73, 536-537, 1959.

Hayre, H. S. , "Radar Scattering Cross Section Applied to Moon Return," Proc. IRE, 49, 1433, 1961.

Hey, J. S., and V. A. Hughes, "Radar Observations of the Moon at 10 cm Wavelength," Paris Symposium on Radio Astronomy, ed. R. N. Bracewell, pp. 13-18, Stanford University Press, Stanford, 1959.

Hughes, V. A., "Roughness of the Moon as a Radar Reflector," Nature, 186, 873-874, 1960.

Hughes, V. A., "Radio Wave Scattering from the Lunar Surface," Proc. Phys. Soc., 78, 988-997, 1961.

Hughes, V. A., "Discussion of paper by Daniels, 'A Theory of Radar Reflections from the Moon and Planets'," J. Geophys. Res., 67, 892-894, 1962.

Ingalls, R. P., L. E. Bird, and J. W. B. Day, "Bandpass Measurements of a Lunar Reflection Circuit," Proc. IRE, 49, 631, 1961.

Kerr, F. J., and C. A. Shain, "Moon Echoes and Transmission through the Ionosphere," Proc. IRE, 39, 236-242, 1951.

Kerr, F. J., Shain C. A., and Higgins, C. S., Nature, 163, 310, 1949.

Kobrin, N. M., "Radio Echoes from the Moon in the X and S-band," Radiotekhn. i Electron, 4, 892-894, 1959.

Leadebrand, R. L., et al., "Radio Frequency Scattering from the Surface of the Moon," Proc. IRE, 48, 932, 1960.

Leaderbrand, R. L., R. B. Dyce, A. Fredriksen, R. I. Presnell, and R. C. Barthle, "Evidence that the Moon is a Rough Scatterer at Radio Frequencies," J. Geophys. Res., 65, 3071-3078, 1960.

Levy, G. S., and D. Schuster, "Venusian and Lunar Radar Depolarization Experiments," Astronom. J., 67, 320, 1962.

Lynn, V. L., Sohigian, M. D., Crocker, E. A., "Radar Observations of the Moon at 8.6 mm Wavelength," Lincoln Laboratory Technical Report 331, 1963.

Millman, G. H., A. E. Sanders, and R. A. Mather, "Radar-Lunar Investigations at a Low Geomagnetic Latitude," J. Geophys. Res., 65, 2619, 1960.

Millman, G. H., and F. L. Rose, "Radar Reflections from the Moon at 425 Mc/s," J. Res. NBS (Radio Propagation) 67, 107, 1963.

Mofeson, J., Electronics, 19, 92, 1946.

Morrow, W. E., Jr., D. Karp, B. Nichols, and R. V. Locke, Jr., "Coefficient of Reflectivity of Lunar Surface at X-band Frequencies," paper presented at URSI Spring Meeting, Washington, 1962.

Muhleman, D. O., "Radar investigation of Venus," Ph. D. Thesis, Harvard University, 1963.

Murray, W. A. S., and J. K. Hargreaves, "Lunar Radio Echoes and the Faraday Effect in the Ionosphere," Nature, 173, 944-945, 1954.

Pettengill, G. H., and J. C. Henry, "Radio Measurements of the Lunar Surface," The Moon, IAU Symposium 14, ed. Z. Kopal and Z. K. Mikhailov, Academic Press, London, 1962a.

Pettengill, G. H., "Measurements of Lunar Reflectivity Using the Millstone Radar," Proc. IRE, 48, 933-934, 1960.

Pettengill, G. H., "Lunar Studies," lecture notes in Radar Astronomy, MIT, 1960.

Pettengill, G. H., and J. C. Henry, "Anomalous Radar Reflectivity of the Lunar Crater Tycho," J. Geophys. Res., November 1962b.

Senior, T. B. A. and K. M. Siegel, "A Theory of Radar Scattering by the Moon," J. Res. NBS, 64D, 217-228, 1960.

Siegel, K. M., and Senior, T. B. A., "A Lunar Theory Reasserted," J. Res. NBS, 66D, 227, 1962.

Senior, T. B. A., and K. M. Siegel, "The Radar Cross-Section of the Moon," Proc. IRE, 49, 1944, 1961.

Senior, T. B. A., and K. M. Siegel, "Radar Reflection Characteristics of the Moon," in Paris Symposium on Radio Astronomy, ed. R. N. Bracewell, pp. 29-46, Stanford University Press, Stanford, 1959.

Spetner, L. M., and L. Katz, "Two Statistical Models of Radar Terrain Return," Trans. IRE (PGAP, AP-S), 242-246, 1960.

Taylor, R. C. , "Terrain Return Measurements at X, Ku, and Ka-band," IRE Convention Record, Part 1, pp. 19-26, 1959.

Trexler, J. H. , "Lunar radio echoes," Proc. IRE, 46, 256-292, 1958.

Victor, W. K. , R. Stevens, and S. W. Golomb, "Radar Exploration of Venus," Jet Propulsion Lab. Tech. Rept., 32-132, 1961.

Webb, D. H. , Sky and telescope, 5. 3. 1946.

Winter, D. F. , "A Theory of Radar Reflections from a Rough Moon," J. Res. NBS, 66D, 215-226, 1962.

Yaplee, B. S. , R. H. Bruton, K. J. Craig, and N. G. Roman, "Radar Echoes from the Moon at a Wavelength of 10 cm," Proc. IRE, 46, 293-297, 1958.

Yaplee, B. S. , N. G. Roman, K. J. Craig, and T. F. Scanlon, "A Lunar Radar Study at 10 cm Wavelength," Paris Symposium on Radio Astronomy, ed. R. N. Bracewell, p. 19, Stanford University Press, Stanford, 1959.



# A LONG-PATH ABSORPTION REFRACTOMETER

W. G. Tank\*

## INTRODUCTION

Because the earth's atmosphere is generally turbulent, the density and water vapor content of air vary, at every point, with time. This heterogeneity of atmospheric composition implies that the speed of electromagnetic signals through the atmosphere is a function of location. Mathematically, this fact can be expressed as  $n = n(x)$ , where  $n$  denotes the normalized propagation speed, or atmospheric refractive index. The conversion factor from time measurement in systems of space measurement based, as are electromagnetic ranging devices, essentially on the simple expression that distance is the product of speed and time, must therefore be the space-averaged propagation speed,

$$\bar{n} = \frac{1}{L} \int_0^L n(x) dx, \quad (1)$$

where  $L$  denotes the propagation path. In determining  $\bar{n}$  with standard meteorological instrumentation, one is always limited, physically, to determining  $n(x)$  at some finite number of values of  $x$  along the path. The integral expression for  $\bar{n}$  permits the interpretation that, even though errorless determinations of the index  $n$  at each of, say,  $k$  sampling points were made, the average index  $\bar{n}$  would still be subject to a finite sampling error to the extent that

$$\frac{1}{k} (n_1 + n_2 + \dots + n_k) \neq \frac{1}{L} \int_0^L n(x) dx.$$

---

\* Boeing Company, Seattle, Washington.

The above inequality constitutes the current limit to the accuracy attainable in distance measurement using electromagnetic ranging techniques. This paper proposes a refractive index measuring system under development at Boeing capable of relaxing that limit.

## THE INSTRUMENT SYSTEM

### Theoretical Background

The refractive index at a point in clear air can be written as the sum of two terms,

$$n = A \sum_{i=1}^N \rho_i + B \rho_w, \quad (2)$$

where the  $\rho$ 's refer to the densities or concentrations of the different atmospheric gases. Specifically,  $\rho_w$  refers to the water vapor density,  $\rho_i$  to the densities of the other constituents (oxygen, nitrogen, argon, etc.). The indicated summation is to proceed over all these latter constituents, thus providing, according to Dalton's Law, a measure of the total dry-air density. Water vapor is by far the most variable constituent of the atmosphere. The dry air components show remarkable constancy in their relative proportions. Hence, knowledge of the air content (i. e. , amount per unit volume) or density of just one of these latter constituents constitutes such knowledge of all the rest.

Accepting Equation (2) and all its implications, the absorption of infrared radiation by different atmospheric gases at selected wavelength bands now provides the basis for an instrument system to determine  $\bar{n}$  as a truly integral function of path length, for the total amount of energy absorbed from a beam propagated through the atmosphere depends only on the amount of the absorbing constituent along the path, and not on its distribution. Hence, monitoring an infrared beam in a water vapor absorption band and in an absorption band of one

of the dry air constituents will provide all the information required to compute refractive indices according to Equation (2), which value, because of the actual physical process of absorption, will then precisely represent the  $\bar{n}$  defined in Equation (1).

### System Description

The idea of determining atmospheric composition by measuring atmospheric infrared absorptions is certainly not new, the idea preceding efficient means of implementation by nearly forty years (Fowle<sup>[1]</sup>). The concept is simplicity itself, requiring, basically, a continuous spectrum radiation source, a radiation detector, and means for effecting narrow-band, wavelength isolation. The need for a precisely calibrated source can be negated by measuring received energy in two different but adjacent bands of the infrared spectrum, one of which is attenuated by the constituent of interest, the other not. The desired constituent density measurement is then provided by the ratio of the two band energies sensed. In this scheme the former band is considered the sensor, the latter the reference. To determine the atmospheric refractive index in this manner, then, a minimum of three wavelength bands must be monitored — two serving as sensors (one for water vapor, the other for any one of the dry-air gases), the third as the reference.

### The Sensing and Reference Bands

The choice as to which three wavelength bands to use is largely arbitrary. The three should, however, be grouped as closely as possible together in order to minimize adverse effects on system accuracy that could be caused by differential scattering effects in a hazy atmosphere (more on this later). Furthermore, to take advantage of the simplicity, reliability, and obtainability offered by lead sulfide cell infrared detectors as system radiation sensors, all wavelengths should be in the region of peak sensitivity of such cells. Accordingly, consider

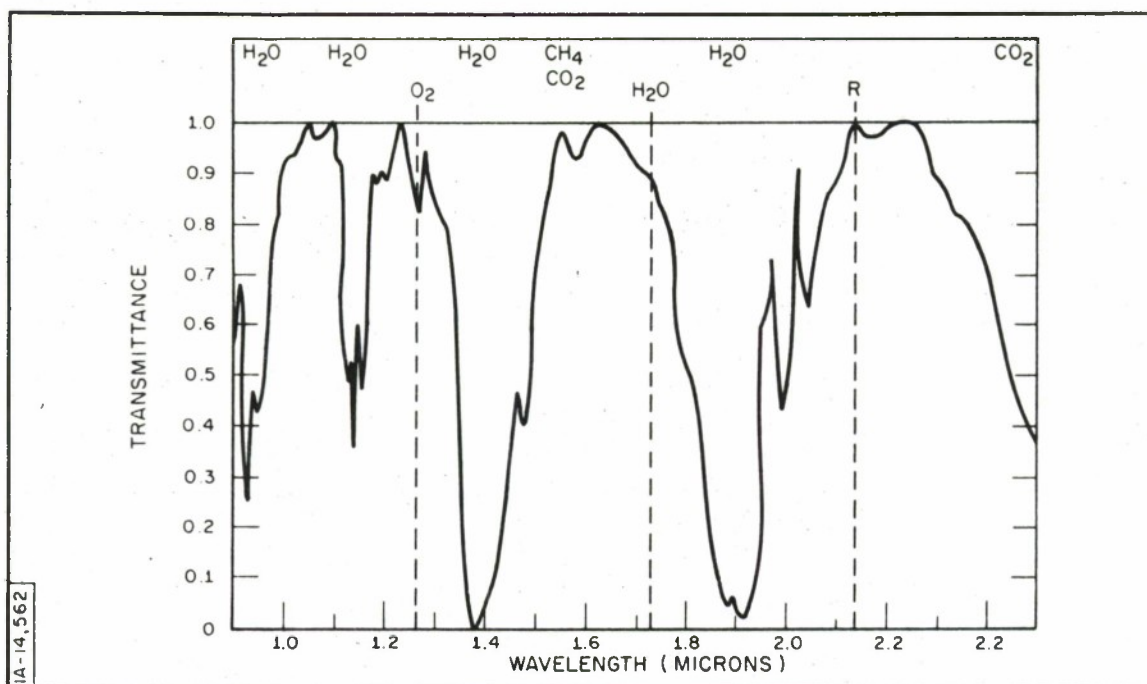


Figure 1. The Near-Infrared Solar Absorption Spectrum (The absorbing atmospheric constituents are identified at the top of the chart above the different absorption bands, the refractometer filter bands by the three dashed abscissas.)

solar absorption spectrum, normalized to peak transmission, presented by Gates<sup>[2]</sup> and shown in Figure 1. The abscissa range indicated defines the wavelength region of peak sensitivity of uncooled lead sulfide cells (Kruse, McGlauchlin and McQuistan<sup>[3]</sup>).

The spectrum shown in Figure 1 is characterized by four strong water vapor absorption bands, four "window" regions, a weak oxygen and a weak carbon dioxide band. Radiation on any of the window regions could be monitored to supply the reference signal, that in any of the water vapor absorption bands to effect the measurement of water vapor content, and that in the oxygen or the carbon dioxide band to determine the dry-air constituent content.



Three narrow wavelength bands satisfying the requirements of an absorption refractometer are thus specified as indicated, centered at wavelengths of  $2.12\ \mu$ ,  $1.73\ \mu$  and  $1.256\ \mu$  for the reference, water vapor and oxygen or dry-air density sampling bands, respectively. The water-vapor sampling band is displaced from the center to the wing of the strong  $1.86\ \mu$  absorption band for two reasons. First, over any sort of range at all, virtually all the  $1.86\ \mu$  radiation would be absorbed from an infrared beam, leaving no signal to effect the desired water vapor measurement. Second, energy in the oxygen band suffers some water vapor absorption by the wing of the  $1.37\ \mu$  water vapor absorption band. Water vapor absorption at  $1.73\ \mu$  is equal to that in the oxygen band. Hence, by referencing the band energy of the latter to that of the former, unwanted water vapor absorptions at  $1.256\ \mu$  can be negated. The  $1.73\ \mu$  water vapor sampling band itself is referenced to the window band.

#### Receiver Optics

An optical system for simultaneously monitoring a beam of infrared radiation at the three wavelengths just specified through a single aperture is shown schematically in Figure 2. A mechanically chopped, collimated beam of energy from a remote, broadband, tungsten filament source of high thermal inertia is directed at the receiver. The Cassegrain collecting optics focus the incoming beam onto a field-stop aperture. The divergent beam then passes through a series of mirror beam splitters, the first of which has a transmission-to-reflection ratio of about 2:1, the second a ratio of 1:1. The beam-splitter series thus serves to split the collected beam into three components, directing approximately one-third of the collected energy onto one of the three indicated narrow bandpass, germanium interference filters. Each arm of the split and filtered beam then impinges on a mixer cone which serves to distribute the filtered energy evenly over the surface of a lead sulfide cell infrared detector.

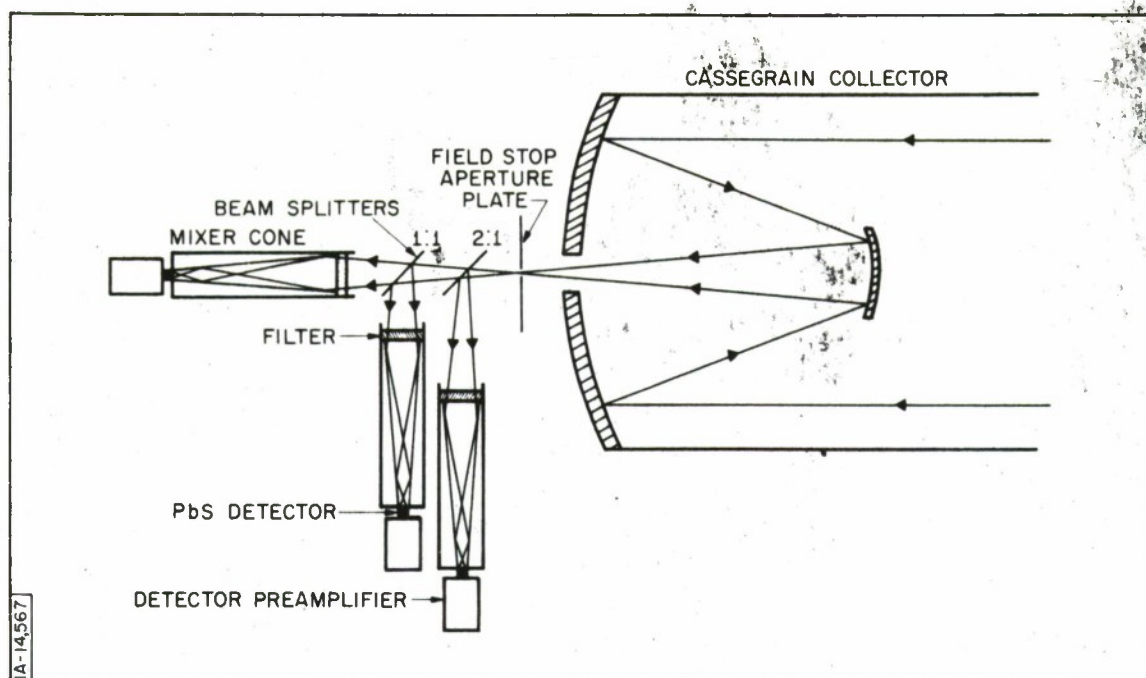


Figure 2. Schematic Diagram of the Refractometer Receiver Bead Optics

This even distribution eliminates shot noise effects that could be caused by inequalities in sensitivity at various spots on the detector surfaces. The interior reflecting surfaces of the mixer cones are gold-plated for the greatest degree of reflection efficiency. Source-to-receiver alignment is accomplished with the aid of 20X spotting telescopes mounted on both the beam and field collimating optics. The entire receiver head is attached to a standard 3-1/2- x 8-inch thread transit head mount for utilization on a standard surveyor's transit tripod.

#### The Read-Out System

The desired comparison between reference and sensing band energies is their ratio, because such a comparison reflects only disproportionate, and not proportionate, energy changes. That is, system response would not re-

reflect a change in the general level of sensed energy caused by the presence of haze or fog in the light beam. The desired ratio is obtained as follows.

Located in the receiver head, directly coupled to the lead sulfide cell detectors, are high input, low output impedance detector preamplifiers (Figure 2). The amplified, essentially alternating-current (as a result of the source chopping) detector signals are then fed into alternating-current, capacitor-coupled (to eliminate the high direct-current cell bias) logarithmic converters. These converters rectify the alternating-current signals and give direct-current outputs proportional to the logarithm of the root mean square value of the input signals. The converter outputs are then combined in a differentiating network to yield a recorded signal proportional to the difference between the logarithms, and hence to the ratio, of the detector input signals. Schematically, the read-out system is shown in Figure 3.

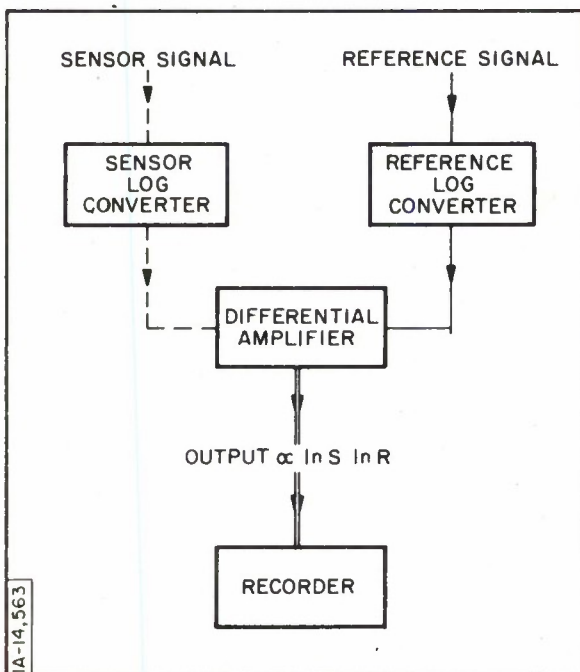


Figure 3. Theoretical Refractometer Readout System

## ANTICIPATED OPERATIONAL CHARACTERISTICS

The instrument just described is still in the development stage. But experience with an infrared absorption hygrometer previously developed and applied (Tank and Wergin<sup>[4]</sup>), and operating according to the philosophy and methods of the proposed refractometer, permits the following refractometer performance characteristic estimates.

### Range Capabilities

An estimate of the range capability of the proposed refractometer boils down, essentially, to the answer to the following question: how far can the source be backed off from the receiver such that the radiant energy collected is still sufficient to generate a signal-to-noise ratio significantly greater than unity? The power received from a remote source emitting a directed beam of energy in the wavelength interval  $\Delta\lambda$  is

$$W_{\lambda} = I_{\lambda} \cdot \frac{A^2}{L^2} \cdot \frac{W_1}{W_2} \cdot \frac{\Delta\lambda}{2\pi} \cdot \tau_0 \cdot \tau_A, \quad (3)$$

where

- $I_{\lambda}$  = intrinsic spectral radiant emittance of the source,  
watts  $\text{cm}^{-2}$  micron<sup>-1</sup>
- $A$  = the area of the collecting optics aperture;
- $\Delta\lambda$  = bandwidth of the wavelength isolation filters, microns
- $\tau_0$  = transmittance of the optics;
- $\tau_A$  = transmittance of the atmosphere; and
- $L$  = propagation path length.

The solid angles  $W_1$  and  $W_2$  are defined by the source collimating optics. Specifically,  $W_1$  is the solid angle subtended by the collimating optics aperture at the source,  $W_2$  the solid angle subtended by the source at the aperture. The



four leading terms on the right side of Equation (4) are thus simply system parameters. Both the beam and field collimators used in the refractometer consist of 8-inch aperture, 128-inch (folded) focal length Cassegrainian reflectors. The filter bandwidths are 0.025 micron. For a half-inch source diameter, then, Equation (3) can be written, utilizing the numerical values of the system parameters and taking as a pessimistic estimate of  $\tau_0$  a value of 0.05, as

$$W_{\lambda} = \left(1.5 \times 10^{-7}\right) \frac{I_{\lambda}}{L^2} \cdot \tau_A \text{ watts} , \quad (4)$$

where  $L$  is expressed in kilometers.

When the source emittance,  $I_{\lambda}$ , is expressed as defined in Equation (3), the power received,  $W_{\lambda}$ , is given in watts. That incident radiation on an uncooled lead sulfide cell which produces a signal-to-noise ratio of unity is, in the wavelength region of interest, of the order  $10^{-11}$  watts (Kruse, McGlauchlin and McQuistan<sup>[3]</sup>). Therefore, for workable signals the following inequality must hold:

$$\left(1.5 \times 10^{-7}\right) I_{\lambda} \frac{\tau_A}{L^2} > 10^{-11} . \quad (5)$$

The emittance of a  $1,400^{\circ}\text{C}$  blackbody (peak emission at about  $1.7 \mu$ ) will be of the order of  $10 \text{ watts cm}^{-2} \text{ micron}^{-1}$ . Utilizing this value for the source emittance, inequality (6) may be expressed as

$$L < \left(1.2 \times 10^2\right) \tau_A^{1/2} . \quad (6)$$

The range at which the refractometer can be worked, then, depends on the atmospheric transmittance. For ranges on the order of tens of kilometers,

the transmittance may (pessimistically) be expected to be on the order of  $10^{-2}$ . This estimate considers both absorption and scattering losses in the propagated beam. Hence, the workable range of the system, too, will be on the order of tens of kilometers.

### Expected Calibration

It is expected that the calibration of the refractometer will prove to be quite predictable. Gates<sup>[2]</sup> has shown that throughout the spectral region  $0.87 \mu$  to  $2.54 \mu$  both the random line (water vapor) and regular line (oxygen) absorption band transmissions vary as the square root of the total amounts of absorbing material in the propagation path according to

$$\ln T = C m^{1/2} \quad (7)$$

In the above Equation (valid for transmissions ranging between 20 and 80 percent),  $T$  represents transmittance,  $C$  a transmission coefficient, and  $m$  the total amount of absorbing constituent. For water vapor, this latter quantity is usually expressed as precipitable centimeters,  $w$ , of water and for oxygen as atmo-km,  $l$ , of oxygen. The recorded signals from the refractometer may thus be expected to vary linearly with  $m^{1/2}$ , as past work with the infrared hygrometer indeed verifies (Tank and Wergin<sup>[4]</sup>). Over the range of  $w$  and  $l$  values to be expected, and for propagation paths ranging in length from 5 to 50 kilometers, the  $l$  and  $w$  calibration curves for the refractometer are as shown in Figure 4. The curves are calculated as dictated by Equation (3) and by the response characteristics of the previously calibrated infrared hygrometer. The dry-air and water vapor densities can be recovered from the measured parameters according to the following relationship:

$$\rho_d = 6.16 \left( \frac{1}{L} \right) \left( \frac{K_g}{m^3} \right), \quad \text{and} \quad (8)$$

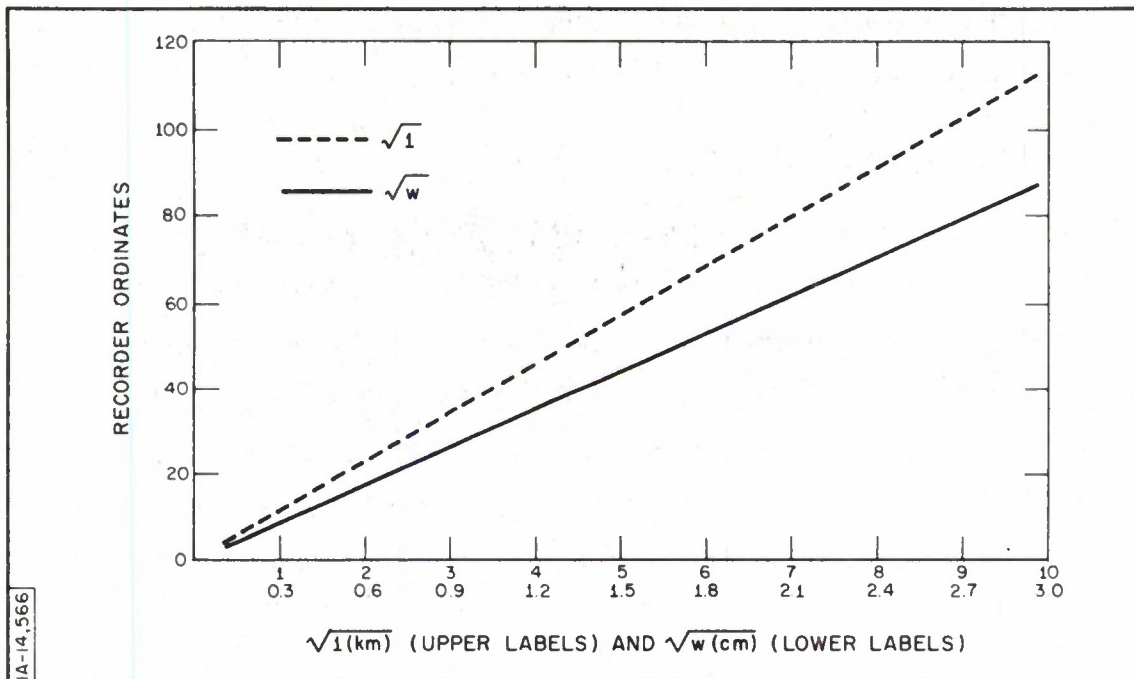


Figure 4. Theoretical Refractometer Calibration Curves

$$\rho_w = 10.0 \left( \frac{w}{L} \right) \left( \frac{\text{gm}}{\text{m}^3} \right), \quad (9)$$

where  $\rho_d$  and  $\rho_w$  denote the dry-air and water vapor densities, respectively, in the units shown. When both  $L$  and  $w$  are given in kilometers and centimeters, respectively, the propagation path length,  $L$ , must be given in kilometers.

#### Expected Accuracy

In estimating the accuracy of dry-air and water vapor measurement achievable with the refractometer, the following factors must be considered: electronic noise effects, ambient temperature and pressure effects on absorption, differential scattering attenuation effects, and the variability of atmospheric carbon dioxide content. The manner in which these factors act

to limit system accuracy, and the expected magnitude of the effect, can be presented as follows.

#### Electronic Noise Level Limits

Amplifier and recorder noise combine to give a system noise level of something less than 10 microvolts. Based on the expected system sensitivity as indicated in Figure 4, such a signal level is equivalent to optical depths of oxygen and water vapor of about  $10^{-7}$  kilometers and  $10^{-6}$  centimeters, respectively. For ranges of orders of kilometers, such magnitudes imply electronic noise errors in oxygen and water vapor densities of orders one part per hundred million and one part per billion, respectively. In other words, the effect is negligible.

#### Ambient Temperature and Pressure Effects

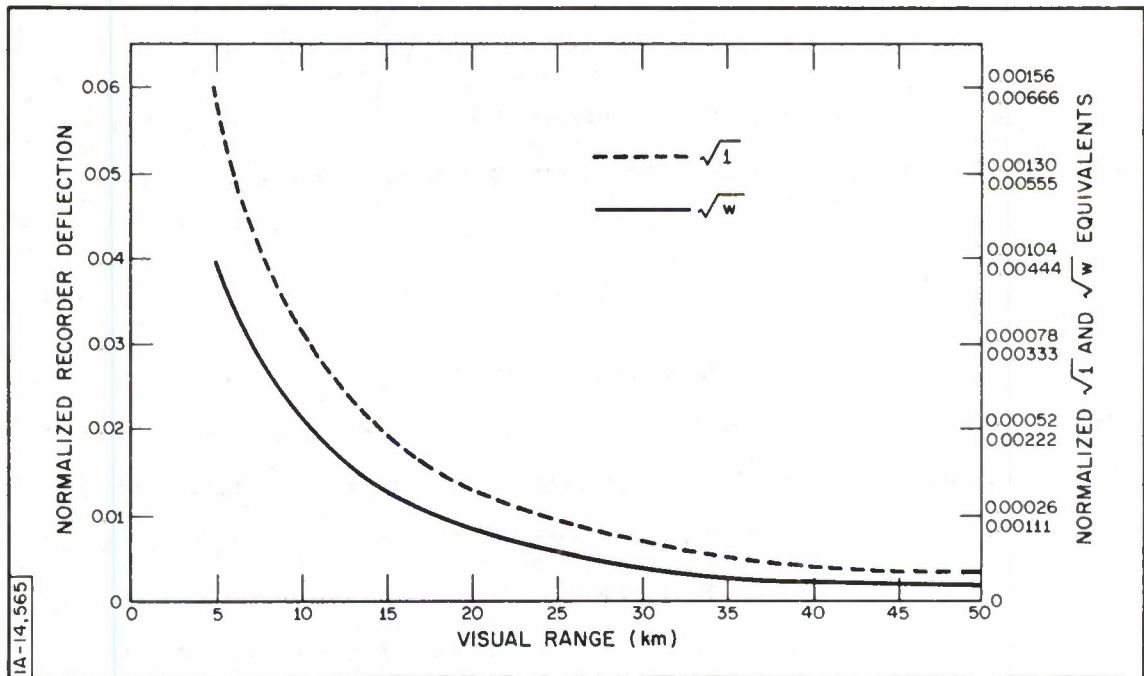
The absorption of energy within a certain wavelength band is dependent to some extent on both atmospheric temperature and pressure. Although such effects become appreciable for drastic changes in ambient temperature and pressure, calibration curves established at given pressure-altitudes should remain insensitive to those changes associated with the normal progression of "weather." This statement is substantiated by past work with the infrared hygrometer (Tank and Wergin<sup>[47]</sup>).

#### Differential Scattering Attenuation Effects

Scattering of near infrared energy by atmospheric haze particles is wavelength-dependent. Specifically, the scattering theory predicts that, for given particle size distributions, the shorter the wavelength the more efficient the scatterer. Consequently, the radiation intensity perceived at  $1.73 \mu$  will be disproportionately less than that perceived at  $2.12 \mu$ , and that at  $1.256 \mu$  will be less than that at  $1.73 \mu$ . Based on data on light transmission through haze



presented by Gibbons, [5] the magnitude of the effect of the refractometer output signals is as shown in Figure 5. Both sets of ordinate labels are normalized



Ordinate labels are normalized to propagation path length in kilometers. The upper set of right-hand ordinate labels refers to atmo-kms of oxygen; the lower set to precipitable cms of water.

Figure 5. Calculated Error Signals, Caused by Differential Scattering Effects in Atmospheric Haze, as Functions of Visual Range

to the propagation path length,  $L$ , in kilometers. The corrections implied are negative corrections, insofar as the equivalent optical depth values express apparent excesses of oxygen and water vapor contents attributable to differential scattering effects. But again the effect is negligible, because for path lengths of the order of 10 kilometers the scattering noise signals are comparable to those associated with electronic noise.

## The Variability of Atmospheric CO<sub>2</sub> Content

Dalton's Law relating total pressure to partial pressure can be expressed in terms of density as

$$\rho_T = (\rho_1 + \rho_2 + \dots + \rho_n). \quad (10)$$

That is, total dry-air density can be considered the sum of the individual atmospheric constituent densities. Individual constituent densities can be expressed as

$$\rho_i = M R_i \rho_T, \quad (11)$$

where  $M R_i$  denotes the  $i^{\text{th}}$  constituents mixing ratio, i. e., its percent by weight of the total dry-air mass per unit volume. At this point, the philosophy of the refractometer is that all dry-air constituents exhibit constant mixing ratios. Though generally true for the so-called permanent atmospheric gases (nitrogen, oxygen, argon, plus helium and hydrogen and the noble gases), the atmospheric carbon dioxide content does show considerable variation. This variation is due to a variety of reasons, chief of which are the release of CO<sub>2</sub> to the atmosphere by combustion processes and the exchange via biological processes of CO<sub>2</sub> with soil and vegetation. At any rate, the CO<sub>2</sub> mixing ratio is more properly expressed as

$$M R_{\text{CO}_2} = \overline{M R}_{\text{CO}_2} + \Delta M R_{\text{CO}_2}, \quad (12)$$

where the overbar denotes a constant "average" mixing ratio and the  $\Delta$  a variable component brought about by the processes must mentioned.

Utilizing Equations (11) and (12) in accordance with Equation (10), then

$$\rho_T = \rho_T \sum_{i=1}^m M r_i + \Delta M R_{\text{CO}_2} \rho_T. \quad (13)$$

The summation in Equation (12) is equal to unity, and the remaining term on the right side is thus interpreted as an error in the inferred density, as measured by the refractometer, ascribable to a variable atmospheric  $\text{CO}_2$  content. The variation in  $\text{CO}_2$  mixing ratio can attain a value of 600 parts per million. Hence, refractometer measured densities will be correct to this same ratio. This, then, is the fundamental limit to the accuracy of density measurements attainable with the refractometer.

It should be remarked that the above limit does not apply to the water vapor density measurement, insofar as this latter quantity is measured directly. System sensitivity will permit water vapor densities to be determined with accuracies of the order of one part per million.

#### CONCLUSIONS

The claims made regarding the performance of the infrared absorption refractometer just described remain to be proved, insofar as the first prototype unit is still to be tested in the field. But in light of past experience with an absorption hygrometer, the claim as to the ability through use of the refractometer to measure dry-air and water vapor densities to within six parts per ten thousand and a few parts per million, respectively, is not considered unreasonable. Such accuracies imply that the atmospheric refractive index may be specified to seven significant figures. And what is just as important relative to use of the refractometer in conjunction with electromagnetic ranging devices is that the refractive index so specified will represent a space averaged value determined as a truly integral function of path length.

## REFERENCES

1. F. E. Fowle, "The Spectroscopic Determination of Aqueous Vapor," Astrophys. J. 35, 149-162, 1912.
2. D. M. Gates, "Near Infrared Atmospheric Transmission to Solar Radiation," J. Opt. Soc. Am., 50, 1299-1304, 1960.
3. P. W. Kruse, L. D. McGlauchlin and R. B. McQuistan, Elements of Infrared Technology: Generation, Transmission, and Detection, New York, John Wiley and Sons, Inc. ,
4. W. G. Tank, and E. J. Wergin, "A Long-Path Infrared Hygrometer," in Humidity and Moisture, Vol. I. A. Wexler, ed., New York, Reinhold Publishing Co. , 1964.
5. M. G. Gibbons, "Wavelength Dependence of the Scattering Coefficient for Infrared Radiation in Natural Haze," J. Opt. Soc. Am., 48, 172-176, 1958.



## EXPERIMENTS AT COLD LAKE, CANADA

L. G. Rowlandson<sup>\*</sup>

### INTRODUCTION

Tropospheric refraction has become a matter of great concern to the Air Force in recent years. It is hard to find a Command and Control System that does not deal with propagation characteristics in one form or another. For quite a few of these systems, propagation has an important effect on the accuracy possible. For example, the failure to meet the accuracy requirements imposed on finders and missile test range tracking radars is not limited by the hardware. Interferometer-type trackers and other advanced radars are inherently capable of measuring angle and range to the required precision. Rather, the accuracy attainable in practice is limited by propagation errors — especially at the low elevation angles that are used to obtain maximum coverage.

The data on our original work involving height finders was presented at a New York Air Defense Sector symposium on height accuracy in 1962. At that time, it was shown that the operational height accuracy required was greater than the system could provide. This fact contributed to the cancellation of a large-scale test the Sector had planned to run, which presumably would have accomplished nothing but the production, at great expense, of information that was already available.

Previous attempts to correct these errors have largely been based on "model" atmospheres that can be set up from the mass of statistical data available on tropospheric refraction. These models represent hypothetical

---

<sup>\*</sup> The MITRE Corporation, Bedford, Massachusetts.

average situations, but the deviations from average actually encountered are so large that this type of model cannot give the accuracy required for present-day tracking problems. We believe the solution to these problems must take into account the actual refractive index profile at the time and place of measurement.

#### LIMITATIONS ON ACCURACY

The factor that essentially limits the system accuracy is the uncontrollable variation of the propagating medium. Conditions change seasonally, daily, and sometimes within a matter of minutes. The subject has enough history to enable something to be said about average behavior — but, unfortunately, the historical averages do not tell us all we need to know about specific situations.

If the index of refraction decreased uniformly with height then we could easily calculate the accumulated bending that has occurred up to any point on the ray. For an ideal hydrostatic atmosphere,  $T$  would vary exponentially with height. It turns out that the atmosphere, on the average, does seem to behave in this way.

We are first seeking to learn to what extent corrections can be made, using methods that are admittedly more appropriate to a laboratory than to an operational system. We are confident that this study phase of the program will lead to the development of practical methods which will give the best compromise between operational feasibility and attainment of ultimate accuracy.

At least two alternatives can answer the question: How can accuracy be increased? One is to simply avoid the problem, at least in part, by rejecting data obtained at low elevation angles. Obviously, however, restriction on the use of low-angle data reduces coverage. The system designer or operations analyst must then establish the best trade-off in lieu of a bonafide correction

for the problem. The second alternative is to use all available surface weather, radiosonde and synoptic meteorological predictions to reduce errors at low elevation angles.

## FACILITIES

Aircraft instrumentation and procedures to test the accuracy of radiosonde sounding have been developed. Furthermore, programs that can assimilate and use both surface weather and radiosonde data in the ray-tracing program have been designed. The mounting arrangement of the instrumentation on the outside of the aircraft being used in the Cold Lake experiment, the two-cavity refractometric probe, and the digital data instrumentation, are shown in Figures 1, 2 and 3, respectively. The use of atmospheric parametric measurements provides a high degree of accuracy in determining propagation errors.

The approach used is to compare the calculated results with independent measurements of the tracking error and of the index profile in a test situation. At the same time, the index profile is correlated with meteorological data relevant to the time and location of the tests. These studies should lead to improved understanding of the relationship between propagation errors and meteorological conditions, and yield estimates of lower bounds for tracking errors. As a result, some insight should be provided into techniques for correcting radar observations to obtain maximum accuracy under operational conditions.

The measurements indicate that:

- (a) at low elevation angles, the error cannot be removed by techniques based on "average" atmospheric behavior;



Figure 1. External View  
of Aircraft  
Probes



Figure 2. Two-Cavity  
Refractometer  
Probe

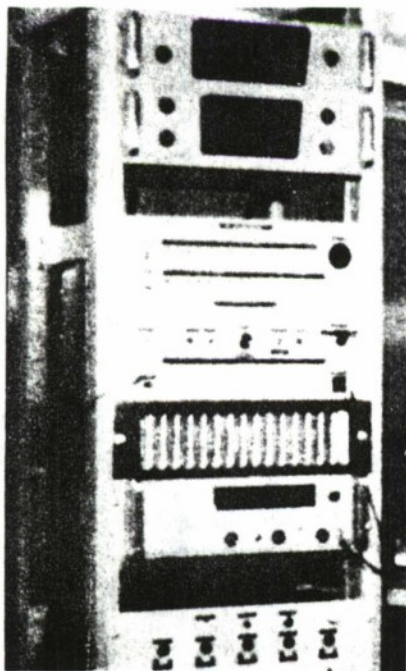
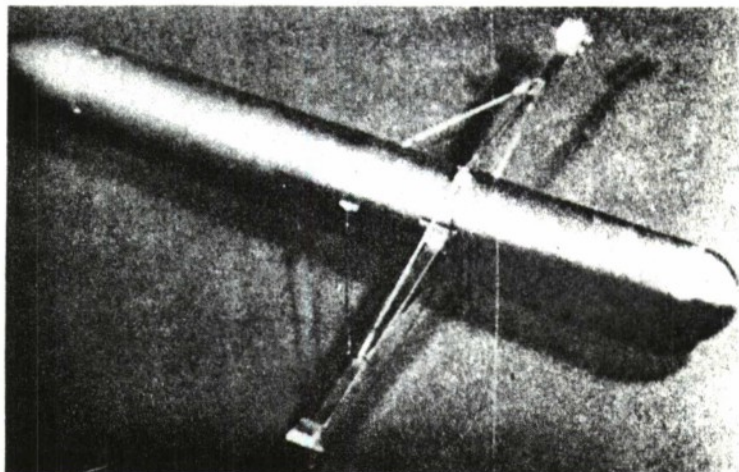


Figure 3. Digital Data Instrumentation



- (b) at high elevation angles, the error is reduced but useful coverage is also reduced; and
- (c) data from the meteorological services could be applied to reduce the errors for low elevation angle operation.

## THE COLD LAKE EXPERIMENT

(The previous discussion serves as background information for the film shown at the meeting. The experiment, conducted and filmed at Cold Lake, Canada, deals with tropospheric ray path corrections based on the atmospheric index of refraction.)

The geographical arrangements of the Cold Lake experiment can be seen in Figure 4. Preliminary tests over the range were conducted in the summer of 1963. An extreme series of tests is scheduled for September and

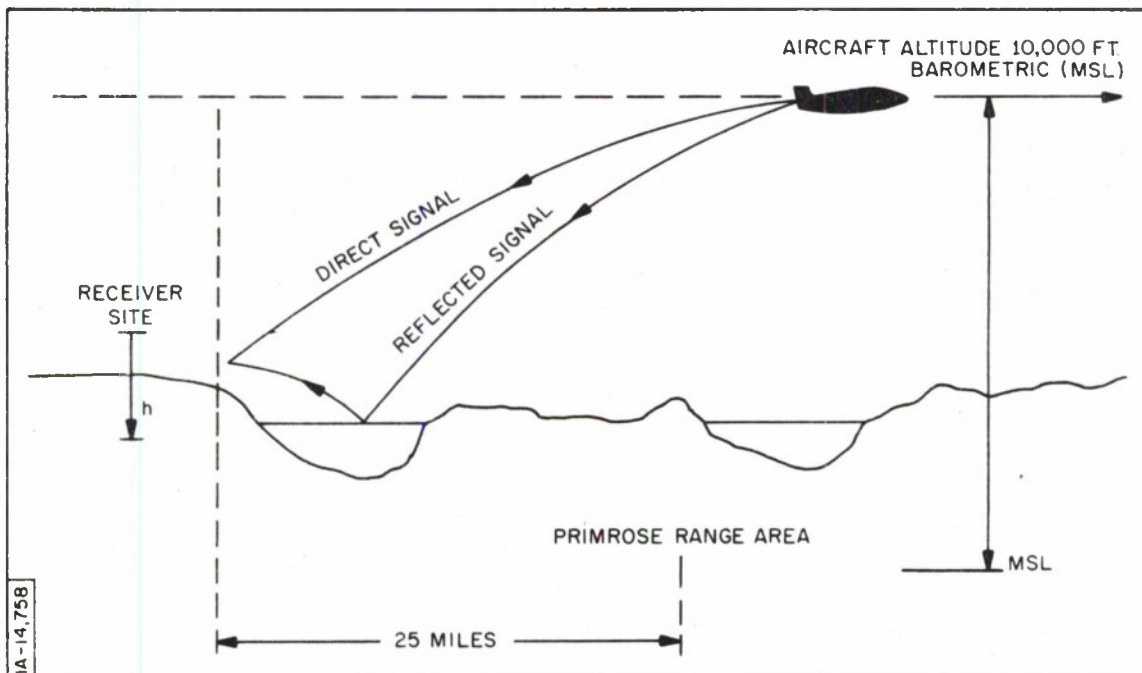


Figure 4. Geographic Arrangement of Cold Lake Experiment

October of 1964. In addition, we plan to conduct some joint measurement experiments with Dr. Hay at the University of Western Ontario in October. In November, we may support Dr. Cummings in the measurement program at the Eastern Test Range. Finally, we plan to join forces with Dr. Eric B. Kraus, Woods Hole Oceanographic Institute, to obtain measurements near Aruba, in the Netherlands Antilles.

The objective of the Cold Lake test is to gather data necessary for determining how accurately propagation errors can be calculated, based on current meteorological sounding techniques. The reflection interferometer served as an independent measure of the propagation errors, thus providing a yardstick for evaluation of the different soundings for prediction techniques.

# WATER VAPOR DENSITY MEASUREMENTS UTILIZING THE ABSORPTION OF VACUUM ULTRAVIOLET RADIATION

James E. Tillman\*

## INTRODUCTION

It should be quite apparent to anyone who has encountered the problem of atmospheric water vapor measurements that a better understanding of the basic characteristics of the currently available instruments is necessary, and that other instruments must be developed because of limitations of these instruments. The present instruments, which are fast and accurate generally, are quite complex, bulky, and expensive, and/or their characteristics have not been adequately documented.<sup>[1, 2, 3, 4, 5]</sup> These problems would suggest that the Lyman  $\alpha$  absorption hygrometer deserves careful study and development because of its potentialities. If it is possible to overcome the basic problems associated with this instrument, it should be one of the most valuable instruments, since it is potentially capable of very fast absolute measurements with a small, light weight, relatively low-cost system.

Consequently, this paper is devoted to describing the basic physical characteristics of the ideal system, the problems one might encounter in realizing this system, their probable solution, and some details of the proposed systems. The major aim of the research done by the author has been to understand the basic elements and properties of the vacuum ultraviolet absorption humidimeters, and to attack the most difficult problems associated with the construction of an ideal operational device. Construction of a system has not been attempted, since this would logically follow the successful solution of the

---

\*Massachusetts Institute of Technology, Round Hill Field Station.

known problems. However, sufficient information is available to construct systems which probably would be satisfactory for many applications, especially measurements in the lower troposphere in the absence of liquid water, and at low humidities.

Any problems that might be encountered are known, but the magnitude remains to be determined. An example is what effect does the adsorption of water vapor on the window have on the measurement of large fluctuations in water vapor near saturation. The effect may be similar to that described by Hay<sup>[4]</sup> in refractometer cavities, or it might be less. A possible solution to this problem is to coat the windows with thin films of other materials which are transparent and which do not adsorb water vapor readily. Such techniques are being investigated. The problem of source spectral purity and lifetime can be solved, but no sources have been constructed by the author with the appropriate components, since the technique is straightforward and further investigation may produce a simpler solution.\*

## THEORY

With reference to Figure 1, if it is assumed that a collimated monochromatic photon source is available, then the energy remaining after traversing a distance  $x$  is

$$I = I_0 \exp - \left( \frac{k_1 \rho_1}{\rho_{10}} + \frac{k_2 \rho_2}{\rho_{20}} + \frac{k_3 \rho_3}{\rho_{30}} + \frac{k_4 \rho_4}{\rho_{40}} + \dots \right) x, \quad (1)$$

---

\* Components utilizing these techniques were constructed and used by Dr. H. A. Hinteregger at Air Force Cambridge Research Laboratories up to 1956 for this problem, but the work was dropped before a report was published.



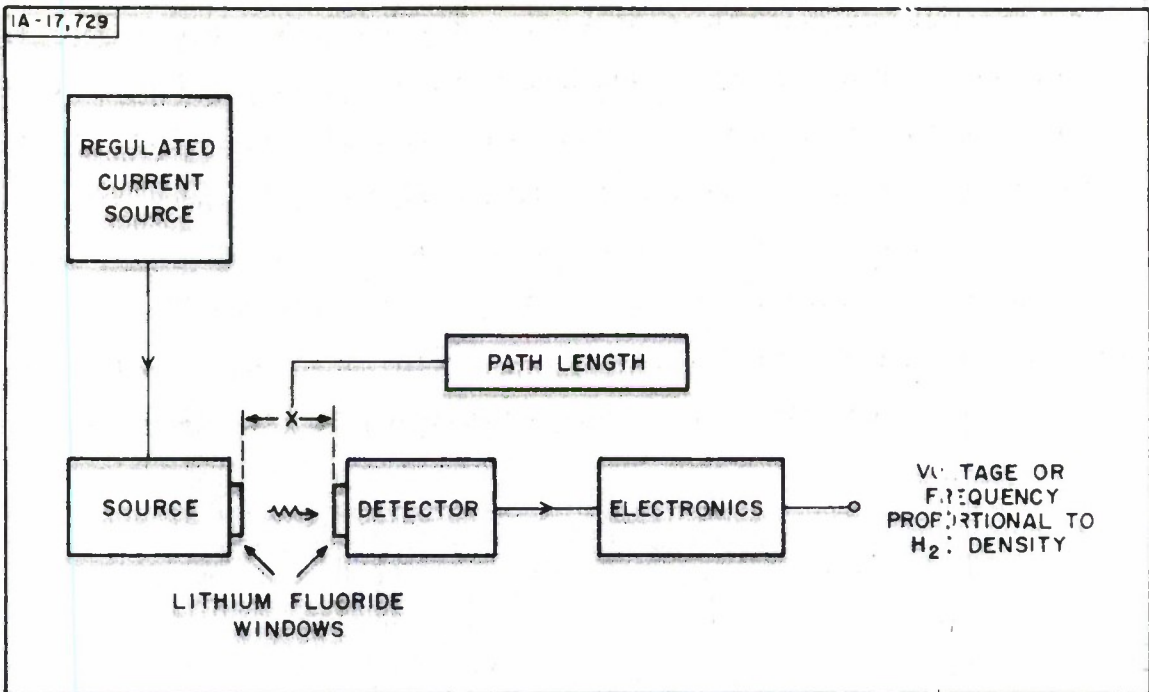


Figure 1. Single-Beam Photon Absorption Water Vapor Density Measuring System

where

$I$  = energy at wavelength  $\lambda$ , incident on surface  $x_i = x$ ,

$I_0$  = energy at wavelength  $\lambda$ , incident on surface  $x_i = 0$ , and

$k_i$  = absorption coefficient of  $i^{\text{th}}$  gas in  $\text{cm}^{-1}$  at wavelength referred to (STP), [6]

$\rho_i$  = density of  $i^{\text{th}}$  gas,

$\rho_{i0}$  = density of  $i^{\text{th}}$  gas at STP (which may be fictitious in some cases).

$i$  = subscript identifying gas:

1  $\rightarrow$   $\text{H}_2\text{O}$ ,  $k_1 = 387$ ;

2  $\rightarrow$   $\text{O}_2$ ,  $k_2 = 0.34$  (slightly pressure-sensitive);

3  $\rightarrow$   $\text{CO}_2$ ,  $k_3 = 1.97$ ;

4  $\rightarrow$   $\text{O}_3$ ,  $k_4 = 640$ ; etc., for any other gases, and

$x$  = path length (cm).

For this equation to hold, it is assumed that the processes producing the absorption are such that the  $k_i$  are independent of pressure and the presence of other gases. If the source is not monochromatic and emits energy at various wavelengths, Equation (1) still may be used to determine the absorption due to several gases if the detector's region of wavelength sensitivity encompasses only one of the emitted wavelengths. If there are several wavelengths or if a continuum of wavelengths is emitted by the source, absorbed by the gases, and detected by the detector, then the equation governing the process becomes

$$I = \int_{\lambda_1}^{\lambda_2} I_o(\lambda) \left\{ \exp - \left[ \frac{k_1(\lambda)\rho_1}{\rho_{1o}} + \frac{k_2(\lambda)\rho_2}{\rho_{2o}} + \frac{k_3(\lambda)\rho_3}{\rho_{3o}} + \frac{k_4(\lambda)\rho_4}{\rho_{4o}} + \dots \right] \right\} d\lambda, \quad (2)$$

where

- ( $\lambda$ ) indicates that the function is now a function of wavelength, the interval from  $\lambda_1$  to  $\lambda_2$  is that wavelength interval in which both emission and detection occur, and
- $I$  is now the total energy at all wavelengths.

The previous assumptions are still necessary, especially the restriction that the  $k_i(\lambda)$  are independent of pressure and composition; if the  $k_i(\lambda)$  are a function of pressure, then the problem becomes even more complex. To determine the response at the output of the detector, an additional term, the detector's response as a function of wavelength must be included inside the integral of Equation (2). In the following discussion, the sole use of Equation (2) will be to qualitatively explore the effects of a non-monochromatic source and of absorption coefficients which vary with wavelength, and to determine the

degree of accuracy to which Equation (1) may be employed when the source is not monochromatic. Alternatively, if a given degree of accuracy is desired, Equation (2) may be used to determine the requisite "spectral purity."

To determine the ease with which the density of a particular gas,  $\rho_i$ , may be measured, Equation (2) should be consulted. As an important example, consider the measurement of water vapor for which  $i = 1$ . First, assume that an essentially monochromatic source can be obtained at any wavelength. Then the problem is to determine the wavelength at which

$$\frac{k_i(\lambda) \rho_1 \rho_{i_0}}{k_i(\lambda) \rho_i \rho_{1_0}}$$

hereafter called the "absolute discrimination ratio" (ADR), is a maximum, considering the range of  $\rho_i$  over which  $\rho_1$  is to be measured. The value of a system operating at this wavelength will then be determined by the minimum value of the ADR, which is dictated by the minimum  $\rho_1$  and/or the maximum  $\rho_i$ . If the ADR is very large for all combinations of  $\rho_1$  and the  $\rho_i$  in the range in which  $\rho_1$  is to be measured, then the system is essentially sensitive to  $H_2O$  alone; however, if the ADR is on the order of 100 or less for some combination of  $\rho_1$  and the  $\rho_i$ , then the  $\rho_i$  must be considered. In measuring  $H_2O$  density in the "vacuum ultraviolet" portion of the spectrum,\* molecular oxygen,  $O_2$ , is the main "background" gas affecting the measurement due to its relative density and to its wide range of absorption coefficient,  $k_2(\lambda)$ ; this is illustrated in Figure 2.<sup>[6]</sup> Figure 3 shows a plot of  $k_1(\lambda)/k_2(\lambda)$ , the "relative discrimination ratio" (RDR), versus wavelength. The ADR is simply equal to the RDR multiplied by  $\rho_1 \rho_{2_0} / \rho_{2_0} \rho_{1_0}$  and, consequently, is a maximum

---

\* Roughly the region below 3500 Å, where 10,000 Å = 1μ or 10 Å = 1mμ.

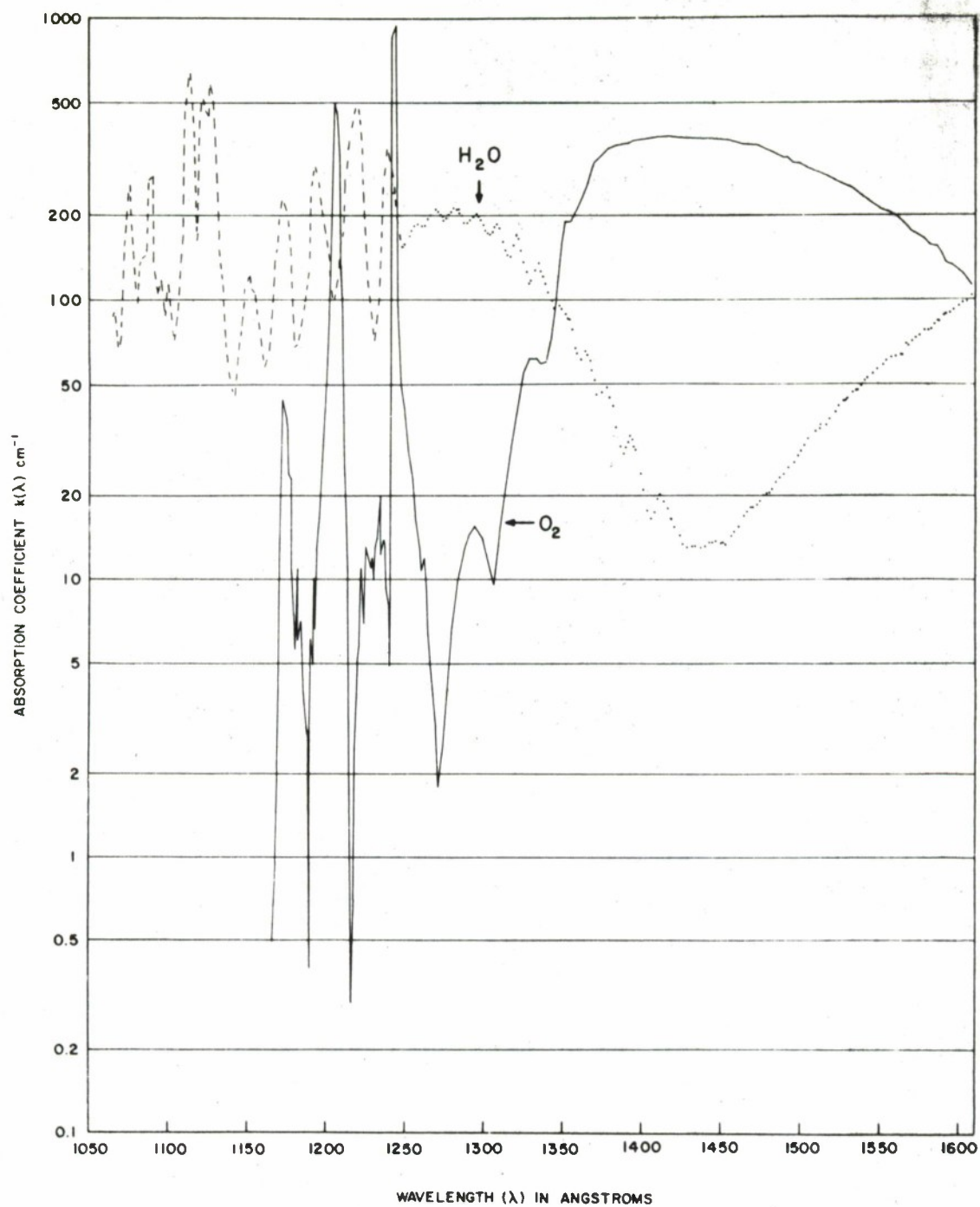


Figure 2. Absorption Coefficients of O<sub>2</sub> and H<sub>2</sub>O vs. Wavelength Referred to STP



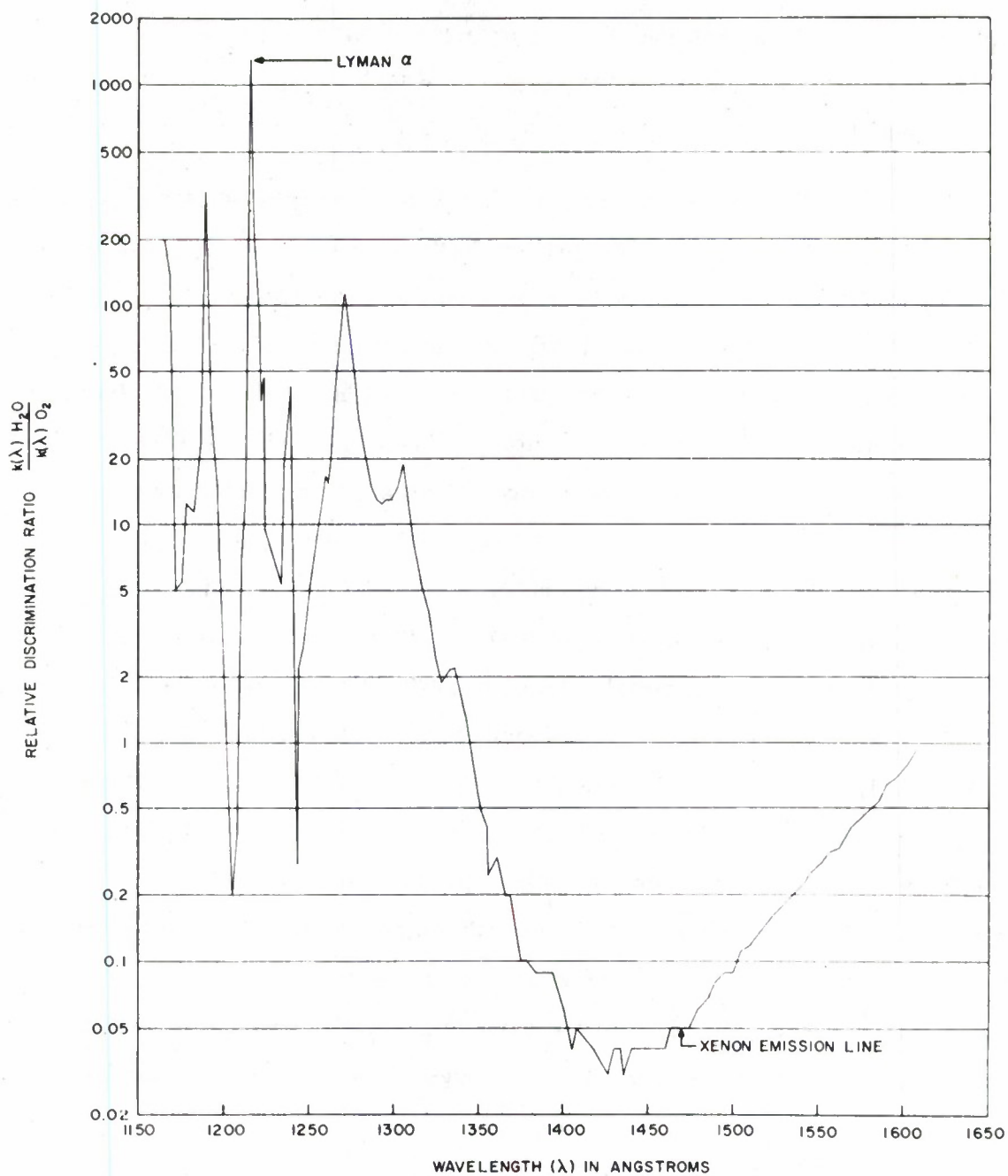


Figure 3. Relative Discrimination Ratio vs. Wavelength

at the same wavelength for which the RDR is a maximum. Notice that the RDR possesses several maxima, the highest being at 1215.6 Å. Also note that the RDR varies by more than four orders of magnitude in the region shown, and that around 1450 Å it is such that any absorption system would be essentially sensitive to  $O_2$  rather than to  $H_2O$ , because the large value of  $\rho_{20} \rho_{10} / \rho_{10} \rho_{20}$ . This point will be considered later in more detail.

Returning to the immediate practical problem of the measurement of  $H_2O$  density, it is a pleasant coincidence that the RDR is maximum at approximately 1215.6 Å, since this also happens to be the Lyman  $\alpha$  emission line of atomic hydrogen. Another useful fact is that all other members of the Lyman series (electronic transitions from the orbits of  $n = 3$  or higher to the  $n = 1$  ground state) are below the short-wavelength cutoff of lithium fluoride, LiF, the only material transparent enough to be used for "windows" in the source and detector.\* The next closest emission lines of atomic hydrogen are the Balmer lines (electronic transitions from the orbits  $n = 3$  or higher to the  $n = 2$  orbit), whose short wavelength limit is 3647 Å. It is quite easy to select a detector whose efficiency essentially drops to zero for wavelengths above 3500 Å or less, and whose short-wavelength cutoff is determined by a LiF window. Such detectors will be discussed in detail in later sections. Therefore, it would seem possible to construct a water vapor density measuring device by using a hydrogen discharge tube to produce the hydrogen atomic spectrum and by selecting an appropriate path length and detector. Since, at first glance, such a system would be sensitive only at Lyman  $\alpha$ , its value should be determined by the ADR of the various gases at Lyman  $\alpha$ . In the troposphere below 10 kilometers, the ADR suggests that  $O_2$  is the main back-

---

\*Other materials such as  $CaF_2$ ,  $MgF_2$ ,  $Al_2O_3$ ,  $SiO_2$ , are transparent only when used in thin films on the order of 1000 Å thick or less.

ground gas because of its large density, even though its absorption coefficient is small; the other gases produce even higher ADR's. Furthermore, the effect of  $O_2$  and the other background gases can be reduced either automatically or by a simple correction based on a relatively inaccurate density measurement. It should be mentioned that a total density measurement accurate to  $\pm 10$  percent of sea level density would provide a water vapor density accuracy of  $\pm 0.02$  gram/cubic meter (equivalent to a  $-55^\circ C$  dew point) as far as background gases are concerned.

#### SOURCE CHARACTERISTICS

The practical realization of an  $H_2O$  density-measuring system operating in the vacuum ultraviolet portion of the spectrum is not quite as simple as is suggested by the atomic emission spectrum of hydrogen, which is almost the ideal spectrum for such a system. The reason is that when the atomic hydrogen emission spectrum is obtained from a hydrogen glow discharge, additional energy, caused by adjacent wavelengths, is obtained at molecular electronic transition. Figure 4 illustrates a spectrum which might be considered typical of a pure hydrogen glow discharge or a hydrogen discharge with a small amount of neon present. Figure 5 shows the same source operated at a much higher hydrogen pressure. The pressure is proportional to the flow, since this is a windowless discharge from a tank of hydrogen into a vacuum system. The wavelength is given in angstrom units; to obtain the actual intensity incident on the detector, a correction must be made for the decreasing transmission with decreasing wavelength of a lithium fluoride window which precedes the detector. The significant increase in the atomic emission, relative to the molecular electronic emission, with decreasing pressure is caused by an increase in electron and/or gas temperature, which, in turn increases the percentage of the dissociated hydrogen in the discharge. The temperature is increased, since the gas

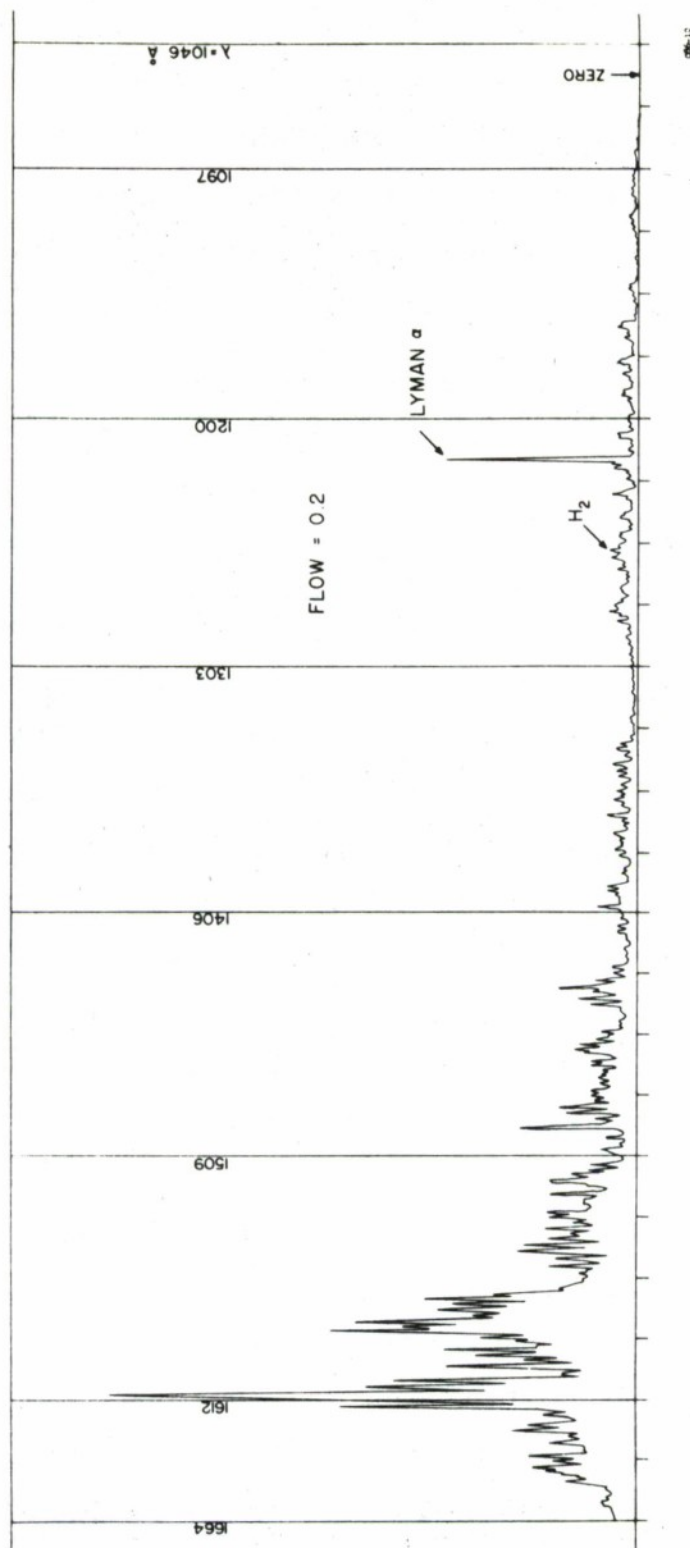


Figure 4. Spectrum of Low-Pressure Hydrogen Glow Discharge; Abcissa: Wavelength,  $\lambda$  ; Ordinate: Relative Intensity



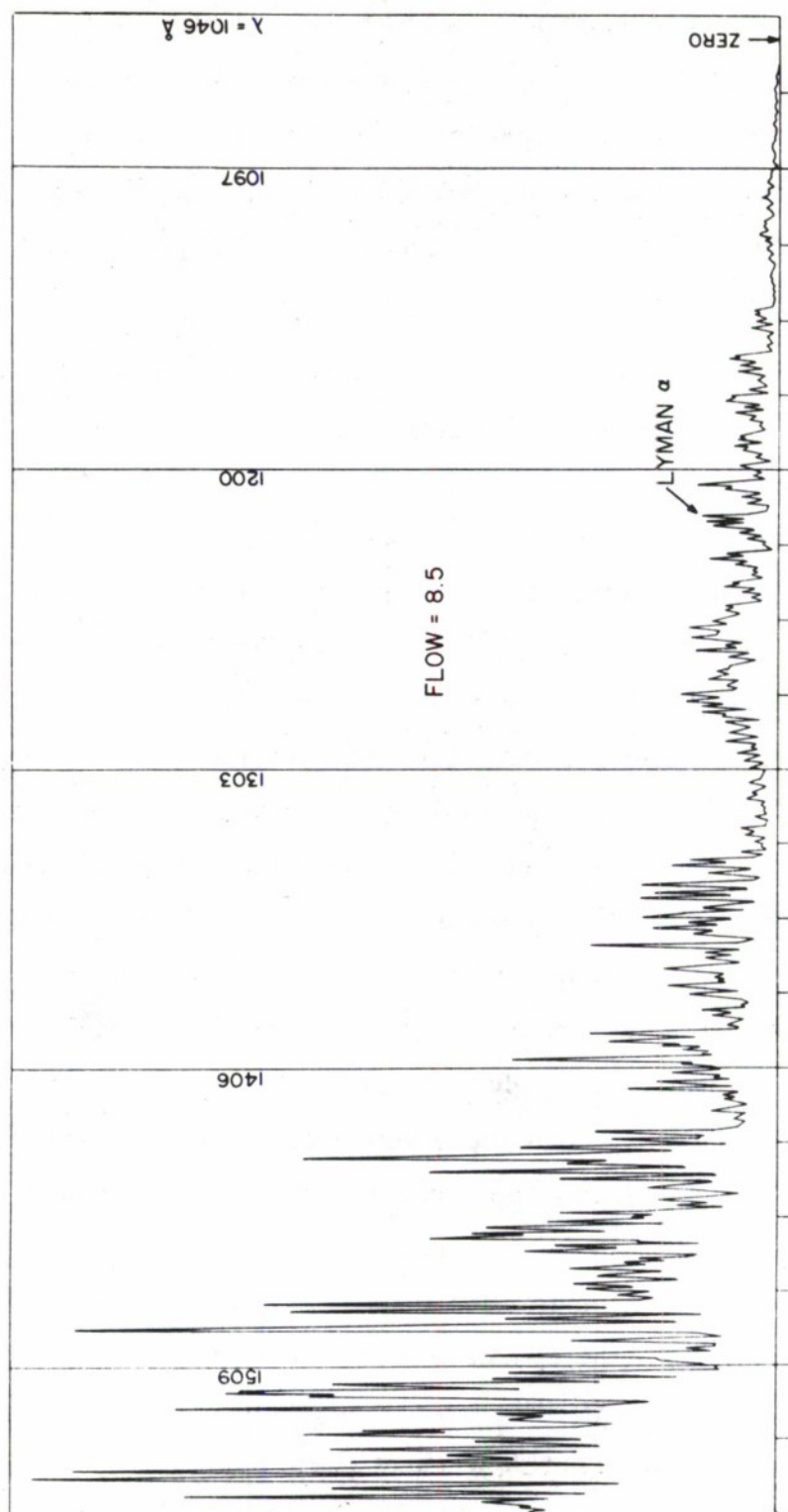


Figure 5. Spectrum of High-Pressure Hydrogen Glow Discharge; Abcissa: Wavelength,  $\lambda$  ; Ordinate: Intensity

density is reduced and the discharge power is kept essentially constant. Further reduction in pressure would continue to improve the spectrum until the electron and/or ion mean free path approaches the dimensions of the electrodes and/or the minimum internal source tube dimensions. These effects will not be discussed, since the relevant information is available in several books on glow discharge processes<sup>[7, 8, 9]</sup> and because there are other simple methods of obtaining the desired spectrum.

Probably a buffered glow discharge (consisting of hydrogen and an inert buffer gas) would be the most direct and simple method of producing the desired monochromatic spectrum in the vacuum ultraviolet portion of the spectrum. Figure 6 shows the emission spectrum of a tank of commercial grade argon, using a source which is essentially the same as that used to produce the previous hydrogen spectra. The discharge power was probably within 20 percent of that in the case of hydrogen, and the pressure was within the range illustrated in the two previous spectra. The emission lines are identified by element, argon, nitrogen, oxygen, and hydrogen being the only elements observed. Since the latter three elements were only impurities in the argon, it should be safe to assume that they constitute 1 percent or less of the total gas. Other tanks of argon have produced similar spectra. Note the almost complete absence of the  $H_2$  emission spectrum, there being a few lines which cannot be positively identified and which, therefore, could be  $H_2$ . However, these lines are almost three orders of magnitude less intense than Lyman  $\alpha$ . To allow the Lyman  $\alpha$  line to remain on the chart, the sensitivity of the electronics was reduced 30 times in the region surrounding Lyman  $\alpha$ . This is indicated by the full-scale photomultiplier current,  $i$ , shown at the top of the chart, which is  $3 \times 10^{-8}$  for the Lyman  $\alpha$  region and  $0.1 \times 10^{-8}$  A for the rest of the region above 1066 Å. The intensities of several lines are indicated, and there are no lithium fluoride windows in the light beam. Note the



Figure 6. Spectrum of Argon-Hydrogen, Oxygen, Nitrogen Glow Discharge; Wavelength,  $\lambda$ ; Ordinate: Intensity

two argon lines at 1048 and 1066 Å. Using the same power, it has been observed that the intensity of the buffered discharge is equal to or greater than that of a pure hydrogen discharge at Lyman  $\alpha$ . Some argon buffered discharges have produced Lyman  $\alpha$  lines which are an order of magnitude more intense than pure hydrogen discharges operating under similar conditions. For a discussion of the spectrum of the buffered discharge, References [1] and [2] should be consulted.

The major criticism of the buffered discharge is that it probably would operate at a lower hydrogen pressure than a pure hydrogen discharge, and, consequently, would have a shorter life due to "cleanup" of the hydrogen. To offset this effect, an increased buffer gas pressure and/or a more carefully constructed source may be required. However, the importance of this problem cannot be determined until quantitative data is obtained on the spectral purity vs buffer gas composition and relative density.

The problem of hydrogen "cleanup" may be solved by using a mixture of uranium and uranium hydride as a hydrogen source.\* This mixture has the property of providing a constant hydrogen pressure at a constant temperature which is essentially independent over a wide range of composition.<sup>[10]</sup> An additional advantage is that the free uranium reacts with any noninert gas in the source, thereby removing impurities from the source. The main disadvantage of such a source is that some method of heating the U-UH<sub>3</sub> mixture must be provided. The degree of temperature regulation of the heater required to produce a given intensity stability remains to be determined. However, a dual-beam technique, to be described later, is capable of removing these variations as long as the power applied to the source remains within the limits

---

\* Such sources were constructed by Dr. H. E. Hinteregger of Air Force Cambridge Research Laboratories until 1956.



in which the source will operate properly. It should be possible to compensate for pressure variations and other factors which would otherwise cause the source intensity to vary by at least a factor of five.

One major assumption in the preceding sections is that the beam emerging from the source is collimated. The degree of collimation determines the degree of accuracy with which Beer's Law predicts the absorption versus density and path length. Little is known about the degree of collimation of the present sources and whether or not they can be collimated with the proper optics. None of the sources previously used possess the required spectral purity to determine how well they follow Beer's Law by absorption measurements, and no known measurements have been made on the distribution of intensity versus angle of the sources.

In a single-beam system, the degree of collimation is not important if an empirical calibration or a function more complex than Beer's Law, incorporating the angular intensity distribution, is satisfactory. However, a question remains as to how appropriate some of the dual-beam techniques (to be described later) are when the source is not well collimated. An important reason for striving for a well-collimated source is that such a source of the required spectral purity can be used to construct an instrument that could easily be the best secondary standard of humidity measurements, since its operation is based on a simple mathematical formula requiring only the knowledge of several physical constants. These constants have been measured to a fair degree of accuracy, and the instrument itself allows the determination of these constants with an accuracy limited only by the accuracy of the system and the primary standard.

Once these constants are known, the absorption versus density is determined by a simple zero absorption calibration, the path length, and the

measurement of any background gas density and pressure, if the latter is necessary to obtain the desired accuracy. The zero absorption measurement can be made by flushing the path with dry nitrogen, which is transparent for all practical purposes; the relatively low absorption by background gases simplifies the measurement of these gases. It should be mentioned that the absorption coefficient of  $O_2$  is slightly pressure-sensitive, thereby requiring the measurement of density and pressure or correcting for this effect.<sup>[11]</sup> In a later section, a technique will be discussed which may be capable of automatically compensating for the background gases encountered in the lower troposphere.

Collimation can be accomplished by restricting the aperture of the detector if the intensity loss is permissible. Such a system, provided with a small removable aperture, is capable of self-calibration when there is a question as to how well Beer's Law applies using the maximum aperture. Calibration would be accomplished by measuring the intensity with the aperture inserted and with it removed for each value of dry air and/or water vapor density, including a zero absorption value provided by an atmosphere of dry nitrogen. In the small aperture case, the absorption should be accurately predicted, given the dry air density and water vapor density. If the system works well in both cases, the  $I/I_0$  should be identical at each value of air and water vapor density.

#### WINDOWS AND FILTERS

The previous discussions assume that there are no problems such as the formation of a thin film of water and/or other material on the surface of the window. However, it is quite obvious that some surface reaction takes place when the transmission of various lithium fluoride windows is investigated with respect to surface treatment and exposure to the atmosphere. Uchida, Kato, and Matsui<sup>[12]</sup> have shown that at Lyman  $\alpha$  the transmission of a freshly

cleaved sample of LiF dropped from 78 to 48 percent after a 10-day exposure to the atmosphere and to 43 percent after an additional 12-day exposure. Additional information may be obtained by studying the data in Table I, which were obtained by the author and Dr. W. J. Scouler of MIT's Lincoln Laboratory; all measurements are at Lyman  $\alpha$ . Note that the transmission is increased by approximately 20 percent by heating to 550 or 600°C. Tests on other crystals from the same batch have produced similar results as long as the temperature exceeded 500°C.

Another disturbing possibility is that the thickness of any adsorbed water vapor film might fluctuate, as the humidity fluctuates around 100 percent RH at temperatures on the order of 0 to 20°C. First, this could cause the system response to deviate from the theoretically predicted absorption, and, second, it could increase the response time to the time required by the film to reach equilibrium. The latter could be the dominant factor in the response time, since the limitations imposed by the source intensity, detector efficiency, and the electronics suggest that the time required to provide a measurement accurate to within 1.0 percent is on the order of 0.03 to 0.001 seconds.

Therefore, a careful investigation of the nature of any surface films and of techniques for reducing them and/or their detrimental effects is in order. Such experiments are planned, since the equipment constructed to measure the crystal transmission can also be used to determine these surface effects by the admission of various mixtures of water density and dry air density.\* However, precautions must be taken so that the surface effects on the cell windows are not misinterpreted as surface effects on the window samples being studied. The

---

\*The systems, excluding the absorption cells and window transmission measuring portions, were designed by Dr. Scouler and have proven capable of maintaining an intensity stability of 0.2 percent or better for periods of 30 minutes or longer.



Table I

History of Window Sample No. 11<sup>\*</sup>

	Trans- mission	Date
Remove from package about 2 years after purchase	0.559	4/9/63
Heat to approximately 550°C in air, place in vacuum system within 30 min.	0.766	4/17/63
30 min. later under vacuum	0.759	
Removed from vacuum and placed in desiccator Possibly exposed to high humidity while being used as a control sample along with other crystals which were being coated with thin films	0.584	5/7/63
Approx. 1 hour later under vacuum	0.568	
Removed from desiccator	0.557	5/13/63
Still under vacuum	0.549	5/14/63
Heat to 600°C 30 min. in air	0.758	5/14/63
In vacuum, liquid nitrogen trapped	0.749	5/15/63
Desiccator 10 days later	0.591	5/25/63

<sup>\*</sup> Size: 1/2-in. by 1/2-in. x (approx.) 2-mm thick.



actual quantitative effects of the variable window transmission may not be as large as has been implied, and possibly may not be important in many applications if zero checks can be carried out every hour or so. The fact that the percentage transmission change appears to decrease with time may be considered favorable, in that the transmission may approach some minimum or at least drop logarithmically, thereby requiring less frequent calibration with increasing time. In addition, if the aging is identical for various windows, a dual-beam technique, to be described later, can compensate for this effect.

It is possible that many of the window problems may be solved by coating the lithium fluoride with a thin film of some other material. Some of the possible advantages of using coated windows are:

- (1) a reduction in the hydrolysis of the window,
- (2) a decrease in the adsorption of water,
- (3) a mechanically tougher and more stable surface, capable of being cleaned, and
- (4) high differential transmission ratios at 1215.6 and 1066 Å.

Because other materials of 1-millimeter thickness are essentially opaque at Lyman  $\alpha$ , the coatings must be quite thin (on the order of 20 to 1000 Å thick), and the short wavelength transmission limit must be as low as possible.

Some of the materials that may be satisfactory are  $\text{CaF}_2$ ,  $\text{MgF}_2$ ,  $\text{Al}_2\text{O}_3$ ,  $\text{MgO}$ , and  $\text{SiO}_2$ . Films of  $\text{CaF}_2$ ,  $\text{MgF}_2$ , and  $\text{Al}_2\text{O}_3$  have been deposited on LiF windows, and their transmissions have been measured, producing values of 15 to 35 percent at Lyman  $\alpha$ , while, in some cases, reducing the transmission at 1066 Å (the aforementioned argon emission line) by a factor of 20. Data have not been obtained on water adsorption properties, however, the exact nature of the surface film and any contaminants is unknown.

It is expected, however, that higher transmission can be obtained with  $\text{Al}_2\text{O}_3$  and  $\text{MgF}_2$ , since the set of crystals coated with  $\text{CaF}_2$  at the same time as the above coatings produced a much lower transmission than previous crystals coated with  $\text{CaF}_2$ . Also, sample No. 11 was used as a control when the crystals were removed from the laboratory to be coated by a commercial firm, and its transmission dropped 20 percent in the process. The main objective of these coatings was to determine if any of these materials could be deposited and if the transmission was adequate to merit further investigation. Considering the relevant factors, all of the materials look promising, and additional work is planned in an effort to obtain the maximum transmission and surface stability.

#### DETECTORS

The detector problem, excluding the window, essentially has been solved, since several satisfactory detectors are commercially available which previously were laboratory items and/or specially modified commercial items. The simplest detector is the nitric oxide (NO) photoionization chamber, previously developed by the Naval Research Laboratory. These devices are sensitive from 1050 Å (limited by the LiF window) to 1353 Å (the long-wavelength limit of photoionization in NO), and possess typical quantum efficiencies\* of from 0.1 to 0.5 at Lyman  $\alpha$ . The response time of this detector is not known by the author, but is probably is in the order of  $10^{-3}$  seconds. The only equipment required to utilize these detectors is a bias supply (a small battery is excellent) of 10 to 50 volts and a current-measuring system; because of the low currents to be measured ( $10^{-7}$  to  $10^{-12}$  A), the current-measuring system generally would consist of an electrometer. Several electrometers quite adequate for most applications are commercially available; some of these units are capable

---

\* The quantum efficiency of a device is defined as the number of photoelectrons produced per incident photon; it ranges from 0.0 to 1.0.

of producing a logarithmic function of the input.\* If the optimum response time and/or ruggedness are desired, the work of Praglin and Nichols<sup>[13]</sup> should be consulted. They suggest that a response time of 0.1 to 0.03 second can be obtained with a sensitivity of  $10^{-12}$  A.

Photomultipliers, sensitive only in the vacuum ultraviolet, also make excellent detectors in some applications. Some devices have been prepared with quantum efficiencies of 10 to 30 percent at Lyman  $\alpha$  and  $10^{-4}$  and  $10^{-8}$  at 2500 A or higher.<sup>[14]</sup> \*\* The photomultiplier output can be measured by measuring the current at the anode (providing an analog output), or by measuring the output pulses due to individual photoelectrons (providing a digital output). The former method requires a carefully regulated power supply, since the photomultiplier gain is proportional to the high voltage of the power supply, while the latter method would require a high-speed counter in order to obtain rapid response and accuracy simultaneously. An advantage of the analog output of the photomultiplier is that currents on the order of  $\mu$ A to 1mA (as opposed to  $\mu\mu$ A for the NO detector) can be obtained, thereby eliminating the need for an electrometer-type current measuring device. The advantage of the digital technique is that a dynamic range of  $10^4$  could be covered with an accuracy of 1 to 0.01 percent, using a measuring time of 1.0 second; various compromises can be made in the dynamic range, accuracy, and measuring time, depending on the applications. The accuracy of the digital system following the detector is  $\pm 1$  part in  $10^6$  to  $10^9$  per day,  $\pm 1$  count. The maximum counting

---

\* For example, Keithley Instruments Inc., 12415 Euclid Ave., Cleveland 6, Ohio.

\*\* This paper also presents data on the quantum efficiency and the spectral response of photodiodes, which should also apply to photomultipliers, with photocathodes of the same material.



rate is limited by the counters available ( $10^8$ /second), and the photomultiplier's transit time ( $10^{-6}$  to  $10^{-9}$  second, depending on construction and voltage).

Because of the high work function of the photocathode materials used in these devices, the "dark current" (in the analog mode) or the noise pulses (in the digital mode), produced by thermal electrons, cosmic rays, radio-active contaminants in the device, and other similar "noise" sources, are equivalent to an input flux of 5 to 50 photons/second. Such background noise can be ignored in most applications, since typical sources produce a Lyman  $\alpha$  flux of  $10^8$  to  $10^{10}$  photons/second, depending on the gases used, power level, source construction, and system geometry.

## SCATTERING

An examination of the error caused by scattering of aerosols and/or liquid water drops shows that it always is less than 2 percent and generally would be from one to two orders of magnitude less. The 2 percent figure assumes a path length of 8 centimeters (a length appropriate for measurements of dew points of  $-30^\circ\text{C}$  or less),\* a partial diameter of  $10^{-5}$  cm (Aitken nuclei), and a density of  $4 \times 10^6$  particles/cubic centimeter (an extremely high value in any location). Since such a concentration rarely would occur, except in a heavily industrialized area at or near the ground, it is highly unlikely that such a low dew point would be observed in the same place at the same time.

A path length of 0.8 centimeter (appropriate for a dew point of  $-10^\circ\text{C}$ ) would reduce the effect to 0.2 percent. Fog with a liquid water content of 0.3 gram/cubic meter and a drop size of 1 to  $10\mu$  would produce an error of 0.004 percent or less on a system with 0.4-centimeter path length (appropriate length

---

\* The appropriate path length versus density will be covered later.



for dew points of  $0^{\circ}\text{C}$  or higher). Smaller drop radii are highly unlikely. Consequently, it is evident that scattering (particulate absorption is considered as a part of the scattering loss) can be ignored in most applications. Scattering may become significant in the measurement of small variations in a relatively high water vapor density; such measurements are often important in the study of turbulence in the atmospheric boundary layer and in the propagation of electromagnetic radiation.

## SYSTEMS

Considering the present state-of-the art in vacuum ultraviolet technology, it does not appear reasonable to expect that one type of system which is the optimum system for all applications can be constructed. For example, a dual-beam system consisting of a reference path probably would be superior to any single-beam system except when size, weight, and cost were major factors. Also, the particular application would determine whether or not some simple operational procedure and a relatively simple system could be substituted for a more complex automatic system. For example, if a dry air reference sample periodically could be introduced in the sampling path, a single-beam system might well be more desirable than a more complex dual-beam system. Also, if the system need not operate for more than an hour or two (as in a radiosonde application), then a significant reduction in size, weight, and cost may be possible. As a general rule, the cost should be directly related to the accuracy, reliability, and response time required and the range of variables encountered, while it should be related inversely to the size, weight, and calibration frequency.

The selection of a good, or the optimum, system for a given application requires a detailed set of requirements and an intimate knowledge of all of the factors concerning the system. Although the present state-of-the-art does not

provide adequate information to construct the optimum system for a given application, it is possible to outline systems that will be adequate in many applications. Enough information is available so that no major unforeseen problems should arise. Further insight into the problems may be gained by considering the construction of a single-beam system. In the following discussions, it will be assumed that the total emission at wavelengths other than Lyman  $\alpha$  is less than 0.1 percent of that at Lyman  $\alpha$ .

First, the influence of the path length on the measurements should be considered. Table II lists the saturation vapor pressure and saturation density versus temperature, along with the path length necessary to reduce the light intensity by  $1/e$  due to water vapor absorption alone at saturation. The columns headed  $k_1 \rho_1 / \rho_0$  and  $k_2 \rho_2 / \rho_0$  indicate how much of the absorption is caused by water vapor and oxygen, respectively, assuming a dry air pressure of 760 millimeters Hg and computing the dry air density STP (760 millimeters and  $0^\circ\text{C}$ ). Note that the two absorptions are equivalent at about  $-35^\circ\text{C}$ . If the range of water vapor density is relatively small and the maximum signal-to-noise ratio and response time are desired, then an appropriate path length is the value indicated. Longer path lengths would drastically decrease the signal, since the absorption is an exponential function of density, while shorter path lengths would require exceptional source stability, because of the reduced intensity change per unit density change. With a slight compromise, it should be possible to satisfy most requirements by providing two or three automatically selected path lengths.

If a wide range must be covered with few or no changes in path length, then a logarithmic amplifier (in an analog system) and a reasonable compromise in path length may suffice. Generally, this combination sacrifices response time or accuracy, or it necessitates a much more intense source.

Table II

## Saturation Vapor Pressure and Density Versus Temperature

$T(^{\circ}\text{C})$	P (mb)	$\rho$ ( $\text{gm}^{-3}$ )	X (cm)	$\frac{k_1 \rho_1}{(k_1 \rho_1 / \rho_{1_o})}$	$\frac{k_2 \rho_2}{(k_2 \rho_2 / \rho_{2_o})}$
<u>Saturated over Water</u>					
+40	73.78	51.19	0.0407	24.6	0.0619
+30	42.43	30.38	0.069	14.6	0.0640
+20	23.37	17.30	0.121	8.32	0.0662
+10	12.27	9.40	0.221	4.52	0.0686
0	6.11	4.85	0.429	2.33	0.0711
-10	2.86	2.36	0.885	1.33	0.0738
-20	1.25	1.07	1.94	.515	0.0767
<u>Saturated over Ice</u>					
-10	2.60	2.14	0.971	1.03	0.0738
-20	1.03	0.884	2.35	0.425	0.0767
-30	0.38	0.338	6.21	0.162	0.0798
-40	0.128	0.119	18.20	0.057	0.083
-50	0.039	0.038	55.5	0.018	0.087

In an attended ground installation, where the path length could be changed when necessary and a dry air sample periodically inserted, a system consisting of a single-beam source, nitric oxide detector, and electrometer should be satisfactory. If the source is well-collimated (which should be possible, since



any intensity loss necessary could be counteracted by decreasing the response time) and the optimum path length is chosen, the error should be less than 0.25 percent of a full-scale 99 percent of the time, assuming:

- (1) a source intensity of  $2 \times 10^7$  photons/second (many orders of magnitude below the maximum obtainable),
- (2) the noise is due to the random photon generation process,\*
- (3) a detector quantum efficiency of 0.2,
- (4)  $1/e$  absorption due to water vapor,
- (5)  $O_2$  absorption corrected, and
- (6) a response time of 1 second.

For a random photon generation process, the noise is inversely proportional to the square root of time. Although other types of single-beam systems can be constructed, using logarithmic electronics or a digital type readout, more intense sources, etc., the rest of the report deals with the dual-beam system.

Figure 7 shows a particular type of dual-beam system in which the output of the reference detector is part of a feedback loop which regulates the source intensity.\*\* If it is assumed that the path lengths are identical, the detectors

---

\* It has been observed that the source constructed for spectrographic use is limited by random photon noise when it is operating properly.

\*\* As far as is known, Dr. H. E. Hinteregger and others of Air Force Cambridge Research Laboratories constructed the first ultraviolet dual-beam sources. This information was obtained from other members of the laboratory. A copy of an unpublished paper, obtained from Dr. Hinteregger, contains excellent information on the techniques of vacuum ultraviolet water vapor measurements. It appears that components of equal quality have not since been duplicated. As is often the case, the aforementioned report was not obtained until these investigations had been in progress for several years.



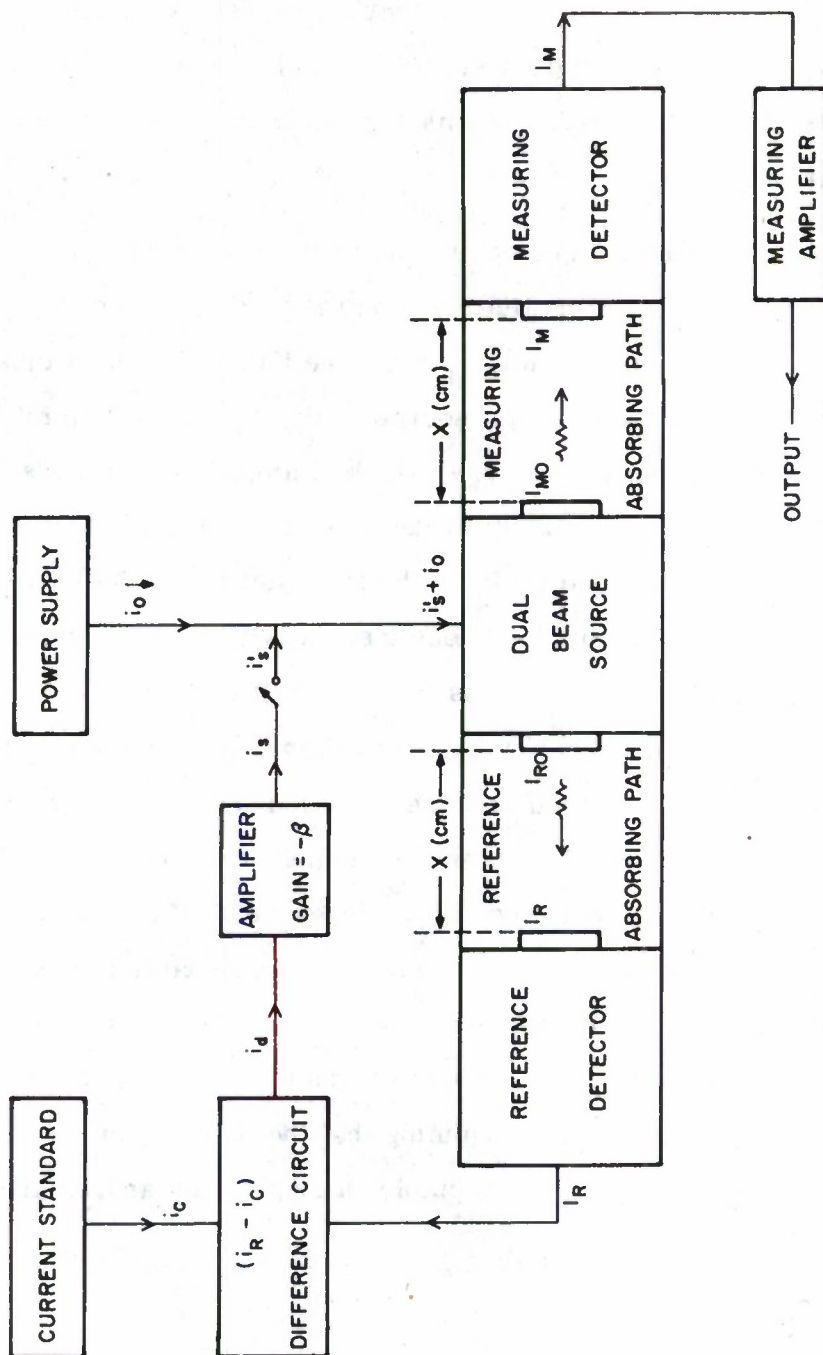


Figure 7. Dual-Beam Absorption Measuring System

and current standard are stable, the intensities of the two beams remain identical with changes, the feedback loop gain is  $10^5$  or more, and the measuring amplifier is stable, then it can be shown that the system compensates for source intensity changes, variation in the feedback amplifier gain, and variations in the dry air absorption if the reference path is filled with dry air of the same density as that of the measuring path.\*

Although it has been completed, the mathematical proof of this statement will not be given, however, a qualitative explanation is in order:  $i$  supplies the main source current and  $i'_s$  (or  $i_s$  when the feedback loop is closed) supplies a correction current. If the source begins to increase in intensity, the difference circuit generates a signal which is amplified and tends to reduce the current to the source. Similarly, a decrease in source intensity would be compensated for by an increase in  $i'_s$ . The same action takes place if the reference path transmission or the detector sensitivity varies. As long as the amplifier gain,  $\beta$ , is high, variations in it have little effect. Therefore, this system can be used to compensate for dry air absorption and source instability. If a dry air correction is obtained in some other manner, and if the reference path is open to the atmosphere and is made much shorter than the measuring path, then this system can compensate for window adsorption, assuming that the effects are similar on all of the windows. If a reasonably intense source is constructed (e. g. ,  $10^{10}$  photons/second), it should be possible to construct a system with a response time of 0.001 second and a peak-to-peak noise level of 1 percent or less of full-scale, assuming that the path length has been optimized. If a slower response is acceptable, a longer path and/or greater accuracy may be obtained.

---

\* In actual practice, the reference path may contain dry air with a density equal to the total air density without producing a significant error.

## DENSITY CORRECTION AND MEASUREMENT

Some form of density measurement, as previously mentioned, is necessary so that a correction for the absorption by  $O_2$  can be made when measuring low water vapor densities. This section describes an absorption measuring system which is capable of satisfying the above requirement and, in addition, is capable of measuring  $O_2$  density from the surface to 60 kilometers (above which the path length becomes excessive), with little or no absorption by background gases. The components for this system are much easier to construct than those for the Lyman  $\alpha$  measurements, and probably can be purchased commercially.

Returning to Figure 3, notice that the RDR at 1469.6 Å (an emission line of xenon) is appropriate for the measurement of  $O_2$ . In addition, either the coefficients and/or the densities of the following "background" gases are such that they may be ignored below 80 kilometers:  $N_2$ ,  $CO_2$ ,  $H_2O$ ,  $NO$ ,  $N_2O$ ,  $O_3$ ,  $O$ , and  $N$ . The absorption coefficient of  $NO_2$  is approximately 300, while its density is unavailable and the coefficient of xenon is unknown; it is doubtful that either would contribute any significant absorption. For this system, the source would be a xenon glow discharge tube, and the detector would be an ethylene sulphide photoionization cell.<sup>[15]</sup> The rest of the system would be similar to those used to measure water vapor. The source should be much more predictable and reliable, since the only gas would be xenon and a uranium "getter" could be used. It is hoped that the details of this device can be published later, since it can essentially be constructed from commercially available components.

## SUMMARY

The theoretical basis for the vacuum ultraviolet humidimeter has been discussed in detail, along with the major fundamental problems associated with the construction of a practical instrument. Different systems have been

mentioned, and the performance of a typical system has been predicted. The effect of absorption and scattering by atmospheric particulate matter has been calculated, along with the system parameters for various operating conditions.

#### ACKNOWLEDGMENTS

The author wishes to express his appreciation to D. L. Randall and others at the Naval Research Laboratory for their kindness in supplying some components for the vacuum ultraviolet portion of this work. Thanks are due to Professor D. P. Keily of the Meteorology Department, of the Massachusetts Institute of Technology, for his advice and encouragement on this problem; to Dr. William Scouler of Lincoln Laboratory, MIT, for his part in the experimental work; and to J. R. Bauer and other members of Group 34 for their support. Also, thanks go to Dr. H. E. Cramer, Dr. F. A. Record, G. Fontes, H. Geary, J. Luby, and J. Peers of Round Hill Field Station for their assistance.

This work was supported in part by the Meteorology Department, U. S. Army Research and Development Activity, Fort Huachuca, Arizona.



## REFERENCES

1. J. E. Tillman, "Water Vapor Density Measurements Utilizing the Absorption of Vacuum Ultraviolet and Infrared Radiation," (paper presented at 1963 International Symposium on Humidity and Moisture, Washington, D. C. , May 1963. )
2. J. E. Tillman, "Atmospheric Humidity Measurements by Ultraviolet Techniques," M. S. thesis, M. I. T. , Department of Meteorology, June 1961.
3. D. L. Randall, T. E. Hanley, and O. K. Laurison. "The N. R. L. Lyman-Alpha Humidiometer," Naval Research Laboratory Progress Report, June 1963.
4. D. R. Hay and H. E. Turner, "Investigation of Refractometer Measurements in the Atmosphere at High Relative Humidities and Temperatures." AFCRL-63-631, Air Force Cambridge Research Laboratories, Bedford, Mass. , 1963.
5. R. E. McGavin, "A Survey of the Techniques for Measuring the Radio Refraction Index," National Bureau of Standards Technical Note 99, Boulder, Colorado, May 1962.
6. K. Watanabe, M. Zelikoff, and E. C. Inn, "Absorption Coefficients of Several Atmospheric Gases," Air Force Cambridge Research Center Technical Report No. 52-23, Geophysical Research Papers, No. 21, June 1953.
7. J. R. Acton, and J. D. Swift, Cold Cathode Discharge Tubes, New York, Academic Press, 1963.
8. L. B. Loeb, Basic Processes of Gaseous Electronics, Berkeley and Los Angeles, California, University of California Press, 1960.
9. S. C. Brown. Basic Data of Plasma Physics, Cambridge, Massachusetts. Technology Press, 1959.
10. F. H. Spedding, A. S. Newton, J. C. Warf, O. Johnson, R. W. Nottory, I. B. Johns and A. H. Daane, Nucleonics, 4, 4 (1949).

11. K. Watanabee, H. Sakai, J. Motti, and T. Nakayama, "Absorption Cross Section of  $O_2$ , NO and  $NO_2$  with an improved Photoelectric Method," Air Force Cambridge Research Center Technical Note 58-658, Scientific Report No. 4, December, 1958.
12. Y. Uchida, R. Kato and E. Matsui, "Optical Properties of Some Solids in the Vacuum Ultraviolet," J. Quant. Spectry. Radiative Transfer, 2, 589-598, 1962.
13. T. Praglin, and W. A. Nichols, "High-speed Electrometers for Rocket and Satellite Experiments," Proc. Inst. Radio Engrs., 48, 771-779, 1960.
14. L. Dunkelman, W. B. Fowler and J. Hennes, "Spectrally Selective Photodetectors for the Middle and Vacuum Ultraviolet," Appl. Opt., 1, 695-700, 1962.
15. J. P. Hennes, R. Scolnik and A. K. Stober, J. Opt. Soc. Am., 51, 1461A, 1951.

## SUMMARY OF REFRACTION RESEARCH ACTIVITIES

L. J. Galbiati

The specific results and conclusions of the individuals who participated in this meeting cannot be summed in the allotted time. I would, however, like to present some general conclusions and observations, based on the excellent discussions of the past two days.

1. A considerable amount of the progress achieved in the refraction effects task during the past six months results from the efforts being aimed at specific Air Force operational-type problems, and not simply from research projects conducted as such.
2. Unresolved differences of opinion exist on methods of solving the problem. The statistical and dynamic measurement approaches complement each other, and both should be followed at this time.
3. Better understanding and identification of critical environmental parameters is needed. An example of this was the relationship of temperature difference and transmitted light density, reported by the Army Ballistic Research Laboratories.
4. New techniques should be developed for both sensing the environment and analyzing the resultant data. The precision humidiometer, developed by D. L. Randall of the Naval Research Laboratory, the rocket-sounding instrumentation, developed by Dr. D. L. Hay of the University of Ontario, the use of the digital profile of the atmosphere by R. Crane, and the MITRE Line Integral Refractometer are examples of this. Again, the greatest progress can be made if these developments are associated with user applications.

5. Old techniques should be reconsidered in view of advancing technology; the long-path absorption refractometer, presented by W. G. Tank of Boeing, and the refraction measurements by lunar radar illumination and tracking, covered by P Kalaghan of Ewen-Knight, are two examples of this.
6. The dependence of all the correction techniques on radiosonde measurements was certainly clear. The measurements currently being obtained at the Eastern Test Range indicate the magnitude of the errors in these measurements from an operational standpoint, and should prove extremely valuable.
7. The original work performed in this field by Archie Straiton and others at the University of Texas, and the basic data provided by Ken Norton and his colleagues at NBS contribute heavily to some of the specific accomplishments in this area.
8. In the early 50's, the fixed-path measurement link was a significant improvement over point measurements. In the late 50's and early 60's, the use of fixed-wing test aircraft, equipped with refractometers and other probes, provided another real advance in measurement capability. Now, techniques for determining the three-dimensional characteristics of the atmosphere should be devised.

With particular reference to the last point, it appears to me that the next logical step to be taken is that of combining the additional dimensional freedom provided by a helicopter with the unique characteristics of the Line Integral Refractometer.



## BIBLIOGRAPHY

The 84 references cited extend the Bibliography listings in the Proceedings of the Second Tropospheric Refraction Effects Technical Review Meeting (409 items), \* and in the first volume\*\* of this report (223 items).

Abramis, B. D., S. Rogers, and C. J. Breitwieser, Atmospheric Refraction Error Estimate of Sighting Error Changes in Phase Velocity, 1947, CVAC/DEVF-4036 (U).

Advisory Committee to AF Systems Command, Report of the Ad Hoc Panel on Electromagnetic Propagation, National Academy of Sciences---National Research Council, 1962.

Agy, V., "Ionospheric Effects Produced by Solar Flare Radiation," Phys. Rev., 102, 3 (1956) 917.

Arendt, P. R., Natural Tolerance Limits of Doppler Measurements of Outer-Space Radio Signals, U. S. Army Signal Research and Development Laboratory, 1962, USASRDE-TR 2253 (U).

Barrows, E. C., Residual Range and Range Rate Errors Due to the Troposphere, National Bureau of Standards Central Radio Propagation Laboratory (Boulder Labs.), 1962.

Bauer, S. J., "On the Structure of the Topside Ionosphere," J. Atmos. Sci. 1962; see also NASA N62-12801, 22 March 1962 (U).

Bean, B. R., B. A. Cahoon, and G. D. Thayer, "Tables for the Statistical Prediction of Radio Ray Bending and Elevation Angle Error Using Surface Values of the Refractive Index," J. Research Natl. Bur. Standards, 64D, 5 (1960) 487-92.

Bean, B. R., G. D. Thayer, and B. A. Cahoon, "Methods of Predicting the Atmospheric Bending of Radio Rays," J. Research Natl. Bur. Standards, 64D, 5 (1960) 487-92.

---

\*See ESD-TDR-64-103, Vol. III, May 1964, pp. 407-440.

\*\*See ESD-TDR-64-148, Vol. I, November 1964, pp. 209-228.

## BIBLIOGRAPHY (Cont'd.)

Blumle, L. J., Studies of the Equatorial Ionosphere Using the Faraday Effect on Satellite Radio Transmissions, Penn. State Univ., Ionosphere Research Laboratory, Scientific Report No. 156, 1961 (U).

Booker, H. G., B. Nichols, D. Farley, P. Nicholson, J. Renau, and P. Weaver, Studies on Propagation in the Ionosphere, Cornell University, School of Electrical Engineering, EE-379, 1958; AD-204119 (U).

Booker, H. B., J. Renau, and D. Farley, Studies on Propagation in the Ionosphere, Cornell University, School of Electrical Engineering, EE-443, 1959; AD-233031 (U).

Bowles, K. L., "Incoherent Scattering by Free Electrons as a Technique for Studying the Ionosphere and Exosphere: Some Observations and Theoretical Considerations," J. Research Natl. Bur. Standards, 65D, 1 (1961) 1-14 (the first 13 pages are the title).

Chivers, H. J. A., Radio Star Scintillations and Spread-F Echoes, National Bureau of Standards Central Radio Propagation Laboratory, 1963; see also, J. Atmos. and Terr. Physics, 25, 8 (1963) 468-72.

Chivers, H. J. A., "The Location of the Irregularities Responsible for Ionospheric Scintillation of a Radio Source," London, Proc. Internatl. Conf. Ionosphere, (1962) 258-66 (U).

Chivers, H. J. A., and R. D. Davies, "A Comparison of Radio Star Scintillations at 1390 Mc/s at Low Angles of Elevation," J. Atmos. and Terr. Physics, 24, (1962) 573-84.

Cunningham, R. M., W. W. Vickers and C. G. Fain, Effects of Clouds and Moist Layer Roughness on Range Rate Errors of Radio Interferometer Tracking and Guidance Systems, Air Force Cambridge Research Laboratory, CRL 63-706, (U).

Davies, K., Doppler Studies of the Ionosphere with Vertical Incidence, 1963, National Bureau of Standards Central Radio Propagation Laboratory, 1961.

## BIBLIOGRAPHY (Cont'd.)

- Doupnik, J. R., A Flexible Method of Determining the Electron Density Distribution in the Ionosphere, Penn State Univ., Ionosphere Research Laboratory, SR-190, 1963 (U).
- Drubin, M., The Ionospheric Effects on a 1000 MCS Pencil Beam, Bedford, Mass., The MITRE Corporation, TM-3008, 1961 (U).
- Farnin, B. M., and K. H. Jehn, Radar Elevations Angle and Range Errors in Representative Air Masses, University of Texas, Electrical Engineering Research Laboratory, EEERL 7-01, 1954; AD-79974 (U).
- Galbiati, L. J. and E. Eames (Maj., USAF), Proceedings of the Second Tropospheric Refraction Effects Technical Review Meeting, I, II, III, 1964; ESD-TDR-64-103, Vol. I, AD-435973; Vol II, AD-441-576; Vol. III, AD-442626 (U).
- Gallet, R. M. The Spectrum of the Electron Density Fluctuations in the Ionosphere, National Bureau of Standards.
- Gautier, T. N., The Ionosphere.
- Gillmore, C. S., and J. K. Hargreaves, "The Occurrence of Short-Duration Cosmic Noise Absorption Events Inside the Southern Auroral Zone," J. Atmos. and Terr. Physics, 25, 6 (1963) 311-17.
- Hill, R. A., and R. B. Dyce, "Some Observations of Ionospheric Faraday Rotation on 106.1 MC/S," J. Geophys. Research, 65, 1 (1960).
- Jackson, J. E., R. W. Knecht, and S. Russel, First Soundings of the Ionosphere, NASA, TN-D-1538, 1963 (U).
- Janes, H. B., and M. C. Thompson, Jr., An Experimental Study of Atmospheric Effects on Precision Radar Tracking, National Bureau of Standards, 1963.
- Katzin, M., Studies in Ionospheric Propagation, Part II---VLF Signal Enhancements and HF Fadeouts During Sudden Ionospheric Disturbances.
- Katzin, M., and B. Y. C. Koo, Studies in Ionospheric Propagation, Part I---The Exact Earth-Flattening Procedure in Ionospheric Propagation Problems, CRL 62-341, 1962; AD-277479 (U).



## BIBLIOGRAPHY (Cont'd.)

Knecht, R. W., and T. W. Van Zandt, "Some Early Results from the Ionospheric Topside Sounder Satellite," J. Geophys. Research, 66, 9 (1961) 3078-81.

Knecht, R. W., T. W. Van Zandt, and J. M. Watts, The Ionospheric Topside Sounder Program March 15, 1960 to January 31, 1961, National Bureau of Standards, 1961, NBS-6740; NASA 1962, N62-11336, (U).

Lawrence, R. S., "An Investigation of the Perturbations Imposed Upon Radio Waves Penetrating the Ionosphere," Proc. IRE, 46, 1 (1958) 315-20 (U).

Lawrence, R. S., J. L. Jespersen, and R. C. Lamp, "Amplitude and Angular Scintillations of the Radio Source Cygnus-A Observed at Boulder, Colo.," J. Research Natl. Bureau Standards, 65D, 4 (1961) 333-50.

Lawrence, R. S. and C. G. Little, "On the Analysis of Polarization Rotation Recordings of Satellite Radio Signals," J. Research Natl. Bureau Standards, 64D, 4 (1960) 335-46.

Lawrence, R. S., C. G. Little, and H. J. A. Chivers, "A Survey of Ionospheric Effects Upon Earth-Space Radio Propagation," Proc. IEEE, 52, 1 (1964) 4-27 (U).

Lawrence, R. S., and J. W. Warwick, "The Use of Interferometer Observations of Satellites for Measurement of Irregular Ionospheric Refraction," CSAGI General Assembly, 1958.

Little, C. G., and H. Leinbach, "The Riometer --- A Device for the Continuous Measurement of Ionospheric Absorption," Proc. IRE, 47, 2 (1959) 315-20 (U).

Matsushita, S., Ionospheric Variations During Geomagnetic Storms, National Bureau of Standards, High Altitude Observatory.

Millman, G. H., Atmospheric and Extraterrestrial Effects on Radio Wave Propagation, G. E. Tech. Info. Series R61EMH29, 1961 (U).

Millman, G. H., "The Geometry of the Earth's Magnetic Field at Ionospheric Heights," J. Research Natl. Bureau Standards, 64, 7 (1959) 717-26.



## BIBLIOGRAPHY (Cont'd.)

Millman, G. H., Ionospheric Investigations by Radar Reflections from Echo I, Syracuse, New York, G. E. Co.

Millman, G. H., Radio Astronomical and Satellite Studies of the Atmosphere, Syracuse, New York, G. E. Co., 1963.

Millman, G. H., A Study of the Ionosphere Utilizing the Incoherent Scatter Technique, Syracuse, New York, G. E. Tech. Info. Series, 1962.

Millman, G. H., A. J. Moceyunas, A. E. Sanders, and R. F. Wyrick, "The Effect of Faraday Rotation on Incoherent Backscatter Observations," J. Geophys. Research, 66, 5 (1961) 1564-68.

Millman, G. H., V. C. Pineo, and D. P. Hynek, "Observations of Ionospheric Movements by Incoherent Scattering," J. Geophys. Research, 64, 10 (1963) 3323-27.

Millman, G. H., and F. L. Rose, "Radar Reflections from the Moon at 425 Mc/s," J. Research Natl. Bureau Standards, 67D, 2 (1963) 107-17.

Millman, G. H., and F. L. Rose, A Study of Ionospheric and Lunar Characteristics by Radar Techniques, Syracuse, New York, G. E. Tech. Info. Series, 1961.

Millman, G. H., and A. E. Sanders, An Analysis of Ionospheric Characteristics from Echo I Radar Measurements, Syracuse, New York, G. E. Tech. Info. Series, 1961.

Millman, G. H., and A. E. Sanders, Incoherent Scatter for Reliable Long Distance Communications, Syracuse, New York, G. E. Tech. Info. Series, 1962.

Millman, G. H., A. E. Sanders, and R. A. Mather, "Radar-Lunar Investigations at a Low Geomagnetic Latitude," J. Geophys. Research, 65, 9 (1960) 2619-26.

Moore, G. G., J. F. Willman, and R. E. Hollingsworth, Tracking Station Instrumentation and Data Analysis Techniques for the Measurement of Ionospheric Refraction Effects as Related to the Transit Navigation Satellite Program, University of Texas, Defense Research Laboratory, DRL 476, 1962 (U).

## BIBLIOGRAPHY (Cont'd.)

Norton, K. A., Effects of Tropospheric Refraction in Earth-Space Links, 14th General Assembly of U.R.S.I., 1963.

Norton, K. A., J. W. Herbstreit, H. B. Janes, K. O. Hornberg, C. F. Peterson, A. F. Barghausen, W. E. Johnson, P. I. Wells, M. C. Thompson, Jr., M. J. Vetter, and A. W. Kirkpatrick, An Experimental Study of Phase Variations in Line-of-Sight Microwave Transmissions, National Bureau of Standards, NBS M-33, 1961 (U).

Ochs, G. R., K. L. Bowles, and J. L. Green, "On the Absolute Intensity of Incoherent Scatter Echoes from the Ionosphere," J. Research Natl. Bureau Standards, 66D, 4 (1962) 395-409.

Ostorey, L. R., "The Joint Use of the Ordinary and Extraordinary Virtual Height Curves in Determining Ionospheric Layer Profiles," J. Research Natl. Bureau Standards, 64D, 2 (1960) 111-24.

Pappas, C. F., L. E. Vogler, and P. L. Rice, "Graphical Determination of Radio Ray Bending in an Exponential Atmosphere," J. Research Natl. Bureau Standards, 65D, 2 (1961) 175-9.

Pineo, V. C., "Oblique-Incidence Measurements of the Heights at Which Ionospheric Scattering of the VHF Radio Wave Occurs," J. Geophys. Research, 1956.

Porcello, L. J., An Experimental Study of Rapid Phase Fluctuation Induced Along a Satellite-to-Earth Propagation Path, University of Michigan, Institute of Science and Technology, Radar Laboratory, Report 4563-57-T, 1964; AD-437587 (U).

Post, E. J., Reasons for the Failure of Radio Interferometers to Achieve Their Expected Accuracy, AF Cambridge Research Laboratory, 1963.

Rome Air Development Center, Atmospheric Refraction Effects on Precision Radar Tracking, Rome, New York, Griffiss AF Base, 1961.

Salpeter, E. E., Scattering of Radio Waves by Electrons Above the Ionosphere, AF Cambridge Research Laboratory, CRC-TN-60-397, 1960; AD-238338 (U).

## BIBLIOGRAPHY (Cont'd.)

Schiffmacher, E. R., The Riometer---A Relative to Ionospheric Opacity Meter, National Bureau of Standards (Boulder Labs.), NBS 7605 (U).

Schmerling, E. R., and D. Grant, An Analysis of the Electron Densities in Region F of the Ionosphere, Penn State University, Ionosphere Research Laboratory, SR-147, 1961 (U).

Schriever, B. A. (Maj. Gen., USAF), private communication to A. V. Astin, Director, National Bureau of Standards, 1957.

Space Defense Systems Laboratory, RADC Propagation Studies---Task 1---Backscatter Studies of Ionospheric Irregularities, Rome, New York, Griffiss AF Base, RADC-TDR 63-388, 1963 (U).

Stakutis, V. J., Meteorological Refractive Effects with Altitude on Horizontal 1000 m.c. Beams, Bedford, Massachusetts, The MITRE Corporation, TM-3107, 1963 (U).

Thayer, G. D., "A Formula for Radio Ray Refraction in an Exponential Atmosphere," J. Research Natl. Bureau Standards, 65D, 2 (1961) 181-2.

Thayer, G. D., and B. R. Bean, An Analysis of Atmospheric Refraction Errors of Phase Measuring Radio Tracking Systems, National Bureau of Standards, NBS 7254 (U).

Thompson, M. C. Jr., H. B. Janes, and A. W. Kirkpatrick, "An Analysis of Time Variations in Tropospheric Refractive Index and Apparent Radio Path Length," J. Geophys. Research, 65, 1 (1960) 193-201.

Unz, H., Simplified Analysis of Ionospheric h'(f) Records, Using Wave Refractive Index, Ohio State University Research Foundation, Department of Electrical Engineering (Antenna Lab.), SR-8, CRL 784, OSURF 1116-112, 1961 (U).

U. S. A. National Committee, International Scientific Radio Union, Publication 880, National Academy of Sciences-National Research Council, 1961.

Wait, J. R., Diurnal Change of Ionospheric Heights Deduced from Phase Velocity Measurements at VLF, National Bureau of Standards, 1952.



## BIBLIOGRAPHY (Cont'd.)

Webb, H. D., Ionospheric Research and Propagation Studies, AD-267852 (U).

Whitcraft, W. A. Jr., Bias Error, Variation and Scintillation of Radar Range at L-Band; Preliminary Report, Bedford, Massachusetts, The MITRE Corporation, 1961.

Wright, J. W., The CRPL Electron Density Profile Programme: Some Features and Early Results.

Wright, J. W., "Comments on Models of the Ionosphere Above  $h_{\max}^{F_1}$ ", J. Geophys. Research, 65, 9 (1960) 2595-96.

Wright, J. W., "The F-Region Seasonal Anomaly," J. Geophys. Research, 68, 14 (1963) 4379-81.

Wright, J. W., Mean Electron Density Variations of the Quiet Ionosphere---No. 13---Summary of One Year of Data, May 1959-April 1960, National Bureau of Standards, NBS TN 40-13, 1962 (U).

Wright, J. W., "A Model of the F. Region Above  $h_{\max}^{F_2}$ ," J. Geophys. Research, 1960; see also AGARDograph, 42 (1959) 211-21.

Wright, J. W., L. R. Wescott, and D. J. Brown, Mean Electron Density Variations of the Quiet Ionosphere, National Bureau of Standards, NBS TN 40-8, 1960 (U).

Wright, J. W., L. R. Wescott, and D. J. Brown, Mean Electron Density Variations of the Quiet Ionosphere---No. 8---October 1959, National Bureau of Standards, NBS TN 40-8, 1962 (U).

Wright, J. W., L. R. Wescott, and D. J. Brown, Mean Electron Density Variations of the Quiet Ionosphere---No. 9---November 1959, National Bureau of Standards NBS TN 40-9, 1963 (U).

Wright, J. W., L. R. Wescott, and D. J. Brown, Mean Electron Density Variations of the Quiet Ionosphere---No. 10---December 1959, National Bureau of Standards, NBS TN 40-10, 1963 (U).



## BIBLIOGRAPHY (Concl'd.)

Wright, J. W., L. R. Wescott, and D. J. Brown, Mean Electron Density Variations of the Quiet Ionosphere---No. 11---January 1960, National Bureau of Standards, NBS TN 40-11, 1963 (U).